Res Electricae Magdeburgenses

MAgdeburger FOrum zur Elektrotechnik

In this work, novel circuit models for coaxial cables with braided shields placed above a ground plane are presented. The models are derived from the transmission line theory and are suitable for integration into SPICE simulation programs.

Two types of models are presented. First, a lumped-circuit model is developed in which the cable is divided into small sections, with each section replaced with an equivalent circuit and connected to represent the entire cable. In the second type, a macromodel is developed from the analytical solutions of the transmission line theory to represent the entire cable without discretizing it. This work demonstrates the efficiency of the macromodel in terms of computing time and accuracy compared to the lumped-circuit model. The designed models can be used to calculate the induced voltage at the termination loads of the cable when an incident uniform plane wave is coupled in. These models can also calculate the coupling results due to interference from lumped sources. The developed models are therefore suitable for the circuit EMC analysis of systems that contain shielded cables and are susceptible to field coupling or interference with other systems. The bidirectional coupling between the inside and outside of the cable shield is taken into account, which enables the analysis of interference immunity and emissions. The mathematical functions for calculating the coupling between the inner and outer systems of the cable are transformed into equivalent circuit diagrams that allow the models to be used in the frequency domain or together with nonlinear elements in the time domain.

The developed models for a single conductor shielded cable are expanded for shielded multiconductor cables within the scope of this work. The circuit models are validated by measurements and field simulations, and the results show excellent agreement.

ISSN 1612-2526
ISBN 978-3-948749-16-3
DOI 10.24352/UB.OVGU-2022-037

Moustafa Raya: Circuit Models of Shielded Cables

MAFO 88

Moustafa Raya

Circuit Models of Shielded Single and Multiconductor Cables for EMC Analyses

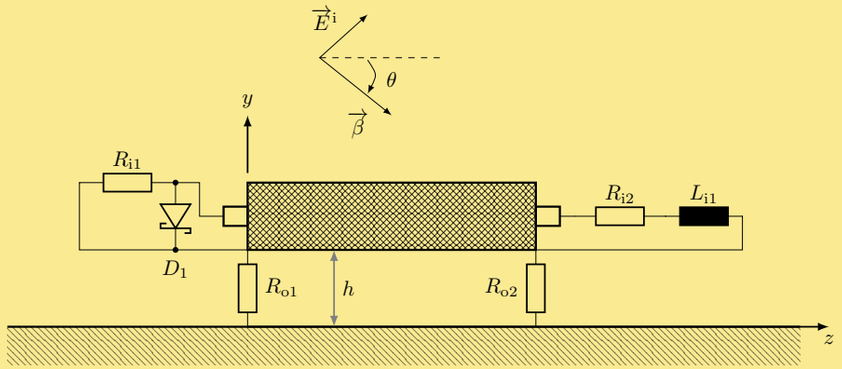

Magdeburg 2022

MAFO
Band 88

Circuit Models of Shielded Single and Multiconductor Cables for EMC Analyses

Dissertation
zur Erlangung des akademischen Grades

Doktoringenieur
(Dr.-Ing.)

von **M.Sc. Moustafa Raya**
geb. am 18.02.1985 in Temnin El Tahta

genehmigt durch die Fakultät für Elektrotechnik und Informationstechnik
der Otto-von-Guericke-Universität Magdeburg

Gutachter:

Univ.-Prof. Dr.-Ing. Ralf Vick

Univ.-Prof. Dr.-rer.nat. habil. Frank Gronwald

Promotionskolloquium am 27. Januar 2022

Res Electricae Magdeburgenses

Magdeburger Forum zur Elektrotechnik, Jg. 20, Band 88, 2022
http://www.mafo.ovgu.de/

IMPRESSUM

Herausgeber:

- Prof. Dr.-Ing. Andreas Lindemann, Lehrstuhl für Leistungselektronik, Institut für Elektrische Energiesysteme
- Prof. Dr.-Ing. habil. Martin Wolter, Lehrstuhl für Elektrische Netze und Erneuerbare Energie, Institut für Elektrische Energiesysteme
- Prof. Dr. rer. nat. Georg Rose, Lehrstuhl für Medizinische Telematik/Medizintechnik, Institut für Medizintechnik
- Prof. Dr.-Ing. Ralf Vick, Lehrstuhl für Elektromagnetische Verträglichkeit, Institut für Medizintechnik

Gründungsherausgeber:

- Prof. Dr. rer. nat. habil. Jürgen Nitsch
- Prof. Dr.-Ing. habil. Zbigniew Antoni Styczynski

alle: Otto-von-Guericke-Universität Magdeburg
Postfach 4120, 39016 Magdeburg

V. i. S. d. P.:
Dr.-Ing. Moustafa Raya
Otto-von-Guericke-Universität Magdeburg, Postfach 4120, 39016 Magdeburg

1. Auflage, Magdeburg, Otto-von-Guericke-Universität, 2022
Zugl.: Magdeburg, Univ., Diss., 2022

Auflage: 100

Redaktionsschluss: Februar 2022

ISSN: 1612-2526
ISBN: 978-3-948749-16-3
DOI: 10.24352/UB.OVGU-2022-037

Druck: docupoint GmbH
Otto-von-Guericke-Allee 14, 39179 Barleben

Declaration of Honor

I hereby declare that I produced this thesis without prohibited external assistance and that none other than the listed references and tools have been used. I did not make use of any commercial consultant concerning graduation. A third party did not receive any nonmonetary perquisites neither directly nor indirectly for activities which are connected with the contents of the presented thesis.

All sources of information are clearly marked, including my own publications.

In particular I have not consciously:

- Fabricated data or rejected undesired results
- Misused statistical methods with the aim of drawing other conclusions than those warranted by the available data
- Plagiarized data or publications
- Presented the results of other researchers in a distorted way

I do know that violations of copyright may lead to injunction and damage claims of the author and also to prosecution by the law enforcement authorities. I hereby agree that the thesis may need to be reviewed with an electronic data processing for plagiarism.

This work has not yet been submitted as a doctoral thesis in the same or a similar form in Germany or in any other country. It has not yet been published as a whole.

Magdeburg, February 4, 2022

Kurzfassung

In dieser Arbeit werden neuartige Schaltungsmodelle für Koaxialkabel mit Geflechtschirm über einer Masseebene vorgestellt. Die Modelle sind aus der Leitungstheorie abgeleitet und eignen sich zur Integration in SPICE-Simulationsprogramme. Es werden zwei Arten von Modellen vorgestellt. Zuerst wird ein konzentriertes Schaltungsmodell (lumped-circuit model) erklärt, bei dem das Kabel in kleine Abschnitte unterteilt ist, wobei jeder Abschnitt durch ein Ersatzschaltbild ersetzt wird. Dann wird aus den analytischen Lösungen der Leitungstheorie ein Makromodell entwickelt, welches das gesamte Kabel ohne Diskretisierung darstellt. Diese Arbeit demonstriert die Effizienz des Makromodells in Bezug auf Rechenzeit und Genauigkeit im Vergleich zum konzentrierten Schaltungsmodell. Die entwickelten Schaltungsmodelle können die eingekoppelte Spannung an den Abschlüssen des Kabels berechnen, wenn eine einfallende ebene Welle in das Kabel eingekoppelt wird. Diese Modelle können auch die Kopplungen aufgrund von Störungen durch konzentrierte Quellen berechnen. Die entwickelten Modelle eignen sich daher für die Schaltungs-EMV-Analyse von Systemen, die geschirmte Kabel enthalten und anfällig für Feldeinkopplungen oder Störungen mit anderen Systemen sind. Die bidirektionale Kopplung zwischen der Innen- und Außenseite des Kabelschirms wird berücksichtigt, was die Analyse der Störfestigkeit und der Emission ermöglicht. Die mathematischen Funktionen zur Berechnung der Kopplung zwischen dem inneren und dem äußeren System des Kabels werden in Ersatzschaltungen umgewandelt, die den Einsatz der Modelle im Frequenzbereich oder zusammen mit nichtlinearen Elementen im Zeitbereich ermöglichen. Die entwickelten Modelle für ein einadriges geschirmtes Kabel werden im Rahmen dieser Arbeit für geschirmte mehradrige Kabel erweitert. Die Schaltungsmodelle werden durch Messungen und Feldsimulationen validiert, wobei die Ergebnisse eine sehr gute Übereinstimmung zeigen.

Abstract

In this thesis, novel circuit models for coaxial cables with braided shields placed above a ground plane are presented. The models are derived from the transmission line theory and are suitable for integration into SPICE simulation programs. Two types of models are presented. First, a lumped-circuit model is developed in which the cable is divided into small sections, with each section replaced with an equivalent circuit and connected to represent the entire cable. In the second type, a macromodel is developed from the analytical solutions of the transmission line theory to represent the entire cable without discretizing it. This work demonstrates the efficiency of the macromodel in terms of computing time and accuracy compared to the lumped-circuit model. The designed models can be used to calculate the induced voltage at the termination loads of the cable when an incident uniform plane wave is coupled in. These models can also calculate the coupling results due to interference from lumped sources. The developed models are therefore suitable for the circuit EMC analysis of systems that contain shielded cables and are susceptible to field coupling or interference with other systems. The bidirectional coupling between the inside and outside of the cable shield is taken into account, which enables the analysis of interference immunity and emissions. The mathematical functions for calculating the coupling between the inner and outer systems of the cable are transformed into equivalent circuit diagrams that allow the models to be used in the frequency domain or together with nonlinear elements in the time domain. The developed models for a single conductor shielded cable are expanded for shielded multiconductor cables within the scope of this work. The circuit models are validated by measurements and field simulations, and the results show excellent agreement.

Contents

Nomenclature

B	magnetic flux density
$B_{\mathrm{n}}^{\mathrm{s}}$	scattered magnetic flux density normal to a flat surface
B_{t}	transverse magnetic flux density
C'	per-unit-length capacitance
$\mathcal{C}$	number of carriers in a cable shield
d	distance between two wires
d	differential operator
d_{fi}	diameter of a filament in a cable shield
$e_x,\ e_y,\ e_z$	unit vector in x-, y-, z-direction
e_{n}	unit normal vector of a flat surface
E	electric field
E_{t}	transverse electric field
E^{i}	incident electric field
E^{e}	excited electric field
E^{r}	reflected electric field
$E_0(\omega)$	amplitude of the electric field at ω
$E_0(t)$	time form of the electric field
$E(\cdot)$	complete elliptic integrals of the second kind
f	frequency
f_{cut}	cut-off frequency
G'	per-unit-length conductance

G	Green function
$\mathcal{G}$	weave angle of a cable shield
h	distance between a cable and a ground plane
H_t	transverse magnetic field
I	electric current
I'_t	per-unit-length transverse current
J	electrical current density
J_i	cylindrical Bessel function of the first kind
K_n	coupling coefficient between two inductors
$\mathcal{K}$	optical coverage of a braided shield
$K(\cdot)$	complete elliptic integrals of the first kind
L'	per-unit-length inductance
$\mathcal{L}$	cable length
l_k	coupling length in the transfer impedance measurement methods for shielded cables
L'_p	porpoising effect in braided cable shield
N_s	number of sections
N_i	cylindrical Bessel function of the second kind
N_fi	number of filaments for each carrier in a cable shield
p_br	distance between two carriers in the longitudinal direction of a cable shield
$\mathcal{Q}$	auxiliary parameters for the field coupling calculation
q'	per-unit-length charges
r	radius of a filament
r_s	radius of a cable shield
r_w	radius of a wire
R'	per-unit-length resistance

S_{12}	forward transmission coefficient
t	time
T_d	one-way time delay of a transmission line
$T_x,\ T_y,\ T_z$	wave time delay in x-, y-, z-direction
$I^+,\ I^-$	forward and backward traveling current waves
V	electric voltage
$V^+,\ V^-$	forward and backward traveling voltage waves
V^s	scattered voltage
v	speed of wave propagation in a medium
v_0	speed of light in vacuum
V_ab	electrical voltage between a and b
V_tan	induced voltage by tangential electric field
V_t	induced voltage by transverse electric field
$x,\ y,\ z$	components in a three-dimensional Cartesian system
Y'_t	per-unit-length transfer admittance
$Y'_\mathrm{i,o}$	per-unit-length shunt admittance of the inner and outer system for a shielded cable
Z_c	characteristic impedance of a transmission line
Z'_t	per-unit-length transfer impedance of a shielded cable
$Z'_\mathrm{i,o}$	per-unit-length series impedance of the inner and outer system for a shielded cable
β	phase constant
γ	propagation constant
δ	skin depth
Δ	screen thickness of a shielded cable
ε	electric permittivity of a medium

ζ	auxiliary parameter for Green's function
θ	angle of incidence of a plane wave
θ_{ij}	angular separation between i-th and j-th conductor
$\mathbf{\Lambda}$	propagation constant matrix
λ	wave length
μ	magnetic permeability of a medium
$\rho_{1,2}$	voltage reflection factors at the loads of a field-coupled line
σ	electric conductivity
$\mathbf{\Phi}(z)$	chain parameter matrix at the z position for a transmission line
Ψ'	per-unit-length magnetic flux
ω	angular frequency
$\mathbf{1}_n$	identity matrix

Subscripts

b	arbitrary behavior source
br	braid
c	conductive coupling
d	disturbance
F	forcing source
f	field coupling
i	inner system
l	left end
M	matched load
m	modal representation
o	outer system
r	right end

s	shield
T	total
t	transverse
w	wire

List of Acronyms

CUT	cable under test
DC	direct current
EMC	electromagnetic compatibility
MTL	multiconductor transmission line
p.u.l.	per-unit-length
SCC	supporting coaxial cable
SPICE	simulation program with integrated circuit emphasis
TEM	transverse electromagnetic field
TL	transmission line
TN	transformation network
VNA	vector network analyzer

List of Figures

Chapter 2

Chapter 3

Chapter 4

Chapter 5

1 Introduction

Today's high demand for hybrid and electric cars raises the question of their immunity and interference effects in an electromagnetic radiation environment. One of the most sensitive components in this environment are the cables, which represent a coupling path for electromagnetic fields. This problem is also becoming more prevalent in renewable energy technologies, such as solar panels and wind turbines. Such systems contain electric elements with higher switching frequencies that pose serious electromagnetic compatibility (EMC) problems. Due to the switching effects, interference can propagate along the cables and couple with other components. These systems are also severely impaired by field couplings on their cables, which significantly reduces their immunity. An EMC-compliant system is when "it does not cause interference with other systems, is not susceptible to emissions from other systems, and does not cause interference with itself" [1]. In order to achieve EMC conformity for these systems, shielded cables are used for this purpose. An essential part of the development is the prediction of problems through simulations. Therefore, the goal is usually to model and simulate such systems together with the cables integrated in them at an earlier stage of development to achieve EMC compliance.

1.1 Problem Statement

Shielded cables are often used between devices that are contained in protective enclosures, with the cable shield usually connected to these enclosures. The cable shielding protects the inner conductor from coupled electrical noise and reduces electromagnetic radiation that could interfere with other cables. When considering types of shielding, braided shielding becomes more important than rigid one because of its better mechanical flexibility. When an electromagnetic interference field is excited or a conductive disturbance occurs on the cable, some of the external current and fields can penetrate the shield and interfere with the inner conductor due to the imperfect behavior of the shield [1, 2]. This can lead to distortion of transmitted signals or, in extreme cases, damage sensitive components, if available. The coupling can also take place from the inner conductor to the outside of the shield. A common mode current is generated and can propagate throughout the system, which can lead to crosstalk with other cables or to coupling with other components. One of the most common examples of this EMC problem is an electric drive system. Electronic circuit simulators such as SPICE (Simulation Program with Integrated Circuit Emphasis) are used to examine and optimize the behavior of a system in the design phase. Such programs include *RLC* components, non-linear elements and basic models of transmission

lines (TLs), but do not include models for shielded cables that are placed over ground. Now the question is:

How can EMC engineers check the emissions and immunity of a system in circuit simulators if they do not contain a model for a shielded cable placed above a ground plane and do not allow field calculations?

This question highlights a major problem in the EMC simulation world when modeling systems with shielded cables in circuit simulator programs. Unfortunately, such an analysis is not possible today with circuit simulators such as SPICE. Only field simulation programs can solve such configurations using so-called co-simulation. Here, the field solver is coupled with the circuit solver and predefined cable libraries [3]. Most of these programs are commercial, where the computational complexity increases enormously with larger circuits and long cable lengths. This work summarizes these problems and provides solutions that enable EMC engineers to perform the required tests in the SPICE environment, presenting circuit models of shielded cables placed over ground.

1.2 Electromagnetic Field Coupling to Transmission Lines

The coupling of incident fields to transmission lines remained one of the most important problems to be solved in EMC. Field coupling is often represented as distributed sources along the transmission lines. The predominant approach is to extend the telegraph equations with the field coupling components. Based on this approach, several solutions for field coupling were presented [4–9]. Advanced work dealt with field coupling on transmission lines within resonating systems [10–13]. For simulation analyses, there remained interest in developing models for field-coupled lines in circuit simulation programs that engineers can use to calculate induced disturbances in advance. An efficient and suitable closed-form solution in SPICE for uniform lines excited by incident field is to replace the distributed sources along the line with equivalent sources at the terminals [14–16]. In [17, 18] for example, SPICE models for single and multiconductor transmission lines (MTL) were presented, which are excited by a uniform plane wave. SPICE models taking into account the losses for MTL appeared later in [19, 20].

An alternative approach in the SPICE environment is to create lumped-circuit models [2, 18, 21]. Here the transmission lines are divided into segments, with each segment being replaced by an equivalent circuit diagram. Certain rules should apply to improve the accuracy of the results. Here the segment length should be smaller than $\lambda/8$, where λ is the wavelength for the maximum frequency of interest. The advantage of this approach is that nonuniform lines can be modeled. The problem is that the computational complexity increases enormously with an increasing number of elements and can lead to a convergence problem. The described cascaded model has been integrated in many cable libraries of commercial field simulation programs in recent years, for example in CST and Feko [3, 22].

1.3 Available Circuit Models for Shielded Cables

In practice, shielded cables are usually placed over a ground plane. Since cable shields are not perfect, electromagnetic coupling between the inner conductor and the outside of the shield may happen. The diffusion of electromagnetic energy through the shielding metal takes place with the lossy tubular and braided shielding. In the case of a braided shield, the electromagnetic fields can penetrate through the small openings in the mesh. An additional induction phenomenon called porpoising occurs due to the overlap of the individual strands of the shield [23, 24]. The induced voltages and currents due to coupling can be described by the transfer impedance and the transfer admittance. Domain decomposition is used for shielded cables in which two coupled systems are defined. The inner system consists of the inner conductor together with the inside of the shield and the outer system consists of the outside of the shield together with the reference plane [2].

Already in 1934 and earlier, an analytical expression for the transfer impedance was sought. Schelkunoff derived a transfer impedance expression for the tubular shield including the skin effect [25]. The braided shield diffusion part basically has the same characteristics as the tubular one, but the model developed by Schelkunoff has been expanded by Vance to incorporate the braided construction [26]. The penetration of magnetic and electrical fields into braided cables was discussed by Lee and Baum [27]. The focus remained on the development of the transfer impedance, since the transfer admittance has little influence in most practical cases.

For simulation analyses, there was continued interest in developing models for shielded cables in circuit simulation programs that can be used to study system immunity and emissions. For this purpose, macromodels were mainly developed from the closed-form solution, where distributed sources along the line were replaced by equivalent sources at the cable terminals. An alternative approach is the lumped-circuit model. In this case, the circuit models are developed with distributed components corresponding to the differential equations. Models of the inner and outer systems are usually developed separately. The coupling between the two systems is typically achieved using controlled sources in the SPICE environment.

A macromodel of a coaxial cable suitable for immunity testing was developed by Caniggia and Maradei in [28]. In later work, the model was expanded considering the field coupling for the case of shielded two parallel wires [29]. The coupling from the outer to the inner system through the braided shield has been presented in the form of Laplace sources in the SPICE environment, which makes it a well applicable model for the frequency domain. The problem is that a simulation in the time domain is only possible with the inverse Fourier transform (IFT), which can lead to high computing costs and inaccuracies with long cable lengths. Circuit models for shielded single and multiconductor cables were

developed in the same way in [30], but field coupling was not considered. However, Laplace sources were used in these models and the problems mentioned above were encountered. Improved models without integration of the Laplace sources were developed by Xie *et al.* for shielded single and multiconductor cables [31, 32]. These models take into account the field coupling and are suitable for immunity tests, whereby the coupling from the inner to the outer system is not taken into account. The models are therefore unsuitable for emission tests. Based on Xie [31, 32] and Paul [17] models, the SACAMOS tool (State-of-the-Art CAble MOdels for Spice) was developed as an open source software for creating SPICE cable models [33]. The developed subcircuits can be integrated in Ngspice [34], LTspice [35] and PSpice [36]. However, the shielded cables available in SACAMOS only consider coupling in one direction. This means that the user must determine in advance whether the coupling should be from the inner to the outer system or vice versa. It should also be noted that the ohmic component of the transfer impedance has not been included directly in the coupling functions in the models presented, but has been lumped in the form of Laplace sources at the cable terminations. It has been shown that this approximation can lead to errors at high frequencies when considering cables whose shields are terminated with very small loads compared to the shield resistance. The field coupling was developed based on Taylor *et al.* formulation [6], and the circuit models were taken from [17, 31]. In any case, novel circuit models for shielded cables compared to those of SACAMOS were developed in this work, with field coupling based on the scattered voltage formulation of Agrawal *et al.* [5]. Bidirectional coupling was considered in this work, and the problem of lower loads on the shield connection did not arise.
SPICE models for evaluating the bulk current injection for shielded cables were developed in [37–40]. Later models for shielded two parallel wires appeared in [41, 42], whereby the focus of these models was on the evaluation of the bulk current injection for shielded cables.

The reported models have been shown to be insufficient for a complete investigation of shielded cables in circuit simulation programs. There is a lack of a model that can perform emission and immunity testing in the time and frequency domains, including field and conductive coupling. To fill this gap in the current state of the art, this work serves as a solution to the problems described and provides cable models including field coupling that can be used for immunity and emission analysis in circuit simulation programs without using Laplace sources.

1.4 Research Objectives and Structure of the Work

The main objective of this work is to develop circuit models for braided shielded cables placed over a ground plane. The models have to be developed in a distributed and closed-form in the SPICE environment, including the coupling of an incident plane wave and the

bidirectional coupling between the inner and outer system. The derived solutions are to be extended for shielded multiconductor cables, whereby frequency domain simulations and time domain simulations with non-linear elements can be carried out. In order to achieve the main goal mentioned, the following intermediate steps are defined.

The fundamentals of transmission line theory for two-conductor lines, multiconductor lines and shielded cables are presented in chapter 2. The transmission line equations are derived with the per-unit-length (p.u.l.) parameters. This is followed by the representation of the frequency and time domain solutions. The different types of cable shields are described. Then the transmission line equations of a shielded cable are explained together with the definition of the transfer parameters.

In chapter 3, a circuit model of a field-coupled single conductor above a perfectly conducting ground plane is developed. Since a shielded cable is viewed as a single conductor for field coupling, this model serves as a preparation for the development of SPICE models for shielded cables. The transmission line equations of the field-coupled line are solved based on the scattered and total voltage formulations. In a later step, the circuit models of both methods were presented and compared.

The development of the electrical circuit for a single conductor shielded cable taking into account the field coupling of a plane wave is presented in chapter 4. A lumped-circuit model consisting of cascaded elements is derived directly from the transmission line equations for the inner and outer systems, respectively. In a later step, the closed-form solutions of the cable are derived. Finally, a macromodel is developed based on these solutions. The two models developed are ultimately compared in terms of accuracy and computational efficiency. Field simulations and measurements are carried out to validate these models.

In chapter 5, lumped-circuit models and macromodels are presented for a field-coupled, shielded multiconductor cable in the SPICE environment. A lumped-circuit model is interpreted directly from the transmission line equations of the cable. Then a closed-form solution is derived using the field coupling approaches from chapter 3. With the similarity transformation, the coupling between the individual conductors in the cable could be separated. Then a macromodel, based on the closed-form solution is presented. The model is validated by field simulations and measurements.

Finally, a summary is given in chapter 6.

2 Transmission Line Theory and Shielded Cables

This chapter introduces the basics of transmission line theory and shielded cables. First, the TL equations for two-conductor lines in the frequency and time domains are developed and solved. The solution is then extended to include multiconductor lines. The transmission line parameters are described taking two-conductor and multiconductor lines into account. At the end of the chapter, the concept of transfer impedance for shielded cables is explained and methods for calculating and measuring this quantity are shown. The basics shown in this chapter are of interest for this work, as the transmission line solutions together with the line parameters will be used in later sections.

2.1 Transmission Line Theory of Two-Conductor Lines

In this section, the fundamentals of the classical transmission line theory for two-conductor lines are discussed with reference to the source [17]. The main condition for solving these parameters in classical transmission line theory is the propagation of the transverse electromagnetic field (TEM) and the associated conditions for the current and charge distribution on the conductors. The transmission line equations and the per-unit-length parameters are derived for two-conductor lines and extended for the case of one conductor over a ground plane and a coaxial cable.

2.1.1 Transmission-Line Equations in Time Domain

Figure 2.1 shows two-conductor lines that run in parallel. If a voltage source is connected between them, a current $I(z,t)$ flows through the first and returns with the second line. This creates a magnetic field H_t around each conductor. An inductance L' results from the passage of this field through the loop between the lines. With open ends, electrical charges accumulate on the conductors and lead to an electrical field E_t in the transverse plane, where the conductors behave like a capacitor. This suggests that a short length of the transmission line can be represented by capacitance and inductance elements, as shown in Fig. 2.2. Since conductors and the dielectric medium around are not ideal in real applications, losses occur which are usually second-order effects and can be neglected at lower frequencies. The loss of conductors is represented by the p.u.l. resistance R' and the loss of the medium by the p.u.l. conductance G', as represented in Fig. 2.2. The parameters $V(z,t)$ and $V(z+\Delta z,t)$ in Fig. 2.2 are the voltages between the two conductors at the beginning and end of Δz.

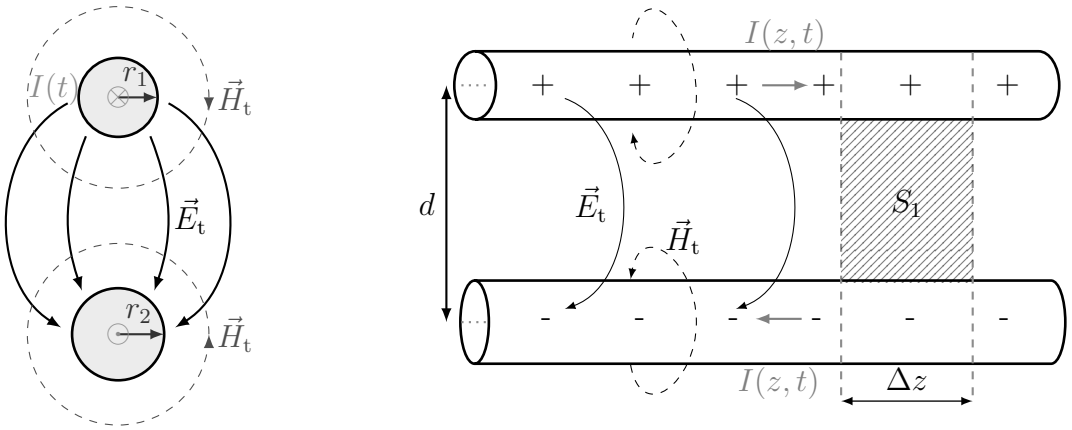

(a) Cross-sectional view (b) Side view

Figure 2.1: Field representation of two-conductor lines.

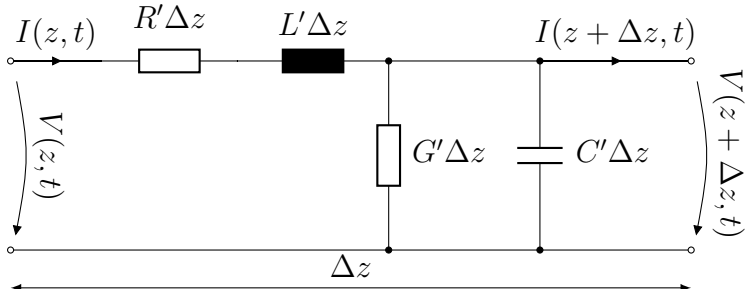

Figure 2.2: Equivalent circuit for a short segment Δz of two-conductor lines.

In preparation for the development of the transmission line equations, Kirchhoff's voltage law is applied in Fig. 2.2 to get

$$V\left(z+\Delta z,t\right)-V\left(z,t\right)=-R'\Delta z I\left(z,t\right)-L'\Delta z\frac{\partial I\left(z,t\right)}{\partial t}. \tag{2.1}$$

Dividing by Δz and taking the limit $\Delta z \to 0$ gives the first transmission line equation

$$\frac{\partial V\left(z,t\right)}{\partial z}=-R'I\left(z,t\right)-L'\frac{\partial I\left(z,t\right)}{\partial t}. \tag{2.2}$$

Applying Kirchhoff's current law to the upper node in Fig. 2.2 gives

$$I\left(z+\Delta z,t\right)-I\left(z,t\right)=-G'\Delta z\cdot V\left(z+\Delta z,t\right)-C'\Delta z\cdot\frac{\partial V\left(z+\Delta z,t\right)}{\partial t}. \tag{2.3}$$

Dividing by Δz and taking the limit $\Delta z \to 0$, the second transmission line equation becomes:

$$\frac{\partial I\left(z,t\right)}{\partial z}=-G'V\left(z,t\right)-C'\cdot\frac{\partial V\left(z,t\right)}{\partial t}. \tag{2.4}$$

The losses of the conductors are ignored in the next derivations. The first and second transmission line equations (2.2) and (2.4) are coupled to one another, where $V(z,t)$ and $I(z,t)$ are included in each case. To decouple them, equation (2.2) was differentiated with respect to z, (2.4) with respect to t, and the second was inserted into the first to get the decoupled equation of $V(z,t)$:

$$\frac{\partial^2 V(z,t)}{\partial z^2} = L'C' \cdot \frac{\partial^2 V(z,t)}{\partial t^2}. \tag{2.5}$$

By differentiating (2.2) by t, (2.4) by z and substituting, the decoupled equation of $I(z,t)$ is obtained by

$$\frac{\partial^2 I(z,t)}{\partial z^2} = L'C' \frac{\partial^2 I(z,t)}{\partial t^2}. \tag{2.6}$$

2.1.2 Transmission-Line Equations in Frequency Domain

The transmission line equations (2.2) and (2.4) derived in the time domain can easily be transformed to the frequency domain by replacing the time derivative with $\mathrm{j}\omega$

$$\frac{\mathrm{d}V(z)}{\mathrm{d}z} = -R'I(z) - \mathrm{j}\omega L'I(z) \tag{2.7}$$

$$\frac{\mathrm{d}I(z)}{\mathrm{d}z} = -G'V(z) - \mathrm{j}\omega C'V(z). \tag{2.8}$$

Differentiating one of these equations with respect to z and substituting it into the other yields the decoupled second order equations for lossless lines

$$\frac{\mathrm{d}^2 V(z)}{\mathrm{d}z^2} = -\omega^2 L'C'V(z) \tag{2.9}$$

$$\frac{\mathrm{d}^2 I(z)}{\mathrm{d}z^2} = -\omega^2 L'C'I(z). \tag{2.10}$$

2.1.3 Per-Unit-Length Parameters

The primary line constants of the two-conductor lines used in the previous equations are explained in more detail here. These parameters are later extended for the case of one conductor above a perfectly conducting ground plane and a coaxial cable.

Two-Conductor Lines

In the two-conductor configuration shown in Fig. 2.1, the p.u.l. inductance L' can be interpreted as the ratio between the p.u.l. magnetic flux Ψ' that penetrates the cross-sectional surface between the two lines and the responsible current I flowing in the

conductors [17].

$$L' = \frac{\Psi'}{I} \tag{2.11}$$

To determine Ψ', the transverse magnetic field H_t is first calculated, which passes through the cross-sectional area S_1 between the wires in Fig. 2.1. After applying Ampere's law to an infinitely long cylindrical wire with radius r and direct current I, this leads to [17]

$$H_\mathrm{t} = \frac{I}{2\pi r}. \tag{2.12}$$

The magnetic flux in the cross-sectional area between the wires is directly proportional to the transverse magnetic flux density $B_\mathrm{t} = \mu H_\mathrm{t}$ of the two wires. The magnetic flux density $B_{\mathrm{t}1}$ is considered for the lower wire and $B_{\mathrm{t}2}$ for the upper wire. Assuming that the wires are perfectly conducting and have the distance d between them, where the radii are r_1 and r_2, as shown in Fig. 2.1. For the length Δz, Ψ' is given by [17]

$$\Psi' = \frac{1}{\Delta z} \cdot \int_{z}^{z+\Delta z} \int_{r_1}^{r_2} \Big(B_{\mathrm{t}1} + B_{\mathrm{t}2}\Big) \mathrm{d}z \, \mathrm{d}r \,, \tag{2.13}$$

where $\mathrm{d}r$ denotes the unit vector derivative in the radial direction. By inserting (2.12) into (2.13) and executing the first integral, Ψ' becomes

$$\Psi' = \int_{r_1}^{d-r_2} \frac{\mu I}{2\pi r} \, \mathrm{d}r + \int_{r_2}^{d-r_1} \frac{\mu I}{2\pi r} \, \mathrm{d}r. \tag{2.14}$$

In the derived equations it is assumed that the wires are infinitely long and that the current is uniformly distributed across the wire cross-sections. Now calculate the definite integrals to get

$$\Psi' = \frac{\mu I}{2\pi} \ln\left(\frac{d - r_2}{r_1}\right) + \frac{\mu I}{2\pi} \ln\left(\frac{d - r_1}{r_2}\right). \tag{2.15}$$

Considering the case where the two wires are close together, the earlier assumption that the current is uniformly distributed over the wires is affected according to the *proximity effect*. For this reason d is considered to be much larger than the wire radii. Substituting (2.15) into (2.11) results in

$$L' = \frac{\mu}{2\pi} \cdot \ln\left(\frac{d^2}{r_1 r_2}\right). \tag{2.16}$$

The property of the logarithmic function was used in (2.16) to write a sum as a multiplication.

The p.u.l. capacitance C' is defined as the ratio of the line charge q' on the wires to the induced voltage V between them [17].

$$C' = \frac{q'}{V} \tag{2.17}$$

To determine C', the parameters q' and V for two-conductor lines must first be resolved. In Fig. 2.1 it was assumed that the charges are concentrated as a filament or evenly distributed in the wires. Under this condition, the transverse electric fields can be represented as [17]

$$E_\mathrm{t} = \frac{q'}{2\pi\,\varepsilon\,r_\mathrm{cy}}, \tag{2.18}$$

where r_cy is the radius of a cylinder enclosing the charge-carrying wire. The voltage between the wires can be calculated simply by applying the integral to E_t, where the voltage between two points a and b around the filament of each wire is given by [17]

$$V_\mathrm{ab} = -\int_{d_\mathrm{a}}^{d_\mathrm{b}} \vec{E}_\mathrm{t}\,\mathrm{d}\vec{l}. \tag{2.19}$$

The parameters d_a and d_b are the distances to the points a and b from the filament. To determine the voltage between the two conductors in Fig. 2.1, (2.18) is substituted into (2.19) and the integral is performed considering the electric field of the two wires, where

$$\begin{aligned} V_\mathrm{ab} &= -\int_{d-r_1}^{r_2} \frac{q'}{2\pi\varepsilon r}\,\mathrm{d}r - \int_{d-r_2}^{r_1} \frac{q'}{2\pi\varepsilon r}\,\mathrm{d}r \\ &= \frac{q'}{2\pi\varepsilon}\ln\left(\frac{d-r_1}{r_2}\right) + \frac{q'}{2\pi\varepsilon}\ln\left(\frac{d-r_2}{r_1}\right). \end{aligned} \tag{2.20}$$

The two-conductors must be widely separated, otherwise the condition for a uniform distribution of the charges will be violated. It was assumed that $d >> r_1, r_2$, thus

$$V_\mathrm{ab} \approx \frac{q'}{2\pi\varepsilon}\cdot\ln\left(\frac{d^2}{r_1 r_2}\right). \tag{2.21}$$

The capacitance C' is obtained by substituting V_ab into (2.17), where

$$C' = \frac{2\pi\varepsilon}{\ln\left(\frac{d^2}{r_1 r_2}\right)}. \tag{2.22}$$

If the surrounding medium is lossy with a conductivity σ, E_t leads to a transverse current that flows from one conductor to another across the medium. For a Δz section, this effect

is represented by the p.u.l. conductance G', where [17]

$$G' = \frac{I'_{\mathrm{t}}}{V}. \tag{2.23}$$

The parameter I'_{t} represents the per-unit-length transverse current. Assuming that the two wires are in a homogeneous medium with constant permittivity ε and constant permeability μ, the following relationship can be used [17]:

$$L'C' = \mu\varepsilon. \tag{2.24}$$

If the medium is lossy and homogeneous with a conductivity σ, then [17]

$$L'G' = \mu\sigma. \tag{2.25}$$

Based on the knowledge of (2.25), G' can be determined directly by substituting L' from (2.16). The same applies to the calculation of L' and C', where only one of the two parameters has to be determined and replaced in (2.24).

It has been shown so far that the TL parameters are independent of the frequency f. Although the current is uniformly distributed across the conductor cross-section at low frequencies, it migrates to the surface at higher frequencies due to the *skin effect*. The *skin depth* is given by [17]

$$\delta = \frac{1}{\sqrt{\pi f \mu \sigma}}. \tag{2.26}$$

The non-uniform current distribution leads to the frequency dependence of the line parameters, where the resistance increases proportionally to $\sqrt{f}$. The frequency dependence also influences the capacitance and conductance, which are proportional to the dielectric constant and conductivity of the medium around the wire. For direct current (DC) and at very low frequencies, the p.u.l. resistance of a wire is simply given by [17]

$$R'_{\mathrm{dc}} = \frac{1}{\sigma\pi r_{\mathrm{w}}^2}. \tag{2.27}$$

The formula given for the DC-resistance remains unchanged if the wire radius is smaller than twice the skin depth $r_{\mathrm{w}} < 2\delta$. If this condition is violated with $r_{\mathrm{w}} > 2\delta$, the resistance becomes [43]

$$R' = \frac{1}{2\pi r_{\mathrm{w}}\sigma\delta} = \frac{1}{2r_{\mathrm{w}}} \cdot \sqrt{\frac{\mu}{\pi\sigma}} \cdot \sqrt{f}, \tag{2.28}$$

where the resistance increases with the square root of the frequency f.

One Conductor Over a Ground Plane

The case of a conductor placed over a perfectly conducting ground plane is considered next in Fig. 2.3.

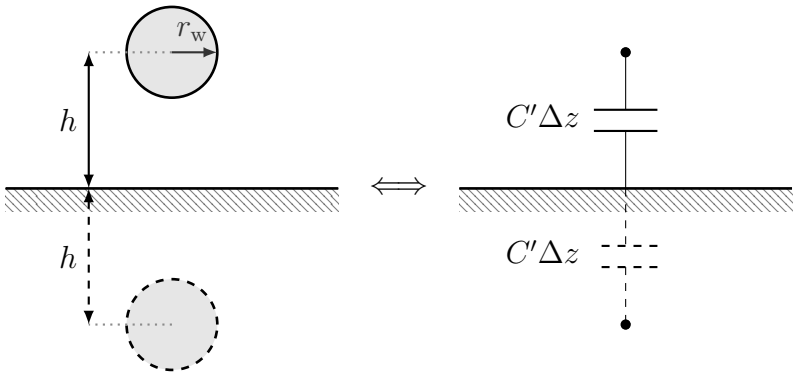

Figure 2.3: One conductor over a ground plane showing the capacitance per-unit-length with the method of images.

When using the method of images, the ground plane is replaced by another conductor at a distance h, so that two-conductor lines are formed. Under this condition, two capacitors between the lines result in Fig. 2.3, where the solution of C' can be taken from (2.22) with $r_1 = r_2 = r_\mathrm{w}$ [17] and

$$C' = \frac{2\pi\varepsilon}{\ln\left(\frac{2h}{r_\mathrm{w}}\right)}. \tag{2.29}$$

For a homogeneous medium, the p.u.l. inductance can easily be derived by inserting (2.29) into (2.24).

$$L' = \frac{\mu}{2\pi} \cdot \ln\left(\frac{2h}{r_\mathrm{w}}\right) \tag{2.30}$$

The same applies to the conductance, which can be calculated with (2.25) if the medium is lossy and homogeneous.

Coaxial Cable

Taking into account the coaxial cable shown in Fig. 2.4, it consists of a cylindrical inner conductor with the radius r_w surrounded by a shield with the inner radius r_s. Both conductors are isolated with a homogenous material. The transmission line conditions defined above also apply to this type of cable. Here the charge distributions are uniform, the field is directed in a radial and transverse direction. With similar steps as before, the

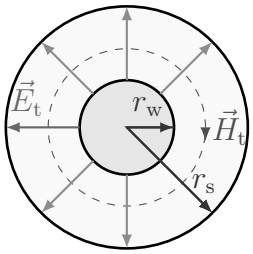

Figure 2.4: Cross-sectional representation of a coaxial cable.

p.u.l. capacitance can be calculated [17], where

$$C' = \frac{2\pi\varepsilon}{\ln\left(\frac{r_\mathrm{s}}{r_\mathrm{w}}\right)}. \tag{2.31}$$

Applying (2.24) to calculate the inductance gives

$$L' = \frac{\mu}{2\pi} \cdot \ln\left(\frac{r_\mathrm{s}}{r_\mathrm{w}}\right). \tag{2.32}$$

Equation (2.25) can be used to calculate the conductance G'.

2.1.4 Frequency-Domain Solution

Next, a solution of the two-conductor lines in the frequency domain is derived. The transmission line equations were presented in (2.9) and (2.10) for lossless lines. Their solution is given by [17]

$$V(z) = V^+ \,\mathrm{e}^{-\mathrm{j}\beta z} + V^- \,\mathrm{e}^{\mathrm{j}\beta z} \tag{2.33}$$

$$I(z) = \frac{V^+}{Z_\mathrm{c}} \,\mathrm{e}^{-\mathrm{j}\beta z} - \frac{V^-}{Z_\mathrm{c}} \,\mathrm{e}^{\mathrm{j}\beta z}. \tag{2.34}$$

The first terms in (2.33) and (2.34) represent the forward-traveling waves, while the second represent the backward-traveling waves. The parameters V^+ and V^- are complex constants that will be determined later. The elements Z_c and β are the characteristic impedance and phase constant, which are defined as

$$Z_\mathrm{c} = \sqrt{\frac{L'}{C'}} \tag{2.35}$$

$$\beta = \frac{\omega}{v}. \tag{2.36}$$

The speed of propagation on the line v is given by

$$v = \frac{1}{\sqrt{L'C'}}. \tag{2.37}$$

Fig. 2.5 shows two-conductor lines of length $\mathcal{L}$, which contain a source V_S with the internal impedance Z_S and the load Z_L at the end.

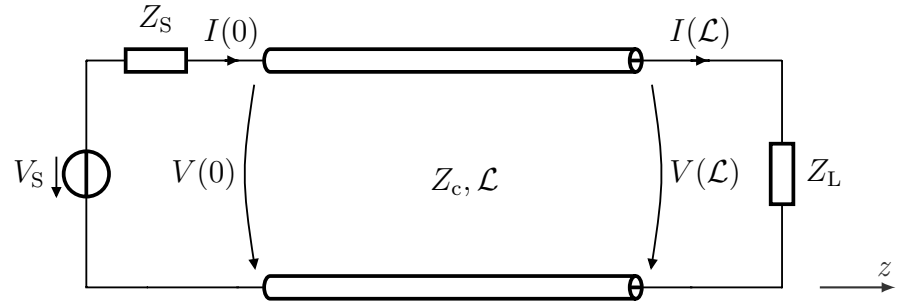

Figure 2.5: Two-conductor lines including source and load.

The complex reflection coefficient at a position z along the line is defined as the ratio of the backward- and forward-traveling voltage waves

$$\Gamma(z) = \frac{V^- \, \mathrm{e}^{\mathrm{j}\beta z}}{V^+ \, \mathrm{e}^{-\mathrm{j}\beta z}}. \tag{2.38}$$

Equations (2.33) and (2.34) can be rewritten with respect to this reflection coefficient as follows:

$$V(z) = V^+ \, \mathrm{e}^{-\mathrm{j}\beta z} \left[1 + \Gamma\left(z\right)\right] \tag{2.39}$$

$$I(z) = \frac{V^+}{Z_\mathrm{c}} \, \mathrm{e}^{-\mathrm{j}\beta z} \left[1 - \Gamma\left(z\right)\right]. \tag{2.40}$$

The complex constant V^+ can be determined by calculating the voltage at the terminal loads and correspondingly calculating the reflection coefficient with [17]

$$V^+ = \frac{V\left(0\right)}{1 + \Gamma\left(0\right)}. \tag{2.41}$$

With the solution presented in (2.39) and (2.40), it is possible to calculate the voltage and current at any position z on the line.

Chain-Parameter Representation

Since in most applications the interest in the voltages and currents lies at the terminations and not along the line, it is possible to represent the line as a two-port element. The

chain-parameter matrix representation is one of the most practical forms that relates the terminal voltages and the current as [17]

$$\begin{bmatrix} V(\mathcal{L}) \\ I(\mathcal{L}) \end{bmatrix} = \underbrace{\begin{bmatrix} \cosh(\mathrm{j}\beta\mathcal{L}) & -Z_\mathrm{c}\sinh(\mathrm{j}\beta\mathcal{L}) \\ -\sinh(\mathrm{j}\beta\mathcal{L})/Z_\mathrm{c} & \cosh(\mathrm{j}\beta\mathcal{L}) \end{bmatrix}}_{\mathbf{\Phi}(\mathcal{L})} \cdot \begin{bmatrix} V(0) \\ I(0) \end{bmatrix}, \tag{2.42}$$

where $\mathbf{\Phi}(\mathcal{L})$ is the chain-parameter matrix for a lossless line. The chain-parameter expression in (2.42) does not take into account the source and loads connected to the lines. To account for these parameters, the terminal conditions in Fig. 2.5 are applied, where

$$V(0) = V_\mathrm{S} - Z_\mathrm{S} I(0) \tag{2.43}$$

$$V(\mathcal{L}) = Z_\mathrm{L} \cdot I(\mathcal{L}). \tag{2.44}$$

Now substitute (2.43) and (2.44) into (2.42) to get

$$V(\mathcal{L}) = \Phi_{11}(\mathcal{L})V_\mathrm{S} + [\Phi_{12}(\mathcal{L}) - \Phi_{11}(\mathcal{L})Z_\mathrm{S}] \cdot I(0) \tag{2.45}$$

$$I(\mathcal{L}) = \Phi_{21}(\mathcal{L})V_\mathrm{S} + [\Phi_{22}(\mathcal{L}) - \Phi_{21}(\mathcal{L})Z_\mathrm{S}] \cdot I(0). \tag{2.46}$$

For a known source V_S and an impedance Z_S at $z = 0$, the voltage and current at $z = \mathcal{L}$ can be calculated using (2.45), (2.46) and vice versa.

2.1.5 Time-Domain Solution

The presented solution in the frequency domain enables the analysis of the line with linear loads. The solution in the time domain or the so-called *transient solution* is now derived. In the time domain solution, arbitrary waveform of the line excitation can be defined together with non-linear loads. First, a tracking method solution is presented that is based on a graphical procedure, where the terminal voltages of the line are sketched against time. This is followed by the solution of a lossless transmission line in SPICE.

Tracking Method

The transmission line equations were derived in an uncoupled, second-order form in (2.5) and (2.6). The solution of these equations takes place according to the approach in [17], which is given by

$$V(z,t) = V^+\left(t - \frac{z}{v}\right) + V^-\left(t + \frac{z}{v}\right) \tag{2.47}$$

$$I(z,t) = \frac{1}{Z_\mathrm{c}} \cdot V^+\left(t - \frac{z}{v}\right) - \frac{1}{Z_\mathrm{c}} \cdot V^-\left(t + \frac{z}{v}\right). \tag{2.48}$$

The parameters V^+ and V^- represent the forward- and backward-traveling waves in the z and $-z$ directions on the line. A comparison of (2.47) and (2.48) with the solution presented in (2.33) and (2.34) in the frequency domain makes it easy to interpret that this solution is its time domain transformation. The voltage and the current of each wave are related to each other by the characteristic impedance Z_c, where [17]

$$I^+\left(t-\frac{z}{v}\right)=\frac{1}{Z_\mathrm{c}}\cdot V^+\left(t-\frac{z}{v}\right) \tag{2.49}$$

$$I^-\left(t+\frac{z}{v}\right)=-\frac{1}{Z_\mathrm{c}}\cdot V^-\left(t+\frac{z}{v}\right). \tag{2.50}$$

For the transmission line shown in Fig. 2.5 of length $\mathcal{L}$, the load reflection coefficient is given by

$$\Gamma_\mathrm{L}=\frac{V^-\left(t+\frac{\mathcal{L}}{v}\right)}{V^+\left(t-\frac{\mathcal{L}}{v}\right)}=\frac{R_\mathrm{L}-Z_\mathrm{c}}{R_\mathrm{L}+Z_\mathrm{c}}. \tag{2.51}$$

The resistor R_L is used instead of Z_L because the problem is treated in the time domain. A simple manipulation of (2.51) enables it to be expressed as follows [17]:

$$V^-\left(t+\frac{\mathcal{L}}{v}\right)=\Gamma_\mathrm{L}\cdot V^+\left(t-\frac{\mathcal{L}}{v}\right). \tag{2.52}$$

The insertion of (2.52) into (2.50) leads to the current representation of the waves in relation to the reflection factor at the load.

$$I^-\left(t+\frac{\mathcal{L}}{v}\right)=-\Gamma_\mathrm{L}\cdot I^+\left(t-\frac{\mathcal{L}}{v}\right) \tag{2.53}$$

It should be noted that the voltage at the load $V(\mathcal{L},t)$ is the sum of the forward- and backward-traveling waves at time t, as shown in (2.47) and (2.48). Considering the voltage and current of each wave at $z=0$ in Fig. 2.5, they become

$$V(0,t)=\frac{Z_\mathrm{c}}{R_\mathrm{S}+Z_\mathrm{c}}\cdot V_\mathrm{S}(t)\quad\text{for } 0\le t\le 2T_\mathrm{d} \tag{2.54}$$

$$I(0,t)=\frac{1}{R_\mathrm{S}+Z_\mathrm{c}}\cdot V_\mathrm{S}(t)\quad\text{for } 0\le t\le 2T_\mathrm{d}, \tag{2.55}$$

where T_d is the one-way time delay on the line given by

$$T_\mathrm{d}=\frac{\mathcal{L}}{v}. \tag{2.56}$$

At the time $t\le 2T_\mathrm{d}$, the reflected wave at the load has not yet reached the source. At a time $t\ge 2T_\mathrm{d}$, the wave reflected by the loads reaches the source and is reflected again if

the load is not matched. The reflection coefficient at the source is defined as [17]

$$\Gamma_\mathrm{S} = \frac{R_\mathrm{S} - Z_\mathrm{c}}{R_\mathrm{S} + Z_\mathrm{c}}. \tag{2.57}$$

Tracking the waves over a longer period of time by observing the reflection and back-reflections between load and source leads to the time-dependent solution of the voltage at $z = 0$ and $z = \mathcal{L}$ with [17]

$$\begin{aligned} V(0,t) = &\frac{Z_\mathrm{c}}{R_\mathrm{S} + Z_\mathrm{c}} \cdot \Big[V_\mathrm{S}(t) + (1+\Gamma_\mathrm{S})\Gamma_\mathrm{L} V_\mathrm{S}(t-2T_\mathrm{d}) + (1+\Gamma_\mathrm{S})\Gamma_\mathrm{S}\Gamma_\mathrm{L}\Gamma_\mathrm{L} V_\mathrm{S}(t-4T_\mathrm{d}) \\ &+ (1+\Gamma_\mathrm{S})(\Gamma_\mathrm{S}\Gamma_\mathrm{L})^2 \Gamma_\mathrm{L} V_\mathrm{S}(t-6T_\mathrm{d}) + \cdots \Big] \end{aligned} \tag{2.58}$$

and

$$\begin{aligned} V(\mathcal{L},t) = &\frac{Z_\mathrm{c}}{R_\mathrm{s} + Z_\mathrm{c}} \cdot \Big[(1+\Gamma_\mathrm{L}) V_\mathrm{S}(t-T_\mathrm{d}) + (1+\Gamma_\mathrm{L})\Gamma_\mathrm{S}\Gamma_\mathrm{L} V_\mathrm{S}(t-3T_\mathrm{d}) \\ &+ (1+\Gamma_\mathrm{L})(\Gamma_\mathrm{S}\Gamma_\mathrm{L})^2 V_\mathrm{S}(t-5T_\mathrm{d}) + (1+\Gamma_\mathrm{L})(\Gamma_\mathrm{S}\Gamma_\mathrm{L})^3 V_\mathrm{S}(t-7T_\mathrm{d}) + \cdots \Big]. \end{aligned} \tag{2.59}$$

For a better interpretation of (2.58) and (2.59), a graphical tracking diagram of the reflected waves is shown in [17].

SPICE Solution

The reflection coefficients Γ_L and Γ_S are contained in the solution presented in (2.58) and (2.59), which makes it impractical when dynamic or non-linear loads are taken into account. A numerical solution for lossless lines has been implemented in the SPICE circuit programs, which overcomes the problems described and enables the analysis of dynamic and non-linear loads in the time domain. The method was originally proposed by Branin [44]. Applying $z = 0$ and z = $\mathcal{L}$ in (2.47) and (2.48) gives

$$V(0,t) = V^+(t) + V^-(t) \tag{2.60a}$$

$$Z_\mathrm{c} \cdot I(0,t) = V^+(t) - V^-(t) \tag{2.60b}$$

and

$$V(\mathcal{L},t) = V^+(t - T_\mathrm{d}) + V^-(t + T_\mathrm{d}) \tag{2.61a}$$

$$Z_\mathrm{c} \cdot I(\mathcal{L},t) = V^+(t - T_\mathrm{d}) - V^-(t + T_\mathrm{d}). \tag{2.61b}$$

The one-way time delay on the line T_d was defined in (2.56). Adding and subtracting (2.60) and (2.61) results in

$$V(0,t) + Z_\mathrm{c} I(0,t) = 2V^+(t) \tag{2.62a}$$
$$V(0,t) - Z_\mathrm{c} I(0,t) = 2V^-(t) \tag{2.62b}$$
$$V(\mathcal{L},t) + Z_\mathrm{c} I(\mathcal{L},t) = 2V^+(t - T_\mathrm{d}) \tag{2.62c}$$
$$V(\mathcal{L},t) - Z_\mathrm{c} I(\mathcal{L},t) = 2V^-(t + T_\mathrm{d}). \tag{2.62d}$$

Additional manipulation to remove the V^+ and V^- dependencies leads to [17]

$$V(0,t) = Z_\mathrm{c} I(0,t) + V_\mathrm{bl}(t), \tag{2.63}$$

where

$$V_\mathrm{bl}(t) = V(\mathcal{L}, t - T_\mathrm{d}) - Z_\mathrm{c} I(\mathcal{L}, t - T_\mathrm{d}). \tag{2.64}$$

The voltage at $z = \mathcal{L}$ can be calculated with similar steps from (2.62), where

$$V(\mathcal{L},t) = -Z_\mathrm{c} I(\mathcal{L},t) + V_\mathrm{br}(t). \tag{2.65}$$

The voltage $V_\mathrm{br}(t)$ is defined as

$$V_\mathrm{br}(t) = V(0, t - T_\mathrm{d}) + Z_\mathrm{c} I(0, t - T_\mathrm{d}). \tag{2.66}$$

The voltages $V_\mathrm{bl}(t)$ and $V_\mathrm{br}(t)$ depend on the voltage and the current at the line ends. For this reason, the index b was defined to represent the behavioral voltages. The indices l and r stand for the left and right side, respectively.

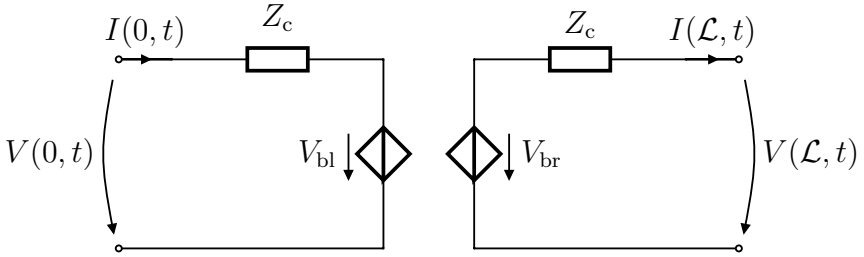

Figure 2.6: SPICE model of a transmission line.

Equations (2.63) and (2.65) represent the solution in SPICE for a transmission line, as shown in Fig. 2.6, [17]. It consists of voltage-controlled sources that contain time-delayed elements and are connected in series with the characteristic impedance Z_c. To use the transmission lines in SPICE, only the characteristic impedance Z_c and the one-way transit delay T_d should be defined.

2.2 Transmission Line Theory of Multiconductor Lines

The transmission line equations and their solutions were discussed in section 2.1 for two-conductor lines. These equations were derived for classical transmission line theory assuming TEM propagation. The solutions presented there are extended in this section to include multiconductor transmission lines, which consist of $n + 1$ conductors (see Fig. 2.7). There are n conductors with a cylindrical shape parallel to a reference conductor labeled 0. The electric current of the jth conductor is represented by $I_j(z,t)$.

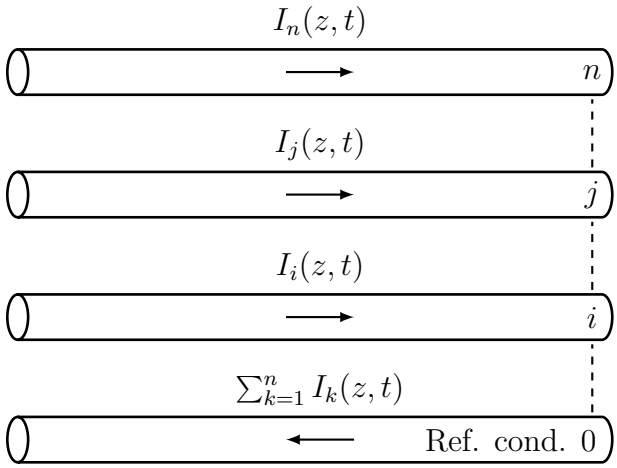

Figure 2.7: Multiconductor lines with $n + 1$ uniform cylindrical wires.

It can be seen that the currents of all n conductors return through the reference conductor. It is assumed that all of these conductors have the same radius r_w and are therefore uniform.

2.2.1 Transmission-Line Equations

An equivalent circuit diagram of a Δz section is shown in Fig. 2.8. Similar to two-conductor lines, it consists of resistances, inductances, conductances, and capacitances. It should be noted that the quantity A_{ii} means the TL parameter of conductor i with respect to the reference conductor. The element A_{ij} represents the TL parameter between the conductors i and j. The application of Kirchhoff's voltage and current law in Fig. 2.8 leads to the first and second MTL equations [17]

$$\frac{\partial}{\partial z}\mathbf{V}(z,t) = -\mathbf{R}'\mathbf{I}(z,t) - \mathbf{L}'\frac{\partial}{\partial t}\mathbf{I}(z,t) \tag{2.67}$$

$$\frac{\partial}{\partial z}\mathbf{I}(z,t) = -\mathbf{G}'\mathbf{V}(z,t) - \mathbf{C}'\frac{\partial}{\partial t}\mathbf{V}(z,t). \tag{2.68}$$

The $n \times 1$ vectors $\mathbf{V}(z,t)$ and $\mathbf{I}(z,t)$ represent the voltage and current with respect to the reference conductor. The $n \times n$ matrix $\mathbf{L}'$ represents the p.u.l. inductance of the MTLs,

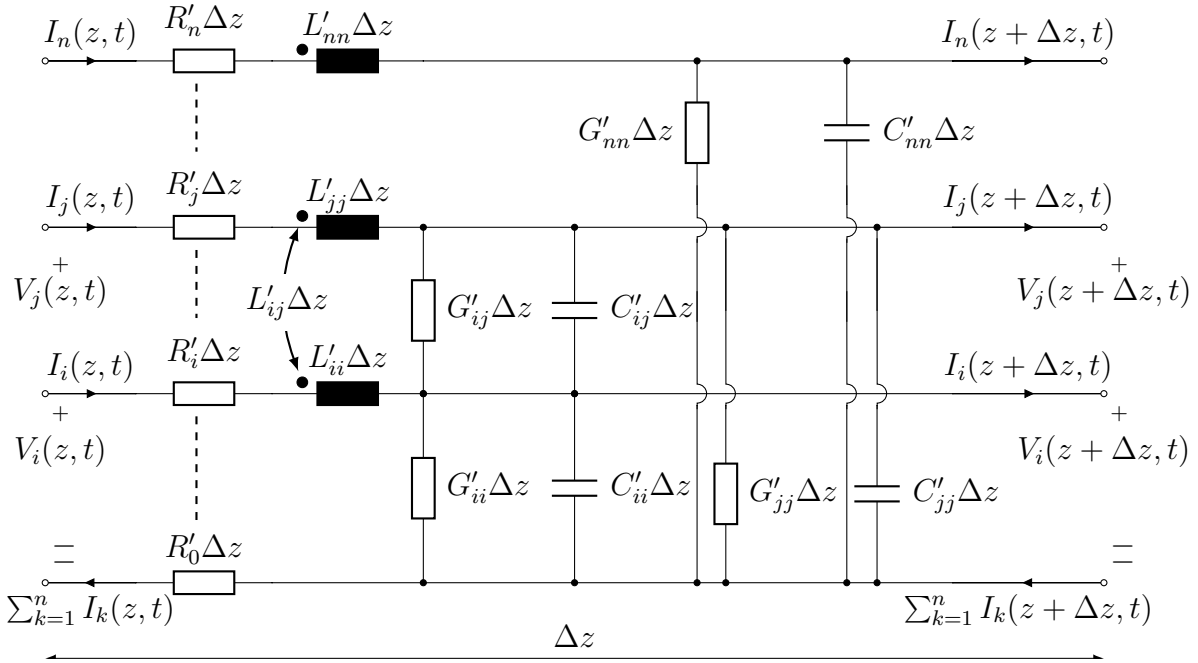

Figure 2.8: Equivalent circuit for a short segment Δz of multiconductor lines.

where

$$\mathbf{L}' = \begin{bmatrix} L'_{11} & L'_{12} & \cdots & L'_{1n} \\ L'_{21} & L'_{22} & \cdots & L'_{2n} \\ \vdots & \vdots & \ddots & \vdots \\ L'_{n1} & L'_{n2} & \cdots & L'_{nn} \end{bmatrix}. \tag{2.69}$$

The element L'_{ii} stands for the p.u.l. self-inductance of the i-th conductor and L'_{ij} for the mutual inductance between the i-th and j-th conductor. The same applies to the p.u.l. resistance, capacitance and conductance matrices $\mathbf{R}'$, $\mathbf{C}'$ and $\mathbf{G}'$. Next, lossless lines with perfect conductors $\mathbf{R}' = 0$ and a lossless surrounding medium $\mathbf{G}' = 0$ are considered. To represent (2.67) and (2.68) in a second-order uncoupled form, they were individually derived by z and t and substituted into each other to obtain [17]

$$\frac{\partial^2}{\partial z^2}\mathbf{V}(z,t) = \mathbf{L}'\mathbf{C}'\frac{\partial^2}{\partial t^2}\mathbf{V}(z,t) \tag{2.70}$$

$$\frac{\partial^2}{\partial z^2}\mathbf{I}(z,t) = \mathbf{C}'\mathbf{L}'\frac{\partial^2}{\partial t^2}\mathbf{I}(z,t). \tag{2.71}$$

2.2.2 Per-Unit-Length Parameters

The transmission line parameters of two-conductor lines developed before are extended in this section for the case of MTLs. The line parameters were also derived in this section for a cylindrical shielded cable with n inner conductors.

In (2.24) and (2.25) a nice property was shown, which relates the transmission line parameters of two-conductor lines in a homogeneous medium. The transmission line parameters of MTLs in a homogeneous medium are similarly related by [17]

$$\mathbf{L}'\mathbf{C}' = \mathbf{C}'\mathbf{L}' = \mu\varepsilon\mathbf{1}_n, \tag{2.72}$$

where $\mathbf{1}_n$ is the $n \times n$ identity matrix containing ones on the main diagonal and zeros elsewhere. If the medium is lossy and homogeneous with a conductivity σ, then [17]

$$\mathbf{L}'\mathbf{G}' = \mathbf{G}'\mathbf{L}' = \mu\sigma\mathbf{1}_n. \tag{2.73}$$

The self-inductance of the i-th wire defined by the entry L'_{ii} is given by [17]

$$L'_{ii} = \left.\frac{\Psi'_i}{I_i}\right|_{I_{1\to(i-1)}=0 \;\&\; I_{(i+1)\to n}=0}, \tag{2.74}$$

where Ψ'_i is the p.u.l. total magnetic flux that permeates the surface between the i-th and the reference conductor. The mutual inductance between the i-th and j-th conductors L'_{ij} is defined as

$$L'_{ij} = \left.\frac{\Psi'_i}{I_j}\right|_{I_{1\to(j-1)}=0 \;\&\; I_{(j+1)\to n}=0}. \tag{2.75}$$

Based on (2.74) and (2.75), the p.u.l. inductance can be determined by calculating Ψ'_i for a defined current in the ith or jth conductor, with all other conductors set to open circuit. Assuming uniform wires with a cylindrical shape and a relatively large distance between them, the self and mutual inductance become [17]

$$L'_{ii} = \frac{\mu}{2\pi} \cdot \ln\left(\frac{d_{i0}^2}{r_{\mathrm{w}}^2}\right) \tag{2.76a}$$

$$L'_{ij} = \frac{\mu}{2\pi} \cdot \ln\left(\frac{d_{i0}d_{j0}}{d_{ij}r_{\mathrm{w}}}\right). \tag{2.76b}$$

Here d_{i0} and d_{j0} are the distances from the i-th and j-th conductor to the reference conductor. The distance d_{ij} is that between the ith and the jth conductors.

The p.u.l. capacitance of the ith conductor relates the p.u.l. total charges q'_i to the induced voltage V_i. In particular, the entry C'_{ii} is given by [17]

$$C'_{ii} = \left.\frac{q'_i}{V_i}\right|_{V_{1\to(i-1)}=0 \;\&\; V_{(i+1)\to n}=0}. \tag{2.77}$$

It can be calculated by determining q'_i under the condition that all voltages except V_i are set to zero. The capacitance between the ith and the jth conductor is defined as [17]

$$C'_{ij} = \left.\frac{q'_i}{V_j}\right|_{V_{1\to(j-1)}=0 \ \& \ V_{(j+1)\to n}=0} . \tag{2.78}$$

The capacitance matrix can also easily be calculated from (2.72), since **L**' entries were determined in (2.76). For lossy and homogeneous medium, **G**' can be determined using equation (2.73).

Case of a Cylindrical Shielded Cable with *n* inner conductors

Since the circuit models for shielded cables with n inner conductors is presented in a later chapter, the cable parameters for this cable type are shown below. Fig. 2.9 shows a cross-section of a perfectly conducting cylindrical shield with radius r_s containing n wires with radii $r_{\mathrm{w}i}$, $r_{\mathrm{w}j}$, etc. The distance of the j-th wire from the shield axis is given by d_j.

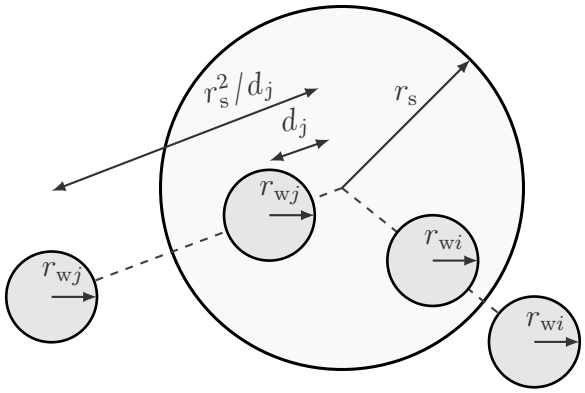

Figure 2.9: Structure of n conductors within a cylindrical shield.

Using the method of images in Fig. 2.9, the shield was replaced with an additional conductor at a distance r_s^2/d_j. The distance calculation also applies to the remaining inner conductors. Under the condition of mirrored wires with no shield, the structure goes back to the case of MTLs, so L'_{jj} and L'_{ij} can be written as [17]

$$L'_{jj} = \frac{\mu}{2\pi} \cdot \ln\left(\frac{r_\mathrm{s}^2 - d_j^2}{r_\mathrm{s} r_{\mathrm{w}j}}\right) \tag{2.79a}$$

$$L'_{ij} = \frac{\mu}{2\pi} \cdot \ln\left(\frac{d_j}{r_\mathrm{s}} \sqrt{\frac{(d_i d_j)^2 + r_\mathrm{s}^4 - 2 d_i d_j r_\mathrm{s}^2 \cos(\theta_{ij})}{(d_i d_j)^2 + d_j^4 - 2 d_i d_j^3 \cos(\theta_{ij})}}\right), \tag{2.79b}$$

where θ_{ij} is the angular separation between the i-th and j-th conductor.

2.2.3 Frequency-Domain Solution

Next, a solution for $n+1$ conductor lines in the frequency domain is derived. The solution is extended to include the chain-parameter representation for MTLs. It should be noted that the solution becomes very similar compared to two-conductor lines. The similarity transformation is used to decouple the MTL equations.

The transmission line equations in (2.70) and (2.71) of $n+1$ lossless conductor lines can easily be transformed into the frequency domain as follows:

$$\frac{\mathrm{d}^2\mathbf{V}(z)}{\mathrm{d}z^2} = -\omega^2 \cdot \mathbf{L}'\mathbf{C}' \cdot \mathbf{V}(z) \tag{2.80}$$

$$\frac{\mathrm{d}^2\mathbf{I}(z)}{\mathrm{d}z^2} = -\omega^2 \cdot \mathbf{C}'\mathbf{L}' \cdot \mathbf{I}(z). \tag{2.81}$$

Note that (2.80) and (2.81) are represented as uncoupled, second-order ordinary differential equations with the voltage and current vectors $\mathbf{V}(z)$ and $\mathbf{I}(z)$ in each equation being independent. Nevertheless, the two equations remain coupled via the matrices $\mathbf{L}'$ and $\mathbf{C}'$, because they are full matrices. Each entry of the voltages and currents $V_i(z)$ and $I_i(z)$ affects all other entries of the voltages and currents, $V_j(z)$ and $I_j(z)$.
The similarity transformation is used to decouple them by first applying a change of variables [17]. Here the voltage and current vectors are converted into *mode quantities* as follows:

$$\mathbf{V}(z) = \mathbf{T}_\mathrm{V} \cdot \mathbf{V}_\mathrm{m}(z) \tag{2.82}$$

$$\mathbf{I}(z) = \mathbf{T}_\mathrm{I} \cdot \mathbf{I}_\mathrm{m}(z). \tag{2.83}$$

The $n \times n$ matrices $\mathbf{T}_\mathrm{V}$ and $\mathbf{T}_\mathrm{I}$ are used to diagonalize the full matrices $\mathbf{L}'$ and $\mathbf{C}'$, as will be shown later. The $n \times 1$ vectors $\mathbf{V}_\mathrm{m}(z)$ and $\mathbf{I}_\mathrm{m}(z)$ are the *mode* voltages and currents. Substituting (2.82) into (2.80) leads to the second-order differential equation for the *mode quantities* as follows:

$$\frac{\mathrm{d}^2\mathbf{V}_\mathrm{m}(z)}{\mathrm{d}z^2} = -\omega^2 \cdot \mathbf{T}_\mathrm{V}^{-1}\mathbf{L}'\mathbf{C}'\mathbf{T}_\mathrm{V} \cdot \mathbf{V}_\mathrm{m}(z) = -\omega^2 \cdot \mathbf{L}'_\mathrm{m}\mathbf{C}'_\mathrm{m} \cdot \mathbf{V}_\mathrm{m}(z) = \boldsymbol{\gamma}^2\ \mathbf{V}_\mathrm{m}(z). \tag{2.84}$$

In the second representation of the above equation, the matrix $\mathbf{T}_\mathrm{I}$ and its inverse $\mathbf{T}_\mathrm{I}^{-1}$ were multiplied between $\mathbf{L}$' and $\mathbf{C}$, where

$$\mathbf{L}'_\mathrm{m} = \mathbf{T}_\mathrm{V}^{-1}\mathbf{L}'\mathbf{T}_\mathrm{I} \tag{2.85}$$

$$\mathbf{C}'_\mathrm{m} = \mathbf{T}_\mathrm{I}^{-1}\mathbf{C}'\mathbf{T}_\mathrm{V}. \tag{2.86}$$

The $n \times n$ matrix $\boldsymbol{\gamma}^2$ in (2.84) is diagonal. It is defined as $\boldsymbol{\gamma}^2 = \mathbf{T}_\mathrm{V}^{-1}\mathbf{L}'\mathbf{C}'\mathbf{T}_\mathrm{V}$, where γ_1 to γ_n are the entries in the main diagonal. The matrices $\mathbf{T}_\mathrm{V}$ and $\mathbf{T}_\mathrm{I}$ should be chosen so that

$\mathbf{L}'_{\mathrm{m}}$ and $\mathbf{C}'_{\mathrm{m}}$ are diagonalized at the same time.
Similarly, the second-order MTL equation for the *mode* currents becomes

$$\frac{\mathrm{d}^2\mathbf{I}_{\mathrm{m}}(z)}{\mathrm{d}z^2} = -\omega^2 \cdot \mathbf{C}'_{\mathrm{m}}\mathbf{L}'_{\mathrm{m}} \cdot \mathbf{I}_{\mathrm{m}}(z) = \boldsymbol{\gamma}^2\ \mathbf{I}_{\mathrm{m}}(z). \tag{2.87}$$

The presented problem is a typical eigenvalue/eigenvector problem of matrices. It can easily be interpreted that the columns of $\mathbf{T}_{\mathrm{V}}$ represent the *eigenvectors* of $\mathbf{L}'\mathbf{C}'$ and the columns of $\mathbf{T}_{\mathrm{I}}$ the *eigenvectors* of $\mathbf{C}'\mathbf{L}'$. The entries in the main diagonal of $\boldsymbol{\gamma}$ are the *eigenvalues* of $\mathbf{C}'\mathbf{L}'$ and $\mathbf{L}'\mathbf{C}'$. The solution of (2.84) and (2.87) with respect to the *mode* voltages and currents is given by [17]

$$\mathbf{V}_{\mathrm{m}}(z) = \mathbf{e}^{-\boldsymbol{\gamma}z}\mathbf{V}^{+}_{\mathrm{m}} + \mathbf{e}^{\boldsymbol{\gamma}z}\mathbf{V}^{-}_{\mathrm{m}} \tag{2.88}$$

$$\mathbf{I}_{\mathrm{m}}(z) = \mathbf{e}^{-\boldsymbol{\gamma}z}\mathbf{I}^{+}_{\mathrm{m}} - \mathbf{e}^{\boldsymbol{\gamma}z}\mathbf{I}^{-}_{\mathrm{m}}\,, \tag{2.89}$$

where $\mathbf{e}^{\pm\boldsymbol{\gamma}z}$ is a diagonal matrix exponential and $\mathrm{e}^{\pm\gamma_1 z}$ to $\mathrm{e}^{\pm\gamma_n z}$ are the entries of the main diagonal. The $n \times 1$ vectors $\mathbf{V}^{\pm}_{\mathrm{m}}$ and $\mathbf{I}^{\pm}_{\mathrm{m}}$ represent the forward and backward-traveling waves of the modes. The solution can be transformed back into actual voltages and currents using (2.82) and (2.83).

Chain-Parameter Representation

Similar to two-conductor lines, the MTLs can be represented with the chain-parameters as $2n$-ports, whereby the voltages and the currents at the ends are related to the chain-parameter matrix with [17]

$$\begin{bmatrix}\mathbf{V}(\mathcal{L})\\ \mathbf{I}(\mathcal{L})\end{bmatrix} = \begin{bmatrix}\boldsymbol{\Phi}_{11}(\mathcal{L}) & \boldsymbol{\Phi}_{12}(\mathcal{L})\\ \boldsymbol{\Phi}_{21}(\mathcal{L}) & \boldsymbol{\Phi}_{22}(\mathcal{L})\end{bmatrix} \cdot \begin{bmatrix}\mathbf{V}(0)\\ \mathbf{I}(0)\end{bmatrix}. \tag{2.90}$$

The $n \times n$ submatrices $\boldsymbol{\Phi}_{ij}$ for lossless lines are given by

$$\boldsymbol{\Phi}_{11}(\mathcal{L}) = \cosh(\mathrm{j}\beta\mathcal{L}) \cdot \mathbf{1}_n \tag{2.91a}$$

$$\boldsymbol{\Phi}_{12}(\mathcal{L}) = -\sinh(\mathrm{j}\beta\mathcal{L}) \cdot \mathbf{Z}_{\mathrm{c}} \tag{2.91b}$$

$$\boldsymbol{\Phi}_{21}(\mathcal{L}) = -\sinh(\mathrm{j}\beta\mathcal{L}) \cdot \mathbf{Z}_{\mathrm{c}}^{-1} \tag{2.91c}$$

$$\boldsymbol{\Phi}_{22}(\mathcal{L}) = \cosh(\mathrm{j}\beta\mathcal{L}) \cdot \mathbf{1}_n\,. \tag{2.91d}$$

The matrix $\mathbf{Z}_{\mathrm{c}}$ represents the characteristic impedance of the lines and is given by

$$\mathbf{Z}_{\mathrm{c}} = v\mathbf{L}', \tag{2.92}$$

where v is the velocity of propagation in a homogeneous medium with $v = 1/\sqrt{\mu\varepsilon}$.
Next, the time domain solution for MTL is presented.

2.2.4 Time-Domain Solution

Section 2.1.5 presented the solution at the terminals of lossless two-conductor lines. The derived solution for two-conductor lines is extended here for the case of lossless MTLs in a homogenous medium.

The chain-parameters defined in (2.91) are rewritten in the following form [17]:

$$\mathbf{\Phi}_{11}(z, \mathrm{j}\omega) = \left(\frac{\mathrm{e}^{\mathrm{j}\omega T_\mathrm{d}} + \mathrm{e}^{-\mathrm{j}\omega T_\mathrm{d}}}{2}\right) \cdot \mathbf{1}_n \tag{2.93a}$$

$$\mathbf{\Phi}_{12}(z, \mathrm{j}\omega) = -\left(\frac{\mathrm{e}^{\mathrm{j}\omega T_\mathrm{d}} - \mathrm{e}^{-\mathrm{j}\omega T_\mathrm{d}}}{2}\right) \cdot \mathbf{Z}_\mathrm{c} \tag{2.93b}$$

$$\mathbf{\Phi}_{21}(z, \mathrm{j}\omega) = -\left(\frac{\mathrm{e}^{\mathrm{j}\omega T_\mathrm{d}} - \mathrm{e}^{-\mathrm{j}\omega T_\mathrm{d}}}{2}\right) \cdot \mathbf{Z}_\mathrm{c}^{-1} \tag{2.93c}$$

$$\mathbf{\Phi}_{22}(z, \mathrm{j}\omega) = \left(\frac{\mathrm{e}^{\mathrm{j}\omega T_\mathrm{d}} + \mathrm{e}^{-\mathrm{j}\omega T_\mathrm{d}}}{2}\right) \cdot \mathbf{1}_n. \tag{2.93d}$$

The phase constant β from (2.36) and the one-way time delay T_d from (2.56) are used as follows:

$$\mathrm{j}\beta\mathcal{L} = \mathrm{j}\omega \cdot \frac{\mathcal{L}}{v} = \mathrm{j}\omega T_\mathrm{d}. \tag{2.94}$$

Substituting (2.93) into (2.90) leads to the terminal voltages and currents as follows [17]:

$$\mathbf{V}(\mathcal{L}, \mathrm{j}\omega) = \left(\frac{\mathrm{e}^{\mathrm{j}\omega T_\mathrm{d}} + \mathrm{e}^{-\mathrm{j}\omega T_\mathrm{d}}}{2}\right) \cdot \mathbf{V}(0, \mathrm{j}\omega) - \left(\frac{\mathrm{e}^{\mathrm{j}\omega T_\mathrm{d}} - \mathrm{e}^{-\mathrm{j}\omega T_\mathrm{d}}}{2}\right) \cdot \mathbf{Z}_\mathrm{c}\mathbf{I}(0, \mathrm{j}\omega) \tag{2.95a}$$

$$\mathbf{I}(\mathcal{L}, \mathrm{j}\omega) = -\left(\frac{\mathrm{e}^{\mathrm{j}\omega T_\mathrm{d}} - \mathrm{e}^{-\mathrm{j}\omega T_\mathrm{d}}}{2}\right) \cdot \mathbf{Z}_\mathrm{c}^{-1}\mathbf{V}(0, j\omega) + \left(\frac{\mathrm{e}^{\mathrm{j}\omega T_\mathrm{d}} + \mathrm{e}^{-\mathrm{j}\omega T_\mathrm{d}}}{2}\right) \cdot \mathbf{I}(0, \mathrm{j}\omega). \tag{2.95b}$$

Multiply (2.95b) by $\mathbf{Z}_\mathrm{c}$, then add and subtract the two equations to get

$$\mathbf{V}(\mathcal{L}, \mathrm{j}\omega) + \mathbf{Z}_\mathrm{c}\mathbf{I}(\mathcal{L}, \mathrm{j}\omega) = \mathrm{e}^{-\mathrm{j}\omega T_\mathrm{d}}\, \mathbf{V}(0, \mathrm{j}\omega) + \mathrm{e}^{-\mathrm{j}\omega T_\mathrm{d}}\, \mathbf{Z}_\mathrm{c}\mathbf{I}(0, \mathrm{j}\omega) \tag{2.96a}$$

$$\mathbf{V}(\mathcal{L}, \mathrm{j}\omega) - \mathbf{Z}_\mathrm{c}\mathbf{I}(\mathcal{L}, \mathrm{j}\omega) = \mathrm{e}^{\mathrm{j}\omega T_\mathrm{d}}\, \mathbf{V}(0, \mathrm{j}\omega) - \mathrm{e}^{\mathrm{j}\omega T_\mathrm{d}}\, \mathbf{Z}_\mathrm{c}\mathbf{I}(0, \mathrm{j}\omega). \tag{2.96b}$$

Now converting the solution to the time domain [17]

$$\mathbf{V}(\mathcal{L}, t) + \mathbf{Z}_\mathrm{c}\mathbf{I}(\mathcal{L}, t) = \mathbf{V}(0, t - T_\mathrm{d}) + \mathbf{Z}_\mathrm{c}\mathbf{I}(0, t - T_\mathrm{d}) \tag{2.97a}$$

$$\mathbf{V}(\mathcal{L}, t) - \mathbf{Z}_\mathrm{c}\mathbf{I}(\mathcal{L}, t) = \mathbf{V}(0, t + T_\mathrm{d}) - \mathbf{Z}_\mathrm{c}\mathbf{I}(0, t + T_\mathrm{d}). \tag{2.97b}$$

It can be seen that the solution relates the voltages and currents at the terminal by the time delay T_d in a manner similar to the solutions in (2.63) and (2.65) for two-conductor lines. The solution presented does not include the terminal loads, which require steps similar to those in section 2.1.5 to be followed.

So far, the fundamentals and solutions of transmission lines have been presented. In the next chapter, the basics of shielded cables are introduced.

2.3 Introduction to Shielded Cables

The different types of shields that are commonly used in practice are presented in this section. The equivalent circuit diagram for a shielded cable is derived together with the transmission line equations. The transfer impedance and the transfer admittance will be explained. Finally, measurement methods and analytical approaches for determining the transfer impedance of a braided shield are shown. The basics for shielded cables presented here mainly refer to the source [2].

An example of a real setup for an EMC-compatible system is shown in Fig. 2.10. The system consists of a source V_1 that transmits signals to the Z_{ir} load via a shielded cable. The cable shield is connected to the metal enclosures and these are connected to the ground. The connection to the ground plane is represented by the loads Z_{ol} and Z_{or}. Such a structure in the real world is often a victim of illuminated electromagnetic waves. A plane wave with the angle of incidence θ and the electric field $\vec{E}^{\mathrm{i}}$ is shown towards $\vec{\beta}$. The field incident on the cable can penetrate the inner conductor due to the imperfection of the shield and reduce the immunity of the system. The currents generated by the coupled field can spread to the load and source and lead to distortions of the transmitted signal or, in the worst case, to system failure. In addition, coupling between the inner conductor and the outer shielding may occur, increasing the emission level and affecting neighboring equipment. Inner to outer coupling occurs when, for example, source V_1 in Fig. 2.10 is active.

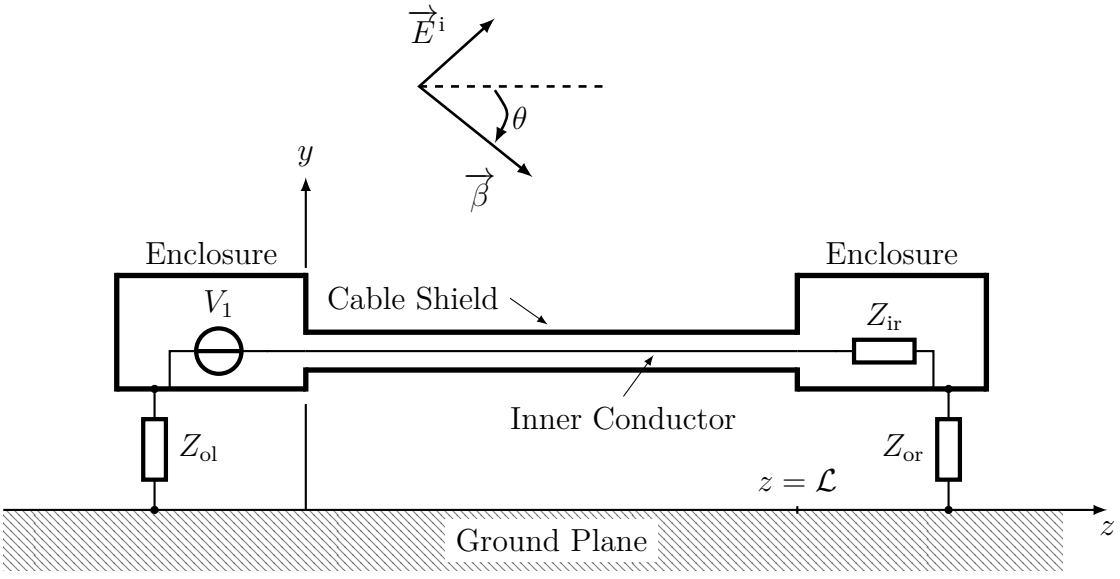

Figure 2.10: Exemplary arrangement in EMC.

A qualitative description of the coupling via the shield can be presented in three categories:

- diffusion of the fields for imperfect electrically conductive shielding material
- field penetration through the openings in the shield, for example when using a braided shield
- an additional inductive coupling results from the overlap of the layer structure of the braid.

The type of shielding used plays an important role in the amount and type of coupling. For this reason, the various types of shielded cables that are used in practice will be briefly explained.

2.3.1 Shielding Types for Cables

One of the first ideas for cable shielding was to use a tubular solid shield, in which the shielding efficiency can be improved by increasing the conductivity of the shielding material and its thickness. Although the tubular solid shield offers 100 % coverage and better electromagnetic protection at higher frequencies compared to other types, it does not offer mechanical flexibility.
An alternative construction with 100 % coverage is the foil shield. It consists of a thin foil that is wrapped lengthways or spirally around the cable core, as shown in Fig. 2.11a. The material used is often aluminum, rarely copper and magnetic alloys. A foil shield offers better mechanical flexibility compared to the tubular one, but has a lower mechanical strength. Due to the thin layer, it does not provide good protection against magnetic fields [45]. The overlapping of the foils creates slits along the cable, which reduce the shielding efficiency at very high frequencies. The foil shield has a higher DC resistance due to the smaller thickness.

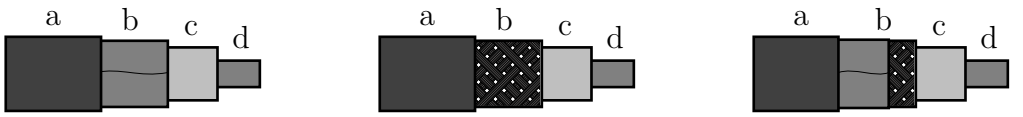

(a) Foil Shield (b) Braided Shield (c) Foil/Braided Shield

Figure 2.11: Different types of shielded cables. a Jacket. b Shield. c Insulator. d Inner conductor.

Another type of shield that has a low DC resistance and is therefore better suited for low-frequency interference is the braid. It consists of groups of copper or aluminum strands called carriers that are woven above and below one another, as can be seen in Fig. 2.11b. Compared to the foil shield, the braided one offers better mechanical strength as well as mechanical flexibility. The overlapping of the carriers with different angles creates

diamond-shaped apertures, so that the coverage is no longer 100 %. It is typically 80 to 95 %. Electromagnetic fields can penetrate through these openings and thus reduce the shielding performance in higher frequency ranges.
In order to take advantage of both described types, foil and braid are combined to form a shield. The combination of foil and braid shown in Fig. 2.11c uses 100 % coverage through the foil shield together with the low DC resistance and the mechanical strength of the braid. It offers a compromise between sufficient flexibility and high electrical performance. A combination of three shield types or more are also common. In addition to the defined types, there are other shields that occur in practice. For example, the spiral shield is used for greater flexibility and low frequencies.

2.3.2 Transmission Line Models of Shielded Cables

The field coupling shown in Fig. 2.10 generates distributed currents along the cable shield and distributed voltages between the shield and the ground plane. The current generated creates an axial electric field within the shield. This field leads to a voltage between the inner conductor and the shield. As mentioned before, this phenomenon is called diffusion. Another coupling process takes place when the external field penetrates through the openings in the shield if the coverage is not 100 %. Lumped sources connected to the cable can also cause these unwanted couplings, and the coupling can be from the inside to the outside of the shield or vice versa.
A shielded cable is shown above a ground plane in Fig. 2.12. The $I_\mathrm{o}(z)$ and $V_\mathrm{o}(z)$ parameters in the same figure represent the current and the voltage between the shield and the ground reference. The elements $I_\mathrm{i}(z)$ and $V_\mathrm{i}(z)$ represent the current and voltage in the inner system between the inner wire and the shield. A quantitative analysis of the described couplings will be explained in more detail in the next steps, taking into account the concept of transfer impedance and transfer admittance.

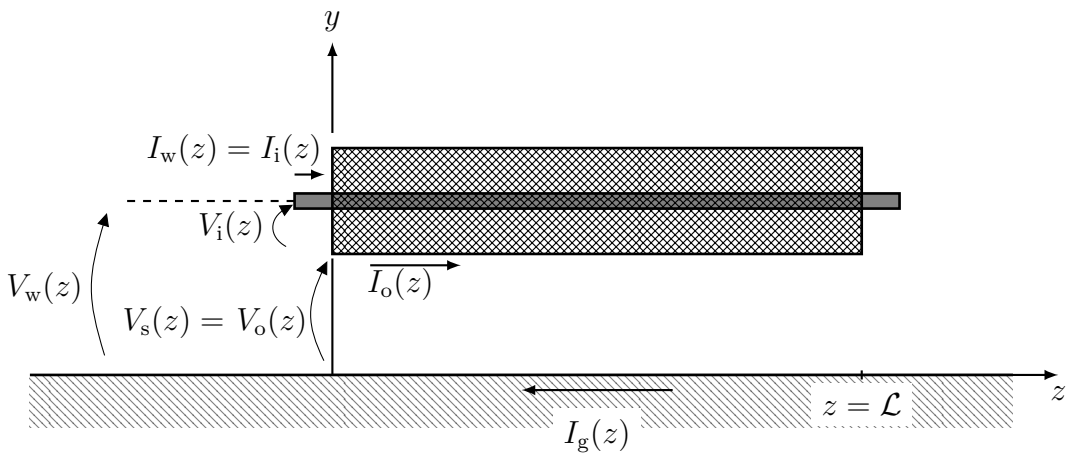

Figure 2.12: Current and voltage distribution on a shielded cable.

Domain Decomposition

Domain decomposition was applied to a shielded cable located above a ground plane, with two systems defined and treated separately. The inner system consists of the inner conductor and the inner side of the shield, the outer system consists of the outer shield and the ground plane. Both systems are coupled via the transfer impedance Z_t and the transfer admittance Y_t, where the p.u.l. transfer impedance and the p.u.l. transfer admittance are given by Z_t' and Y_t'. The shield is considered a local reference in the inner system. In order to represent the voltage of the inner system in relation to the ground plane as a global reference, the following transformation matrices must be applied [46]:

$$\begin{bmatrix} V_\mathrm{w}(z) \\ V_\mathrm{s}(z) \end{bmatrix} = \begin{bmatrix} 1 & 1 \\ 0 & 1 \end{bmatrix} \cdot \begin{bmatrix} V_\mathrm{i}(z) \\ V_\mathrm{o}(z) \end{bmatrix}. \tag{2.98}$$

The parameters $V_\mathrm{w}(z)$ and $V_\mathrm{s}(z)$ represent the voltages of the inner conductor and the shield with the ground plane as a global reference. In a similar way the transformation matrix of the currents is defined as

$$\begin{bmatrix} I_\mathrm{i}(z) \\ I_\mathrm{g}(z) \end{bmatrix} = \begin{bmatrix} 1 & 0 \\ 1 & 1 \end{bmatrix} \begin{bmatrix} I_\mathrm{w}(z) \\ I_\mathrm{o}(z) \end{bmatrix}, \tag{2.99}$$

where $I_\mathrm{w}(z) = I_\mathrm{i}(z)$ is the wire current. The element $I_\mathrm{g}(z)$ represents the total current flowing in the ground plane. The following indices have been used: i for the inner system, w for the wire, o for the outer system and s for the shield. An equivalent circuit diagram of a short section Δz for the shielded cable from Fig. 2.12 is shown in Fig. 2.13. Two coupled circuits can be observed. The equivalent circuit of the inner system comprises the series impedance $Z_\mathrm{i}'\Delta z$ and the shunt admittance $Y_\mathrm{i}'\Delta z$, which are formed by the inner conductor and the shield. The voltage and current sources $V_\mathrm{di}'\Delta z$ and $I_\mathrm{di}'\Delta z$ represent the coupling from the outer system and are directly proportional to Z_t' and Y_t'. The index d stands for disturbance, for example V_di' is the p.u.l. disturbance voltage in the inner system. The outer system circuit consists of the series impedance $Z_\mathrm{o}'\Delta z$ and the shunt admittance $Y_\mathrm{o}'\Delta z$ between the shield and the ground plane together with the voltage and current sources $V_\mathrm{do}'\Delta z$ and $I_\mathrm{do}'\Delta z$, which include the coupling from the inner system and the coupling to the environment. The transmission line equations for the inner system can be easily derived using Kirchhoff's voltage and current laws in Fig. 2.13 [2].

$$\frac{\mathrm{d}}{\mathrm{d}z}\begin{bmatrix} V_\mathrm{i}(z) \\ I_\mathrm{i}(z) \end{bmatrix} = \begin{bmatrix} 0 & -Z_\mathrm{i}' \\ -Y_\mathrm{i}' & 0 \end{bmatrix} \cdot \begin{bmatrix} V_\mathrm{i}(z) \\ I_\mathrm{i}(z) \end{bmatrix} + \begin{bmatrix} V_\mathrm{di}'(z) \\ I_\mathrm{di}'(z) \end{bmatrix} \tag{2.100}$$

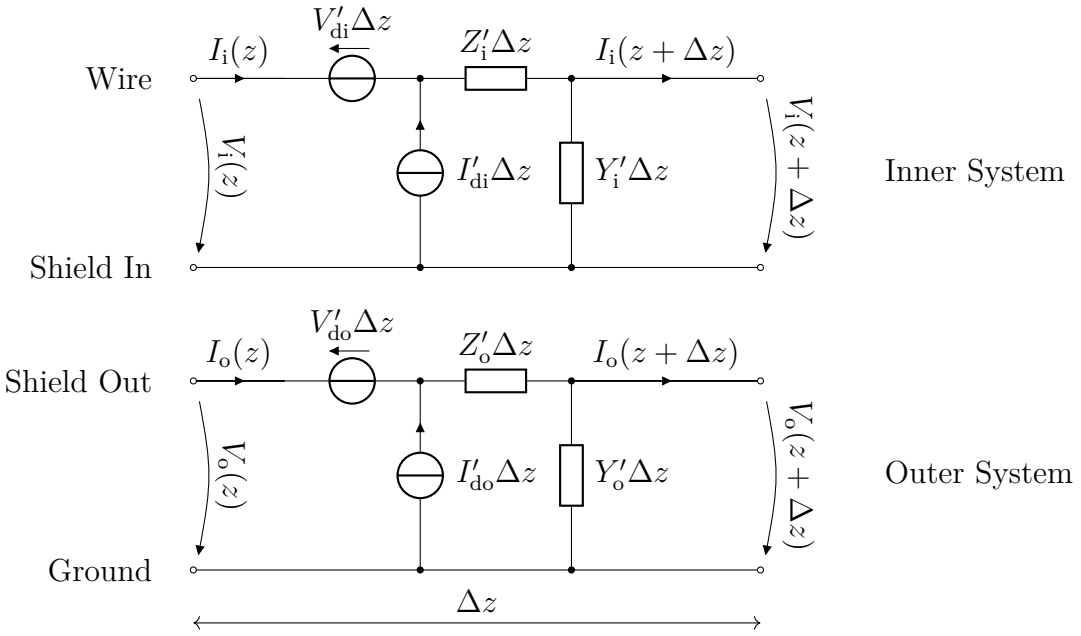

Figure 2.13: Equivalent circuit for a short segment of a shielded cable.

The sources $V'_\mathrm{di}(z)$ and $I'_\mathrm{di}(z)$ are given by

$$V'_\mathrm{di}(z) = Z'_\mathrm{t} I_\mathrm{o}(z) \tag{2.101a}$$

$$I'_\mathrm{di}(z) = -Y'_\mathrm{t} V_\mathrm{o}(z). \tag{2.101b}$$

The transmission line equations for the outer system are presented in the same way as follows [2]:

$$\frac{\mathrm{d}}{\mathrm{d}z}\begin{bmatrix} V_\mathrm{o}(z) \\ I_\mathrm{o}(z) \end{bmatrix} = \begin{bmatrix} 0 & -Z'_\mathrm{o} \\ -Y'_\mathrm{o} & 0 \end{bmatrix} \cdot \begin{bmatrix} V_\mathrm{o}(z) \\ I_\mathrm{o}(z) \end{bmatrix} + \begin{bmatrix} V'_\mathrm{do}(z) \\ I'_\mathrm{do}(z) \end{bmatrix}. \tag{2.102}$$

The interference sources of the outer system result from the coupling of the inner system and the coupling with the environment. Assuming that the field coupling is taken into account, the field distributed voltages and currents $V'_\mathrm{f}(z)$ and $I'_\mathrm{f}(z)$ are added as follows:

$$V'_\mathrm{do}(z) = Z'_\mathrm{t} I_\mathrm{i}(z) + V'_\mathrm{f}(z) \tag{2.103a}$$

$$I'_\mathrm{do}(z) = -Y'_\mathrm{t} V_\mathrm{i}(z) + I'_\mathrm{f}(z). \tag{2.103b}$$

The transfer parameters of the cable shield are explained in more detail in the following sections.

2.3.3 Transfer Parameter Definition

As mentioned above, the coupling between the inner and outer systems depends mainly on the transfer impedance and the transfer admittance of the cable. This section explains the mathematical definition and measurement methods for these parameters.

Transfer Impedance

The transfer impedance is a quantitative measure for the efficiency of the cable shield. With a higher Z'_t, the efficiency becomes worse and the interference voltage $V'_\mathrm{di}(z)$ in (2.101a) is higher [47]. The mathematical form represents the ratio of an open circuit voltage induced in the inner system to one ampere current, which is impressed in the outer system in a cable of one meter. The cable should be electrically short, where the wavelength for the frequency of interest must be much greater than one meter. The formula can be derived by setting $I_\mathrm{i}(z)$ to zero in (2.100) and using (2.101a), as described in [2]. It is given by

$$Z'_\mathrm{t} = \frac{1}{I_\mathrm{o}(z)} \cdot \left.\frac{\mathrm{d}V_\mathrm{i}(z)}{\mathrm{d}z}\right|_{I_\mathrm{i}=0}. \tag{2.104}$$

One of the first analytical models for the transfer impedance of a solid tubular shield was derived by Schelkunoff [25]. Taking into account a cable with a shielding conductivity σ, an inner radius $r_\mathrm{tu,i}$ and an outer radius $r_\mathrm{tu,o}$, the general form of the transfer impedance was defined as [25]

$$Z'_\mathrm{t} = \frac{\gamma_0}{2\pi\sigma r_\mathrm{tu,o}} \cdot \frac{J_1(\gamma_0 r_\mathrm{tu,i})N_0(\gamma_0 r_\mathrm{tu,i}) - N_1(\gamma_0 r_\mathrm{tu,i})J_0(\gamma_0 r_\mathrm{tu,i})}{J_1(\gamma_0 r_\mathrm{tu,i})N_1(\gamma_0 r_\mathrm{tu,o}) - N_1(\gamma_0 r_\mathrm{tu,i})J_1(\gamma_0 r_\mathrm{tu,o})}, \tag{2.105}$$

where

$$\gamma_0 = \sqrt{\mathrm{j}\omega\mu(\sigma + \mathrm{j}\omega\varepsilon)}. \tag{2.106}$$

The index tu stands for tubular shield. The elements J_i and N_i with the order i represent the cylindrical Bessel function of the first and second kind. The parameters ε and μ are the permittivity and the permeability of the sheath material. Equation (2.106) can be simplified in the classic transmission line theory, in which the screen thickness $\Delta = (r_\mathrm{tu,o} - r_\mathrm{tu,i})$ is much smaller than the radius $r_\mathrm{tu,i}$ of the cable and $r_\mathrm{tu,i}$ is much smaller than the wavelength of interest. In this case, the equation is approximated by

$$Z'_\mathrm{t} \approx R'_0 \cdot \frac{(1+\mathrm{j})\Delta/\delta}{\sinh\left((1+\mathrm{j})\Delta/\delta\right)}, \tag{2.107}$$

where

$$R'_0 = \frac{1}{\pi\sigma(r_\mathrm{tu,o} + r_\mathrm{tu,i})(r_\mathrm{tu,o} - r_\mathrm{tu,i})} \approx \frac{1}{2\pi\sigma r_\mathrm{tu,i}\Delta}. \tag{2.108}$$

The parameter R'_0 represents the DC p.u.l. resistance of the shield. The term δ is the skin depth defined in (2.26). A simplification for low and high frequency cases was developed by Vance [26]. At low frequencies, $\Delta/\delta \ll 1$ and

$$Z'_\mathrm{t} \approx R'_0. \tag{2.109}$$

At higher frequencies this condition no longer applies and $\Delta/\delta \gg 1$, which leads to

$$Z'_\mathrm{t} = 2\sqrt{2}\, R'_\mathrm{hf}\, \mathrm{e}^{-(1+\mathrm{j})\Delta/\delta}\, \mathrm{e}^{\mathrm{j}\pi/4}\,. \tag{2.110}$$

The parameter R'_hf is defined as $R'_\mathrm{hf} = 1/(2\pi r_{\mathrm{tu,i}}\delta\sigma)$.

Transfer Admittance

The transfer admittance represents the ratio of the current $I_\mathrm{i}(z)$ generated in the inner system of a shielded cable in Fig. 2.12 to the voltage $V_\mathrm{o}(z)$ applied as a source of interference in the outer system. The transfer admittance is defined in this way under the conditions that the cable length is 1 m, the inner conductor is short-circuited to the shield and the interference voltage is set to 1 V. The cable should be electrically short compared to the frequency of interest. The mathematical form can easily be derived by setting $V_\mathrm{i}(z)$ to zero in (2.100) and using (2.101b). It is given by [2]

$$Y'_\mathrm{t} = -\frac{1}{V_\mathrm{o}(z)} \cdot \left.\frac{\mathrm{d}I_\mathrm{i}(z)}{\mathrm{d}z}\right|_{V_\mathrm{i}=0}. \tag{2.111}$$

In most analytical and practical work, the focus continued to be on the transfer impedance for shielded cables, since this term mostly dominates and the transfer admittance part is regarded as a weak coupling. The solid tubular shield can very well prevent the electric field, whereby the contribution of Y'_t can be neglected. In the case of a braided shielding, the electric fields can penetrate through the openings and lead to a coupling via the transfer admittance. However, in most practical cases, Y'_t was ignored because the shield is normally connected to the ground plane. Therefore, the transfer impedance is discussed in more detail in this work.

2.3.4 Measurement of the Transfer Impedance

In order to measure the transfer impedance defined in (2.104), the induced voltage in the inner system should be determined for a properly defined injected current in the outer system. Such measurements have been carried out in several works [48–50]. Two standards for measuring the transfer impedance have been defined and are described in this section.

Triaxial Method

The triaxial method defined in the IEC 62153-4-3 [51] standard represents the measurement of Z'_t in a triple coaxial structure, as shown in Fig. 2.14.

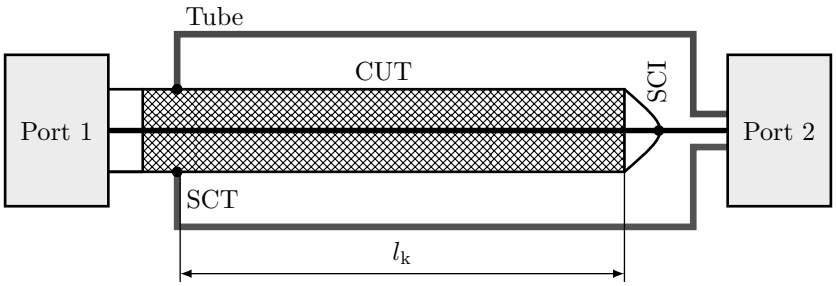

Figure 2.14: Setup of the triaxial measurement method for a single conductor shielded cable. SCI short circuit inner conductor with shield. SCT short circuit tube with shield.

The coaxial cable is placed into a solid metal tube. The outer circuit of the structure consists of the outer shield together with the metal tube and the inner circuit consists of the inner conductor together with the inside of the shield. The outer circuit is short-circuited on the left-hand side and the inner circuit is short-circuited on the right-hand side as shown in Fig. 2.14 by SCT and SCI.

When a voltage signal is fed to port 2, it causes a current to flow along the outer shield of the cable under test (CUT). This current is coupled into the inner circuit and induces a voltage that can be measured at port 1. This structure is well suited for measuring the transfer impedance with a sensitivity of 1 µΩ for a cable length $l \leq \lambda/10$ and λ is the wavelength of the maximum frequency of interest.
The IEC 62153-4-3 standard defines other methods than the one shown in Fig. 2.14. In other procedures, the source and sink are interchanged. An impedance matching device is added when the internal circuit impedance deviates from the generator impedance.
The cut-off frequency f_cut at which the transfer impedance can be measured using the method presented in Fig. 2.14 is given by [51]

$$f_\mathrm{cut} = \frac{30\,\mathrm{MHz} \cdot 1\,\mathrm{m}}{l_\mathrm{k}}, \tag{2.112}$$

where l_k is the coupling length. The method can be used for a frequency range of up to 30 MHz with a cable length of 1 m and up to 100 MHz with a cable length of 0.3 m, where $l_\mathrm{k} \leq \lambda/10$. Other parts of the same standard are expanded to include connectors within the measurement. The transfer impedance can be calculated as follows [51]:

$$Z'_\mathrm{t} = \frac{Z_0}{2l_\mathrm{k}} \cdot 10^{\frac{S_{21}}{20}}, \tag{2.113}$$

where Z_0 is the input impedance of the measuring system at port 1 and port 2, typically $50\,\Omega$ using a network analyzer. The parameter S_{21} is the scattering parameter between port 1 and port 2 in dB.

The triaxial method can also be used for balanced, shielded multiconductor cables. Balanced, shielded multiconductor cables mean that the inner conductors are arranged at the same distance from each other and from the shield. In the triaxial method, the cable is then treated as a quasi-coaxial system with all inner conductors connected at both ends, as shown in Fig. 2.15. The transfer impedance defined in (2.113) for the single conductor can also be used here.

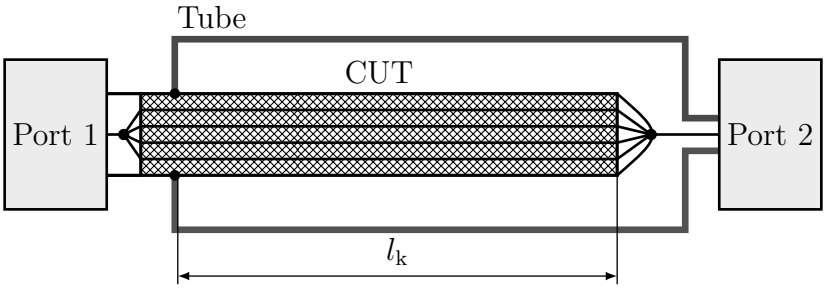

Figure 2.15: Setup of the triaxial measurement method for a balanced multiconductor shielded cable.

The triaxial method has also been defined for the measurement of the transfer admittance in IEC 62153-4-8 [52]. The measurement setup is defined similarly to the transfer impedance. It is not dealt with here in this work, since Y_t' is neglected in later analyzes.

Line Injection Method

The triaxial method is a widely used standard and offers good immunity to the environment due to the metal tube that encloses the cable. However, the measurement setup is relatively complex and has a comparatively low cut-off frequency. An alternative method is the line injection measurement method defined in the standard IEC 62153-4-6 [53]. The basic idea is to couple defined radio frequency energy into the CUT with an unshielded wire that is evenly arranged near to it. In practice, this is achieved by tying a supporting coaxial cable (SCC) to the CUT, as shown in Fig. 2.16. The outer shield of the SCC is galvanic connected to the outer shield of the CUT. The shield and insulation material of the SCC are removed along the coupling length l_k, where its inner conductor uses the outer shield of the CUT as a reference to act as a transmission line. The loads R_1 and R_2 are set to the characteristic impedances of the CUT and the SCC, respectively. The cut-off frequency

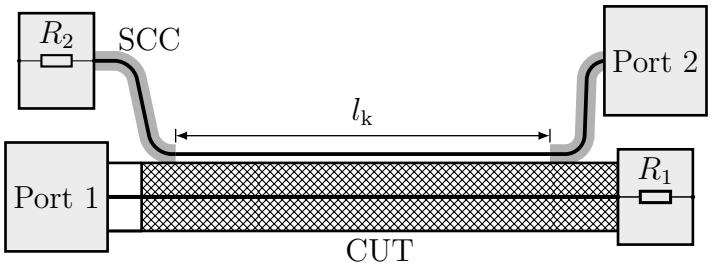

Figure 2.16: Setup of the line injection measurement method for a single conductor shielded cable.

f_{cut} is given by [53]

$$f_{\text{cut}} = \frac{v_0}{\pi \cdot l_k \left| \sqrt{\varepsilon_{r1}} - \sqrt{\varepsilon_{r2}} \right|}, \tag{2.114}$$

where v_0 is the speed of light in free space, l_k is the coupling length and ε_{r1} and ε_{r2} are the relative dielectric constants of the CUT and the SCC. The coupling length depends on the highest frequency to be measured and must be at least 0.3 m according to the standard. The p.u.l. transfer impedance for matched loads at the cable ends is defined as [53]

$$Z'_t = \frac{R_1 + Z_0}{l_k} \cdot 10^{\frac{S_{21}}{20}}. \tag{2.115}$$

The parameter Z_0 represents the impedance of the measuring system, typically 50 Ω when using a network analyzer. The parameter S_{21} is the scattering parameter between port 1 and 2 in dB. The attenuation between port 2 and the load R_2 should be calibrated out before the measurement is performed. Fig. 2.16 shows the measurement at the far end. Port 2 and R_2 must be exchanged for the near end measurement. The measurement of different cable types with this method was carried out in [54, 55].
The line injection method can also be used for balanced shielded multiconductor cables in which all inner conductors are short-circuited and connected at both ends, as in the triaxial method in Fig. 2.15.

2.3.5 Characteristic of Braided Shields

In addition to the existing measurement methods for transfer impedance, analytical approaches were developed. Fig. 2.17 shows an unwrapped braided shield of a cable with radius r_{br}. The braid parameters are defined as follows: $\mathcal{G}$ is the weave angle, σ is the electrical conductivity of the shielding material, $\mathcal{C}$ is the number of carriers, p_{br} is the distance between two carriers in the longitudinal direction of the cable, N_{fi} is the number of filament for each carrier and d_{fi} is the diameter of the filament. The shield consists of many carriers that are woven above and below each other. In the present case in Fig. 2.17, each

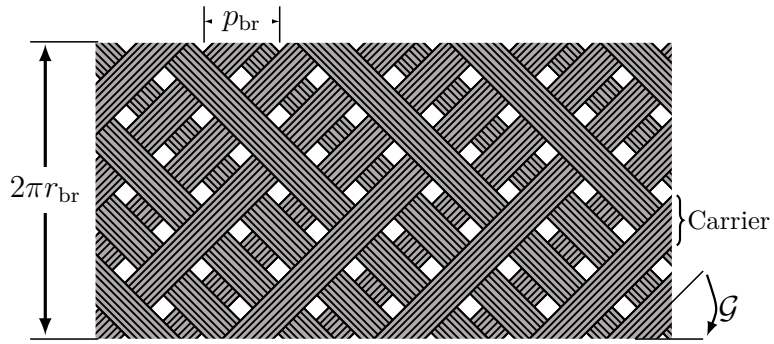

Figure 2.17: Basic structure of a braided shield.

carrier consists of eight parallel wire filaments. This structure does not provide complete coverage due to the openings between the carriers. This allows fields to penetrate and couple the inner conductor. In order to calculate the inductive coupling, approaches for a single aperture in a solid coaxial shield were considered, then the solution was extended for the case of braided shield with several apertures [27]. Vance expanded this approach to include the diffusion term Z'_{d}, which gave the first expression for the transfer impedance as follows [2, 26]:

$$Z'_{\mathrm{t}} = Z'_{\mathrm{d}} + \mathrm{j}\omega L'_{\mathrm{t}}. \tag{2.116}$$

The inductive term L'_{t} for $\mathcal{G} < 45°$ is defined as

$$L'_{\mathrm{t}} = \frac{\pi\mu_0}{6\mathcal{C}} \cdot (1-\mathcal{K})^{3/2} \cdot \frac{e^2}{E(e) - (1-e^2)\,K(e)}. \tag{2.117}$$

For $\mathcal{G} > 45°$, L'_{t} is given by

$$L'_{\mathrm{t}} = \frac{\pi\mu_0}{6\mathcal{C}} \cdot (1-\mathcal{K})^{3/2} \cdot \frac{e^2/\sqrt{1-e^2}}{E(e) - (1-e^2)\,K(e)}, \tag{2.118}$$

where $K(\cdot)$ and $E(\cdot)$ represent the complete elliptic integrals of the first and second kind. The parameters e and $\mathcal{K}$ denote the eccentricity of the ellipse and the optical coverage of the braid, respectively. The diffusion term Z'_{d} has been extended from the expression for the solid shield defined in (2.107)

$$Z'_{\mathrm{d}} = \frac{4}{\pi\, d_{\mathrm{fi}}^2\, N_{\mathrm{fi}}\, \mathcal{C}\, \sigma\, \cos(\mathcal{G})} \cdot \frac{(1+\mathrm{j})d_{\mathrm{fi}}/\delta}{\sinh\left((1+\mathrm{j})d_{\mathrm{fi}}/\delta\right)}, \tag{2.119}$$

where R'_0 was replaced to include the braid properties.
The model proposed by Vance was experimentally tested by Degauque and Hamelin [56]. The results showed higher deviations for samples of a braided shield with a weave angle $\mathcal{G} \ll 45°$ or a high optical coverage. For samples with $\mathcal{G} \approx 45°$ and poor optical coverage,

adequate agreement with the measured data was observed. This leads to the interpretation that the transfer impedance in (2.116) can be used under the latter conditions. Further studies have shown that a $\sqrt{f}$ term must be added to the formula to get better results in the case of high optical coverage or if $\mathcal{G}$ differs widely from 45°.
The dependence of the transfer impedance on $\sqrt{f}$ was called the *porpoising effect*. The superposition of the carriers leads to an inter-contact resistance which, at higher ohmic values, forces the current to flow in its own carriers [57]. Another reason for this effect is the twist in the carriers, which causes an additional inductive term. Based on the studies mentioned, new terms were added to the Vance model to improve the expression of the transfer impedance.

Model of Tyni

Tyni added the term L'_p to the transfer impedance, which is given by [23]

$$Z'_\mathrm{t} = Z'_\mathrm{d} + \mathrm{j}\omega L'_\mathrm{t} + \mathrm{j}\omega L'_\mathrm{p}. \tag{2.120}$$

The first two parts represent the diffusion and aperture penetration, as previously indicated. The last term represents the porpoising effect caused by the mutual inductance between carriers. It is given by

$$L'_\mathrm{p} = \frac{\mu_0 h_\mathrm{br}}{4\pi D_\mathrm{br}} \cdot \left(1 - \tan^2(\mathcal{G})\right), \tag{2.121}$$

where h_br is the effective distance between two layers of the braid and $D_\mathrm{br} = 2r_\mathrm{br}$ is the outer diameter of the cable shield. Based on Kaden's work [58], a $\sqrt{f}$ term was added to L'_p as follows [23]:

$$L'_\mathrm{pl} = L'_\mathrm{p}\left(1 + \frac{a_\mathrm{br}}{\sqrt{\mathrm{j}\omega}}\right). \tag{2.122}$$

Here a_br is an auxiliary factor that was not explicitly determined in the mentioned source.

Model of Demoulin

The porpoising effect was also considered by Demoulin, where he explained that this effect is due to the eddy current flow in the braid [59]. The current is related to the surface conductivity of the carriers, which is proportional to the square root of the frequency. He suggested an expression of four parts, given by

$$Z'_\mathrm{t} = Z'_\mathrm{d} + \mathrm{j}\omega L'_\mathrm{t} + k'\sqrt{\omega}\ \mathrm{e}^{\mathrm{j}\pi/4} \pm \mathrm{j}\omega L'_\mathrm{p}, \tag{2.123}$$

where Z'_{d}, L'_{t} and L'_{p} were defined before. The parameter L'_{p} depends on $\mathcal{G}$, where L'_{p} is positive if $\mathcal{G} > 45°$ and negative if $\mathcal{G} < 45°$. The element k' is defined as

$$k' = -\frac{1.16}{\mathcal{C} d_{\mathrm{fi}}^2 N_{\mathrm{fi}}} \cdot \arctan\left(\frac{N_{\mathrm{fi}}}{3}\right) \cdot \sin\left(\frac{\pi}{2} - 2\mathcal{G}\right) \cdot \sqrt{\frac{\mu}{\sigma}}. \tag{2.124}$$

The elements $\mathcal{C}$, d_{fi}, N_{fi}, $\mathcal{G}$, μ and σ were previously defined. It should be noted here that $k' = 0$ when $\mathcal{G} = 45°$. In this case the porpoising effect disappears and Z'_{t} takes the same form as that defined by Vance in (2.116).

Model of Kley

The transfer impedance model proposed by Kley [60] is given by

$$Z'_{\mathrm{t}} = Z'_{\mathrm{d}} + \mathrm{j}\omega L'_{\mathrm{k}} + (1 + \mathrm{j})\,\omega L'_{\mathrm{s}}, \tag{2.125}$$

where Z'_{d} is the diffusion term as previously defined in (2.119). The expression L'_{k} is given by

$$L'_{\mathrm{k}} = M'_{\mathrm{l}} + M'_{\mathrm{g}}, \tag{2.126}$$

where M'_{l} is the modified aperture penetration effects, taking into account the braid curvature and the thickness of the braid openings. It is defined by $M'_{\mathrm{l}} = 0.875 L'_{\mathrm{t}} \mathrm{e}^{-\tau_{\mathrm{h}}}$, where

$$\tau_{\mathrm{h}} = 9.6 F_{\mathrm{br}} \left(\frac{\mathcal{K}^2 d_{\mathrm{fi}}}{2 r_{\mathrm{br}}}\right)^{1/3}. \tag{2.127}$$

The parameter L'_{t} is defined in (2.117) and (2.118). The parameter F_{br} represents the shield fill factor. The porpoising effect is taken into account by M'_{g}, where

$$M'_{\mathrm{g}} \approx -\mu_0 \cdot \frac{0.11 d_{\mathrm{fi}}}{4\pi r_{\mathrm{br}} F_0} \cdot \cos\left(2 k_1 \mathcal{G}\right) \tag{2.128}$$

with $F_0 = F_{\mathrm{br}} \cos(\mathcal{G})$ is the minimal filling factor and

$$k_1 = \frac{\pi}{4} \cdot \left(\frac{2}{3} F_0 + \frac{\pi}{10}\right)^{-1}. \tag{2.129}$$

The term $(1 + \mathrm{j})\,\omega L'_{\mathrm{s}}$ in (2.125) takes into account the eddy current generated in the walls of the braid openings, which is proportional to $\sqrt{f}$ and is defined as

$$\omega L'_{\mathrm{s}} = \frac{1}{\pi \sigma \delta} \cdot \left(\frac{1}{D_{\mathrm{l}}} + \frac{1}{D_{\mathrm{g}}}\right) \tag{2.130}$$

with

$$D_{\mathrm{l}}^{-1} \approx 10\pi F_0^2 \cdot \frac{\cos(\mathcal{G})}{2r_{\mathrm{br}}} \cdot (1 - F_{\mathrm{br}})\, \mathrm{e}^{-\tau_{\mathrm{e}}} \tag{2.131}$$

and

$$D_{\mathrm{g}}^{-1} \approx -\frac{3.3}{4\pi r_{\mathrm{br}} F_0} \cdot \cos\left(2k_2\mathcal{G}\right). \tag{2.132}$$

The parameters k_2 and τ_{e} are given by $k_2 = (\pi/4) \cdot (2/3\ F_0 + 3/8)^{-1}$ and $\tau_{\mathrm{e}} = 12 \cdot F_{\mathrm{br}} \left(0.5 \cdot \mathcal{K}^2 d_{\mathrm{fi}}/r_{\mathrm{br}}\right)^{1/3}$.

So far, the state of the art for transmission line theory and shielded conductors has been presented. Next, the field coupling on a line above a ground plane is dealt with.

3 Circuit Models of a Field-Coupled Single Conductor above a Ground Plane

The EMC system shown in Fig. 2.10 contains a shielded cable that has been coupled with an electromagnetic field. In order to calculate the field coupling to the outer system of the cable, this is regarded as a simple TL. For this reason, a circuit model for a field-coupled conductor above a perfectly conductive ground plane is first developed in this section. This serves as preparation for the development of circuit models for shielded conductors and at the same time represents an independent model.

The field coupling is calculated according to the scattered voltage formulation shown in the work of Agrawal *et al.* in [5] and the total voltage formulation derived by Taylor *et al.* in [6]. Existing solutions of the scattered voltage formulation are extended in this work to calculate the load responses for the plane wave excitation. From these solutions, circuit models are developed. The total voltage formulation was applied to develop the circuit model of the field-coupled wire with steps similar to those in [17]. At this point, it is important to clarify that the scattered voltage formulation model was developed in this work and is not obtained from other sources. In contrast, the total voltage formulation model was reproduced using some specifications from [17].

In earlier work [16], circuit models were developed for one conductor above a ground plane and for a three-conductor line based on the total voltage formulation. In [61] the circuit model for shielded cables with field coupling was presented, in which the field coupling was treated on the basis of the scattered voltage formulation.
At the end of this section, it is shown that the solution for the total voltage formulation gave the same result as for the case of the scattered one and therefore the same circuit model was interpreted. This can be regarded as a very good insight when compared to the prior art, where it was shown that the two different approaches to field coupling led to the same circuit model.

Taking into account a lossless conductor of length $\mathcal{L}$ in Fig. 3.1, which is placed at a height h above a perfectly conducting ground plane and is irradiated with an incident uniform plane wave. The vector $\vec{\beta}$ represents the direction of propagation of the wave with the angle θ and the incident electric field $\vec{E}^{\mathrm{i}}$. The two loads Z_{l} and Z_{r} are connected to the ends of the conductor. The indices l and r stand for the left and right-hand side, respectively. Next, the transmission line equations are derived.

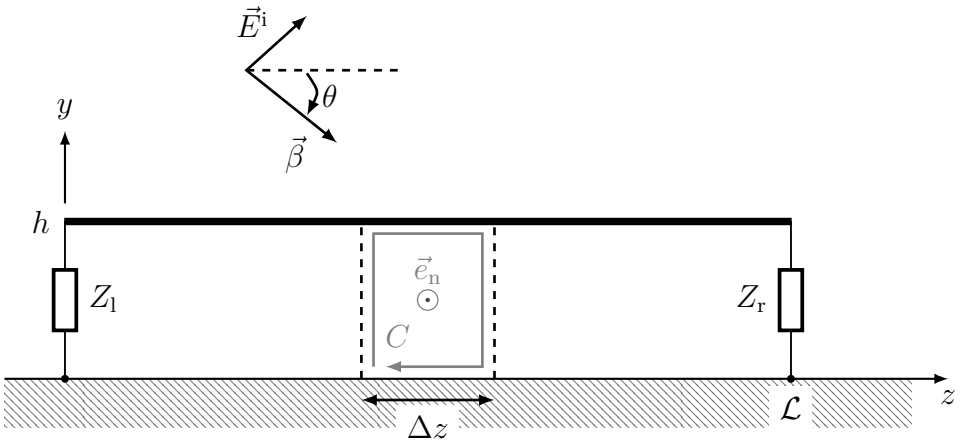

Figure 3.1: Field-coupled single conductor over a perfectly conducting ground plane.

3.1 TL Equations Based on Total Voltage Formulation

The law of induction indicates the relationship between the electric field and the magnetic flux density and is represented in the Maxwell equations as

$$\oint_C \vec{E}\,\mathrm{d}\vec{l} = \mathrm{j}\omega \iint_S \vec{B}\cdot\vec{e}_{\mathrm{n}}\,\mathrm{d}S, \tag{3.1}$$

where $\mathrm{d}\vec{l}$ is the vector differential path in the $y-z$ plane and $\vec{e}_{\mathrm{n}}$ denotes the unit normal vector of the flat surface S enclosed in the contour C, as shown in Fig. 3.1. The usual minus sign on the right-hand side of (3.1) is not taken into account since the unit normal vector $\vec{e}_{\mathrm{n}}$ in Fig. 3.1 is directed outwards. Applying (3.1) to the contour C with the segment Δz for the width results in [17]

$$\begin{aligned} &-\int_0^h \left[E_{\mathrm{y}}(y,z+\Delta z)-E_{\mathrm{y}}(y,z)\right]\,\mathrm{d}y + \int_z^{z+\Delta z}\left[E_{\mathrm{z}}(h,z)-E_{\mathrm{z}}(0,z)\right]\,\mathrm{d}z \\ &= \mathrm{j}\omega \int_0^h \int_z^{z+\Delta z} B_{\mathrm{n}}(y,z)\,\mathrm{d}y\,\mathrm{d}z. \end{aligned} \tag{3.2}$$

The transverse component of the electric field at position z is represented by $E_{\mathrm{y}}(y,z)$. The elements $E_{\mathrm{z}}(h,z)$ and $E_{\mathrm{z}}(0,z)$ are the tangential components of the electric field at $y=h$ and $y=0$, respectively. The component $B_{\mathrm{n}}(y,z)$ denotes the magnetic flux density that is normal to the flat surface S. Dividing both sides in (3.2) by Δz and taking the limit

$\Delta z \to 0$, leads to

$$-\frac{\partial}{\partial z}\int_0^h E_\mathrm{y}(y,z)\,\mathrm{d}y + E_\mathrm{z}(h,z) - E_\mathrm{z}(0,z) = \mathrm{j}\omega\int_0^h B_\mathrm{n}(y,z)\,\mathrm{d}y. \tag{3.3}$$

The transverse voltage along the line is defined as

$$V(z) = -\int_0^h E_\mathrm{y}(y,z)\,\mathrm{d}y. \tag{3.4}$$

The total of the tangential components $E_\mathrm{z}(h,z) - E_\mathrm{z}(0,z)$ in (3.3) is set to zero, since it is assumed that the ground plane and the conductor are perfectly conducting material. Applying this assumption in (3.3) together with (3.4) leads to [17]

$$\frac{\mathrm{d}V(z)}{\mathrm{d}z} = \mathrm{j}\omega\int_0^h B_\mathrm{n}^\mathrm{e}(y,z)\,\mathrm{d}y + \mathrm{j}\omega\int_0^h B_\mathrm{n}^\mathrm{s}(y,z)\,\mathrm{d}y, \tag{3.5}$$

where the magnetic flux density $B_\mathrm{n}(y,z)$ is decomposed into an excited $B_\mathrm{n}^\mathrm{e}(y,z)$ and a scattered component $B_\mathrm{n}^\mathrm{s}(y,z)$. The excited magnetic flux density is the sum of the incident $B_\mathrm{n}^\mathrm{i}(y,z)$ and the reflected $B_\mathrm{n}^\mathrm{r}(y,z)$ with $B_\mathrm{n}^\mathrm{e}(y,z) = B_\mathrm{n}^\mathrm{i}(y,z) + B_\mathrm{n}^\mathrm{r}(y,z)$. The scattered one is related to the p.u.l. inductance of the line L' with [17]

$$\int_0^h B_\mathrm{n}^\mathrm{s}(y,z)\,\mathrm{d}y = -L'I(z), \tag{3.6}$$

where $I(z)$ is the current at the wire. Inserting (3.6) into (3.5) yields the first Telegraph equation [6]

$$\frac{\mathrm{d}V(z)}{\mathrm{d}z} + \mathrm{j}\omega L'I(z) = \mathrm{j}\omega\int_0^h B_\mathrm{n}^\mathrm{e}(y,z)\,\mathrm{d}y. \tag{3.7}$$

The second Telegraph equation can be derived using the Ampere-Maxwell equation

$$\nabla\times\vec{H} = \vec{J} + \mathrm{j}\omega\varepsilon_0\vec{E}, \tag{3.8}$$

where $\vec{J}$ represents the current density. Applying similar steps as before gives the second Telegraph equation [6]

$$\frac{\mathrm{d}I(z)}{\mathrm{d}z} + \mathrm{j}\omega C'V(z) = -\mathrm{j}\omega C'V_\mathrm{t}(z), \tag{3.9}$$

where C' represents the p.u.l. capacitance of the line, $V_\mathrm{t}(z)$ is the transverse voltage represented by the integral of the transverse part $E^\mathrm{e}_\mathrm{y}(y,z)$ of the excited electrical field.

$$V_\mathrm{t}(z) = \int_0^h E^\mathrm{e}_\mathrm{y}(y,z)\,\mathrm{d}y \tag{3.10}$$

The excited electrical field $E^\mathrm{e}(y,z)$ is the sum of the incident $E^\mathrm{i}(y,z)$ and reflected field $E^\mathrm{r}(y,z)$ in the absence of the wire.

$$E^\mathrm{e}(y,z) = E^\mathrm{i}(y,z) + E^\mathrm{r}(y,z) \tag{3.11}$$

The comparison of (3.7) and (3.9) shows that the field response on the right-hand side of the equations depends on the incident magnetic and electric fields. In order to write the equations only in relation to the electric field, Faraday's law is used to replace the excited magnetic field as follows [17]:

$$\mathrm{j}\omega \int_0^h B^\mathrm{e}_\mathrm{n}(y,z)\,\mathrm{d}y = -\frac{\partial}{\partial z}V_\mathrm{t}(z) + E^e_\mathrm{z}(h,z), \tag{3.12}$$

where $E^e_\mathrm{z}(h,z)$ is the sum of the tangential components of the incident and reflected electric field at $z = h$ in the absence of the wire. It is given by

$$E^e_\mathrm{z}(h,z) = E^\mathrm{i}_\mathrm{z}(h,z) + E^\mathrm{r}_\mathrm{z}(h,z). \tag{3.13}$$

After inserting (3.12), equations (3.7) and (3.9) are rewritten using the so-called forcing functions $V'_\mathrm{F}(z)$ and $I'_\mathrm{F}(z)$ as follows:

$$\frac{\mathrm{d}V(z)}{\mathrm{d}z} + \mathrm{j}\omega L' I(z) = V'_\mathrm{F}(z) \tag{3.14a}$$

$$\frac{\mathrm{d}I(z)}{\mathrm{d}z} + \mathrm{j}\omega C' V(z) = I'_\mathrm{F}(z), \tag{3.14b}$$

where

$$V'_\mathrm{F}(z) = E^e_\mathrm{z}(h,z) - \frac{\partial}{\partial z}V_\mathrm{t}(z) \tag{3.15a}$$

$$I'_\mathrm{F}(z) = -\mathrm{j}\omega C' V_\mathrm{t}(z). \tag{3.15b}$$

The formulation shown in (3.7) and (3.9) was derived in the work of Taylor *et al.* [6]. An equivalent circuit for these equations is developed in Fig. 3.2. It consists of the TL parameter together with the forcing functions added as voltage and current sources, where $V_\mathrm{F}(z) = V'_\mathrm{F}(z)\Delta z$ and $I_\mathrm{F}(z) = I'_\mathrm{F}(z)\Delta z$.

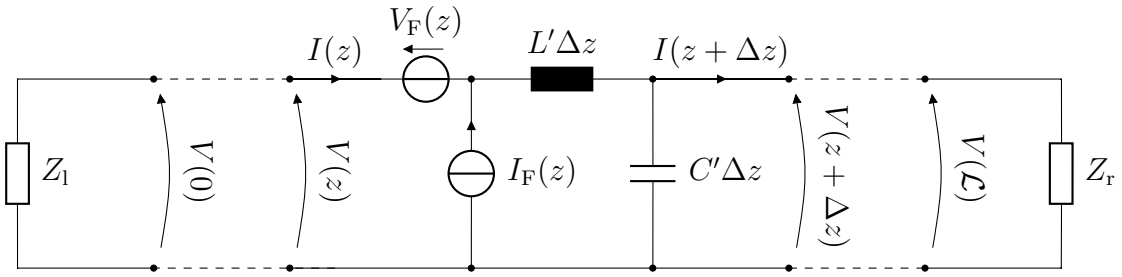

Figure 3.2: Equivalent circuit of a field-coupled single conductor over a perfectly conducting ground plane according to the total voltage formulation.

The differential equations (3.14a) and (3.14b) were derived for the small segment Δz, which means the wire of length $\mathcal{L}$ in Fig. 3.2 is represented by a series of the distributed parameters.

3.2 TL Equations Based on Scattered Voltage Formulation

A further representation of the field coupling on transmission lines was introduced by Agrawal *et al.* [5], where the scattered voltage $V^\mathrm{s}(z)$ was included in the equations. It is defined as the line integral from the ground to wire along the scattered electric field [5].

$$V^\mathrm{s}(z) = -\int_0^h E_\mathrm{y}^\mathrm{s}(y,z)\,\mathrm{d}y \tag{3.16}$$

The parameter $E_\mathrm{y}^\mathrm{s}(y,z)$ is the y-component of the scattered electric field $E^\mathrm{s}(y,z)$, which represents the reaction of the line to the incident field. The total voltage results from the excited and the scattered electric field, it is given by [5]

$$V(z) = -\int_0^h E_\mathrm{y}^\mathrm{s}(y,z)\,\mathrm{d}y - \int_0^h E_\mathrm{y}^\mathrm{e}(y,z)\,\mathrm{d}y = V^\mathrm{s}(z) + V^\mathrm{e}(z). \tag{3.17}$$

The TL equations of a field-coupled line placed above a ground plane using the scattered voltage is defined as [5]

$$\frac{\mathrm{d}V^\mathrm{s}(z)}{\mathrm{d}z} + \mathrm{j}\omega L' I(z) = E_\mathrm{z}^e(h,z) = V_\mathrm{F}'(z) \tag{3.18a}$$

$$\frac{\mathrm{d}I(z)}{\mathrm{d}z} + \mathrm{j}\omega C' V^\mathrm{s}(z) = 0. \tag{3.18b}$$

The advantage of this equation system is that the magnetic field components of the excited field defined in (3.7) are not included; instead, only the tangential part of the excited electric field $E_\mathrm{z}^\mathrm{e}(y,z)$ is considered. In addition, the second TL equation has no forcing

functions, which makes the solution and the numerical calculations much easier and more efficient. The field $E_z^e(h,z)$ represented by the forcing function $V_F'(z)$ is the sum of the tangential components of the incident and the reflected electric field $E_z^i(h,z)$ and $E_z^r(h,z)$, as represented in (3.13). For a line of length $\mathcal{L}$ with the loads Z_l and Z_r, as shown in Fig. 3.1, the boundary conditions with regard to the scattered voltage and the total current are defined as

$$V^s(0) = -Z_l I(0) + V_{t1} \tag{3.19}$$

$$V^s(\mathcal{L}) = Z_r I(\mathcal{L}) + V_{t2}. \tag{3.20}$$

The expressions V_{t1} and V_{t2} stand for the transverse voltages at the line terminations and are calculated from (3.10) for $z = 0$ and $z = \mathcal{L}$ as follows:

$$V_{t1} = \int_0^h E_y^e(y,0)\,\mathrm{d}y \tag{3.21}$$

$$V_{t2} = \int_0^h E_y^e(y,\mathcal{L})\,\mathrm{d}y. \tag{3.22}$$

A close examination of (3.18) with the boundary conditions defined in (3.19) and (3.20) shows that the total voltage at the loads consists of the distributed scattered voltages along the line together with the transverse voltages at the line ends. An equivalent circuit in Fig. 3.3 was interpreted. It consists of the TL parameters together with the forcing voltage source $V_F(z) = V_F'(z)\Delta z$. In order to form the total voltages at the ends, the transverse terms V_{t1} and V_{t2} are added to the loads.

Another form of representation of the field coupling equations was derived by Rachidi [9]. In his model, only the magnetic field components in the forcing functions were defined. In contrast to the representation of Agrawal *et al.*, his model includes scattered current and total voltage. This form of equation is not discussed further in this work.

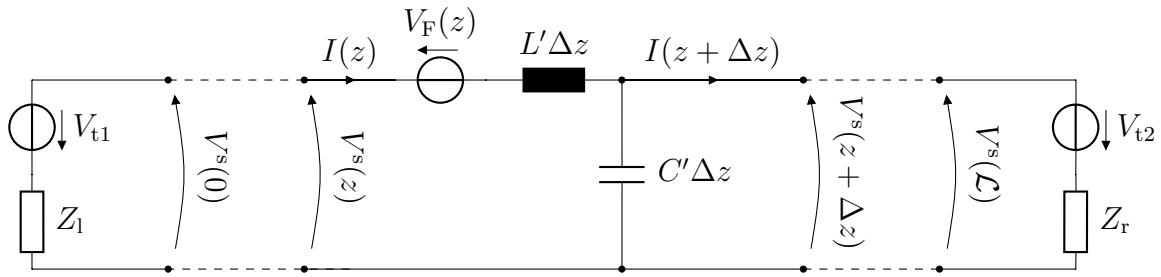

Figure 3.3: Equivalent circuit of a field-coupled single conductor over a perfectly conducting ground plane according to the scattered voltage formulation.

3.3 Solution of the Scattered Voltage Formulation

The differential equations in (3.18) can be solved with Green's function by applying the boundary conditions in (3.19) and (3.20). Green's function was used in transmission line theory to obtain the solution of the voltage and current at each position z on a line excited by a concentrated voltage and/or a current source at position z_s. Since (3.18) contains only the p.u.l. voltage source $V'_\mathrm{F}(z)$ without another current source, Green's functions for the current and the voltage in case of a concentrated voltage source positioned at the point z_s are shown here [2]:

$$G_\mathrm{I}(z, z_\mathrm{s}) = \frac{\mathrm{e}^{-\mathrm{j}\beta\mathcal{L}}}{2Z_\mathrm{c}\left(1-\rho_1\rho_2\,\mathrm{e}^{-2\mathrm{j}\beta\mathcal{L}}\right)} \cdot \left(\mathrm{e}^{-\mathrm{j}\beta(z_>-\mathcal{L})} - \rho_2\,\mathrm{e}^{\mathrm{j}\beta(z_>-\mathcal{L})}\right) \cdot \left(\mathrm{e}^{\mathrm{j}\beta z_<} - \rho_1\,\mathrm{e}^{-\mathrm{j}\beta z_<}\right) \quad (3.23)$$

$$G_\mathrm{V}(z, z_\mathrm{s}) = \frac{\zeta\,\mathrm{e}^{-\mathrm{j}\beta\mathcal{L}}}{2\left(1-\rho_1\rho_2\,\mathrm{e}^{-2\mathrm{j}\beta\mathcal{L}}\right)} \cdot \left(\mathrm{e}^{-\mathrm{j}\beta(z_>-\mathcal{L})} + \zeta\rho_2\,\mathrm{e}^{\mathrm{j}\beta(z_>-\mathcal{L})}\right) \cdot \left(\mathrm{e}^{\mathrm{j}\beta z_<} - \zeta\rho_1\,\mathrm{e}^{-\mathrm{j}\beta z_<}\right), \quad (3.24)$$

where

- Z_c is the line characteristic impedance defined in (2.35),
- β is the phase constants defined in (2.36),
- $z_<$ represents the smaller of z or z_s, and $z_>$ represents the larger of z or z_s,
- $\zeta = 1$ for $z > z_\mathrm{s}$ and $\zeta = -1$ for $z < z_\mathrm{s}$,
- ρ_1 and ρ_2 are the voltage reflection factors at the loads defined as

$$\rho_1 = \frac{Z_\mathrm{l} - Z_\mathrm{c}}{Z_\mathrm{l} + Z_\mathrm{c}} \qquad\qquad \rho_2 = \frac{Z_\mathrm{r} - Z_\mathrm{c}}{Z_\mathrm{r} + Z_\mathrm{c}}. \quad (3.25)$$

The solution of the current and the voltage in the case of a concentrated voltage source V_co is given by

$$I(z) = G_\mathrm{I}(z, z_\mathrm{s}) \cdot V_\mathrm{co} \quad (3.26)$$

$$V(z) = G_\mathrm{V}(z, z_\mathrm{s}) \cdot V_\mathrm{co}. \quad (3.27)$$

In the case of distributed sources such as in (3.18), the solution of the total current and the scattered voltage can be derived using the integral of the Green's functions [2].

$$I(z) = \int_0^{\mathcal{L}} G_\mathrm{I}(z, z_\mathrm{s})\, V'_\mathrm{F}(z)\,\mathrm{d}z_\mathrm{s} + G_\mathrm{I}(z, 0)\, V_\mathrm{t1} - G_\mathrm{I}(z, \mathcal{L})\, V_\mathrm{t2} \quad (3.28)$$

$$V^\mathrm{s}(z) = \int_0^{\mathcal{L}} G_\mathrm{V}(z, z_\mathrm{s})\, V'_\mathrm{F}(z)\,\mathrm{d}z_\mathrm{s} + G_\mathrm{V}(z, 0)\, V_\mathrm{t1} - G_\mathrm{V}(z, \mathcal{L})\, V_\mathrm{t2} \quad (3.29)$$

It should be noted here that the concentrated sources at the ends were multiplied by Green's functions without an integral, since they are not distributed along the line. The total voltage along the line can be calculated using (3.17).

If someone is interested in solving the response only at the termination loads, the problem can be solved with the Baum-Liu-Tesche (BLT) equations [8]. However, this approach is not discussed in this work.

3.3.1 Uniform Plane Wave Excitation

The problem described so far has been discussed for general field coupling. Refering to a uniform plane wave, the incident electric field with an amplitude of $E_0(\omega)$ is defined as

$$\vec{E}^{\mathrm{i}}(y,z,\omega) = E_0(\omega)\,(e_y\vec{a}_y + e_z\vec{a}_z)\,\mathrm{e}^{-\mathrm{j}\beta_y y}\mathrm{e}^{-\mathrm{j}\beta_z z}. \tag{3.30}$$

The reflected field on a perfectly conducting ground plane is given by

$$\vec{E}^{\mathrm{r}}(y,z,\omega) = E_0(\omega)\,(e_y\vec{a}_y - e_z\vec{a}_z)\,\mathrm{e}^{\mathrm{j}\beta_y y}\mathrm{e}^{-\mathrm{j}\beta_z z}. \tag{3.31}$$

The components e_y and e_z along the unit vectors $\vec{a}_y$ and $\vec{a}_z$ in Fig. 3.1 are defined as

$$e_y = \cos(\theta) \tag{3.32a}$$
$$e_z = \sin(\theta). \tag{3.32b}$$

The components of the phase constants along the axes are given by

$$\beta_{\mathrm{y}} = -\beta\cdot\sin(\theta) \tag{3.33a}$$
$$\beta_{\mathrm{z}} = \beta\cdot\cos(\theta). \tag{3.33b}$$

Inserting (3.30) and (3.31) into (3.13) and using (3.32) and (3.33) for $y = h$, the tangential part of the excited electric field $E^e_{\mathrm{z}}(h,z)$ results in

$$\begin{aligned} E^e_{\mathrm{z}}(h,z) &= E^i_{\mathrm{z}}(h,z) + E^r_{\mathrm{z}}(h,z) \\ &= E_0(\omega)\cdot e_z\cdot\left(\mathrm{e}^{-\mathrm{j}\beta_y h} - \mathrm{e}^{\mathrm{j}\beta_y h}\right)\cdot\mathrm{e}^{-\mathrm{j}\beta_z z} \\ &= \underbrace{-\mathrm{j}2E_0(\omega)\cdot\sin(\theta)\cdot\sin(\beta_y h)}_{V_{\mathrm{s}}^{e\prime}(h)}\cdot\mathrm{e}^{-\mathrm{j}\beta_z z}. \end{aligned} \tag{3.34}$$

The transverse part of the excited electric field can be calculated by inserting (3.30) and

(3.31) into (3.11).

$$\begin{aligned} E_{\mathrm{y}}^{\mathrm{e}}(y,z) &= E_{\mathrm{y}}^{\mathrm{i}}(y,z) + E_{\mathrm{y}}^{\mathrm{r}}(y,z) \\ &= E_0(\omega) e_y \Big(\mathrm{e}^{-\mathrm{j}\beta_{\mathrm{y}} y} + \mathrm{e}^{\mathrm{j}\beta_{\mathrm{y}} y} \Big) \mathrm{e}^{-\mathrm{j}\beta_{\mathrm{z}} z} \\ &= 2E_0(\omega) e_{\mathrm{y}} \cdot \cos\Big(\beta_{\mathrm{y}} y\Big) \cdot \mathrm{e}^{-\mathrm{j}\beta_{\mathrm{z}} z} \end{aligned} \tag{3.35}$$

In order to calculate the transverse voltage along the line, (3.35) is inserted into (3.10), which leads

$$\begin{aligned} V_{\mathrm{t}}(z) &= 2E_0(\omega) \cdot e_{\mathrm{y}} \cdot \frac{\sin(\beta_{\mathrm{y}} h)}{\beta_{\mathrm{y}}} \cdot \mathrm{e}^{-\mathrm{j}\beta_{\mathrm{z}} z} \\ &= 2h e_{\mathrm{y}} E_0(\omega) \cdot \mathrm{sinc}(\beta_{\mathrm{y}} h) \cdot \mathrm{e}^{-\mathrm{j}\beta_{\mathrm{z}} z} \\ &\cong 2h e_{\mathrm{y}} E_0(\omega) \cdot \mathrm{e}^{-\mathrm{j}\beta_{\mathrm{z}} z} \,. \end{aligned} \tag{3.36}$$

In the second step, the denominator and the numerator were multiplied by h to represent $\mathrm{sinc}(\beta_{\mathrm{y}} h)$ function. In the last step, $\mathrm{sinc}(\beta_{\mathrm{y}} h)$ function was set to one because the time delay between the line and the ground level is ignored, as will be explained now. The function β_{y} from (3.33a) and β from (2.36) are set into $\mathrm{sinc}(\beta_{\mathrm{y}} h)$ to obtain

$$\mathrm{sinc}(\beta_{\mathrm{y}} h) = \frac{\sin(\beta_{\mathrm{y}} h)}{\beta_{\mathrm{y}} h} = \frac{\sin\Big(\omega \cdot \sin(\theta) \cdot h / v_0\Big)}{\omega \cdot \sin(\theta) \cdot h / v_0} = \frac{\sin(\omega T_{\mathrm{y}})}{\omega T_{\mathrm{y}}}, \tag{3.37}$$

where

$$T_{\mathrm{y}} = -\sin(\theta) \cdot \frac{h}{v_0}. \tag{3.38}$$

The propagation velocity in free space is given by v_0. The wave time delay along the y-axis T_y between the ground plane and the line is approximately zero, provided the line cross-sectional dimension is electrically very small. The wave time delay along the z-axis T_z is defined as

$$T_{\mathrm{z}} = \cos(\theta) \cdot \frac{\mathcal{L}}{v_0} = \cos(\theta) T_{\mathrm{d}}, \tag{3.39}$$

where T_{d} represents the one-way time delay of the line and is given by

$$T_{\mathrm{d}} = \frac{\mathcal{L}}{v_0}. \tag{3.40}$$

The transverse voltages V_{t1} and V_{t2} at the line ends were defined in (3.21) and (3.22) for the general field coupling. In the case of a uniform plane wave, they can easily be derived

from (3.36) by replacing $z = 0$ and $z = \mathcal{L}$.

$$V_{\mathrm{t}1} \cong 2he_{\mathrm{y}}E_0(\omega) \tag{3.41}$$

$$V_{\mathrm{t}2} \cong V_{\mathrm{t}1}\mathrm{e}^{-\mathrm{j}\beta_{\mathrm{z}}\mathcal{L}} \tag{3.42}$$

So far, the field coupling parameters have been rewritten for the case of an incident uniform plane wave. Since the goal in this section is to develop a circuit model of the field-coupled line, only the current response is calculated initially. The voltage response is calculated from the current for matched termination loads, as will be shown in the lower part.

The total current can be calculated by substituting (3.23), (3.34), (3.41) and (3.42) into (3.28). This current was solved analytically in several works [7, 12, 62]. It is represented here in a practical form as follows:

$$I(z) = I_0\mathrm{e}^{-\mathrm{j}\beta_{\mathrm{z}}z} + I_1\mathrm{e}^{-\mathrm{j}\beta z} + I_2\mathrm{e}^{\mathrm{j}\beta z}. \tag{3.43}$$

The element I_0 is the wave forced by the external field and corresponds to the current that is generated for an infinitely long wire above a perfectly conducting ground plane. It is given by

$$I_0 = -\frac{\mathrm{j}\omega C' \cdot V_{\mathrm{s}}'^{\mathrm{e}}(h)}{\beta^2 - \beta_{\mathrm{z}}^2}. \tag{3.44}$$

The parameter C' is the p.u.l. capacitance of the TL. The p.u.l. voltage $V_{\mathrm{s}}'^{\mathrm{e}}(h)$ results from the sum of the tangential electrical field components as defined in (3.34). The currents I_1 and I_2 in (3.43) are given by

$$I_1 = \frac{1}{1 - \rho_1\rho_2 \cdot \mathrm{e}^{-\mathrm{j}2\beta\mathcal{L}}} \cdot \left[I_0 \left(\mathcal{Q}_1 - \rho_1\mathcal{Q}_2\,\mathrm{e}^{-\mathrm{j}\mathcal{L}(\beta+\beta_{\mathrm{z}})} \right) + \frac{V_{\mathrm{t}1}}{Z_{\mathrm{l}} + Z_{\mathrm{c}}} + V_{\mathrm{t}2} \cdot \frac{\rho_1\,\mathrm{e}^{-\mathrm{j}\beta\mathcal{L}}}{Z_{\mathrm{r}} + Z_{\mathrm{c}}} \right] \tag{3.45}$$

$$I_2 = \frac{1}{1 - \rho_1\rho_2 \cdot \mathrm{e}^{-\mathrm{j}2\beta\mathcal{L}}} \cdot \left[I_0 \left(\mathcal{Q}_2\,\mathrm{e}^{-\mathrm{j}\mathcal{L}(\beta+\beta_{\mathrm{z}})} - \rho_2\mathcal{Q}_1\,\mathrm{e}^{-\mathrm{j}2\beta\mathcal{L}} \right) - V_{\mathrm{t}1} \cdot \frac{\rho_2\,\mathrm{e}^{-\mathrm{j}2\beta\mathcal{L}}}{Z_{\mathrm{l}} + Z_{\mathrm{c}}} - V_{\mathrm{t}2} \cdot \frac{\mathrm{e}^{-\mathrm{j}\beta\mathcal{L}}}{Z_{\mathrm{r}} + Z_{\mathrm{c}}} \right]. \tag{3.46}$$

The reflection factors ρ_1 and ρ_2 were shown in (3.25). The parameters $\mathcal{Q}_1$ and $\mathcal{Q}_2$ are given by

$$\mathcal{Q}_1 = -\frac{Z_{\mathrm{l}} + Z_{\mathrm{c}} \cdot \cos(\theta)}{Z_{\mathrm{l}} + Z_{\mathrm{c}}}, \qquad \mathcal{Q}_2 = -\frac{Z_{\mathrm{r}} - Z_{\mathrm{c}} \cdot \cos(\theta)}{Z_{\mathrm{r}} + Z_{\mathrm{c}}}. \tag{3.47}$$

So far, the current generated by the field coupling has been calculated in (3.43). Next, a circuit model for the field-coupled line is derived.

3.4 Circuit Model Based on the Scattered Voltage Formulation

The following steps are carried out to develop the circuit model: the voltage response is calculated in the frequency domain at the cable ends, taking into account the case of matched termination loads. The solution is then transformed into the time domain, from which a circuit model is interpreted directly. It should be noted that the macromodel developed at the end allows the analysis of mismatched termination loads. To clarify that this model was developed within the scope of this work and was not taken from other sources.

3.4.1 Matched Termination Loads

The solution is derived for matched termination loads with $Z_\mathrm{l} = Z_\mathrm{r} = Z_\mathrm{c}$ in Fig. 3.1 and therefore $\rho_1 = \rho_2 = 0$ is considered in (3.25). Under this condition, the currents I_1 and I_2 in (3.45) and (3.46) become

$$I_{1\mathrm{M}} = I_0 \mathcal{Q}_{1\mathrm{M}} + \frac{V_{\mathrm{t}1}}{2Z_\mathrm{c}} \tag{3.48}$$

$$I_{2\mathrm{M}} = I_0 \mathcal{Q}_{2\mathrm{M}} \cdot \mathrm{e}^{-\mathrm{j}(\beta+\beta_\mathrm{z})\mathcal{L}} - V_{\mathrm{t}2} \cdot \frac{\mathrm{e}^{-\mathrm{j}\beta\mathcal{L}}}{2Z_\mathrm{c}}. \tag{3.49}$$

The index M was used to represent the case of matching loads. The parameters $\mathcal{Q}_{1\mathrm{M}}$ and $\mathcal{Q}_{2\mathrm{M}}$ in (3.47) become

$$\mathcal{Q}_{1\mathrm{M}} = -\frac{1+\cos(\theta)}{2}, \qquad \mathcal{Q}_{2\mathrm{M}} = -\frac{1-\cos(\theta)}{2} = -\mathcal{Q}_{1\mathrm{M}} - 1. \tag{3.50}$$

The term $\mathcal{Q}_{2\mathrm{M}}$ is presented as a function of $\mathcal{Q}_{1\mathrm{M}}$, since this approach will be used later. The p.u.l. voltage $V_\mathrm{s}^{e\prime}(h)$ defined in (3.34) is solved here as follows:

$$\begin{aligned} V_\mathrm{s}^{e\prime}(h) &= -\mathrm{j}2E_0(\omega) \cdot \sin(\theta) \cdot \sin(\beta_\mathrm{y} h) = -\mathrm{j}2E_0(\omega) \cdot \sin(\theta) \cdot \beta_\mathrm{y} h \cdot \frac{\sin(\beta_\mathrm{y} h)}{\beta_\mathrm{y} h} \\ &\cong -\mathrm{j}2E_0(\omega) \cdot \sin(\theta) \cdot \beta_\mathrm{y} h. \end{aligned} \tag{3.51}$$

It has been simplified by applying the sinc function as described in (3.36) and (3.37). When inserting $V_\mathrm{s}^{e\prime}(h)$ into (3.44) and using (3.33), the current I_0 becomes

$$I_0 = -\frac{\mathrm{j}\omega C' \cdot \mathrm{j}2E_0(\omega) \cdot \sin(\theta) \cdot \beta \cdot \sin(\theta) \cdot h}{\beta^2(1-\cos^2(\theta))}. \tag{3.52}$$

Replace $1-\cos^2(\theta)$ with $\sin^2(\theta)$ and simplify the fraction to get

$$I_0 = \frac{\omega C' 2E_0(\omega) h}{\beta} = \frac{2hC'E_0(\omega)}{\sqrt{L'C'}} = 2hE_0(\omega) \cdot \sqrt{\frac{C'}{L'}} = \frac{2hE_0(\omega)}{Z_\mathrm{c}}. \tag{3.53}$$

In the second step β was replaced by $\omega\sqrt{L'C'}$, as defined in (2.36). In the last step the equation was represented with respect to Z_c instead of C' as defined in (2.35).
To reduce the number of variables, the current $I_{2\mathrm{M}}$ is expressed as a function of I_0 and $I_{1\mathrm{M}}$, where the voltage $V_{\mathrm{t}2}$ from (3.42) and the parameter $\mathcal{Q}_{2\mathrm{M}}$ from (3.50) are inserted into (3.49), which gives

$$\begin{aligned} I_{2\mathrm{M}} &= -I_0 \cdot \mathcal{Q}_{1\mathrm{M}} \cdot \mathrm{e}^{-\mathrm{j}(\beta+\beta_\mathrm{z})\mathcal{L}} - \frac{V_{\mathrm{t}1}\,\mathrm{e}^{-\mathrm{j}(\beta+\beta_\mathrm{z})\mathcal{L}}}{2Z_\mathrm{c}} - I_0 \cdot \mathrm{e}^{-\mathrm{j}(\beta+\beta_\mathrm{z})\mathcal{L}} \\ &= -\left(\mathcal{Q}_{1\mathrm{M}} \cdot I_0 + \frac{V_{\mathrm{t}1}}{2Z_\mathrm{c}}\right) \mathrm{e}^{-\mathrm{j}(\beta+\beta_\mathrm{z})\mathcal{L}} - I_0 \cdot \mathrm{e}^{-\mathrm{j}(\beta+\beta_\mathrm{z})\mathcal{L}} \\ &= -I_{1\mathrm{M}} \cdot \mathrm{e}^{-\mathrm{j}(\beta+\beta_\mathrm{z})\mathcal{L}} - I_0 \cdot \mathrm{e}^{-\mathrm{j}(\beta+\beta_\mathrm{z})\mathcal{L}}\,. \end{aligned} \tag{3.54}$$

In the second step $\mathrm{e}^{-\mathrm{j}(\beta+\beta_\mathrm{z})\mathcal{L}}$ was excluded. In the third step, the function in parentheses was replaced by $I_{1\mathrm{M}}$ after comparing it to (3.48).

As part of this work, the current elements I_0, I_1 and I_2 from (3.43) were simplified for later use. As a reminder, the defined goal was to calculate the voltage response at the termination loads of the line. For this purpose, the boundary conditions of matched termination loads are applied, where

$$V_\mathrm{M}(0) = -I_\mathrm{M}(0)Z_\mathrm{c} \tag{3.55}$$

$$V_\mathrm{M}(\mathcal{L}) = I_\mathrm{M}(\mathcal{L})Z_\mathrm{c}. \tag{3.56}$$

Inserting $z = 0$ in (3.43) and using the equations of I_0, $I_{1\mathrm{M}}$ and $I_{2\mathrm{M}}$ from (3.53), (3.48) and (3.54), the voltage $V_\mathrm{M}(0, \mathrm{j}\omega)$ can be calculated in (3.55) as follows:

$$\begin{aligned} V_\mathrm{M}(0,\mathrm{j}\omega) = -Z_\mathrm{c} \cdot \Bigg[&\frac{2hE_0(\omega)}{Z_\mathrm{c}} + \mathcal{Q}_{1\mathrm{M}} \cdot \frac{2hE_0(\omega)}{Z_\mathrm{c}} + \frac{he_\mathrm{y}E_0(\omega)}{Z_\mathrm{c}} \\ &- \left(\mathcal{Q}_{1\mathrm{M}} \cdot \frac{2h}{Z_\mathrm{c}} + \frac{he_\mathrm{y}}{Z_\mathrm{c}}\right) E_0(\omega) \cdot \mathrm{e}^{-\mathrm{j}(\beta+\beta_\mathrm{z})\mathcal{L}} - \frac{2hE_0(\omega)}{Z_\mathrm{c}} \cdot \mathrm{e}^{-\mathrm{j}(\beta+\beta_\mathrm{z})\mathcal{L}} \Bigg]. \end{aligned} \tag{3.57}$$

The voltage response $V_\mathrm{M}(\mathcal{L}, \mathrm{j}\omega)$ on the right-hand side can be calculated analogously by substituting $z = \mathcal{L}$ into (3.43) and later in (3.56), as will be shown in the next steps.

It was previously informed that $V_\mathrm{M}(0, \mathrm{j}\omega)$ and $V_\mathrm{M}(\mathcal{L}, \mathrm{j}\omega)$ represent the induced voltages at the ends of the line for matched termination loads. A simplified equivalent circuit of the field-coupled line can therefore be developed as a TL that includes these functions at the ends, as shown in Fig. 3.4. The problem with this representation is that the voltage sources $V_\mathrm{M}(0)$ and $V_\mathrm{M}(\mathcal{L})$ are not galvanic isolated, which leads to a current flow from one source to another and distorts the result. A second problem arises from the fact that these functions are in the frequency domain, making them difficult to integrate into the circuit simulation environment. One possible solution is the use of Laplace sources, as explained

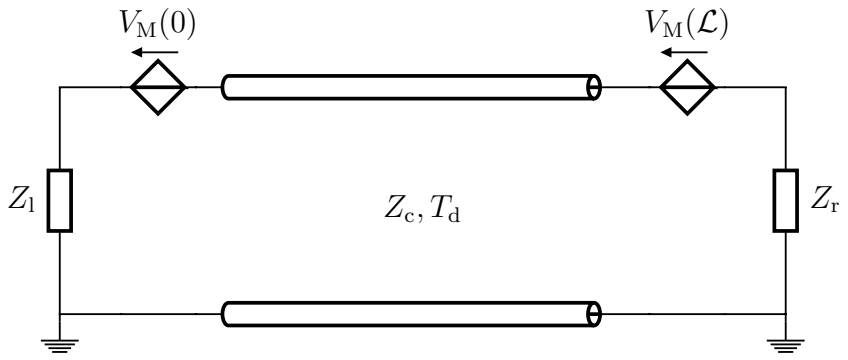

Figure 3.4: Simplified circuit model of an irradiated single conductor over a perfectly conducting ground plane based on scattered voltage formulation.

in [28]. In any case, it has been shown that this approach is not suitable in the time domain and thus limits the use of the model. To solve these problems, a macromodel was developed in Fig. 3.5, in which these sources were decoupled. Circuit models have been developed for the $V_{\mathrm{M}}(0)$ and $V_{\mathrm{M}}(\mathcal{L})$ functions so that they are not integrated as Laplace sources. The development steps of this model are described in the next section.

3.4.2 Macromodel

Within the scope of this work, the calculated voltage in (3.57) is manipulated and prepared for the time domain transformation. For this purpose (2.36) and (3.33b) were substituted into β and β_{z} and presented as follows:

$$\mathrm{j}(\beta + \beta_{\mathrm{z}}) = \mathrm{j}\omega \left(\frac{1}{v_0} + \frac{\cos(\theta)}{v_0} \right). \tag{3.58}$$

Now inserting (3.58) into (3.57) and rewriting the voltage $V_{\mathrm{M}}(0, \mathrm{j}\omega)$ leads to

$$\begin{aligned} V_{\mathrm{M}}(0,\mathrm{j}\omega) = -\Bigg[& \left(2h\mathcal{Q}_{1\mathrm{M}} + he_{\mathrm{y}} + 2h\right) E_0(\omega) \\ & - \Big(2h\mathcal{Q}_{1\mathrm{M}} + he_{\mathrm{y}} + 2h\Big) E_0(\omega)\, \mathrm{e}^{-\mathrm{j}\omega\left(\frac{\mathcal{L}}{v_0} + \frac{\mathcal{L}\cos(\theta)}{v_0}\right)} \Bigg] \\ = -h & \left[2\mathcal{Q}_{1\mathrm{M}} + e_{\mathrm{y}} + 2\right] \cdot \left[E_0(\omega) - E_0(\omega)\, \mathrm{e}^{-\mathrm{j}\omega\left(\frac{\mathcal{L}}{v_0} + \frac{\mathcal{L}\cos(\theta)}{v_0}\right)}\right] \\ = -h & \Big[2\mathcal{Q}_{1\mathrm{M}} + e_{\mathrm{y}} + 2\Big] \cdot \Big[E_0(\omega) - E_0(\omega)\, \mathrm{e}^{-\mathrm{j}\omega(T_{\mathrm{d}} + T_{\mathrm{z}})}\Big]. \end{aligned} \tag{3.59}$$

In the second step, the common factors were excluded. In the last step T_{z} and T_{d} were substituted from (3.39) and (3.40). In order to create a circuit model of the function $V_{\mathrm{M}}(0, \mathrm{j}\omega)$, a transformation into the time domain is applied using the time delay approach

given by

$$\mathrm{e}^{\pm \mathrm{j}\omega T_\mathrm{d}}\, \mathcal{F}(\omega) \iff f(t \pm T_\mathrm{d}), \tag{3.60}$$

where $\mathcal{F}(\omega)$ and $f(t)$ are the functions in the frequency and time domain. The transformation into the time domain gives

$$\begin{aligned} V_\mathrm{M}(0,t) &= -h\Big[2\mathcal{Q}_\mathrm{1M} + e_\mathrm{y} + 2\Big] \cdot \Big[E_0(t) - E_0(t - T_\mathrm{d} - T_\mathrm{z})\Big] \\ &= -h\Big[E_0(t) - \underbrace{E_0(t - T_\mathrm{d} - T_\mathrm{z})}_{\mathcal{V}_\mathrm{iii}}\Big]. \end{aligned} \tag{3.61}$$

The term $E_0(t)$ is the time form of the electric field. In the last calculation step, it was found that the function $2\mathcal{Q}_\mathrm{1M} + e_\mathrm{y} + 2 = 1$ after replacing the parameters e_y and $\mathcal{Q}_\mathrm{1M}$ from (3.32a) and (3.50). The function is now displayed in a suitable form so that an equivalent circuit can be interpreted.

To calculate the voltage response on the right-hand side, $z = \mathcal{L}$ was inserted into (3.43) and I_0, I_1M, and I_2M were applied from (3.53), (3.48) and (3.54) to get

$$\begin{aligned} V_\mathrm{M}(\mathcal{L}, \mathrm{j}\omega) = Z_\mathrm{c}\Bigg[&\frac{2hE_0(\omega)}{Z_\mathrm{c}}\,\mathrm{e}^{-\mathrm{j}\beta_\mathrm{z}\mathcal{L}} + \left(\mathcal{Q}_\mathrm{1M}\cdot\frac{2hE_0(\omega)}{Z_\mathrm{c}} + \frac{he_\mathrm{y}E_0(\omega)}{Z_\mathrm{c}}\right)\mathrm{e}^{-\mathrm{j}\beta\mathcal{L}} \\ &- \left(\mathcal{Q}_\mathrm{1M}\cdot\frac{2h}{Z_\mathrm{c}} + \frac{he_\mathrm{y}}{Z_\mathrm{c}}\right)E_0(\omega)\cdot\mathrm{e}^{-\mathrm{j}\beta_\mathrm{z}\mathcal{L}} - \frac{2hE_0(\omega)}{Z_\mathrm{c}}\cdot\mathrm{e}^{-\mathrm{j}\beta_\mathrm{z}\mathcal{L}}\Bigg]. \end{aligned} \tag{3.62}$$

If Z_c is shortened and $\mathrm{e}^{-\mathrm{j}\beta_\mathrm{z}\mathcal{L}}$ together with $\mathrm{e}^{-\mathrm{j}\beta\mathcal{L}}$ are excluded, the function becomes

$$\begin{aligned} V_\mathrm{M}(\mathcal{L}, \mathrm{j}\omega) &= h\Big[-\Big(2\mathcal{Q}_\mathrm{1M} + e_\mathrm{y}\Big)E_0(\omega)\,\mathrm{e}^{-\mathrm{j}\beta_\mathrm{z}\mathcal{L}} + \Big(2\mathcal{Q}_\mathrm{1M} + e_\mathrm{y}\Big)E_0(\omega)\,\mathrm{e}^{-\mathrm{j}\beta\mathcal{L}}\Big] \\ &= h\Big[2\mathcal{Q}_\mathrm{1M} + e_\mathrm{y}\Big]\cdot\Big[E_0(\omega)\,\mathrm{e}^{-\mathrm{j}\beta\mathcal{L}} - E_0(\omega)\,\mathrm{e}^{-\mathrm{j}\beta_\mathrm{z}\mathcal{L}}\Big] \\ &= h\Big[2\mathcal{Q}_\mathrm{1M} + e_\mathrm{y}\Big]\cdot\Big[E_0(\omega)\,\mathrm{e}^{-\mathrm{j}\omega\frac{\mathcal{L}}{v_0}} - E_0(\omega)\,\mathrm{e}^{-\mathrm{j}\omega\frac{\cos(\theta)\mathcal{L}}{v_0}}\Big] \\ &= h\Big[2\mathcal{Q}_\mathrm{1M} + e_\mathrm{y}\Big]\cdot\Big[E_0(\omega)\,\mathrm{e}^{-\mathrm{j}\omega T_\mathrm{d}} - E_0(\omega)\,\mathrm{e}^{-\mathrm{j}\omega T_\mathrm{z}}\Big] \end{aligned} \tag{3.63}$$

In the second step $2\mathcal{Q}_\mathrm{1M} + e_\mathrm{y}$ was excluded. In the third step β and β_z were replaced by (2.36) and (3.33b). In the last step T_z and T_d were used from (3.39) and (3.40). The transformation into the time domain using the time delay approach defined in (3.60) leads to

$$\begin{aligned} V_\mathrm{M}(\mathcal{L}, t) &= h\Big[2\mathcal{Q}_\mathrm{1M} + e_\mathrm{y}\Big]\cdot\Big[E_0(t - T_\mathrm{d}) - E_0(t - T_\mathrm{z})\Big] \\ &= -h\Big[\underbrace{E_0(t - T_\mathrm{d})}_{\mathcal{V}_\mathrm{i}} - \underbrace{E_0(t - T_\mathrm{z})}_{\mathcal{V}_\mathrm{ii}}\Big]. \end{aligned} \tag{3.64}$$

Comparing (3.61) and (3.64), it can be seen that both equations consist of time delayed $E_0(t)$ terms multiplied by the parameter h. A time delay can be realized in the circuit solvers by a lossless matched TL.
The circuit model of $V_\mathrm{M}(0)$ and $V_\mathrm{M}(\mathcal{L})$ is shown in Fig. 3.5b. The time delay of $E_0(t)$, denoted by $\mathcal{V}_\mathrm{i}$, $\mathcal{V}_\mathrm{ii}$ and $\mathcal{V}_\mathrm{iii}$ in (3.61) and (3.64), was realized with three matched TLs. For a better understanding, a comparison of (3.61) and (3.64) with Fig. 3.5b should be done first. To ensure matching lines, the termination loads of the TLs in Fig. 3.5b are equal to the characteristic impedance Z_c, where these lines are fed with a voltage source of the function $E_0(t)$. The transmission lines used are lossless with the time delays T_d, T_z and $T_\mathrm{d} + T_\mathrm{z}$ according to $\mathcal{V}_\mathrm{i}$, $\mathcal{V}_\mathrm{ii}$ and $\mathcal{V}_\mathrm{iii}$ in (3.61) and (3.64). The multiplication, addition and subtraction are carried out with controlled sources that feed an arbitrary load.

The models described so far have been calculated for the case of matched termination loads. To simulate arbitrary loads, $V_\mathrm{M}(0)$ and $V_\mathrm{M}(\mathcal{L})$ are now integrated into the macromodel of the field-coupled line, presented in Fig. 3.5a. In contrast to the one shown in Fig. 3.4, this consists of a TL, at the ends of which controlled sources are connected. Such controlled sources decouple the voltages $V_\mathrm{M}(0)$ and $V_\mathrm{M}(\mathcal{L})$ and solve the problem described above. The controlled sources in Fig. 3.5 are defined as follows:

$$V_\mathrm{bl} = V_\mathrm{l} + V_\mathrm{M}(0) \tag{3.65a}$$

$$I_\mathrm{bl} = I(0) + \frac{V_\mathrm{M}(0)}{Z_\mathrm{c}} \tag{3.65b}$$

$$I_\mathrm{br} = I(\mathcal{L}) + \frac{V_\mathrm{M}(\mathcal{L})}{Z_\mathrm{c}} \tag{3.65c}$$

$$V_\mathrm{br} = V_\mathrm{r} + V_\mathrm{M}(\mathcal{L}). \tag{3.65d}$$

Controlled sources are referred to as behavior sources, where the index b stands for behavior. The sources V_bl and I_bl in (3.65) include the voltage V_l and the current $I(0)$, which allows current to flow from the left to the right end of the line. The same applies to V_br and I_br on the right-hand side. In circuit simulation, the TLs must have a positive time delay parameter. In order to avoid negative values for T_z, the absolute value is applied in (3.39). If θ is greater than 90°, the left-hand and right-hand sides of the line in Fig. 3.1 are swapped from the point of view of the incident wave, so $V_\mathrm{M}(0)$ and $V_\mathrm{M}(\mathcal{L})$ should be exchanged in (3.65). Such an action can easily be implemented in SPICE with logic circuits, e.g. with a programmable switch.

In summary, Fig. 3.5 shows the complete circuit model for calculating the field coupling response at the loads of one conductor over a perfectly conductive ground plane. The macromodel is shown in Fig. 3.5a. To which any termination loads can be connected, also non-linear loads. The macromodel contains the field coupling response $V_\mathrm{M}(0)$ and $V_\mathrm{M}(\mathcal{L})$ in its controlled sources. A circuit model of $V_\mathrm{M}(0)$ and $V_\mathrm{M}(\mathcal{L})$ was developed in Fig. 3.5b.

To operate the model in the frequency domain, the voltage sources $E_0(t)$ should be defined accordingly as a function of the frequency $E_0(\omega)$.

As a proper part of this work, a circuit model based on the scattered voltage formulation was developed in this section. In the next section, the solution based on the total voltage formulation is presented according to [17].

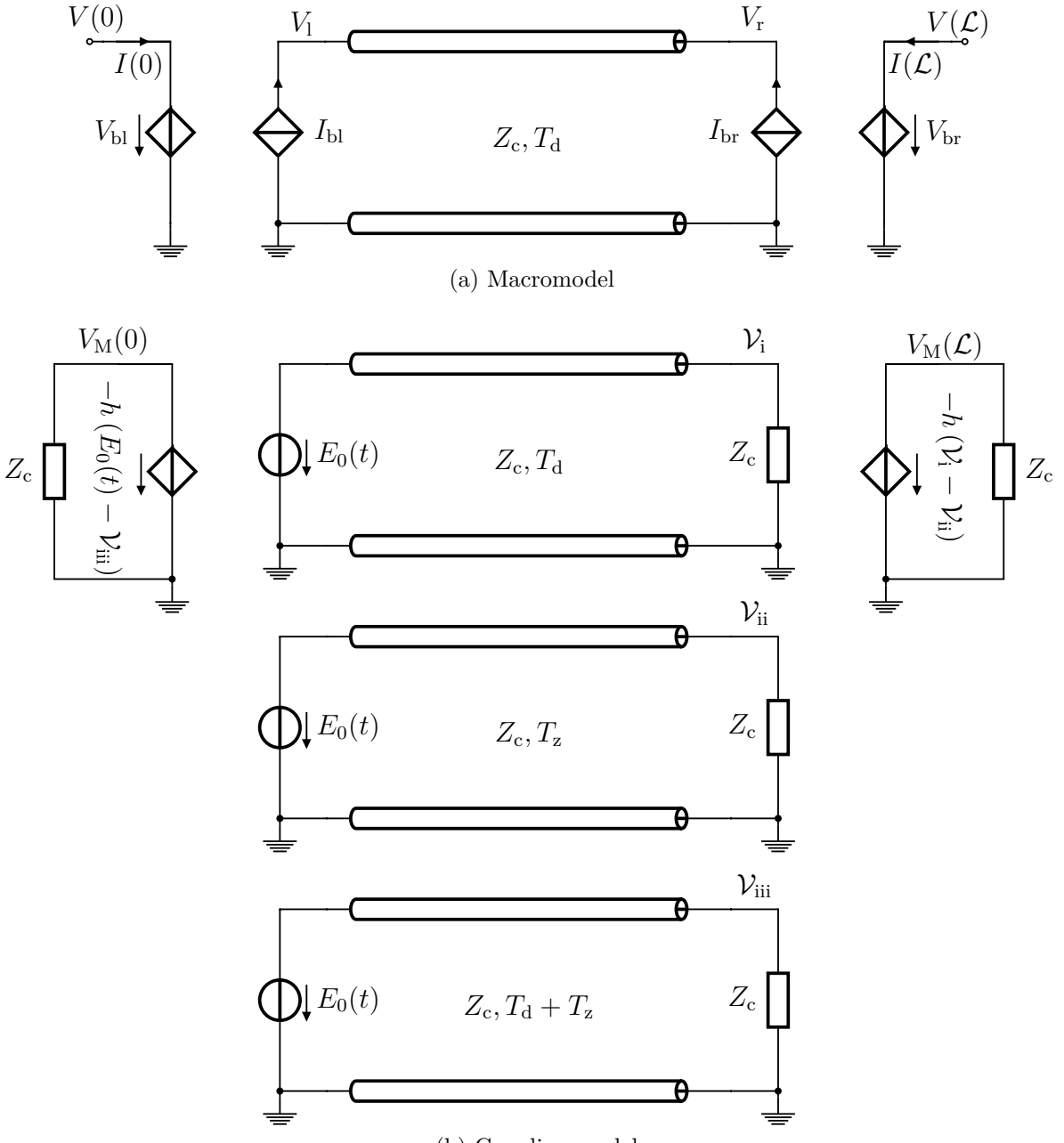

(a) Macromodel

(b) Coupling model

Figure 3.5: SPICE model for one-conductor over a ground plane.

3.5 Solution of the Total Voltage Formulation

In last section, a solution for the scattered voltage formulation was derived within the scope of this work and a circuit model was interpreted from it. In contrast, the solution of the total voltage formulation is performed with similar steps as in [17]. In Fig. 3.2, a cascaded model with distributed elements was created based on the total voltage formulation. However, the closed-form solution at the line ends remains of interest, since the cascaded form with a higher number of elements requires a high computing effort and can lead to convergence problems.

The coupled equations (3.14a) and (3.14b) are first-order ordinary differential equations which have the same form as *state variable equations* [17,63]. A solution for these equations in the frequency domain will be developed using the chain-parameters of the transmission line. The chain-parameters representation was described in section 2.1.4. Considering the line with the length $\mathcal{L}$ in Fig. 3.1, the solution for the voltage and the current at $z = \mathcal{L}$ is obtained as follows [17]:

$$\begin{bmatrix} V(\mathcal{L}) \\ I(\mathcal{L}) \end{bmatrix} = \mathbf{\Phi}(\mathcal{L}) \begin{bmatrix} V(0) \\ I(0) \end{bmatrix} + \begin{bmatrix} V_{\mathrm{FT}}(\mathcal{L}) \\ I_{\mathrm{FT}}(\mathcal{L}) \end{bmatrix}, \tag{3.66}$$

where

$$\mathbf{\Phi}(z) = \begin{bmatrix} \cosh(\gamma z) & -Z_{\mathrm{c}} \cdot \sinh(\gamma z) \\ -\frac{\sinh(\gamma z)}{Z_{\mathrm{c}}} & \cosh(\gamma z) \end{bmatrix} \tag{3.67}$$

is the chain-parameter matrix of the line. For a lossless line the propagation constant is defined as $\gamma = \mathrm{j}\omega\sqrt{L'C'} = \mathrm{j}\beta$, as shown in (2.42). The parameter Z_{c} is the characteristic impedance of the line given in (2.35). The total forcing functions $V_{\mathrm{FT}}(\mathcal{L})$ and $I_{\mathrm{FT}}(\mathcal{L})$ are given by [17]

$$\begin{bmatrix} V_{\mathrm{FT}}(\mathcal{L}) \\ I_{\mathrm{FT}}(\mathcal{L}) \end{bmatrix} = \int_0^{\mathcal{L}} \begin{bmatrix} \Phi_{11}(\mathcal{L}-z)V'_{\mathrm{F}}(z) + \Phi_{12}(\mathcal{L}-z)I'_{\mathrm{F}}(z) \\ \Phi_{21}(\mathcal{L}-z)I'_{\mathrm{F}}(z) + \Phi_{22}(\mathcal{L}-z)I'_{\mathrm{F}}(z) \end{bmatrix} \mathrm{d}z, \tag{3.68}$$

where $V'_{\mathrm{F}}(z)$ and $I'_{\mathrm{F}}(z)$ are the forcing functions defined in (3.15). It can be seen that this solution represents the convolution of the distributed sources together with the chain-parameters.

The voltage and current solution at $z = 0$ can be represented by multiplying the inverse of

the chain-parameter matrix $\mathbf{\Phi}(\mathcal{L})^{-1}$ by (3.66) and rearranging [17].

$$\begin{aligned}\begin{bmatrix} V(0) \\ I(0) \end{bmatrix} &= \mathbf{\Phi}^{-1}(\mathcal{L}) \begin{bmatrix} V(\mathcal{L}) \\ I(\mathcal{L}) \end{bmatrix} - \mathbf{\Phi}^{-1}(\mathcal{L}) \begin{bmatrix} V_{\mathrm{FT}}(\mathcal{L}) \\ I_{\mathrm{FT}}(\mathcal{L}) \end{bmatrix} \\ &= \mathbf{\Phi}(-\mathcal{L}) \begin{bmatrix} V(\mathcal{L}) \\ I(\mathcal{L}) \end{bmatrix} - \mathbf{\Phi}(-\mathcal{L}) \begin{bmatrix} V_{\mathrm{FT}}(\mathcal{L}) \\ I_{\mathrm{FT}}(\mathcal{L}) \end{bmatrix} \\ &= \mathbf{\Phi}(-\mathcal{L}) \begin{bmatrix} V(\mathcal{L}) \\ I(\mathcal{L}) \end{bmatrix} + \begin{bmatrix} V_{\mathrm{FT}}(0) \\ I_{\mathrm{FT}}(0) \end{bmatrix}\end{aligned} \tag{3.69}$$

It should be pointed out here that the inverse $\mathbf{\Phi}^{-1}(\mathcal{L})$ is equal to $\mathbf{\Phi}(-\mathcal{L})$ [17]. The elements $V_{\mathrm{FT}}(0)$ and $I_{\mathrm{FT}}(0)$ represent the total forcing functions at the left end of the line. Multiply $\mathbf{\Phi}(-\mathcal{L})$ by (3.68) and use the property $\mathbf{\Phi}(-\mathcal{L}) \cdot \mathbf{\Phi}(\mathcal{L} - z) = \mathbf{\Phi}(-z)$ to obtain

$$\begin{bmatrix} V_{\mathrm{FT}}(0) \\ I_{\mathrm{FT}}(0) \end{bmatrix} = -\int_0^{\mathcal{L}} \begin{bmatrix} \Phi_{11}(-z)V'_{\mathrm{F}}(z) + \Phi_{12}(-z)I'_{\mathrm{F}}(z) \\ \Phi_{21}(-z)I'_{\mathrm{F}}(z) + \Phi_{22}(-z)I'_{\mathrm{F}}(z) \end{bmatrix} \mathrm{d}z. \tag{3.70}$$

Equations (3.66) and (3.69) represent the solutions for a line with matched loads. The boundary conditions at the line terminations must be taken into account in order to obtain the solution for arbitrary loads. These are considered in the developed circuit model, as will be shown below.

To calculate the total forcing function $V_{\mathrm{FT}}(\mathcal{L})$, (3.15) is substituted into (3.68), which gives [17]

$$\begin{aligned}V_{\mathrm{FT}}(\mathcal{L}) = &\int_0^{\mathcal{L}} \Phi_{11}(\mathcal{L} - z)E_{\mathrm{z}}^{\mathrm{e}}(h, z)\,\mathrm{d}z - \int_0^{\mathcal{L}} \Phi_{11}(\mathcal{L} - z) \cdot \frac{\partial}{\partial z}V_{\mathrm{t}}(z)\,\mathrm{d}z \\ &- \mathrm{j}\omega C' \int_0^{\mathcal{L}} \Phi_{12}(\mathcal{L} - z)V_{\mathrm{t}}(z)\,\mathrm{d}z.\end{aligned} \tag{3.71}$$

Using the product rule in the second term of (3.71) gives [17]

$$\begin{aligned}V_{\mathrm{FT}}(\mathcal{L}) = &\int_0^{\mathcal{L}} \Phi_{11}(\mathcal{L} - z)E_{\mathrm{z}}^{\mathrm{e}}(h, z)\,\mathrm{d}z - \int_0^{\mathcal{L}} \frac{\partial}{\partial z}\Big[\Phi_{11}(\mathcal{L} - z)V_{\mathrm{t}}(z)\Big]\,\mathrm{d}z \\ &+ \int_0^{\mathcal{L}} \Bigg[\underbrace{\frac{\partial}{\partial z}\Phi_{11}(\mathcal{L} - z) - \mathrm{j}\omega C'\Phi_{12}(\mathcal{L} - z)}_{=0}\Bigg] V_{\mathrm{t}}(z)\,\mathrm{d}z.\end{aligned} \tag{3.72}$$

The last term of (3.72) is zero. To prove this, the chain-parameters from (3.67) should be used. The second term contains an integral of a function with defined limits via a

derivative, where the result is the function itself with respect to the limits. The equation becomes

$$V_{\mathrm{FT}}(\mathcal{L}) = \int_0^{\mathcal{L}} \Phi_{11}(\mathcal{L}-z) E_{\mathrm{z}}^{\mathrm{e}}(h,z)\,\mathrm{d}z - \Phi_{11}(0) V_{\mathrm{t}}(\mathcal{L}) + \Phi_{11}(\mathcal{L}) V_{\mathrm{t}}(0). \tag{3.73}$$

Now applying the chain-parameter elements from (3.67) to become [17]

$$V_{\mathrm{FT}}(\mathcal{L}) = \int_0^{\mathcal{L}} \cosh\left(\gamma\left(\mathcal{L}-z\right)\right) \cdot E_{\mathrm{z}}^{\mathrm{e}}(h,z)\,\mathrm{d}z - V_{\mathrm{t2}} + \cosh(\gamma\mathcal{L}) \cdot V_{\mathrm{t1}}. \tag{3.74}$$

The terms $V_{\mathrm{t}}(0)$ and $V_{\mathrm{t}}(\mathcal{L})$ were replaced by V_{t1} and V_{t2}, as defined in (3.21) and (3.22). By applying similar steps to $I_{\mathrm{FT}}(\mathcal{L})$ in (3.68), this becomes [17]

$$I_{\mathrm{FT}}(\mathcal{L}) = -\int_0^{\mathcal{L}} \frac{\sinh\left(\gamma(\mathcal{L}-z)\right)}{Z_{\mathrm{c}}} \cdot E_{\mathrm{z}}^{\mathrm{e}}(h,z)\,\mathrm{d}z - \frac{\sinh(\gamma\mathcal{L})}{Z_{\mathrm{c}}} \cdot V_{\mathrm{t1}}. \tag{3.75}$$

The voltage response $V_{\mathrm{FT}}(0)$ in (3.70) can be easily calculated with similar steps [17]

$$V_{\mathrm{FT}}(0) = -\int_0^{\mathcal{L}} \cosh\left(\gamma z\right) \cdot E_{\mathrm{z}}^{\mathrm{e}}(h,z)\,\mathrm{d}z - V_{\mathrm{t1}} + \cosh(\gamma\mathcal{L}) \cdot V_{\mathrm{t2}}. \tag{3.76}$$

The same applies to $I_{\mathrm{FT}}(0)$ [17].

$$I_{\mathrm{FT}}(0) = \int_0^{\mathcal{L}} \frac{\sinh\left(\gamma z\right)}{Z_{\mathrm{c}}} \cdot E_{\mathrm{z}}^{\mathrm{e}}(h,z)\,\mathrm{d}z - \frac{\sinh(\gamma\mathcal{L})}{Z_{\mathrm{c}}} \cdot V_{\mathrm{t2}}. \tag{3.77}$$

So far, the total forcing functions at the line ends for adapted loads were calculated according to [17]. Next, the circuit models are developed from these solutions.

3.6 Circuit Model Based on the Total Voltage Formulation

The closed-form solutions in (3.66) and (3.69) were developed as previously mentioned for a reflectionless line. To create a circuit model from these solutions, it was assumed that the line in Fig. 3.1 has matched termination loads. The simplified equivalent circuit diagram of (3.66) and (3.69) can therefore be interpreted as a decoupled transmission line with the time delay T_{d} and the characteristic impedance Z_{c}. At whose ends the forcing controlled sources $V_{\mathrm{FT}}(0)$, $I_{\mathrm{FT}}(0)$, $V_{\mathrm{FT}}(\mathcal{L})$ and $I_{\mathrm{FT}}(\mathcal{L})$ are located, as shown in Fig. 3.6. Controlled sources instead of simple sources are included in the circuit because they depend on the incident field, as shown in (3.74), (3.75), (3.76) and (3.77). The problem with this

representation is that the field coupling via these sources occurs simultaneously at both ends. Therefore, the induced voltage and the current generated at the sources couple from the left to the right end and vice versa, as explained in the case of the scattered voltage formulation. This problem has been solved in this work in Fig. 3.5, where controlled sources were included in the macromodel, allowing the use of mismatched termination loads. The macromodel in [17] was developed in a different way, but nevertheless the forcing functions for the total voltage formulation were calculated according to the same source. The forcing functions at $z = \mathcal{L}$ in Fig. 3.6 consist of a voltage and a current source $V_{\mathrm{FT}}(\mathcal{L})$ and $I_{\mathrm{FT}}(\mathcal{L})$, respectively. These can be represented as a single voltage source $V_{\mathrm{Fr}}(\mathrm{j}\omega)$ by applying the so-called Thevenin and Norton source circuit, as will now be explained.

If the TL in Fig. 3.6 is replaced by its characteristic impedance Z_{c} and the voltage source $V_{\mathrm{FT}}(\mathcal{L})$ is ignored for the time being, one can see on the right-hand side of the line that the current source $I_{\mathrm{FT}}(\mathcal{L})$ together with Z_{c} forms a Norton source, as shown on the left side of Fig. 3.7. When $V_{\mathrm{FT}}(\mathcal{L})$ is considered in series with Z_{c}, it forms a Thevenin source, as shown in the middle of Fig. 3.7. The circuit on the right-hand side of Fig. 3.7 is obtained when the two sources are considered together with the load resistance $Z_{\mathrm{r}} = Z_{\mathrm{c}}$ by keeping Z_{c} instead of the TL. The resulting voltage from both sources $V_{\mathrm{Fr}}(\mathrm{j}\omega)$ can easily be calculated using Kirchhoff's circuit laws. It is given by

$$V_{\mathrm{Fr}}(\mathrm{j}\omega) = \frac{V_{\mathrm{FT}}(\mathcal{L}, \mathrm{j}\omega) + Z_{\mathrm{c}} I_{\mathrm{FT}}(\mathcal{L}, \mathrm{j}\omega)}{2}. \tag{3.78}$$

Within the scope of this work, it was possible to combine the current and voltage sources in (3.78) to a voltage function. The forcing sources on the left-hand side can also be combined in a voltage source $V_{\mathrm{Fl}}(\mathrm{j}\omega)$ as follows:

$$V_{\mathrm{Fl}}(\mathrm{j}\omega) = \frac{V_{\mathrm{FT}}(0, \mathrm{j}\omega) + Z_{\mathrm{c}} I_{\mathrm{FT}}(0, \mathrm{j}\omega)}{2}. \tag{3.79}$$

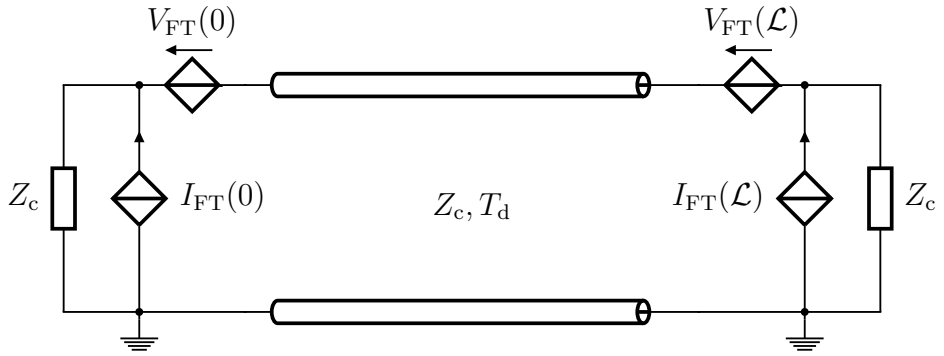

Figure 3.6: Simplified circuit model of an irradiated single conductor over a perfectly conducting ground plane based on total voltage formulation.

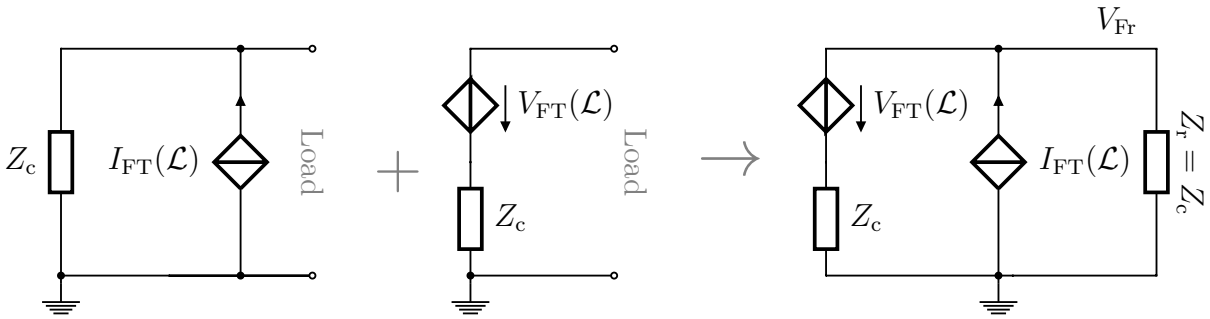

Figure 3.7: Representation of the coupling using Thevenin and Norton sources.

The indices l and r represent the left and the right side ends of the line. Equations (3.78) and (3.79) can also be derived using the Generalized Thevenin Equivalent representation for terminal conditions as explained in [17]. Since the considered line is lossless with $\gamma = \mathrm{j}\beta$, the following applies:

$$\cosh(\gamma\mathcal{L}) = \frac{\mathrm{e}^{\mathrm{j}\omega\frac{\mathcal{L}}{v_0}} + \mathrm{e}^{-\mathrm{j}\omega\frac{\mathcal{L}}{v_0}}}{2}, \tag{3.80}$$

where β was used from (2.36). Substituting T_d from (3.40), it leads to

$$\cosh(\gamma\mathcal{L}) = \frac{\mathrm{e}^{\mathrm{j}\omega T_\mathrm{d}} + \mathrm{e}^{-\mathrm{j}\omega T_\mathrm{d}}}{2} \tag{3.81a}$$

$$\sinh(\gamma\mathcal{L}) = \frac{\mathrm{e}^{\mathrm{j}\omega T_\mathrm{d}} - \mathrm{e}^{-\mathrm{j}\omega T_\mathrm{d}}}{2}. \tag{3.81b}$$

Now inserting (3.74) and (3.75) into (3.78) and using (3.81), which gives

$$V_\mathrm{Fr}(\mathrm{j}\omega) = \frac{1}{2} \cdot \left[\mathrm{e}^{-\mathrm{j}\omega T_\mathrm{d}} \int_0^{\mathcal{L}} \mathrm{e}^{\mathrm{j}\omega z/v_0}\, E_\mathrm{z}^\mathrm{e}(h,z)\,\mathrm{d}z + \mathrm{e}^{-\mathrm{j}\omega T_\mathrm{d}}\, V_\mathrm{t1} - V_\mathrm{t2} \right]. \tag{3.82}$$

The substitution of (3.76) and (3.77) into (3.79) using (3.81) leads to

$$V_\mathrm{Fl}(\mathrm{j}\omega) = -\frac{1}{2} \cdot \left[\int_0^{\mathcal{L}} \mathrm{e}^{-\mathrm{j}\omega z/v_0}\, E_\mathrm{z}^\mathrm{e}(h,z)\,\mathrm{d}z + V_\mathrm{t1} - \mathrm{e}^{-\mathrm{j}\omega T_\mathrm{d}}\, V_\mathrm{t2} \right]. \tag{3.83}$$

The total forcing functions at $z = 0$ and $z = \mathcal{L}$ were combined in (3.82) and (3.83) in the form of voltage sources $V_\mathrm{Fr}(\mathrm{j}\omega)$ and $V_\mathrm{Fl}(\mathrm{j}\omega)$, which are directly dependent on the field of incidence. Next, a plane wave for the field coupling is considered.

3.6.1 Uniform Plane Wave Excitation

When considering an incident uniform plane wave, the field parameter $E_\mathrm{z}^e(h,z)$ together with the voltages V_t1 and V_t2 can be represented as defined in (3.34), (3.41) and (3.42).

Inserting these parameters into (3.82) and executing the integral in the first term leads, after some mathematical manipulations, to

$$\begin{aligned} V_{\mathrm{Fr}}(\mathrm{j}\omega) =& \frac{1}{2} \cdot \Bigg[- \frac{2 \cdot \sin^2(\theta) \cdot h}{1 - \cos(\theta)} \cdot \mathrm{e}^{-\mathrm{j}\omega T_{\mathrm{d}}} E_0(\omega) \left(\mathrm{e}^{\mathrm{j}\omega \frac{\mathcal{L}}{v_0}} \mathrm{e}^{-\mathrm{j}\omega \frac{\mathcal{L}\cos(\theta)}{v_0}} - 1 \right) \\ & + 2 e_{\mathrm{y}} h E_0(\omega) \mathrm{e}^{-\mathrm{j}\omega T_{\mathrm{d}}} - 2 e_{\mathrm{y}} h E_0(\omega) \mathrm{e}^{-\mathrm{j}\omega \frac{\mathcal{L}\cos(\theta)}{v_0}} \Bigg]. \end{aligned} \tag{3.84}$$

When replacing the rational trigonometric function $\sin^2(\theta)/(1-\cos(\theta))$ by $1+\cos(\theta)$, enclosing $\mathrm{e}^{-\mathrm{j}\omega T_{\mathrm{d}}} E_0(\omega)$ in the parentheses in the first term of the equation, replacing $\mathcal{L}\cos(\theta)/v_0$ by T_{z} as defined in (3.39) and finally excluding $e_{\mathrm{y}}h$ in the last two terms, this leads to

$$\begin{aligned} V_{\mathrm{Fr}}(\mathrm{j}\omega) =& \Bigg[- h \left(1 + \cos(\theta)\right) \left(E_0(\omega) \mathrm{e}^{-\mathrm{j}\omega T_{\mathrm{z}}} - E_0(\omega) \mathrm{e}^{-\mathrm{j}\omega T_{\mathrm{d}}} \right) \\ & + e_{\mathrm{y}} h \left(E_0(\omega) \mathrm{e}^{-\mathrm{j}\omega T_{\mathrm{d}}} - E_0(\omega) \mathrm{e}^{-\mathrm{j}\omega T_{\mathrm{z}}} \right) \Bigg]. \end{aligned} \tag{3.85}$$

Replacing $(1+\cos(\theta))$ by $\mathcal{Q}_{1\mathrm{M}}$ as defined in (3.50) and manipulating the equation, it results in

$$V_{\mathrm{Fr}}(\mathrm{j}\omega) = h \cdot \Big[2\mathcal{Q}_{1\mathrm{M}} + e_{\mathrm{y}} \Big] \cdot \Big[E_0(\omega) \mathrm{e}^{-\mathrm{j}\omega T_{\mathrm{d}}} - E_0(\omega) \mathrm{e}^{-\mathrm{j}\omega T_{\mathrm{z}}} \Big]. \tag{3.86}$$

If one now compares (3.86) with the derived solution (3.63) for the case of the scattered voltage formulation, it can be seen that both solutions are identical. It is thus demonstrated in this work that the same field response was obtained using the scattered and the total voltage formulation. A circuit model for $V_{\mathrm{Fr}}(\mathrm{j}\omega)$ is therefore the same as the $V_{\mathrm{M}}(\mathcal{L}, \mathrm{j}\omega)$ shown in Fig. 3.5b.

The voltage response on the left-hand side can be calculated by substituting (3.34), (3.41) and (3.42) into (3.83) and using similar steps as for $V_{\mathrm{Fr}}(\mathrm{j}\omega)$.

$$V_{\mathrm{Fl}}(\mathrm{j}\omega) = -h \cdot \Big[2\mathcal{Q}_{1\mathrm{M}} + e_{\mathrm{y}} + 2 \Big] \cdot \Big[E_0(\omega) - E_0(\omega) \mathrm{e}^{-\mathrm{j}\omega(T_{\mathrm{d}} + T_{\mathrm{z}})} \Big] \tag{3.87}$$

It can again be clearly seen that the function is identical to the solution from the scattered voltage formulation shown in (3.59) and therefore its circuit model is the same as that for $V_{\mathrm{M}}(0, \mathrm{j}\omega)$ in Fig. 3.5b.

As described above, (3.66) and (3.69) represent the solution for field coupling on a TL with matched loads, whereby the simplified equivalent circuit diagram of these equations was developed in Fig. 3.6. The problem with this circuit was that the current source $I_{\mathrm{FT}}(0)$ supplied the left load and the right load simultaneously, so that the coupling is integrated

several times, which leads to incorrect results. The same applies to $I_{\mathrm{FT}}(\mathcal{L})$, $V_{\mathrm{FT}}(0)$ and $V_{\mathrm{FT}}(\mathcal{L})$. This problem was shown in the case of the scattered voltage formulation in Fig. 3.4 too. However, the problem was solved in Fig. 3.5, where controlled sources were used. This means that the SPICE model developed for the field-coupled line in Fig. 3.5 can also be used for the total voltage formulation. In (3.65), V_{Fl} and V_{Fr} should be used instead of $V_{\mathrm{M}}(0, \mathrm{j}\omega)$ and $V_{\mathrm{M}}(\mathcal{L}, \mathrm{j}\omega)$.

In this section, it was proven that the scattered and the total voltage formulation ultimately led to identical solutions and therefore an identical circuit model was designed for both methods. In the next step the model is validated.

3.7 Model Validation

The circuit model developed in Fig. 3.5 is built in the SPICE environment with the analog electronic circuit simulator LTspice [35]. For validation, the simulation results are compared with those of the CST Studio Suite 2019 [3]. First, the simulation process of the tools used is explained, then the results are discussed. No measurements were carried out, since such measurements were difficult to achieve with a quantitatively accurate evaluation.

3.7.1 Simulation Setup

The circuit simulation tool LTspice [35] is based on SPICE, which stands for "Simulation Program with Integrated Circuit Emphasis". LTspice enables the simulation in the transient and the frequency domain, which are mainly investigated in this work. Other simulation commands are defined in the simulator, here `DC Sweep`, in which a DC analysis is carried out while the DC value of a source is swept; `Noise` for analyzing the noise in a circuit; `DC Transfer Function`, which can determine the DC small signal transfer function of a branch current or node voltage and `DC Operating Point`, which calculates the DC operating point by treating the capacitance as an open circuit and the inductance as a short circuit. In the transient analysis, convergence problems may occur and the simulation can be stopped in previous iterations before a valid solution is reached. They are many reasons that lead to this problem, such related to design, e.g. a missing path of the DC current to the ground. Other reasons related to the settings such as the case of an unrealistic rise and fall time in a source, invalid initial conditions or unrealistic tolerance ranges. This problem is usually solved by correcting the circuit design or changing the simulator options. Since there were no convergence issues in the proposed models, the SPICE options were kept by default. These are defined as follows: `Gmin = 1e-12`, `Abstol = 1e-12`, `Reltol = 0.001`, `Chgtol = 1e-14`, `Trtol = 1`, `Volttol = 1e-6`, `Sstol = 0.001` and `MinDeltaGmin = 0.0001`.

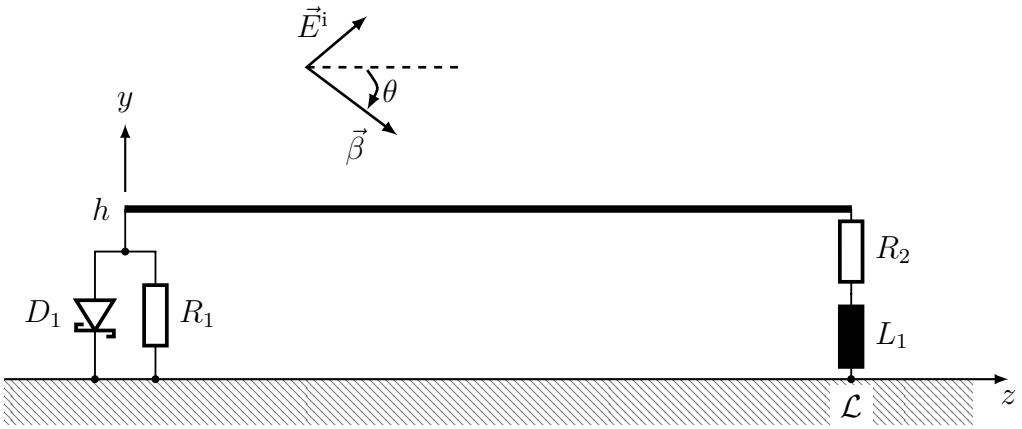

Figure 3.8: Setup for the validation of a field-coupled single conductor over a perfectly conducting ground plane.

The following describes how the setup in Fig. 3.8 is simulated in CST. It consists of a conductor of length $\mathcal{L}$ connected to loads at its ends and coupled by an incident plane wave. The simulation model is shown in Fig. 3.9. The software CST Studio Suite 2019 [3] contains several packages that can be combined with the so-called co-simulation. Three main packages are used in this work: CST Microwave Studio, CST Design Studio and CST Cable Studio. The flowchart of the simulation process is explained in Fig. 3.10. The 3D EM simulation is carried out in the CST Microwave Studio tool, which contains various solvers for the time and frequency domain simulation. The model is integrated in this tool and consists of the reference ground plane and the wire path above it, which corresponds to Figs. 3.8 and 3.9. The loads are defined in CST Design Studio in Fig. 3.9b analogously to the setup shown in Fig. 3.8. The ground plane was connected to the `Open` boundary conditions to avoid reflection of the generated current. In the y-direction above the wire, the boundary conditions were set to `Open Add Space`, which means that a distance between the `Open` condition and the model is maintained to allow wave propagation. In

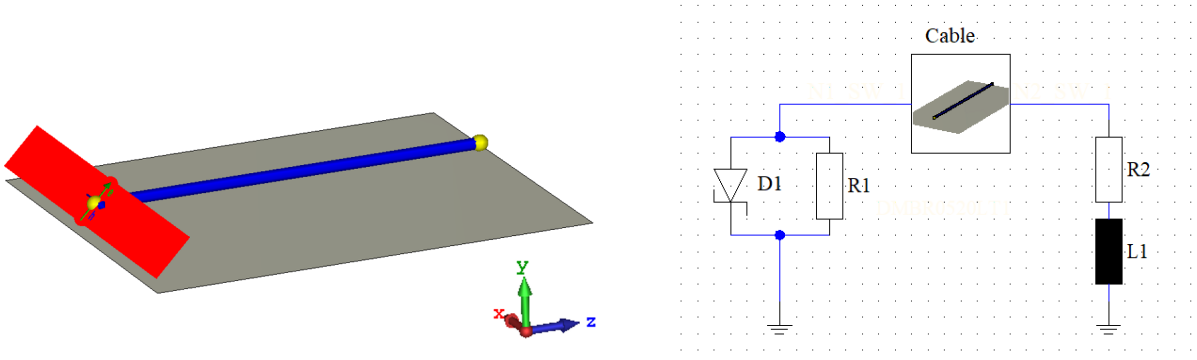

(a) Field-coupled line in CST Microwave Studio

(b) Circuit model in CST Design Studio

Figure 3.9: Simulation model of a single conductor line over a ground plane in CST [3].

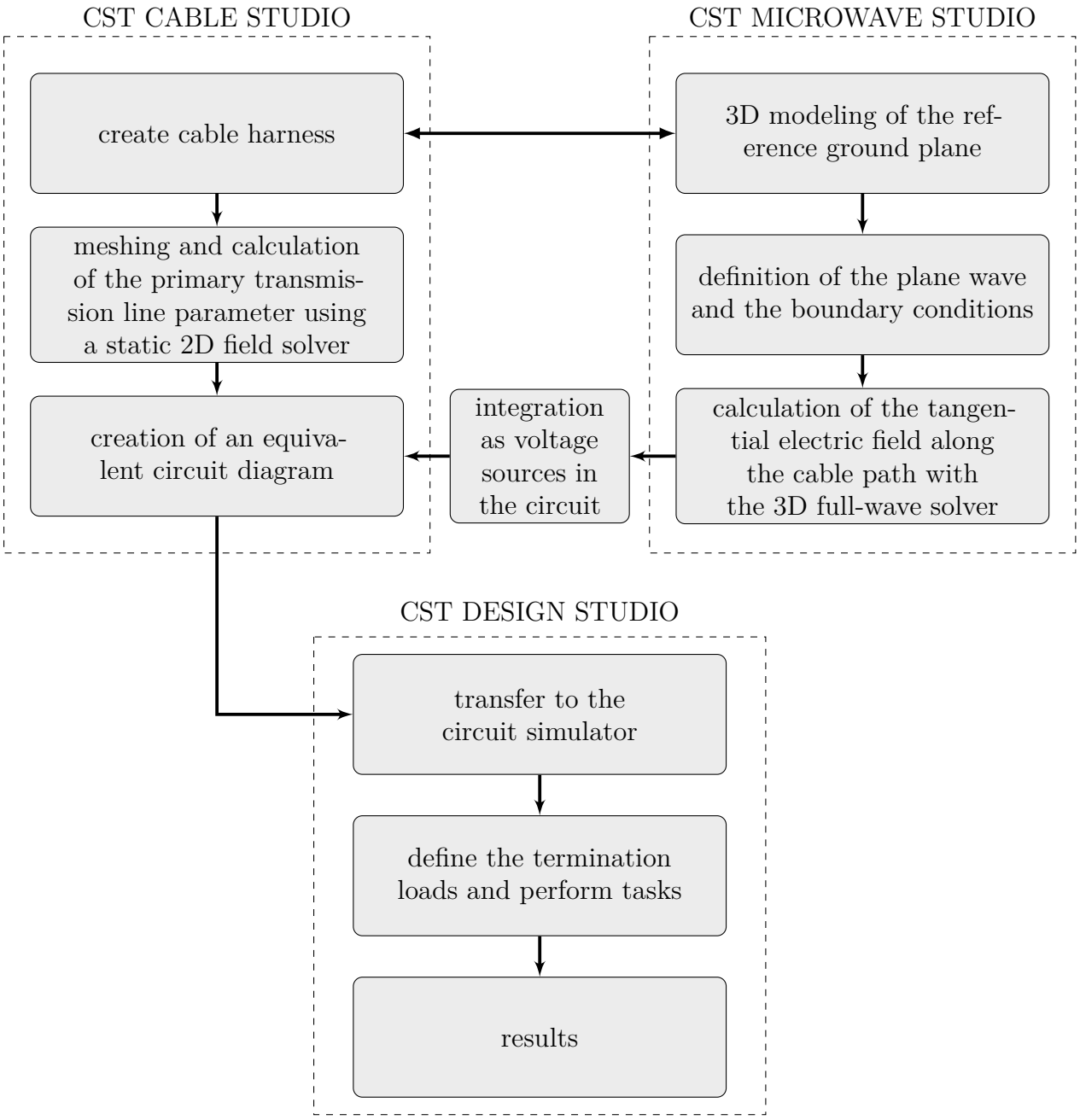

Figure 3.10: Flowchart of the simulation process in CST Studio Suite.

the simulated model, a minimum distance of $\lambda/2$ of the center frequency was defined. It has to be mentioned that the wire in CST Microwave Studio was not designed as a 3D structure. It was represented by a line path on which the tangential electric field was calculated and transferred to the CST Cable Studio in the form of lumped sources, as explained in Figs. 3.9 and 3.10. Various cable types are defined in CST Cable Studio, including shielded and twisted cable types, with which a complex cable harness with an interface to the 3D field simulation can be easily defined. The wire was designed in the CST Cable Studio, where an equivalent circuit diagram from the wire harness is created

based on the classic transmission line theory (see Fig. 3.10). The cable is meshed along its length and the transmission line parameters on these segments are calculated using a static solver. A minimum sample length of 5 mm was considered for the mesh, where the losses were not taken into account. A circuit model is then created as cascaded cells with concentrated elements that represent the cable. The cable model is interconnected in a co-simulation with the CST Design Studio, in which terminating loads are added, as described in Figs. 3.9 and 3.10. The transient solver was used in the 3D EM simulator using a hexahedral mesh. This solver is based on the Finite Integration Technique (FIT) [64].

3.7.2 Results and Discussion

A 3 m wire was placed 2 cm above the ground plane as shown in Fig. 3.8. The wire has a radius of 0.25 mm with a characteristic impedance of 306.4 Ω. A Schottky diode of type MBR0520LT1 with a resistance $R_1 = 100\,\Omega$ in parallel are connected at $z = 0$. On the right-hand side the resistor $R_2 = 10\,\Omega$ is connected in series with $L_1 = 1\,\text{mH}$. In the transient analysis, a uniform plane wave with the angle of incidence $\theta = 45°$ was excited. A trapezoidal shape of the electric field is defined with a magnitude of $10\,\frac{\text{V}}{\text{m}}$. The rise, hold and fall times are 2 ns, 10 ns and 3 ns, respectively. The voltage response across D_1 is shown in Fig. 3.11, where the SPICE results are in excellent agreement with those of CST.

The diode D_1 was removed for the frequency domain analysis. The angle of incidence is set to 30° and the electric field has a magnitude of $10\,\frac{\text{V}}{\text{m}}$. The voltage across R_2 and L_1 as magnitude and phase was simulated and shown in Fig. 3.12. The resonance frequency at 25 MHz together with its harmonics corresponds to the electrical length of the wire.
The resonance behavior can be clearly observed due to the mismatch loads at the ends. The SPICE results are in excellent agreement with those of CST.

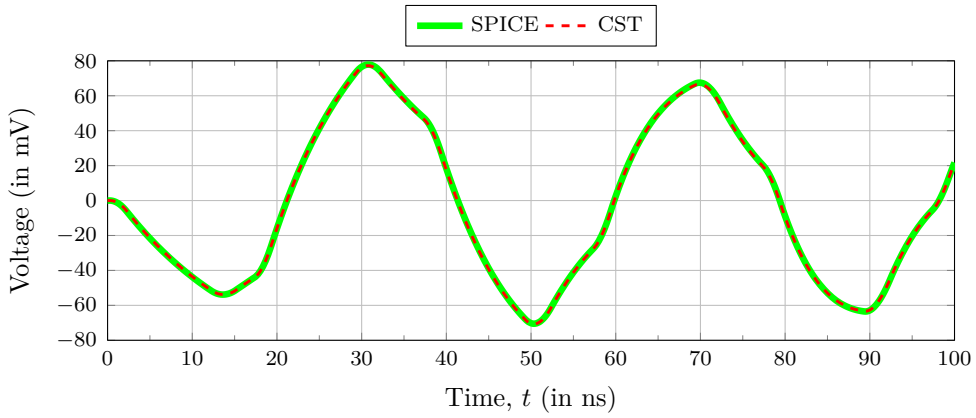

Figure 3.11: Voltage response across D_1 in transient analysis.

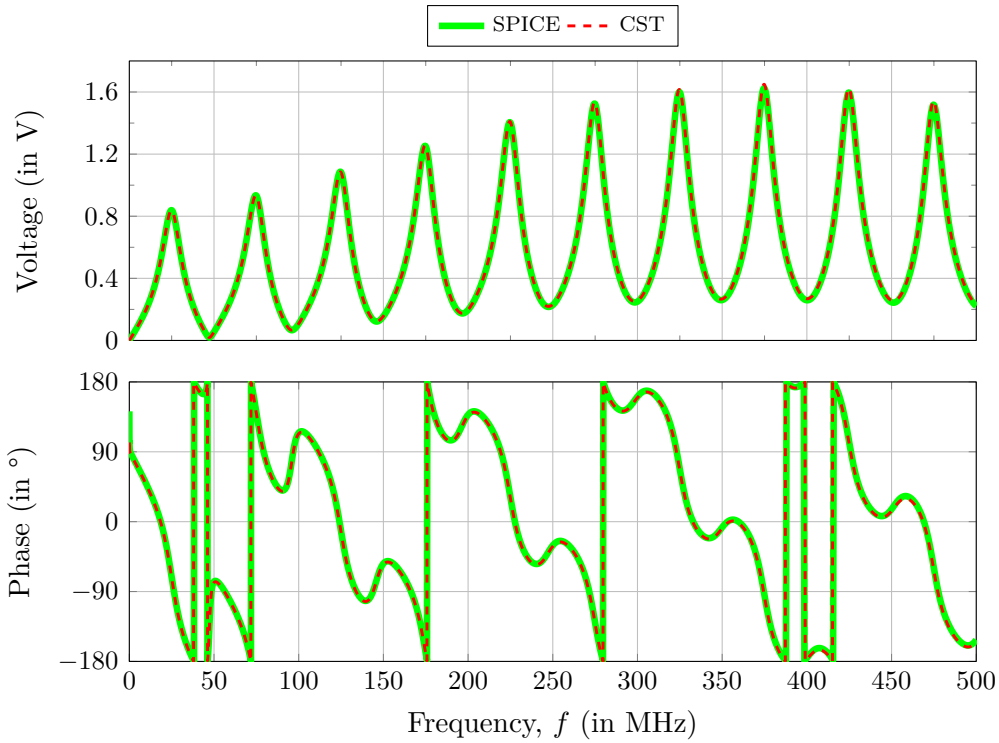

Figure 3.12: Voltage response across R_2 and L_1 in frequency domain.

In this chapter, circuit models were developed for a field-coupled conductor above a perfectly conducting ground plane. The field coupling was calculated according to the scattered voltage formulation and the total voltage formulation. It was shown that both methods lead to the same circuit model. The models presented so far for a field-coupled line are used in the next section to develop circuit models for shielded single conductors.

4 Circuit Models of Single Conductor Shielded Cables

In this chapter, circuit models are developed based on two methods for a field-coupled, single conductor shielded cable that is laid over a ground plane. The first method presents a circuit model with cascaded lumped circuit elements in which the cable is divided into segments. This model is referred to as the "lumped-circuit model" and is developed in section 4.1. The second method is based on a closed-form solution without discretizing the cable into segments. The model developed on the basis of this method is called "Macromodel". It is presented in section 4.2 for the analysis of the conductive coupling. The macromodel is expanded to include field coupling to the cable in section 4.3. Both models were validated by measurements and field simulations. It was found that the lumped-circuit model is easy to create. On the other hand, the macromodel with a closed-form solution can simulate any cable length without reaching a limit.

The cable with length $\mathcal{L}$ and height h above the ground plane in Fig. 4.1 will be used for the next investigations. An inner and an outer system are defined on the cable structure, as described in section 2.3.2. Fig. 4.1 shows the currents and voltages at the cable ends, the directions of which are based on the models developed later. The terms $V_\mathrm{w}(0)$ and $V_\mathrm{w}(\mathcal{L})$ represent the voltages between the inner wire and the ground plane at $z = 0$ and $z = \mathcal{L}$. On the other hand, the parameters $V_\mathrm{i}(0)$ and $V_\mathrm{i}(\mathcal{L})$ represent the voltages between the inner wire and the screen at $z = 0$ and $z = \mathcal{L}$. The currents $I_\mathrm{i}(0)$, $I_\mathrm{i}(\mathcal{L})$, $I_\mathrm{o}(0)$ and $I_\mathrm{o}(\mathcal{L})$

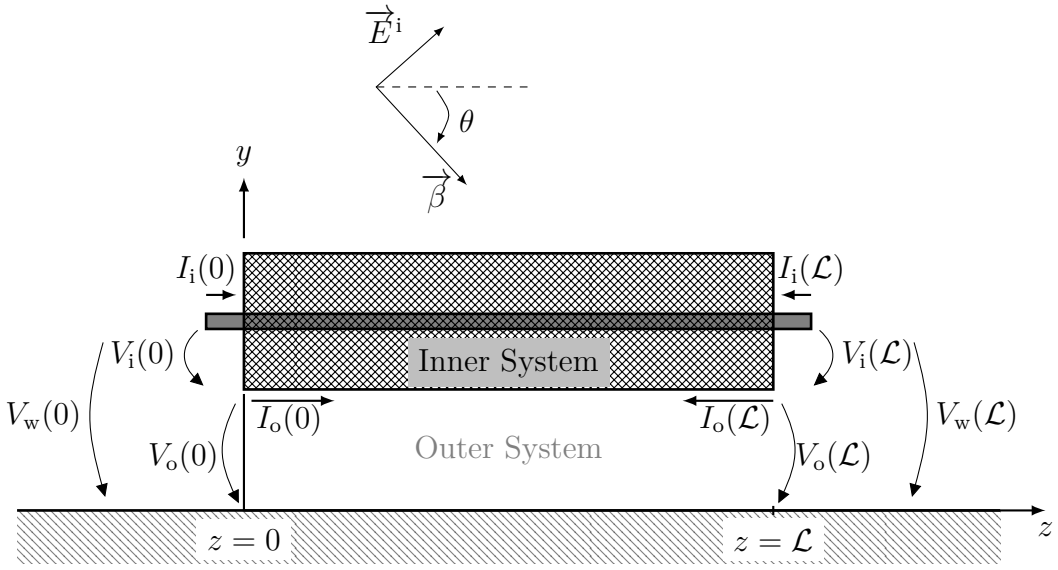

Figure 4.1: Shielded cable over a ground plane with voltage and current declaration.

are those of the inner and outer systems at $z = 0$ and $z = \mathcal{L}$, respectively. An incident uniform plane wave excites the cable in the $\overrightarrow{\beta}$ direction with an incident electric field $\overrightarrow{E}^{\mathrm{i}}$ and an angle of incidence θ. A braided shield with a braid angle $\mathcal{G} = 45°$ is considered, where the transfer impedance Z_t' takes the form of the Vance definition in (2.116). To prove this, the parameter $\mathcal{G} = 45°$ must be inserted into the model of Demoulin in (2.123) and into that of Tyni in (2.120), thus eliminating the porpoising effect. The p.u.l. transfer impedance is thus given by

$$Z_{\mathrm{t}}' = R_{\mathrm{t}}' + \mathrm{j}\omega L_{\mathrm{t}}'. \tag{4.1}$$

The frequency dependency was neglected in the diffusion part Z_{d}' and replaced by DC losses of the shielding R_{t}'. The parameter Z_{d}' in (2.116) contains the skin depth with the square root of the frequency, which makes the analysis very complex and almost impossible to interpret an equivalent circuit diagram of the cable. The parameter L_{t}' represents the inductive coupling of magnetic fields penetrating through the holes in the braid, as described in section 2.3.5. The transfer impedance dominates in most applications, particularly when the cable shield is shortened to ground. In this case, the transfer admittance has a minimal influence on the coupled power and is therefore neglected in this work [26, 38].

Next, the lumped-circuit model of a single conductor shielded cable is developed.

4.1 Lumped-Circuit Model for Single Conductor Shielded Cables

In this section, a lumped-circuit model for single conductor shielded cables with a braided shield above a ground plane is presented. The model takes into account the bidirectional coupling between the inner and outer system, which enables the analysis of emission and immunity tests. The field coupling of a plane wave is considered, allowing the model to perform field coupling tests. In earlier work, lumped-circuit models for shielded cables were presented in [65], with results validated in the frequency and time domains. Further lumped-circuit models were developed for power cables without a ground plane and without taking into account the field coupling in [66, 67].

For modeling, the shielded cable in Fig. 4.1 must be divided into segments of length $l_{\mathrm{step}} < \lambda/10$, where λ is the wavelength of the maximum frequency of interest. This frequency can be calculated from the switching time in the time domain, e.g. from the rise and fall times of a rectangular pulse. In the frequency domain, it is simply the maximum simulation frequency. Equivalent circuit diagrams are created for each segment and connected in series to represent the entire cable, as shown in Fig. 4.2. Each segment consists of an inner and an outer system as described in section 2.3.2. The inner system includes the coupling from the outer one, in contrast the outer system includes the coupling

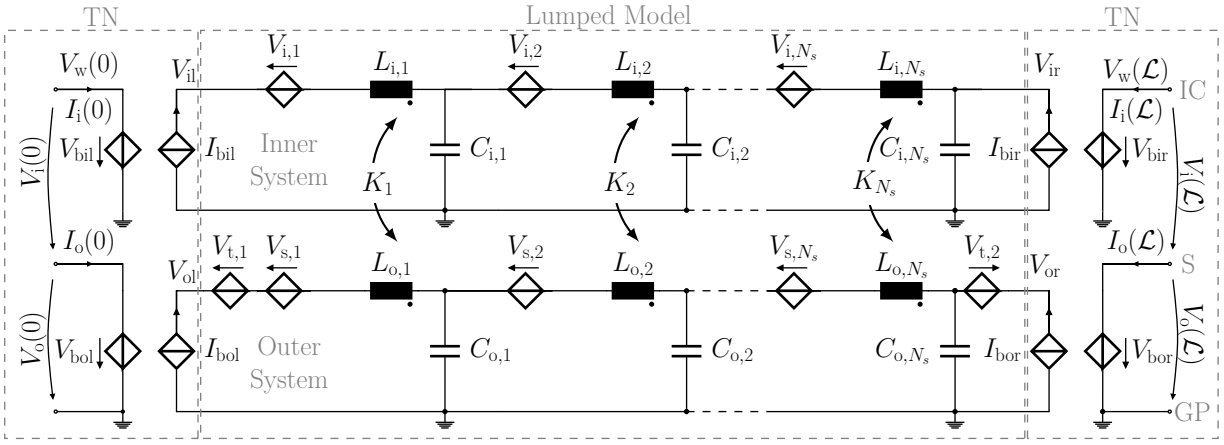

Figure 4.2: Lumped-circuit model of a field-coupled shielded cable over a perfectly conducting ground plane. IC inner conductor. S shield. GP ground plane. TN transformation network.

from the inner system and the coupling to the environment, here exactly the field coupling.

The model shown in Fig. 4.2 consists of three main parts. The lumped model in the middle contains the distributed elements. At the ends, two transformation networks (TN) are modeled. These are used to combine the inner and outer systems into suitable connections, including the inner conductor, shielding and ground plane. The TNs can represent the voltage of the inner system with respect to ground, as explained in (2.98). The voltage $V_{\mathrm{i}}(0)$ in Fig. 4.2 is the voltage between the inner conductor and the shield, while $V_{\mathrm{w}}(0)$ is the voltage between the inner conductor and the ground plane. For comparison, these voltages are shown on the cable in Fig. 4.1. The same applies to $V_{\mathrm{i}}(\mathcal{L})$ and $V_{\mathrm{w}}(\mathcal{L})$. The outlined comparison leads to the interpretation of the controlled sources used for the inner system, which are defined as follows:

$$V_{\mathrm{bil}} = V_{\mathrm{il}} + V_{\mathrm{ol}} \tag{4.2a}$$

$$I_{\mathrm{bil}} = I_{\mathrm{i}}(0) \tag{4.2b}$$

$$I_{\mathrm{bir}} = I_{\mathrm{i}}(\mathcal{L}) \tag{4.2c}$$

$$V_{\mathrm{bir}} = V_{\mathrm{ir}} + V_{\mathrm{or}}. \tag{4.2d}$$

Similarly, those for the outer system are given by

$$V_{\mathrm{bol}} = V_{\mathrm{ol}} \tag{4.3a}$$

$$I_{\mathrm{bol}} = I_{\mathrm{i}}(0) + I_{\mathrm{o}}(0) \tag{4.3b}$$

$$I_{\mathrm{bor}} = I_{\mathrm{i}}(\mathcal{L}) + I_{\mathrm{o}}(\mathcal{L}) \tag{4.3c}$$

$$V_{\mathrm{bor}} = V_{\mathrm{or}}. \tag{4.3d}$$

These equations can be better understood by considering the transformation matrices in (2.98) and (2.99). The calculation of the individual elements for the model is explained in the next steps, whereby these are treated separately for the inner and outer system.
The solution of the inner system is considered next.

4.1.1 Solution of the Inner System

The transmission line equations for the inner system of a shielded cable above a ground plane was presented in (2.100). It is rewritten here with the transfer impedance shown in (4.1) as follows:

$$\frac{\mathrm{d}}{\mathrm{d}z}\begin{bmatrix} V_\mathrm{i}(z) \\ I_\mathrm{i}(z) \end{bmatrix} = \begin{bmatrix} 0 & -\mathrm{j}\omega L'_\mathrm{i} \\ -\mathrm{j}\omega C'_\mathrm{i} & 0 \end{bmatrix} \cdot \begin{bmatrix} V_\mathrm{i}(z) \\ I_\mathrm{i}(z) \end{bmatrix} + \begin{bmatrix} V'_\mathrm{di}(z) \\ 0 \end{bmatrix}, \tag{4.4}$$

where the interference voltage $V'_\mathrm{di}(z)$ is given by

$$V'_\mathrm{di}(z) = (R'_\mathrm{t} + \mathrm{j}\omega L'_\mathrm{t}) \cdot I_\mathrm{o}(z). \tag{4.5}$$

The element $I_\mathrm{o}(z)$ is the current of the outer system. The voltage $V_\mathrm{i}(z)$ and the current $I_\mathrm{i}(z)$ are those of the inner system, as shown in Figs. 4.1 and 2.12. The elements C'_i and L'_i are the primary line constants of the inner system, which can be calculated using (2.31) and (2.32). The losses of the cable are neglected, taking into account R'_t in $V'_\mathrm{di}(z)$, as it is responsible for the coupling via diffusion.
An equivalent circuit diagram for this equation system was developed in Fig. 4.2. To understand the interpretation process, the first differential equation in (4.4) is written out with respect to Δz as follows:

$$\frac{V_\mathrm{i}(z)}{\Delta z} = \mathrm{j}\omega L'_\mathrm{i} I_\mathrm{i}(z) - V'_\mathrm{di}(z) + \frac{V_\mathrm{i}(z+\Delta z)}{\Delta z}. \tag{4.6}$$

The differential equation in this form is easier to interpret as an equivalent circuit diagram. Applying Kirchhoff's voltage law to the inner system of Fig. 2.13 leads to the same equation. Therefore, the equivalent circuit diagram in Fig. 2.13 of a Δz segment can be used for the inner system. The transfer admittance is ignored, which is why I'_di is omitted here. Now divide the cable shown in Fig. 4.1 into N_s segments of length l_step. Under these conditions, the equivalent circuit diagram in Fig. 2.13 can be applied to each segment. The equivalent circuit diagram of the entire cable was created by connecting the circuits in series, which consist of N_s cells (see Fig. 4.2). The nth cell of the inner system contains the interference voltage $V_{\mathrm{i},n}$ and the element $L_{\mathrm{i},n}$ in series. To eliminate the length dependence of the cable

parameters, they should be multiplied by the unit length l_{step} as follows:

$$L_{\text{i},n} = L'_{\text{i}} \cdot l_{\text{step}} \tag{4.7a}$$

$$C_{\text{i},n} = C'_{\text{i}} \cdot l_{\text{step}}, \tag{4.7b}$$

where l_{step} is given by

$$l_{\text{step}} = \frac{\mathcal{L}}{N_{\text{s}}}. \tag{4.8}$$

The capacitane $C_{\text{i},n}$ is connected in parallel between inner conductor and reference in Fig. 4.2. The voltage $V_{\text{i},n}$ represents the diffusion part of the coupling from the outer system. It is a current-controlled voltage source, which represents the induced voltage in the inner system due to the current at the outer system $I_{\text{o}}(z)$. It is given by

$$V_{\text{i},n} = R'_{\text{t},n} I_{\text{o},n}(z) \cdot l_{\text{step}}. \tag{4.9}$$

So far, the coupling via diffusion has been considered. What still has to be taken into account is the inductive coupling via L'_{t}. In SPICE simulation programs like LTspice [35], it is possible to calculate the inductive coupling between two inductors by the coupling coefficient K_n. It is defined as

$$K_n = -\frac{L'_{\text{t}}}{\sqrt{L'_{\text{o}} L'_{\text{i}}}}, \tag{4.10}$$

where L'_{o} is the p.u.l. inductance of the outer system. In Fig. 4.2, the coefficients K_1 to K_{N_s} are added to demonstrate this coupling. This means that when a current $I_{\text{o}}(z)$ flows through $L_{\text{o},n}$ in the outer system, a voltage is induced across $L_{\text{i}n}$ and vice versa. Next, the calculation of the outer elements is derived.

4.1.2 Solution of the Outer System

In the outer system, two coupling mechanisms must be taken into account, the coupling from the inner system and the field coupling. The coupling from the inner system of the nth cell in Fig. 4.2 takes place via K_n and $V_{\text{s},n}$, where the inductive coupling coefficient K_n was defined in (4.10) and the controlled voltage source $V_{\text{s},n}$ is given by

$$V_{\text{s},n} = V_{\text{o},n} + V_{\text{tan},n}. \tag{4.11}$$

The voltage $V_{\text{s},n}$ contains the diffusion coupling represented by $V_{\text{o},n} = R'_{\text{t},n} I_{\text{i}}(z) \cdot l_{\text{step}}$ and the coupling of the tangential electric field represented by $V_{\text{tan},n}$. The shielded cable above the ground plane is treated as a single conductor in the field coupling. In section 3, two

possible solutions were presented, the so-called scattered voltage formulation and the total voltage formulation. In the next calculations, the scattered voltage formulation of Agrawal *et al.* [5] is applied.
The differential equation for the field coupling on the outer system can therefore be written as follows:

$$\frac{\mathrm{d}}{\mathrm{d}z}\begin{bmatrix} V_{\mathrm{o}}^{\mathrm{s}}(z) \\ I_{\mathrm{of}}(z) \end{bmatrix} = \begin{bmatrix} 0 & -\mathrm{j}\omega L_{\mathrm{o}}' \\ -\mathrm{j}\omega C_{\mathrm{o}}' & 0 \end{bmatrix} \begin{bmatrix} V_{\mathrm{o}}^{\mathrm{s}}(z) \\ I_{\mathrm{of}}(z) \end{bmatrix} + \begin{bmatrix} E_{\mathrm{z}}^{e}(h,z) \\ 0 \end{bmatrix}. \tag{4.12}$$

It has the same form as in (3.18), but the names of the elements have been changed accordingly. The parameter $I_{\mathrm{of}}(z)$ stands for the current generated in the outer system due to the field coupling. The elements C_{o}' and L_{o}' are the primary line constants of the outer system. The parameter $E_{\mathrm{z}}^{e}(h,z)$ is the superimposition of the tangential electric field on the cable shield, as defined in (3.13). Considering the excitation of a plane wave, the incident and reflected tangential part of the electric fields together with their addition on the cable can be taken from (3.30), (3.31) and (3.34), respectively. The element $E_{\mathrm{z}}^{e}(h,z)$ can therefore be written as follows:

$$\begin{aligned} E_{\mathrm{z}}^{e}(h,z) &= E_{\mathrm{z}}^{i}(h,z) + E_{\mathrm{z}}^{r}(h,z) \\ &= \underbrace{-\mathrm{j}2E_0(\omega)\cdot\sin(\theta)\cdot\sin(\beta_{\mathrm{y}}h)}_{V_{\mathrm{tan}}{}'(h)}\cdot \mathrm{e}^{-\mathrm{j}\beta_{\mathrm{z}}z}. \end{aligned} \tag{4.13}$$

The phase constants along the axes β_{y} and β_{z} were defined in (3.33). The parameter θ is the angle of incidence, as shown in Fig. 4.1. The parameter $V_{\mathrm{tan}}{}'(h)$ represents the p.u.l. voltage induced along the cable in distributed form, so that its solution in Fig. 4.2 is implemented in the distributed sources $V_{\mathrm{s},1}$ to V_{s,N_s}.
If only $V_{\mathrm{tan}}{}'(h)$ is included in the cells, the resulting voltage across the loads will include the scattered voltages $V_{\mathrm{o}}^{\mathrm{s}}(0)$ and $V_{\mathrm{o}}^{\mathrm{s}}(\mathcal{L})$, but not the total voltages $V_{\mathrm{o}}(0)$ and $V_{\mathrm{o}}(\mathcal{L})$. To calculate $V_{\mathrm{o}}(0)$ and $V_{\mathrm{o}}(\mathcal{L})$, the voltages induced by the transverse field must be added, as explained in (3.17). The total voltage across the cable loads is therefore given by

$$V_{\mathrm{o}}(0) = V_{\mathrm{o}}^{\mathrm{s}}(0) - \underbrace{\int_0^h \left(E_{\mathrm{y}}^{i}(0) + E_{\mathrm{y}}^{r}(0)\right)\mathrm{d}y}_{V_{\mathrm{t},1}} \tag{4.14a}$$

$$V_{\mathrm{o}}(\mathcal{L}) = V_{\mathrm{o}}^{\mathrm{s}}(\mathcal{L}) - \underbrace{\int_0^h \left(E_{\mathrm{y}}^{i}(\mathcal{L}) + E_{\mathrm{y}}^{r}(\mathcal{L})\right)\mathrm{d}y}_{V_{\mathrm{t},2}}, \tag{4.14b}$$

where $V_{\mathrm{t},1}$ and $V_{\mathrm{t},2}$ are the transverse voltages across the loads. The elements E_{y}^{i} and E_{y}^{r} are the transverse parts of the incident and reflected electric field. In order to take the field coupling into account in the equivalent circuit diagram, the tangential voltages $V_{\mathrm{tan},n}$

are added to each cell via $V_{\mathrm{s},n}$ in (4.11) and $V_{\mathrm{t},1}$, $V_{\mathrm{t},2}$ are added to the loads, as shown in Fig. 4.2.

In the next steps, the tangential voltage $V_{\tan}(h)$ and the transverse voltages $V_{\mathrm{t},1}$ and $V_{\mathrm{t},2}$ are calculated.

Tangential Voltages

The function $V'_{\tan(h)}$ in (4.13) exists in a form that cannot be directly integrated into the SPICE environment. In particular the $\sin(\beta_{\mathrm{y}}h)$ part, which is a sinus of frequency and therefore difficult to interpret in time domain. A simplification was applied to $V'_{\tan,n}$ in (3.51), where $\sin(\beta_{\mathrm{y}}h)$ was transformed into a $\mathrm{sinc}(\beta_{\mathrm{y}}h)$ function that was solved in (3.37). It should be mentioned here that $V'_{\tan(h)} = V_{\mathrm{s}}^{e\prime}(h)$. The sinc function was set to one in a later step because the time delay T_{y} is approximately zero, as described in (3.38). Substituting the simplified form of $V'_{\tan}(h)$ from (3.51) into (4.13) leads to

$$E_{\mathrm{z}}^{e}(h,z) \approx -\mathrm{j}2E_0(\omega)\cdot\sin(\theta)\cdot\beta_y h\cdot \mathrm{e}^{-\mathrm{j}\beta_{\mathrm{z}}z}. \tag{4.15}$$

Replace β_{y} and β_{z} from (3.33) and use (2.36), the equation becomes

$$E_{\mathrm{z}}^{e}(h,z) \approx 2h\cdot\frac{\sin^2(\theta)}{v_0}\cdot\mathrm{j}\omega\cdot E_0(\omega)\cdot\mathrm{e}^{-\mathrm{j}\omega\frac{\cos(\theta)}{v_0}z}. \tag{4.16}$$

Converting the equation into the time domain after using (3.60), it leads to

$$E_{\mathrm{z}}^{e}(t) = 2h\cdot\frac{\sin^2(\theta)}{v_0}\cdot\frac{\mathrm{d}\left(E_0\left(t-\frac{\cos(\theta)}{v_0}z\right)\right)}{\mathrm{d}t}. \tag{4.17}$$

The function $E_{\mathrm{z}}^{e}(t)$ is a per-unit-length voltage. Since the response of the tangential electric field is represented as distributed voltage sources in the model, $E_{\mathrm{z}}^{e}(t)$ must be multiplied by the segment length l_{step}. This gives the following equation for the nth cell in Fig. 4.2:

$$V_{\tan,n}(t) = \overbrace{2l_{\mathrm{step}}\cdot h\cdot\frac{\sin^2(\theta)}{v_0}}^{\eta}\cdot\frac{\mathrm{d}\left(E_0\Big(t-\overbrace{\frac{\cos(\theta)\cdot n\cdot l_{\mathrm{step}}}{v_0}}^{T_{\mathrm{do}}}\Big)\right)}{\mathrm{d}t}. \tag{4.18}$$

The variable z has been replaced by $n\times l_{\mathrm{step}}$. It should be mentioned that $V_{\tan,n}(t)$ is integrated in $V_{\mathrm{s},n}$ in (4.11) and thus in the model in Fig. 4.2. Equation (4.18) consists of a time-delayed electric field $E_0(t)$, which is derived with respect to time and is multiplied by a factor η. An equivalent circuit diagram was derived in Fig. 4.3. The time delay was achieved by a voltage source $E_0(t)$, which feeds an adapted transmission line with a time delay T_{do}. The time derivative was realized by calculating the current I_{C_1}, which feeds the capacitor $C_1 = 1\,\mathrm{F}$ set in parallel to v_{i}. The controlled voltage source v_{i} contains the

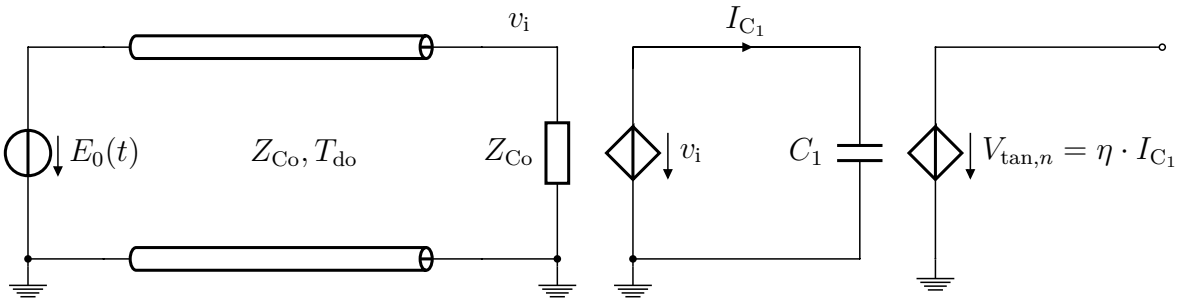

Figure 4.3: Equivalent circuit diagram for the tangential voltage in the n-th cell $V_{\mathrm{tan},n}(t)$.

time-delayed electric field $E_0(t - T_\mathrm{do})$. A controlled voltage source is ultimately used to multiply the factor η. The response of $V_{\mathrm{tan},n}$ in Fig. 4.3 can be integrated directly into (4.11) and later in Fig. 4.2. The same applies to the other segments.

Since a circuit model has been developed for the tangential voltages $V_{\mathrm{tan},n}$, the solution for the transverse voltages $V_{\mathrm{t},1}$ and $V_{\mathrm{t},2}$ is derived in the next step.

Transverse Voltages

To complete the model shown in Fig. 4.2, the transverse voltages at the loads $V_{\mathrm{t},1}$ and $V_{\mathrm{t},2}$ still have to be resolved. Both functions include the transverse electric field as shown in (4.14). For a uniform plane wave, $V_{\mathrm{t},1}$ and $V_{\mathrm{t},2}$ were solved in (3.41) and (3.42) as follows:

$$V_{\mathrm{t},1} \cong 2he_\mathrm{y}E_0(\omega) \tag{4.19}$$

$$V_{\mathrm{t},2} \cong V_{\mathrm{t}1}\mathrm{e}^{-\mathrm{j}\beta_\mathrm{z}\mathcal{L}}. \tag{4.20}$$

The function $V_{\mathrm{t},1}$ consists of a simple multiplication that can be implemented directly in SPICE environment. After inserting β_z from (3.33) into (4.20), $V_{\mathrm{t},2}$ is converted into the time domain as follows:

$$V_{\mathrm{t},2} = V_{\mathrm{t},1}\left(t - \frac{\overbrace{\cos(\theta)\mathcal{L}}^{T_\mathrm{do2}}}{v_0}\right). \tag{4.21}$$

The function $V_{\mathrm{t},2}$ is delayed with T_do2. It can be represented in SPICE as a voltage source $V_{\mathrm{t},1}$ feeding a matched transmission line with the time delay T_do2, as shown in Fig. 4.4. The response of this circuit can be integrated directly into Fig. 4.2 so that the model is completed and ready for simulations.

Next, the developed model is validated in the time and frequency domain.

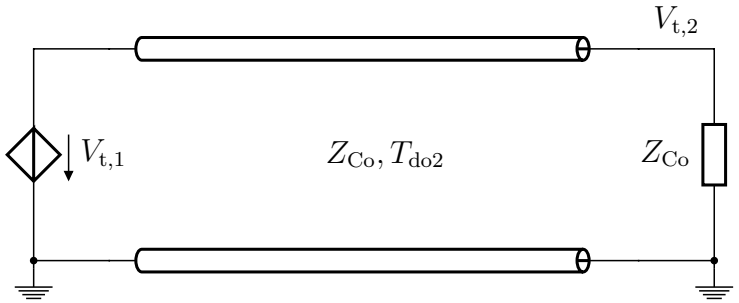

Figure 4.4: Equivalent circuit diagram for the transverse voltage $V_{t,2}(t)$.

4.1.3 Model Validation

The developed lumped-circuit model of the shielded cable was implemented in the SPICE-based simulator LTspice [35]. The transformation networks from Fig. 4.2 were created directly in LTspice. In contrast, a netlist was created with MATLAB [68] and then transferred to LTspice to represent the cascaded model of the shielded cable in between. A netlist by dividing the cable into 8 sections can be found in Appendix A.1. For validation, the simulation results were compared with those of CST Microwave Studio 2019 [3] in the time and frequency domains. The simulation results of CST were validated with measurements in section 4.2.4, therefore this simulation tool will be used as a comparative reference for the considered cases. A co-simulation is carried out in the CST Microwave Studio to couple the 3D full-wave solver with the circuit solver, as explained in Figs. 3.9 and 3.10. In the settings described there, a shielded cable is used instead of one conductor line, in which the transfer impedance parameters have been entered manually according to (4.1). A PC with an Intel i7-6700 CPU 3:40 GHz and 16 GB RAM installed was used to run the simulation. The computing time of the SPICE model depends on the maximum frequency of interest and the associated number of cells N_s. There was no convergence problem for the developed models in the examples shown below.

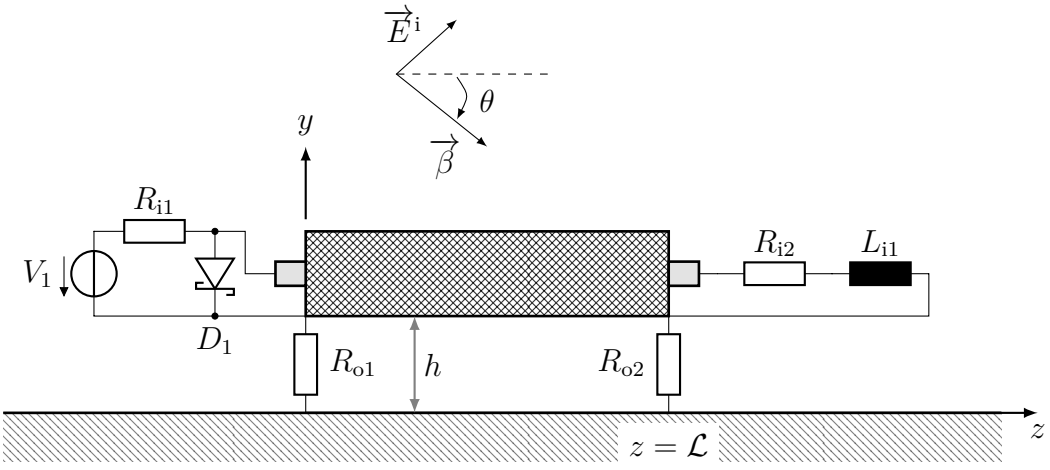

Figure 4.5: Field-coupled shielded cable over a perfectly conducting ground plane.

As shown in Fig. 4.5, a cable of type RG58 with a length of $\mathcal{L} = 2\,\mathrm{m}$ and a height of $h = 1\,\mathrm{cm}$ above the ground plane is used for validation. The primary line constants are $L'_\mathrm{i} = 226.65\,\frac{\mathrm{nH}}{\mathrm{m}}$, $C'_\mathrm{i} = 90.81\,\frac{\mathrm{pF}}{\mathrm{m}}$, $L'_\mathrm{o} = 520.31\,\frac{\mathrm{nH}}{\mathrm{m}}$ and $C'_\mathrm{o} = 21.38\,\frac{\mathrm{pF}}{\mathrm{m}}$. The parameters of the transfer impedance are $R'_\mathrm{t} = 14\,\frac{\mathrm{m\Omega}}{\mathrm{m}}$ and $L'_\mathrm{t} = 1\,\frac{\mathrm{nH}}{\mathrm{m}}$. The inductance coupling coefficient is calculated using (4.10) with $K_\mathrm{n} = -0.0029$.

Time Domain

In the transient analysis, an immunity test is carried out, where a uniform plane wave with $\theta = 45°$ was excited. The electric field of the incident wave has a trapezoidal shape with a magnitude of $50\,\frac{\mathrm{V}}{\mathrm{m}}$. The rise, hold, and fall times are 2 ns, 10 ns and 3 ns, respectively. The component D_1 in Fig. 4.5 is a Schottky diode of the type MBR0520L. The voltage source V_1 is short-circuited for this investigation. The loads at the cable ends are set to $R_\mathrm{i1} = R_\mathrm{i2} = 15\,\Omega$ and $L_\mathrm{i1} = 1\,\mathrm{mH}$. The excitation source has a rise time of 2 ns, which corresponds to $\lambda/10 = 4.4\,\mathrm{cm}$. The cable in Fig. 4.5 should therefore be divided into 46 sections for adequate results. The voltage response of the plane wave across D_1 at $z = 0$ is shown in Fig. 4.6 for a different number of sections.

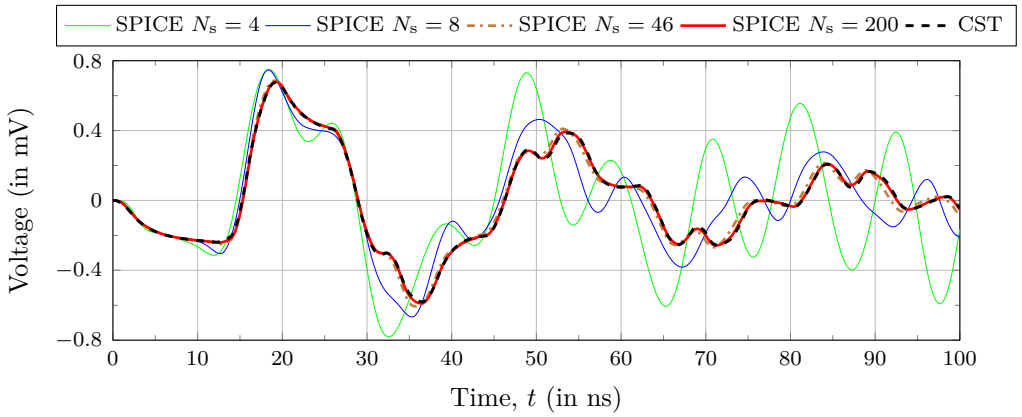

Figure 4.6: Voltage response across D_1 for the lumped-circuit model of a single conductor shielded cable in transient analysis.

For the section length $l_\mathrm{step} \gg \lambda/10$, the deviation is relatively large, as is the case with $N_\mathrm{s} = 4$. For $N_\mathrm{s} = 8$ the deviation becomes smaller and for $N_\mathrm{s} = 46$ the results fit with a small difference. If the number of sections N_s is further increased, the result improves, and thus the calculation time increases. Therefore a very good agreement of the results can be seen for $N_\mathrm{s} = 200$. The simulation time of the SPICE model was 1.7 s for $N_\mathrm{s} = 46$ and 32 s for $N_\mathrm{s} = 200$. In contrast, the simulation time with CST was 3.5 min.

The voltage response of the plane wave at $z = \mathcal{L}$ across R_i2 and L_i1 is shown in Fig. 4.7. Again, a different number of sections is taken into account, whereby a similar effect as before can be observed. The higher the number of sections, the better the results match.

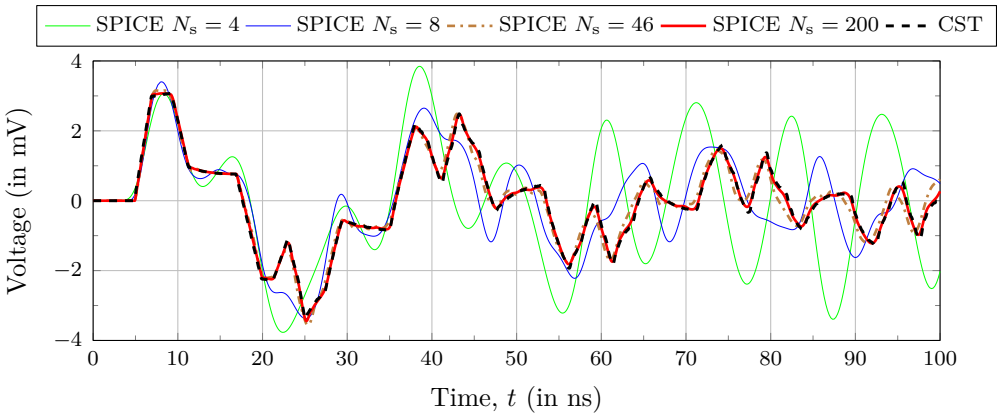

Figure 4.7: Voltage response across R_{i2} and L_{i1} for the lumped-circuit model of a single conductor shielded cable in transient analysis.

The result shows hardly any deviations at $N_s = 200$.

Frequency Domain

In the frequency domain, the coupling from the inner to the outer system was examined. Therefore the voltage source V_1 in Fig. 4.5 is set to 1 V and no field coupling was considered. The diode D_1 was removed in the frequency domain. A frequency sweep with 4000 points between 10 kHz and 500 MHz was carried out in SPICE and CST. The voltage across R_{o2} is shown as magnitude and phase in Fig. 4.8 for a different number of sections. For $N_s = 8$, the result matches at lower frequencies and shows relatively higher deviations at higher frequencies. For $N_s = 200$ the result fits well. The simulation time of the SPICE model was 3.4 s for $N_s = 200$, in contrast to this, CST took 21 s. The resonance behavior at 75 MHz corresponds to that of the outer system due to mismatch. Further results of the model validation are available in [65].

In this section, a lumped-circuit model for a coaxial cable with a braided shield was presented. The model consists of cascaded cells containing lumped elements and controlled sources. The cells of the inner and outer system are coupled via mutual inductance and voltage-controlled sources.

Next, a macromodel derived from the closed-form solution is developed, in which the cable is not divided into segments.

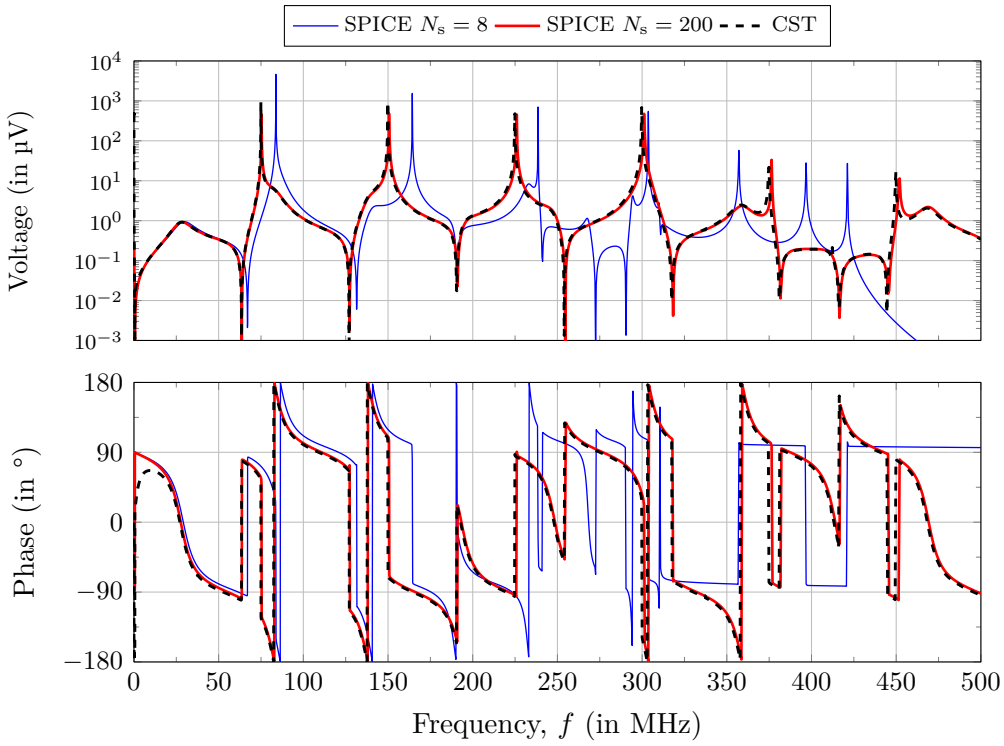

Figure 4.8: Voltage response across R_{o2} for the lumped-circuit model of a single conductor shielded cable in frequency domain.

4.2 Macromodel for the Analysis of Conductive Coupling

In the lumped-circuit model presented above it was shown that the accuracy of the results is improved with a higher number of cascaded cells and thus higher computational effort. This shows the limitations of the model for longer cables and higher frequency of interest. In this section, these problems are addressed by developing a macromodel based on a closed-form solution. A closed-form solution means that the cable is not divided into sections and therefore no cascading processes and no additional elements are required for higher accuracy. Instead of distributed elements, the differential equations of a shielded cable over a ground plane are solved analytically.

The shielded cable above the ground plane in Fig. 4.1 will be considered for the next investigations. Two types of coupling must be taken into account: the field coupling due to the incident plane wave and the conductive coupling. Their influences shall be considered on the inner and outer system. In the case of conductive coupling, the cause of the interference is a lumped source, which is galvanic connected to the cable.

For a constructive structure of this work, which leads to a simpler understanding, it was decided to first develop a macromodel in this section that only takes the conductive coupling into account and to expand the model to include the field coupling in section 4.3. Therefore, in section 4.2.1, the transmission line equations for conductive coupling were

solved. A macromodel for conductive coupling followed in section 4.2.2. In section 4.2.3 the conductive forcing functions were developed. Model validation of conductive coupling was performed in section 4.2.4.

4.2.1 Conductive Coupling Solution

Only conductive coupling is considered in this section, which means that the cause of the disturbance is due to a lumped source rather than an incident wave. An example of conductive coupling is when the voltage source V_1 in Fig. 4.5 is active, the current on the inner side of the shield induces a voltage in the outer system.

Outer System

The conductive coupling in the outer system represents the coupled power via the transfer impedance from the inner system. The index c is used for the conductive coupling. The transmission line equation of the outer system, which considers only the conductive coupling, was derived from Figs. 2.12 and 2.13 in (2.102). It is rewritten here as follows:

$$\frac{\mathrm{d}}{\mathrm{d}z}\begin{bmatrix} V_{\mathrm{oc}}(z) \\ I_{\mathrm{oc}}(z) \end{bmatrix} = \begin{bmatrix} 0 & -\mathrm{j}\omega L'_{\mathrm{o}} \\ -\mathrm{j}\omega C'_{\mathrm{o}} & 0 \end{bmatrix} \cdot \begin{bmatrix} V_{\mathrm{oc}}(z) \\ I_{\mathrm{oc}}(z) \end{bmatrix} + \begin{bmatrix} V'_{\mathrm{doc}}(z) \\ 0 \end{bmatrix}, \tag{4.22}$$

where the transfer admittance Y'_{t} has been ignored. The p.u.l. disturbance voltage $V'_{\mathrm{doc}}(z)$ is given by

$$V'_{\mathrm{doc}}(z) = Z'_{\mathrm{t}} \cdot I_{\mathrm{ic}}(z) = (R'_{\mathrm{t}} + \mathrm{j}\omega L'_{\mathrm{t}}) \cdot I_{\mathrm{ic}}(z), \tag{4.23}$$

where $I_{\mathrm{ic}}(z)$ is the current in the inner system, as shown in Fig. 4.1 without the index c. The voltage and current of the outer system $V_{\mathrm{oc}}(z)$ and $I_{\mathrm{oc}}(z)$ were defined in the same figure. The differential equation in (4.22) is a state-space equation which has the same form as that for the field coupling to one conductor over a ground plane in (3.14). The forcing function $I'_{\mathrm{F}}(z)$ is not included in (4.22) because Y'_{t} has been neglected. To represent the voltage and current waveform at $z = \mathcal{L}$, the derived solution in (3.66) can be adopted here as follows:

$$\begin{bmatrix} V_{\mathrm{oc}}(\mathcal{L}) \\ I_{\mathrm{oc}}(\mathcal{L}) \end{bmatrix} = \mathbf{\Phi_o}(\mathcal{L}) \begin{bmatrix} V_{\mathrm{oc}}(0) \\ I_{\mathrm{oc}}(0) \end{bmatrix} + \begin{bmatrix} V_{\mathrm{ocr}} \\ I_{\mathrm{ocr}} \end{bmatrix}. \tag{4.24}$$

The matrix $\mathbf{\Phi_o}(\mathcal{L})$ represents the chain-parameters of the outer system and is given by

$$\mathbf{\Phi_o}(z) = \begin{bmatrix} \cosh(\gamma_{\mathrm{o}} z) & -Z_{\mathrm{Co}} \cdot \sinh(\gamma_{\mathrm{o}} z) \\ -\frac{\sinh(\gamma_{\mathrm{o}} z)}{Z_{\mathrm{Co}}} & \cosh(\gamma_{\mathrm{o}} z) \end{bmatrix}. \tag{4.25}$$

The element Z_{Co} is the characteristic impedance of the outer system, defined as

$$Z_{\mathrm{Co}} = \sqrt{\frac{L'_{\mathrm{o}}}{C'_{\mathrm{o}}}}. \tag{4.26}$$

The forcing functions V_{ocr} and I_{ocr} are calculated according to (3.68), where

$$\begin{bmatrix} V_{\mathrm{ocr}} \\ I_{\mathrm{ocr}} \end{bmatrix} = \int_0^{\mathcal{L}} \begin{bmatrix} \Phi_{\mathrm{o}11}(\mathcal{L}-z) \cdot Z'_{\mathrm{t}} \cdot I_{\mathrm{ic}}(z) \\ \Phi_{\mathrm{o}21}(\mathcal{L}-z) \cdot Z'_{\mathrm{t}} \cdot I_{\mathrm{ic}}(z) \end{bmatrix} \mathrm{d}z. \tag{4.27}$$

The solution in (4.27) is the integral from 0 to $\mathcal{L}$ of the convolution of $V'_{\mathrm{do}}(z)$ with the chain-parameters so that the distributed voltages $V'_{\mathrm{doc}}(z)$ are summed up to represent the final solution at the loads.

In a similar step to (3.69), the solution at $z = 0$ can be solved by multiplying $\mathbf{\Phi_o}(-\mathcal{L})$ by (4.24). After rearranging the equation, it becomes

$$\begin{bmatrix} V_{\mathrm{oc}}(0) \\ I_{\mathrm{oc}}(0) \end{bmatrix} = \mathbf{\Phi_o}(-\mathcal{L}) \begin{bmatrix} V_{\mathrm{oc}}(\mathcal{L}) \\ I_{\mathrm{oc}}(\mathcal{L}) \end{bmatrix} + \begin{bmatrix} V_{\mathrm{ocl}} \\ I_{\mathrm{ocl}} \end{bmatrix}, \tag{4.28}$$

where

$$\begin{bmatrix} V_{\mathrm{ocl}} \\ I_{\mathrm{ocl}} \end{bmatrix} = -\int_0^{\mathcal{L}} \begin{bmatrix} \Phi_{\mathrm{o}11}(-z) \cdot Z'_{\mathrm{t}} \cdot I_{\mathrm{ic}}(z) \\ \Phi_{\mathrm{o}21}(-z) \cdot Z'_{\mathrm{t}} \cdot I_{\mathrm{ic}}(z) \end{bmatrix} \mathrm{d}z. \tag{4.29}$$

The solutions in (4.24) and (4.28) represent the outer system as two ports with the interference voltages V_{ocr}, V_{ocl} and the interference currents I_{ocr}, I_{ocl} calculated for the whole cable length and added at its ends. The chain-parameters in (4.25) are those of a transmission line with the characteristic impedance Z_{Co} as defined in (4.26).

Based on (4.24) and (4.28), the circuit model of the outer system was created in the lower part of Fig. 4.9. It is simply interpreted as a transmission line. Controlled sources are connected to the ends of the line containing the forcing functions, as shown later. The voltages and currents $V_{\mathrm{oc}}(0)$, $V_{\mathrm{oc}}(\mathcal{L})$, $I_{\mathrm{oc}}(0)$ and $I_{\mathrm{oc}}(\mathcal{L})$ in (4.24) and (4.28) can be compared in Figs. 4.1 and 4.9. The one-way time delay of the outer system T_{o} in Fig. 4.9 is given by

$$T_{\mathrm{o}} = \frac{\mathcal{L}}{v_0} \cdot \sqrt{\varepsilon_{\mathrm{ro}}}, \tag{4.30}$$

where $\varepsilon_{\mathrm{ro}}$ is the dielectric constant of the outer system and v_0 is the speed of light in vacuum.

Next, the conductive coupling in the inner system is considered.

Inner System

The differential equation of the inner system was derived from Figs. 2.12 and 2.13 in (2.100) and (4.4) and is rewritten here for the conductive coupling as follows:

$$\frac{\mathrm{d}}{\mathrm{d}z}\begin{bmatrix} V_{\mathrm{ic}}(z) \\ I_{\mathrm{ic}}(z) \end{bmatrix} = \begin{bmatrix} 0 & -\mathrm{j}\omega L'_{\mathrm{i}} \\ -\mathrm{j}\omega C'_{\mathrm{i}} & 0 \end{bmatrix} \begin{bmatrix} V_{\mathrm{ic}}(z) \\ I_{\mathrm{ic}}(z) \end{bmatrix} + \begin{bmatrix} V'_{\mathrm{dic}}(z) \\ 0 \end{bmatrix}, \tag{4.31}$$

where

$$V'_{\mathrm{dic}}(z) = Z'_{\mathrm{t}} \cdot I_{\mathrm{oc}}(z) = (R'_{\mathrm{t}} + \mathrm{j}\omega L'_{\mathrm{t}}) \cdot I_{\mathrm{oc}}(z). \tag{4.32}$$

The voltage $V_{\mathrm{ic}}(z)$ and the current $I_{\mathrm{ic}}(z)$ are those of the inner system, as defined in Fig. 4.1 without the c notation. The element $V'_{\mathrm{dic}}(z)$ is the p.u.l. disturbance voltage in the inner system.

The solution of the differential equation (4.31) for $z = \mathcal{L}$ is solved analogously to (4.24) and represented with the chain-parameter matrix as follows:

$$\begin{bmatrix} V_{\mathrm{ic}}(\mathcal{L}) \\ I_{\mathrm{ic}}(\mathcal{L}) \end{bmatrix} = \mathbf{\Phi_i}(\mathcal{L}) \begin{bmatrix} V_{\mathrm{ic}}(0) \\ I_{\mathrm{ic}}(0) \end{bmatrix} + \begin{bmatrix} V_{\mathrm{icr}} \\ I_{\mathrm{icr}} \end{bmatrix}. \tag{4.33}$$

The chain-parameter matrix $\mathbf{\Phi_i}(\mathcal{L})$ is defined in (4.43), with the propagation constant γ_{i} and the characteristic impedance Z_{Ci}. The conductive forcing functions V_{icr} and I_{icr} at $z = \mathcal{L}$ are calculated according to (3.68) with

$$\begin{bmatrix} V_{\mathrm{icr}} \\ I_{\mathrm{icr}} \end{bmatrix} = \int_0^{\mathcal{L}} \begin{bmatrix} \Phi_{\mathrm{i}11}(\mathcal{L} - z) \cdot Z'_{\mathrm{t}} \cdot I_{\mathrm{oc}}(z) \\ \Phi_{\mathrm{i}21}(\mathcal{L} - z) \cdot Z'_{\mathrm{t}} \cdot I_{\mathrm{oc}}(z) \end{bmatrix} \mathrm{d}z. \tag{4.34}$$

Analogous to (4.28), the solution at $z = 0$ can be solved by multiplying (4.33) by $\mathbf{\Phi_i}(-\mathcal{L})$ and rearranging it as follows:

$$\begin{bmatrix} V_{\mathrm{ic}}(0) \\ I_{\mathrm{ic}}(0) \end{bmatrix} = \mathbf{\Phi_i}(-\mathcal{L}) \begin{bmatrix} V_{\mathrm{ic}}(\mathcal{L}) \\ I_{\mathrm{ic}}(\mathcal{L}) \end{bmatrix} + \begin{bmatrix} V_{\mathrm{icl}} \\ I_{\mathrm{icl}} \end{bmatrix}, \tag{4.35}$$

where the conductive forcing functions at $z = 0$ are defined as

$$\begin{bmatrix} V_{\mathrm{icl}} \\ I_{\mathrm{icl}} \end{bmatrix} = -\int_0^{\mathcal{L}} \begin{bmatrix} \Phi_{\mathrm{i}11}(-z) \cdot Z'_{\mathrm{t}} \cdot I_{\mathrm{oc}}(z) \\ \Phi_{\mathrm{i}21}(-z) \cdot Z'_{\mathrm{t}} \cdot I_{\mathrm{oc}}(z) \end{bmatrix} \mathrm{d}z. \tag{4.36}$$

It was possible to demonstrate the solution of the inner system as two-port chain-parameters in (4.33) and (4.35). The chain-parameters of these equations are defined in (4.43) and represent a transmission line. This leads to the conclusion that the inner system can be represented as a simple transmission line, as done in the upper part of Fig. 4.9. The forcing functions V_{icl}, V_{icr}, I_{icl} and I_{icr} from (4.33) and (4.35) are added to the controlled sources

at the ends, as shown in the next section. The transmission line of the inner system in Fig. 4.9 has a time delay T_i with

$$T_\mathrm{i} = \frac{\mathcal{L}}{v_0} \cdot \sqrt{\varepsilon_\mathrm{ri}} \tag{4.37}$$

and ε_ri is the dielectric constant of the inner system. The characteristic impedance of the inner system is given by

$$Z_\mathrm{Ci} = \sqrt{\frac{L'_\mathrm{i}}{C'_\mathrm{i}}}. \tag{4.38}$$

Next, the macromodel for the conductive coupling will be described.

4.2.2 Macromodel for Conductive Analyses

In (4.24), (4.28), (4.33) and (4.35) the solution for the outer and inner system of a shielded cable was shown, whereby the macromodel of the cable was interpreted in Fig. 4.9. The forcing functions V_ocr, V_ocl, I_ocr, I_ocl, V_icl, V_icr, I_icl and I_icr in these equations are part of the solution and must be added to the transmission lines. The inclusion methodology for these functions has already been demonstrated in Figs.3.4 and 3.6, where it has been shown that direct galvanic integration leads to a wrong model. This problem was solved in Fig. 3.5, where controlled sources were used. The same approach is used here.
The forcing functions presented for the inner system and the outer system are added to

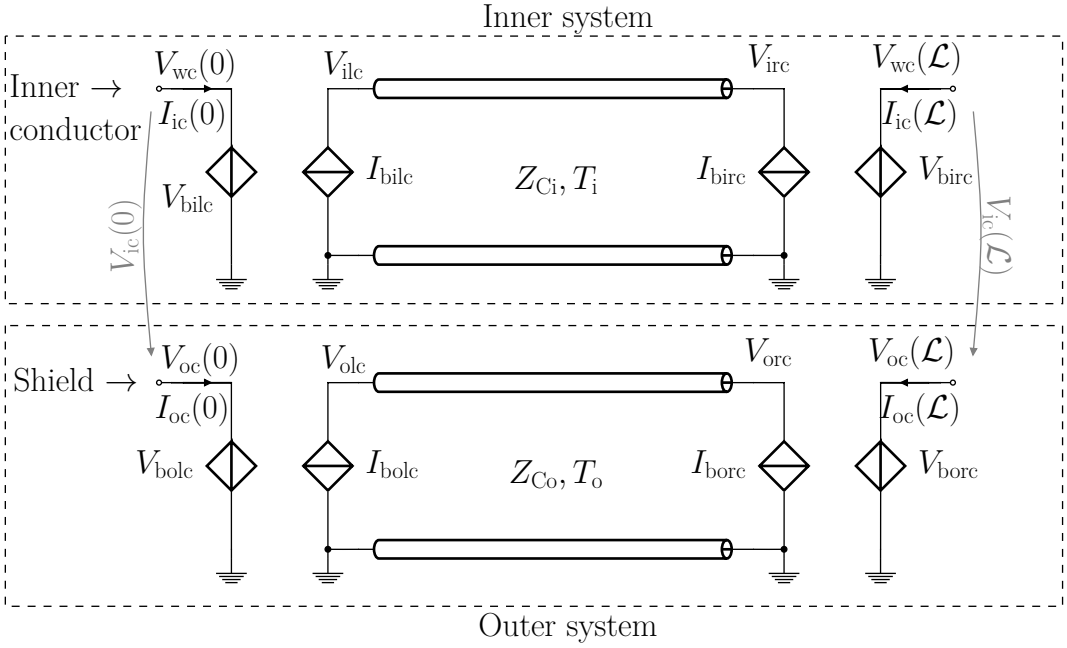

Figure 4.9: Macromodel based on a closed-form solution for conductive analysis of a shielded cable over a perfectly conductive ground plane.

the controlled sources in the macromodel as follows:

$$V_{\mathrm{bilc}} = V_{\mathrm{ilc}} + V_{\mathrm{oc}}(0) + V_{\mathrm{iclT}} \tag{4.39a}$$

$$I_{\mathrm{bilc}} = I_{\mathrm{ic}}(0) + V_{\mathrm{iclT}}/Z_{\mathrm{Ci}} \tag{4.39b}$$

$$V_{\mathrm{birc}} = V_{\mathrm{irc}} + V_{\mathrm{oc}}(\mathcal{L}) + V_{\mathrm{icrT}} \tag{4.39c}$$

$$I_{\mathrm{birc}} = I_{\mathrm{ic}}(\mathcal{L}) + V_{\mathrm{icrT}}/Z_{\mathrm{Ci}}. \tag{4.39d}$$

The index b was used for the behavior sources in Fig. 4.9. The voltage and current forcing functions were combined at the left-hand side using the Thevenin and Norton sources as explained in (3.78) and (3.79). They are given by

$$V_{\mathrm{iclT}} = \frac{1}{2} \cdot \left(V_{\mathrm{icl}} + Z_{\mathrm{Ci}} I_{\mathrm{icl}} \right) \tag{4.40a}$$

$$V_{\mathrm{icrT}} = \frac{1}{2} \cdot \left(V_{\mathrm{icr}} + Z_{\mathrm{Ci}} I_{\mathrm{icr}} \right). \tag{4.40b}$$

Likewise, the controlled sources are defined on the outer system.

$$V_{\mathrm{bolc}} = V_{\mathrm{olc}} + V_{\mathrm{oclT}} \tag{4.41a}$$

$$I_{\mathrm{bolc}} = I_{\mathrm{oc}}(0) + I_{\mathrm{ic}}(0) + V_{\mathrm{oclT}}/Z_{\mathrm{Co}} \tag{4.41b}$$

$$V_{\mathrm{borc}} = V_{\mathrm{orc}} + V_{\mathrm{ocrT}} \tag{4.41c}$$

$$I_{\mathrm{borc}} = I_{\mathrm{oc}}(\mathcal{L}) + I_{\mathrm{ic}}(\mathcal{L}) + V_{\mathrm{ocrT}}/Z_{\mathrm{Co}} \tag{4.41d}$$

The voltage and current forcing functions at the right end are combined using the Thevenin and Norton sources as explained in (3.78) and (3.79).

$$V_{\mathrm{ocrT}} = \frac{1}{2} \cdot \left(V_{\mathrm{ocr}} + Z_{\mathrm{Co}} I_{\mathrm{ocr}} \right) \tag{4.42a}$$

$$V_{\mathrm{oclT}} = \frac{1}{2} \cdot \left(V_{\mathrm{ocl}} + Z_{\mathrm{Co}} I_{\mathrm{ocl}} \right) \tag{4.42b}$$

A good understanding of (4.39) and (4.41) is obtained by comparing the macromodel in Fig. 4.9 with the cable in Figs. 4.1 and 2.3.2. It can be clearly seen that $V_{\mathrm{bilc}} = V_{\mathrm{wc}}(0)$ in (4.39) and in Fig. 4.9 which is the voltage between the inner conductor and the ground plane, and is represented by $V_{\mathrm{w}}(0)$ in Fig 4.1. The voltages $V_{\mathrm{ic}}(0)$ and $V_{\mathrm{ic}}(\mathcal{L})$ in Fig. 4.9 are those between the inner conductor and the shield, as defined in Fig 4.1. The current I_{borc} in (4.41) and in Fig. 4.9 is the same as $I_{\mathrm{g}}(z)$ in Fig. 2.12, which is derived in (2.99). The boundary conditions are included in the macromodel so that it can be connected to arbitrary, including non-linear loads.

The controlled sources of the inner system in (4.39) include V_{iclT} and V_{icrT}, which are functions of V_{icl}, I_{icl}, V_{icr} and I_{icr} in (4.40). The latter functions are directly proportional to the current in the outer system $I_{\mathrm{oc}}(z)$, as defined in (4.34) and (4.36). The conclusion is

that the controlled sources in the inner system are directly proportional to the current of the outer system. A current flow in the outer system $I_{\mathrm{oc}}(z)$ leads to a voltage induction in the controlled sources of the inner system. Thus, the inner and outer systems are coupled in Fig. 4.9.

To run the simulation with this model, the following parameters must be entered: Z_{Ci}, Z_{Co}, $\varepsilon_{\mathrm{ri}}$, $\varepsilon_{\mathrm{ro}}$, R'_{t}, L'_{t}, $\mathcal{L}$ and h. The characteristic impedance Z_{Co} can be calculated with (4.26). That of the inner system Z_{Ci} was defined in (4.38). The primary line constants of the cable can be calculated with (2.29) to (2.32) or by simulation with a static 2D solver. The transfer impedance parameters R'_{t} and L'_{t} can be calculated using (2.116) or they can be measured using one of the methods defined in Figs. 2.14 and 2.16.

An application example is shown in Fig 4.5. To simulate the cable structure there, the voltage source V_1 must be connected between the inner conductor and shield across $V_{\mathrm{ic}}(0)$ in Fig. 4.9. In this case, the induced voltage can be measured via $V_{\mathrm{oc}}(0)$ and $V_{\mathrm{oc}}(\mathcal{L})$ between shield and ground at the left and right ends. Further examples for conductive coupling are presented in section 4.3.4.

So far, a macromodel of a shielded cable could be configured for the conductive analysis. The forcing functions in (4.27), (4.29), (4.34) and (4.36) were included in the controlled sources of the macromodel in (4.39) to (4.42), but these functions are in a form that cannot be solved in a circuit solver such as SPICE. They contain integrals with frequency-dependent parameters. To complete the model, these functions will be solved next and converted into electrical circuits that can be included in the SPICE environment.

4.2.3 Calculation of the Conductive Forcing Functions

The conductive forcing functions in (4.40) and (4.42), which are part of the macromodel shown in Fig.4.9, are solved separately for the inner and outer systems in this section. The analytical solutions are derived and transformed into the time domain to be interpreted as electrical circuits in the SPICE environment.

Outer System

The conductive forcing functions of the outer system defined in (4.27) and (4.29) are first solved. The electric current of the inner system $I_{\mathrm{ic}}(z)$ in (4.27) and (4.29) is unknown and difficult to solve with respect to z. It can be represented by the chain-parameter matrix similar to (2.42) as follows:

$$\begin{bmatrix} V_{\mathrm{ic}}(z) \\ I_{\mathrm{ic}}(z) \end{bmatrix} = \underbrace{\begin{bmatrix} \cosh(\gamma_{\mathrm{i}} z) & -Z_{\mathrm{Ci}} \cdot \sinh(\gamma_{\mathrm{i}} z) \\ -\frac{\sinh(\gamma_{\mathrm{i}} z)}{Z_{\mathrm{Ci}}} & \cosh(\gamma_{\mathrm{i}} z) \end{bmatrix}}_{\boldsymbol{\Phi_{\mathrm{i}}(z)}} \cdot \begin{bmatrix} V_{\mathrm{ic}}(0) \\ I_{\mathrm{ic}}(0) \end{bmatrix}. \tag{4.43}$$

After performing the multiplication in the above equation, the electric current $I_{\mathrm{ic}}(z)$ results in

$$I_{\mathrm{ic}}(z) = \Phi_{\mathrm{i21}}(z)V_{\mathrm{ic}}(0) + \Phi_{\mathrm{i22}}(z)I_{\mathrm{ic}}(0). \tag{4.44}$$

The electrical current $I_{\mathrm{ic}}(0)$ and the voltage $V_{\mathrm{ic}}(0)$ can be represented as a function of $\mathcal{L}$ as follows:

$$\begin{bmatrix} V_{\mathrm{ic}}(0) \\ I_{\mathrm{ic}}(0) \end{bmatrix} = \mathbf{\Phi_i}(-\mathcal{L}) \cdot \begin{bmatrix} V_{\mathrm{ic}}(\mathcal{L}) \\ I_{\mathrm{ic}}(\mathcal{L}) \end{bmatrix}. \tag{4.45}$$

After substituting (4.45) into (4.43), the electric current $I_{\mathrm{ic}}(z)$ is expressed as follows:

$$I_{\mathrm{ic}}(z) = \Phi_{\mathrm{i21}}(z-\mathcal{L}) \cdot V_{\mathrm{ic}}(\mathcal{L}) + \Phi_{\mathrm{i22}}(z-\mathcal{L}) \cdot I_{\mathrm{ic}}(\mathcal{L}). \tag{4.46}$$

The electric current $I_{\mathrm{ic}}(z)$ was deliberately calculated as a function of $V_{\mathrm{ic}}(0)$ and $I_{\mathrm{ic}}(0)$ in (4.44) and later calculated in (4.46) as a function of $V_{\mathrm{ic}}(\mathcal{L})$ and $I_{\mathrm{ic}}(\mathcal{L})$. Both forms of representation are used when calculating the forcing functions. It was found in earlier work that the forcing functions of the outer system at $z = \mathcal{L}$ should be represented as a function of $V_{\mathrm{ic}}(\mathcal{L})$ and $I_{\mathrm{ic}}(\mathcal{L})$, in order to deliver correct results [69]. The same applies to V_{ocl} and I_{ocl} in (4.29), these should be calculated as a function of $V_{\mathrm{ic}}(0)$ and $I_{\mathrm{ic}}(0)$. In other words, the forcing functions on the right-hand side of the outer system should be expressed as a function of the electrical current and the voltage of the inner system on the same side and vice verse. Further details can be found in [69, 70].

Substituting (4.25) and (4.44) into (4.29), the forcing functions at $z = 0$ become

$$V_{\mathrm{ocl}} = \frac{Z'_{\mathrm{t}}V_{\mathrm{ic}}(0)}{Z_{\mathrm{Ci}}} \int_0^{\mathcal{L}} \cosh(\gamma_{\mathrm{o}}z)\sinh(\gamma_{\mathrm{i}}z)\,\mathrm{d}z - Z'_{\mathrm{t}}I_{\mathrm{ic}}(0) \int_0^{\mathcal{L}} \cosh(\gamma_{\mathrm{o}}z)\cosh(\gamma_{\mathrm{i}}z)\,\mathrm{d}z \tag{4.47}$$

$$I_{\mathrm{ocl}} = \frac{Z'_{\mathrm{t}}V_{\mathrm{ic}}(0)}{Z_{\mathrm{Co}}Z_{\mathrm{Ci}}} \int_0^{\mathcal{L}} \sinh(\gamma_{\mathrm{o}}z)\sinh(\gamma_{\mathrm{i}}z)\,\mathrm{d}z - \frac{Z'_{\mathrm{t}}I_{\mathrm{ic}}(0)}{Z_{\mathrm{Co}}} \int_0^{\mathcal{L}} \sinh(\gamma_{\mathrm{o}}z)\cosh(\gamma_{\mathrm{i}}z)\,\mathrm{d}z. \tag{4.48}$$

The parameters Z'_{t} and $V_{\mathrm{ic}}(0)$ were excluded from the integral because they are independent of the position z. By inserting (4.25) and (4.46) into (4.27) the forcing functions at $z = \mathcal{L}$ become

$$V_{\mathrm{ocr}} = -\frac{Z'_{\mathrm{t}}V_{\mathrm{ic}}(\mathcal{L})}{Z_{\mathrm{Ci}}} \int_0^{\mathcal{L}} \cosh(\gamma_{\mathrm{o}}z)\sinh(\gamma_{\mathrm{i}}z)\,\mathrm{d}z + Z'_{\mathrm{t}}I_{\mathrm{ic}}(\mathcal{L}) \int_0^{\mathcal{L}} \cosh(\gamma_{\mathrm{o}}z)\cosh(\gamma_{\mathrm{i}}z)\,\mathrm{d}z \tag{4.49}$$

$$I_{\mathrm{ocr}} = -\frac{Z'_{\mathrm{t}}V_{\mathrm{ic}}(\mathcal{L})}{Z_{\mathrm{Co}}Z_{\mathrm{Ci}}} \int_0^{\mathcal{L}} \sinh(\gamma_{\mathrm{o}}z)\sinh(\gamma_{\mathrm{i}}z)\,\mathrm{d}z + \frac{Z'_{\mathrm{t}}I_{\mathrm{ic}}(\mathcal{L})}{Z_{\mathrm{Co}}} \int_0^{\mathcal{L}} \sinh(\gamma_{\mathrm{o}}z)\cosh(\gamma_{\mathrm{i}}z)\,\mathrm{d}z. \tag{4.50}$$

By comparing V_{ocl} in (4.47) and V_{ocr} in (4.49), one can see that the integral parts have the same functions. The same applies to equations (4.48) and (4.50).

So far, the forcing functions of the outer system were calculated in integral form. These functions in this form with integrals and frequency dependency cannot yet be integrated directly into the SPICE environment. For this purpose, first the integrals are solved analytically and in a further step circuit models of these functions are developed.
After replacing the sinh and cosh functions in (4.47) by their exponential form, the equation becomes

$$\begin{aligned} V_{\mathrm{ocl}}(\mathrm{j}\omega) =& \frac{Z'_{\mathrm{t}} V_{\mathrm{ic}}(0,\mathrm{j}\omega)}{Z_{\mathrm{Ci}}} \int_0^{\mathcal{L}} \frac{\mathrm{e}^{\gamma_{\mathrm{o}} z} + \mathrm{e}^{-\gamma_{\mathrm{o}} z}}{2} \cdot \frac{\mathrm{e}^{\gamma_{\mathrm{i}} z} - \mathrm{e}^{-\gamma_{\mathrm{i}} z}}{2}\,\mathrm{d}z \\ & - Z'_{\mathrm{t}} I_{\mathrm{ic}}(0,\mathrm{j}\omega) \int_0^{\mathcal{L}} \frac{\mathrm{e}^{\gamma_{\mathrm{o}} z} + \mathrm{e}^{-\gamma_{\mathrm{o}} z}}{2} \cdot \frac{\mathrm{e}^{\gamma_{\mathrm{i}} z} + \mathrm{e}^{-\gamma_{\mathrm{i}} z}}{2}\,\mathrm{d}z, \end{aligned} \tag{4.51}$$

where γ_{i} and γ_{o} are the propagation constants of the inner and outer systems. After calculating the integral and arranging the equation in an appropriate form, the following is obtained

$$\begin{aligned} V_{\mathrm{ocl}}(\mathrm{j}\omega) =& \frac{Z'_{\mathrm{t}} \cdot V_{\mathrm{ic}}(0,\mathrm{j}\omega)}{4 Z_{\mathrm{Ci}}} \left[\frac{\mathrm{e}^{\mathcal{L}(\gamma_{\mathrm{i}}+\gamma_{\mathrm{o}})} + \mathrm{e}^{-\mathcal{L}(\gamma_{\mathrm{i}}+\gamma_{\mathrm{o}})} - 2}{\gamma_{\mathrm{i}} + \gamma_{\mathrm{o}}} + \frac{\mathrm{e}^{\mathcal{L}(\gamma_{\mathrm{i}}-\gamma_{\mathrm{o}})} + \mathrm{e}^{-\mathcal{L}(\gamma_{\mathrm{i}}-\gamma_{\mathrm{o}})} - 2}{\gamma_{\mathrm{i}} - \gamma_{\mathrm{o}}} \right] \\ & - \frac{Z'_{\mathrm{t}} \cdot I_{\mathrm{ic}}(0,\mathrm{j}\omega)}{4} \left[\frac{\mathrm{e}^{\mathcal{L}(\gamma_{\mathrm{i}}+\gamma_{\mathrm{o}})} - \mathrm{e}^{-\mathcal{L}(\gamma_{\mathrm{i}}+\gamma_{\mathrm{o}})}}{\gamma_{\mathrm{i}} + \gamma_{\mathrm{o}}} + \frac{\mathrm{e}^{\mathcal{L}(\gamma_{\mathrm{i}}-\gamma_{\mathrm{o}})} - \mathrm{e}^{-\mathcal{L}(\gamma_{\mathrm{i}}-\gamma_{\mathrm{o}})}}{\gamma_{\mathrm{i}} - \gamma_{\mathrm{o}}} \right]. \end{aligned} \tag{4.52}$$

The propagation constants of the inner and outer systems γ_{i} and γ_{o} for a lossless cable can be represented in the following form:

$$\gamma_{\mathrm{i}} = \mathrm{j}\omega \sqrt{L'_{\mathrm{i}} C'_{\mathrm{i}}} = \mathrm{j}\omega \cdot \frac{\sqrt{\varepsilon_{\mathrm{ri}}}}{v_0} = \mathrm{j}\omega \xi_{\mathrm{i}} \tag{4.53}$$

$$\gamma_{\mathrm{o}} = \mathrm{j}\omega \sqrt{L'_{\mathrm{o}} C'_{\mathrm{o}}} = \mathrm{j}\omega \cdot \frac{\sqrt{\varepsilon_{\mathrm{ro}}}}{v_0} = \mathrm{j}\omega \xi_{\mathrm{o}}, \tag{4.54}$$

where the elements ξ_{i} and ξ_{o} are auxiliary parameters and v_0 is the speed of light, as defined before. Substituting (4.53) and (4.54) together with (4.1) in (4.52), the equation becomes

$$\begin{aligned} V_{\mathrm{ocl}}(\mathrm{j}\omega) =& \frac{(R'_{\mathrm{t}} + \mathrm{j}\omega L'_{\mathrm{t}})\, V_{\mathrm{ic}}(0,\mathrm{j}\omega)}{4 Z_{\mathrm{Ci}}} \left[\frac{\mathrm{e}^{-\mathrm{j}\omega\mathcal{L}(\xi_{\mathrm{i}}+\xi_{\mathrm{o}})} + \mathrm{e}^{\mathrm{j}\omega\mathcal{L}(\xi_{\mathrm{i}}+\xi_{\mathrm{o}})} - 2}{\mathrm{j}\omega\,(\xi_{\mathrm{i}} + \xi_{\mathrm{o}})} + \frac{\mathrm{e}^{-\mathrm{j}\omega\mathcal{L}(\xi_{\mathrm{i}}-\xi_{\mathrm{o}})} + \mathrm{e}^{\mathrm{j}\omega\mathcal{L}(\xi_{\mathrm{i}}-\xi_{\mathrm{o}})} - 2}{\mathrm{j}\omega\,(\xi_{\mathrm{i}} - \xi_{\mathrm{o}})} \right] \\ & + \frac{(R'_{\mathrm{t}} + \mathrm{j}\omega L'_{\mathrm{t}})\, I_{\mathrm{ic}}(0,\mathrm{j}\omega)}{4} \left[\frac{\mathrm{e}^{-\mathrm{j}\omega\mathcal{L}(\xi_{\mathrm{i}}+\xi_{\mathrm{o}})} - \mathrm{e}^{\mathrm{j}\omega\mathcal{L}(\xi_{\mathrm{i}}+\xi_{\mathrm{o}})}}{\mathrm{j}\omega\,(\xi_{\mathrm{i}} + \xi_{\mathrm{o}})} + \frac{\mathrm{e}^{-\mathrm{j}\omega\mathcal{L}(\xi_{\mathrm{i}}-\xi_{\mathrm{o}})} - \mathrm{e}^{\mathrm{j}\omega\mathcal{L}(\xi_{\mathrm{i}}-\xi_{\mathrm{o}})}}{\mathrm{j}\omega\,(\xi_{\mathrm{i}} - \xi_{\mathrm{o}})} \right]. \end{aligned} \tag{4.55}$$

Finally, the voltage $V_{\mathrm{ocl}}(\mathrm{j}\omega)$ was solved in the frequency domain in (4.55). This function is difficult to interpret in this form as circuit elements in the SPICE environment, so first a transformation to the time domain is made. The transformation into the time domain

was applied using the time delay approach defined in (3.60) and taking advantage of T_{io} and T_{oi}, where

$$T_{\mathrm{io}} = \mathcal{L}\left(\xi_{\mathrm{i}} + \xi_{\mathrm{o}}\right) \tag{4.56}$$

$$T_{\mathrm{oi}} = \mathcal{L}\left(\xi_{\mathrm{i}} - \xi_{\mathrm{o}}\right). \tag{4.57}$$

In the time domain (4.55) becomes

$$\begin{aligned}
V_{\mathrm{ocl}}(t) = \frac{L'_{\mathrm{t}}}{4Z_{\mathrm{Ci}}\left(\xi_{\mathrm{i}}^2 - \xi_{\mathrm{o}}^2\right)} \Bigg[& \\
& \left(\xi_{\mathrm{i}} - \xi_{\mathrm{o}}\right) \cdot \Bigg(\underbrace{V_{\mathrm{ic}}\left(0, t - T_{\mathrm{io}}\right) + V_{\mathrm{ic}}\left(0, t + T_{\mathrm{io}}\right)}_{v_{\mathrm{i}}} - 2V_{\mathrm{ic}}\left(0, t\right) \Bigg) \\
& + \left(\xi_{\mathrm{i}} + \xi_{\mathrm{o}}\right) \cdot \Bigg(\underbrace{V_{\mathrm{ic}}\left(0, t - T_{\mathrm{oi}}\right) + V_{\mathrm{ic}}\left(0, t + T_{\mathrm{oi}}\right)}_{v_{\mathrm{iii}}} - 2V_{\mathrm{ic}}\left(0, t\right) \Bigg) \Bigg] \\
& + \frac{R'_{\mathrm{t}}}{4Z_{\mathrm{Ci}}\left(\xi_{\mathrm{i}}^2 - \xi_{\mathrm{o}}^2\right)} \Bigg[\\
& \left(\xi_{\mathrm{i}} - \xi_{\mathrm{o}}\right) \cdot \Bigg(\underbrace{\int_0^t \left[V_{\mathrm{ic}}\left(0, \tau - T_{\mathrm{io}}\right) + V_{\mathrm{ic}}\left(0, \tau + T_{\mathrm{io}}\right) \right] \mathrm{d}\tau}_{v_{\mathrm{ii}}} - 2 \underbrace{\int_0^t V_{\mathrm{ic}}\left(0, \tau\right) \mathrm{d}\tau}_{v_{\mathrm{v}}} \Bigg) \\
& + \left(\xi_{\mathrm{i}} + \xi_{\mathrm{o}}\right) \cdot \Bigg(\underbrace{\int_0^t \left[V_{\mathrm{ic}}\left(0, \tau - T_{\mathrm{oi}}\right) + V_{\mathrm{ic}}\left(0, \tau + T_{\mathrm{oi}}\right) \right] \mathrm{d}\tau}_{v_{\mathrm{iv}}} - 2 \underbrace{\int_0^t V_{\mathrm{ic}}\left(0, \tau\right) \mathrm{d}\tau}_{v_{\mathrm{v}}} \Bigg) \Bigg] \\
& + \frac{L'_{\mathrm{t}}}{4\left(\xi_{\mathrm{i}}^2 - \xi_{\mathrm{o}}^2\right)} \Bigg[\\
& \left(\xi_{\mathrm{i}} - \xi_{\mathrm{o}}\right) \cdot \underbrace{\Big(I_{\mathrm{ic}}\left(0, t - T_{\mathrm{io}}\right) - I_{\mathrm{ic}}\left(0, t + T_{\mathrm{io}}\right) \Big)}_{i_{\mathrm{i}}} \\
& + \left(\xi_{\mathrm{i}} + \xi_{\mathrm{o}}\right) \cdot \underbrace{\Big(I_{\mathrm{ic}}\left(0, t - T_{\mathrm{oi}}\right) - I_{\mathrm{ic}}\left(0, t + T_{\mathrm{oi}}\right) \Big)}_{i_{\mathrm{iii}}} \Bigg] \\
+ \frac{R'_{\mathrm{t}}}{4\left(\xi_{\mathrm{i}}^2 - \xi_{\mathrm{o}}^2\right)} \Bigg[& \\
& \left(\xi_{\mathrm{i}} - \xi_{\mathrm{o}}\right) \cdot \underbrace{\int_0^t \left[I_{\mathrm{ic}}\left(0, \tau - T_{\mathrm{io}}\right) - I_{\mathrm{ic}}\left(0, \tau + T_{\mathrm{io}}\right) \right] \mathrm{d}\tau}_{i_{\mathrm{ii}}} \\
& + \left(\xi_{\mathrm{i}} + \xi_{\mathrm{o}}\right) \cdot \underbrace{\int_0^t \left[I_{\mathrm{ic}}\left(0, \tau - T_{\mathrm{oi}}\right) - I_{\mathrm{ic}}\left(0, \tau + T_{\mathrm{oi}}\right) \right] \mathrm{d}\tau}_{i_{\mathrm{iv}}} \Bigg].
\end{aligned} \tag{4.58}$$

The elements $V_{\mathrm{ic}}(0,t)$ and $I_{\mathrm{ic}}(0,t)$ in (4.58) are the voltages and currents at $z = 0$ with respect to the time t. Equation (4.58) exists in a form that can be interpreted as an electrical circuit in the SPICE environment. The voltage v_{i} represents the solution of a transmission line with the time delay T_{io} and a reflection factor Γ_{L} of 1, as shown in (2.47) and (2.51). An equivalent circuit diagram can therefore be derived from Fig. 2.5, in which Z_{L} should be set to a very high value so that the line behaves like an open circuit and $\Gamma_{\mathrm{L}} = 1$. To avoid complex calculations in SPICE with extremely high Z_{L} values, it is possible to convert the circuit in Fig. 2.5 into a simple transmission line with a matched load at the end, fed by a source with no inner impedance. Therefore, the voltage v_{i} was calculated accordingly with a matched TL in Fig. 4.10 (top left) . The voltage response v_{i} can be measured at the end of the line. The voltage v_{iii} in (4.58) has a similar form and therefore the same circuit was also developed in Fig. 4.10. For the sake of simplicity, the characteristic impedance $Z_{\mathrm{c}} = 50\,\Omega$ was chosen for all transmission lines and their loads in Fig. 4.10.

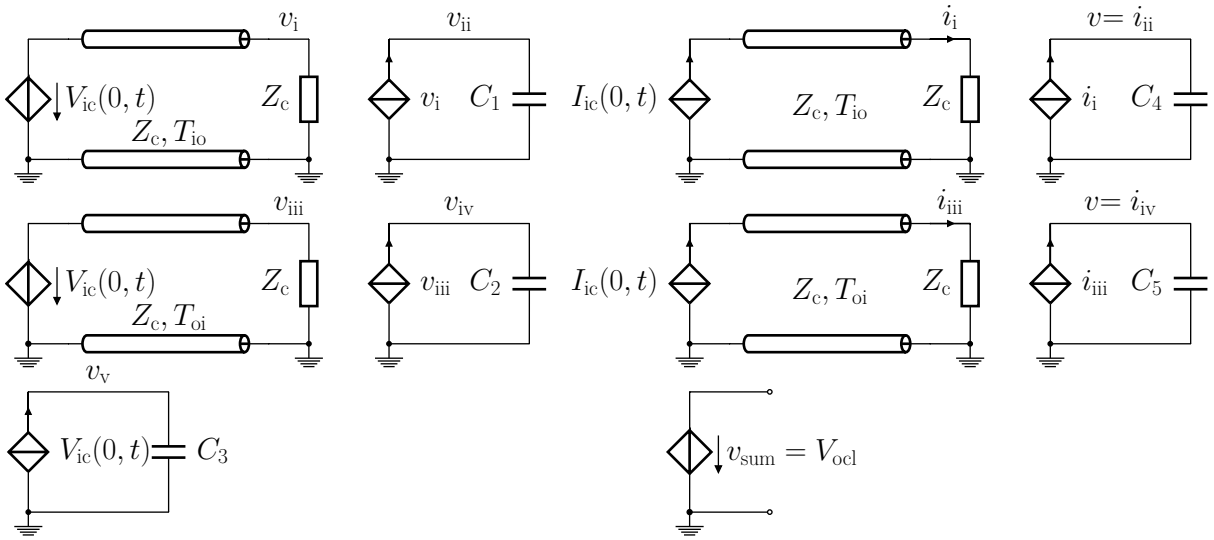

Figure 4.10: Equivalent circuit for the solution of V_{ocl}.

The voltages v_{ii} and v_{iv} in (4.58) are the mathematical integrals of v_{i} and v_{iii}. An integral can be realized in the SPICE environment by calculating the voltage for a given current across a 1 F capacitor or the current for a given voltage through a 1 H inductance. The integrals of v_{ii}, v_{iv} and v_{v} are obtained in Fig. 4.10 by calculating the voltage for a given current across the capacitors C_1, C_2, and C_3, where $C_{1-5} = 1\,\mathrm{F}$.
The electric current i_{i} in (4.58) represents the solution for the current propagation in a transmission line of the time delay T_{io} and a reflection factor Γ_{L} of 1, as explained in (2.48) and (2.53). An equivalent circuit was constructed using a current-controlled current source feeding a matched transmission line in Fig. 4.10. The electric current response at the end of the line is fed into C_4 to represent the integral for i_{ii}. The currents i_{iii} and i_{iv}

are calculated similarly in the circuit. The individual elements calculated so far are added to the voltage-controlled voltage source v_{sum} in Fig. 4.10 to represent the final result. The voltage response v_{sum} can now be inserted directly into the macromodel in Fig. 4.9.

The remaining forcing functions in (4.48), (4.49) and (4.50) have a similar mathematical form as (4.47), with changed parameters, which leads to the same equivalent circuit diagram in Fig. 4.10. In order to avoid redundancies, their SPICE models are not shown in this work.

In this section, the conductive forcing functions of the outer system were solved and an equivalent circuit diagram was developed in Fig. 4.10. Next, the conductive forcing functions of the inner system are discussed.

Inner System

The conductive forcing functions of the inner system presented in (4.34) and (4.36) are solved in this section. Substituting the chain-parameter matrix $\mathbf{\Phi_i}(z)$ from (4.43) together with (4.1) into (4.34) and (4.36), the conductive forcing functions become

$$V_{\mathrm{icl}} = \frac{Z'_{\mathrm{t}} V_{\mathrm{oc}}(0)}{Z_{\mathrm{Co}}} \int_0^{\mathcal{L}} \cosh(\gamma_{\mathrm{i}} z)\sinh(\gamma_{\mathrm{o}} z)\,\mathrm{d}z - Z'_{\mathrm{t}} I_{\mathrm{oc}}(0) \int_0^{\mathcal{L}} \cosh(\gamma_{\mathrm{i}} z)\cosh(\gamma_{\mathrm{o}} z)\,\mathrm{d}z \tag{4.59}$$

$$I_{\mathrm{icl}} = \frac{Z'_{\mathrm{t}} V_{\mathrm{oc}}(0)}{Z_{\mathrm{Ci}} Z_{\mathrm{Co}}} \int_0^{\mathcal{L}} \sinh(\gamma_{\mathrm{i}} z)\sinh(\gamma_{\mathrm{o}} z)\,\mathrm{d}z - \frac{Z'_{\mathrm{t}} I_{\mathrm{oc}}(0)}{Z_{\mathrm{Ci}}} \int_0^{\mathcal{L}} \sinh(\gamma_{\mathrm{i}} z)\cosh(\gamma_{\mathrm{o}} z)\,\mathrm{d}z \tag{4.60}$$

$$V_{\mathrm{icr}} = -\frac{Z'_{\mathrm{t}} V_{\mathrm{oc}}(\mathcal{L})}{Z_{\mathrm{Co}}} \int_0^{\mathcal{L}} \cosh(\gamma_{\mathrm{i}} z)\sinh(\gamma_{\mathrm{o}} z)\,\mathrm{d}z + Z'_{\mathrm{t}} I_{\mathrm{oc}}(\mathcal{L}) \int_0^{\mathcal{L}} \cosh(\gamma_{\mathrm{i}} z)\cosh(\gamma_{\mathrm{o}} z)\,\mathrm{d}z \tag{4.61}$$

$$I_{\mathrm{icr}} = -\frac{Z'_{\mathrm{t}} V_{\mathrm{oc}}(\mathcal{L})}{Z_{\mathrm{Ci}} Z_{\mathrm{Co}}} \int_0^{\mathcal{L}} \sinh(\gamma_{\mathrm{i}} z)\sinh(\gamma_{\mathrm{o}} z)\,\mathrm{d}z + \frac{Z'_{\mathrm{t}} I_{\mathrm{oc}}(\mathcal{L})}{Z_{\mathrm{Ci}}} \int_0^{\mathcal{L}} \sinh(\gamma_{\mathrm{i}} z)\cosh(\gamma_{\mathrm{o}} z)\,\mathrm{d}z. \tag{4.62}$$

Comparing (4.59) to (4.62) with (4.47) to (4.50), it is seen that both systems of equations have the same form. In Fig. 4.10 a circuit model for V_{ocl} was developed. Circuit models can be developed in a similar way for (4.59) to (4.62), but their representation is omitted here for reasons of space and redundancy. In earlier work, a circuit model called V'_{Zin} was developed for V_{icl} in [69].

The presented macromodel in Fig.4.9 is now complete and ready for EMC analysis, eliminating the limited scope of many applications. The conductive forcing functions for the inner and outer system were calculated and equivalent circuits were interpreted. These circuits must be built together with the macromodel in Fig.4.9 in order to perform the simulations of a shielded cable. Evaluation examples can be observed in the next section.

4.2.4 Model Validation of the Conductive Coupling

Field simulations and measurements are carried out for model validation. The field simulations are performed with CST Studio Suite 19 [3] using a co-simulation, where the solver in CST Microwave Studio is combined with the CST Cable Studio harness solver, as described in Figs. 3.9 and 3.10. The simulation of the macromodel from Fig. 4.9 was carried out with LTspice [35]. The PC defined in section 4.1.3 was used for all simulations.

Time Domain

To validate the conductive coupling, measurements were carried out in the time domain, as shown in Fig. 4.11. The cable under test (CUT) was installed 2 cm above a ground plane using insulation material. An RG58 cable with a length of 4.8 m was selected for testing. To simulate the setup shown in Fig. 4.11, the macromodel in Fig. 4.9 was created in LTspice. In Fig. 4.9, R_{CL} was connected between the inner conductor and shield across $V_{\mathrm{ic}}(0)$. An interference voltage source was placed between shield and ground in parallel to V_{bolc}. On the right-hand side, a resistor was set up across $V_{\mathrm{ic}}(\mathcal{L})$ to represent the oscilloscope and R_{SR} in parallel with V_{borc}. The transfer impedance parameters are set to $R'_{\mathrm{t}} = 14\,\frac{\mathrm{m\Omega}}{\mathrm{m}}$ and $L'_{\mathrm{t}} = 1\,\frac{\mathrm{nH}}{\mathrm{m}}$ when simulating this cable. The characteristic impedance of the outer system is 182 Ω. The resistor R_{CL} on the left-hand side of the cable in Fig. 4.11 was set to 50 Ω, which corresponds to the characteristic impedance of the inner system. A waveform signal generator was used to generate an interference voltage between the shield and the ground plane on the left-hand side of the cable in Fig. 4.11. The generator has an internal impedance of 50 Ω. In order to consider this impedance in simulations, an interference source with an internal resistance of 50 Ω was defined in SPICE and CST. A trapezoidal wave of 0/10 V with a rise and fall time of 8 ns was defined. The holding time is 50 ns. The voltage response was measured between the inner conductor and the shield on the right-hand side of the cable using an oscilloscope, as shown in Fig. 4.11. The terminating resistor of the oscilloscope was set to 50 Ω during the measurement. Since the signal generator and the oscilloscope share the same ground, the shield and the

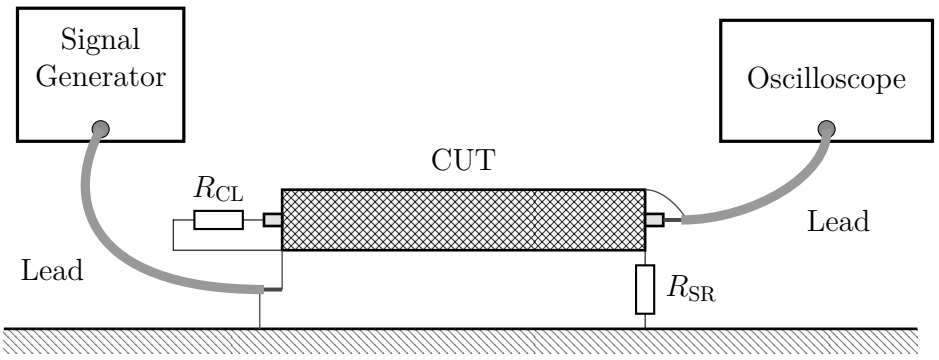

Figure 4.11: Measurement setup in the time domain of a single conductor shielded cable.

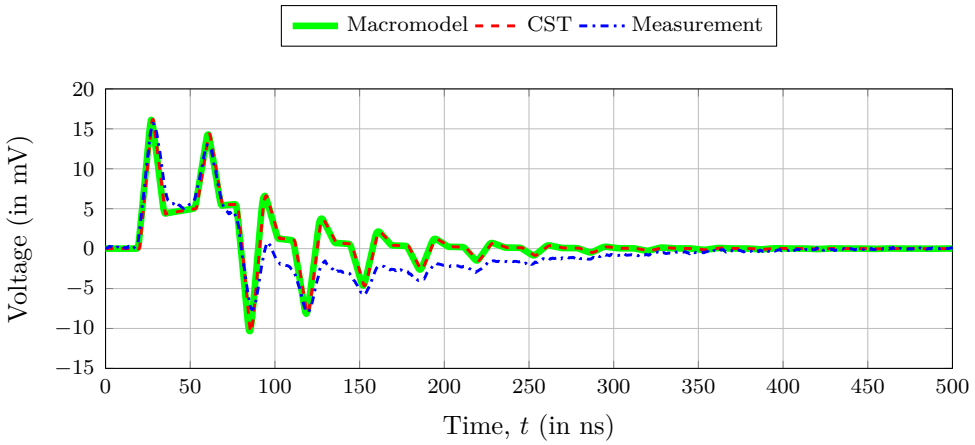

Figure 4.12: Measured voltage response in the transient analysis of the RG58 cable.

ground plane on the right-hand side of the cable were short-circuited. For this reason, the resistance R_{SR} in Fig. 4.11 was set to 10 mΩ in the simulations. The oscilloscope and the signal generator in Fig. 4.11 are connected to the CUT via the measurement cables, so-called leads. To take the influence of the leads into account, transmission lines were included in the simulations that replicate their electrical lengths. The measurement results are shown in Fig. 4.12. They are compared with the simulation results of the macromodel and those of CST. The results agree well with each other. After a few oscillations over time, a certain deviation can be observed. This happens because cable attenuation and radiation losses are not taken into account in the simulation models. The attenuation is caused by ohmic losses including skin effect, eddy currents due to changing magnetic fields and dielectric losses. A slight shift along the curves is due to the difference in the propagation velocity of the waves between the simulation and the real setup. This is due to the imprecisely known electrical properties of the material used in the insulation material of the inner system and the sheath material of the outer system. This effect can be better observed in the results of the frequency domain measurement in Fig. 4.14, where a resonance shift can obviously be seen.

Frequency Domain

The RG58 cable measured in the time domain was also tested in the frequency domain with the setup shown in Fig. 4.13. A vector network analyzer (VNA) was used for the measurement. Port 1 was connected at the left end between wire and shield. Port 2 was connected at the right end between shield and ground.
During the measurement, a 50 Ω terminating resistor was connected between the inner conductor and the shield at the right end. The measuring cables (leads) were calibrated out during the measurement. A frequency sweep between 10 kHz and 500 MHz with 2100 points was performed. The same number of points was also used for the simulations. The feed power in the VNA was set to 10 mW. The transmission parameters S_{12} were measured

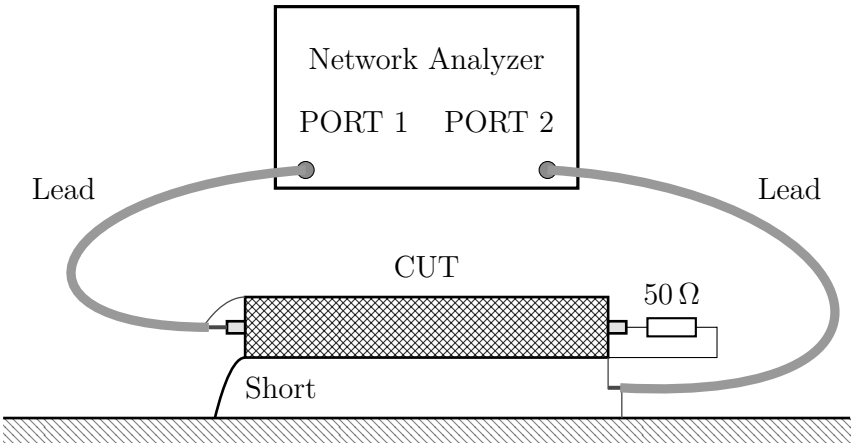

Figure 4.13: Measurement setup in the frequency domain of a single conductor shielded cable.

as shown in Fig. 4.14. The measured results agree well with those of the macromodel and CST. As described above, the simulation models do not take into account the cable losses, which is why an attenuation of the measurement curves over the frequency can be observed. The resonance peaks at higher frequencies show a slight shift over the frequency. As interpreted in the time domain measurement, these deviations may occur due to the imprecisely known electrical properties of the inner insulation material and the sheath material of the measured cable.

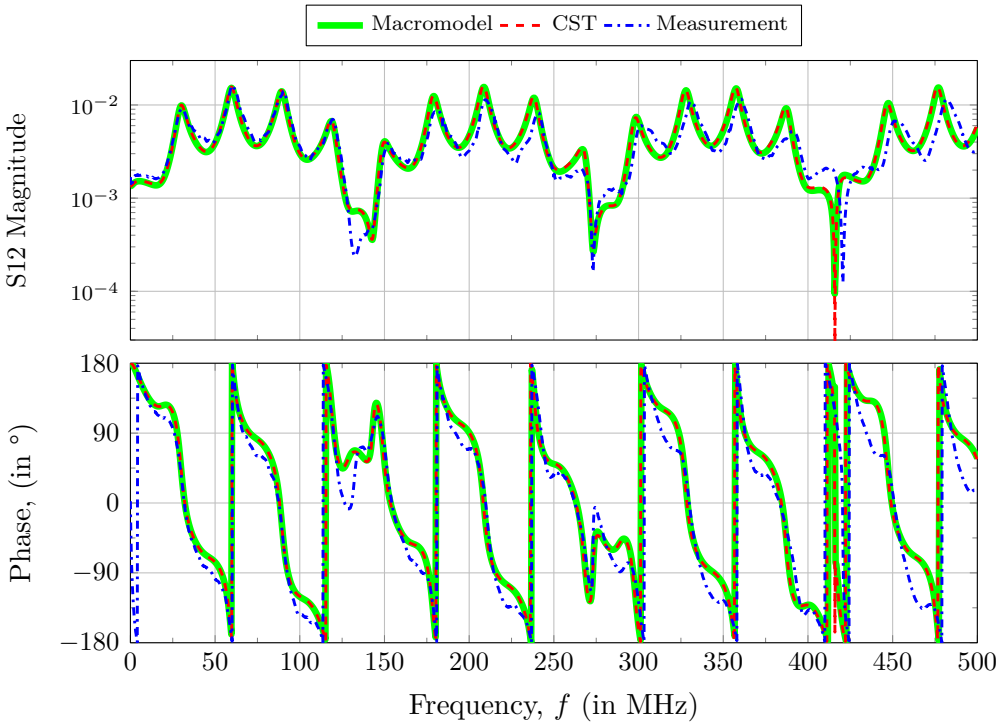

Figure 4.14: Measurement of the transmission coefficient S_{12} for the RG58 cable.

So far, the macromodel of a shielded cable has been developed and validated for conductive coupling. The field coupling will be considered next.

4.3 Macromodel for the Analysis of Field Coupling

The macromodel for the conductive coupling of a single conductor shielded cable was developed in the upper part, where the model was validated with measurements and simulations. Now the field coupling is considered and the model from Fig. 4.9 is extended accordingly using the following steps. The transmission line equations considering the field coupling were solved in section 4.3.1. The macromodel including field coupling was further developed in section 4.3.2. The forcing functions for the field coupling were derived later in section 4.3.3. Model validation of field coupling was performed in section 4.3.4.

4.3.1 Field Coupling Solution

In this section, the field coupling to a shielded cable is extended to the transmission line solutions. Again, the outer and inner systems are considered separately.

Outer System

For field coupling it is assumed that the outer system of the cable in Fig. 4.1 acts as one conductor above a ground plane. The differential equation based on the scattered voltage formulation was defined in (4.12). An analytical solution of the current distribution $I_{\mathrm{ofM}}(z)$ using Green's function was shown in (3.43). It is rewritten here for a line with matched termination loads as follows:

$$I_{\mathrm{ofM}}(z) = I_0 \mathrm{e}^{-\mathrm{j}\beta_{\mathrm{oz}} z} + I_{1\mathrm{M}} \mathrm{e}^{-\mathrm{j}\beta_{\mathrm{o}} z} + I_{2\mathrm{M}} \mathrm{e}^{\mathrm{j}\beta_{\mathrm{o}} z}, \tag{4.63}$$

where

$$I_0 = \frac{2hE_0}{Z_{\mathrm{Co}}} \tag{4.64}$$

$$I_{1\mathrm{M}} = I_0 \mathcal{Q}_{1\mathrm{M}} + \frac{V_{\mathrm{t1}}}{2Z_{\mathrm{Co}}} \tag{4.65}$$

$$I_{2\mathrm{M}} = -I_{1\mathrm{M}} \cdot \mathrm{e}^{-\mathrm{j}(\beta_{\mathrm{o}}+\beta_{\mathrm{oz}})\mathcal{L}} - I_0 \cdot \mathrm{e}^{-\mathrm{j}(\beta_{\mathrm{o}}+\beta_{\mathrm{oz}})\mathcal{L}}. \tag{4.66}$$

The derivation of I_0, $I_{1\mathrm{M}}$ and $I_{2\mathrm{M}}$ is shown in (3.53), (3.48) and (3.54). The voltage behavior at the line ends, taking into account matched termination loads, was shown in

(3.61) and (3.64). It is given by

$$V_{\mathrm{oflM}}(t) = -h\Big[E_0(t) - \underbrace{E_0(t - T_{\mathrm{o}} - T_{\mathrm{oz}})}_{\mathcal{V}_{\mathrm{iii}}}\Big] \tag{4.67}$$

$$V_{\mathrm{ofrM}}(t) = -h\Big[\underbrace{E_0(t - T_{\mathrm{o}})}_{\mathcal{V}_{\mathrm{i}}} - \underbrace{E_0(t - T_{\mathrm{oz}})}_{\mathcal{V}_{\mathrm{ii}}}\Big]. \tag{4.68}$$

The parameters T_{o} and T_{oz} represent the one-way time delay of the outer system and the one-way time delay along the z-axis, respectively. The time delay T_{o} was defined in (4.30). The time delay T_{oz} is given by

$$T_{\mathrm{oz}} = T_{\mathrm{o}} \cdot \cos(\theta). \tag{4.69}$$

The voltages V_{oflM} and V_{ofrM} in (4.67) and (4.68) represent the complete field coupling response of the outer system at $z = 0$ and $z = \mathcal{L}$, respectively. These functions can be simply added to the developed solution in (4.24) and (4.28) as follows:

$$\begin{bmatrix} V_{\mathrm{o}}(\mathcal{L}) \\ I_{\mathrm{o}}(\mathcal{L}) \end{bmatrix} = \mathbf{\Phi_o}(\mathcal{L}) \begin{bmatrix} V_{\mathrm{o}}(0) \\ I_{\mathrm{o}}(0) \end{bmatrix} + \begin{bmatrix} V_{\mathrm{ocr}} + V_{\mathrm{ofrM}} \\ I_{\mathrm{ocr}} \end{bmatrix} \tag{4.70}$$

$$\begin{bmatrix} V_{\mathrm{o}}(0) \\ I_{\mathrm{o}}(0) \end{bmatrix} = \mathbf{\Phi_o}(-\mathcal{L}) \begin{bmatrix} V_{\mathrm{o}}(\mathcal{L}) \\ I_{\mathrm{o}}(\mathcal{L}) \end{bmatrix} + \begin{bmatrix} V_{\mathrm{ocl}} + V_{\mathrm{oflM}} \\ I_{\mathrm{ocl}} \end{bmatrix}. \tag{4.71}$$

The subscript c has been removed from these equations as they are no longer restricted to conductive couplings. The elements $V_{\mathrm{o}}(0)$, $I_{\mathrm{o}}(0)$, $V_{\mathrm{o}}(\mathcal{L})$, $I_{\mathrm{o}}(\mathcal{L})$ represent the voltage and current of the outer system at $z = 0$ and $z = \mathcal{L}$, as shown in Fig. 4.1. The chain-parameter representation in (4.70) and (4.71) shows the complete solution of the outer system including the conductive and field coupling. The form of this equation has hardly changed compared to the conductive solution in (4.24) and (4.28), where only V_{oflM} and V_{ofrM} were added. Under this proof, the outer system of the shielded cable in Fig. 4.15 was further interpreted as TL, with the field forcing functions V_{oflM} and V_{ofrM} added to the controlled sources at the line ends.

So far, the field coupling was integrated into the solutions of the outer system. Next, the field coupling is integrated into the inner system.

Inner System

The differential equation of the inner system, taking the field coupling into account, is rewritten from (4.31) as follows:

$$\frac{\mathrm{d}}{\mathrm{d}z}\begin{bmatrix} V_\mathrm{i}(z) \\ I_\mathrm{i}(z) \end{bmatrix} = \begin{bmatrix} 0 & -\mathrm{j}\omega L'_\mathrm{i} \\ -\mathrm{j}\omega C'_\mathrm{i} & 0 \end{bmatrix} \begin{bmatrix} V_\mathrm{i}(z) \\ I_\mathrm{i}(z) \end{bmatrix} + \begin{bmatrix} V'_\mathrm{di}(z) \\ 0 \end{bmatrix}, \tag{4.72}$$

where

$$V'_\mathrm{di}(z) = Z'_\mathrm{t} \cdot I_\mathrm{o}(z) = Z'_\mathrm{t}\Big(I_\mathrm{ofM}(z) + I_\mathrm{ocf}(z)\Big). \tag{4.73}$$

The current of the outer system $I_\mathrm{o}(z)$ has been divided into two parts, $I_\mathrm{ofM}(z)$ and $I_\mathrm{ocf}(z)$. The element $I_\mathrm{ofM}(z)$ is the current generated on the outer system by field coupling for matched termination loads, as shown in (4.63). The electric current $I_\mathrm{ocf}(z)$ comprises the conductive current $I_\mathrm{oc}(z)$ in the outer system together with the reflection response of the field-coupled current. In Fig. 4.15, a circuit called "Circuit for I_ocf" was created to represent the current $I_\mathrm{ocf}(z)$.
The solution of the differential equation (4.72) for $z = \mathcal{L}$ can be represented with the chain-parameter matrix analogous to (4.33) as follows:

$$\begin{bmatrix} V_\mathrm{i}(\mathcal{L}) \\ I_\mathrm{i}(\mathcal{L}) \end{bmatrix} = \mathbf{\Phi_i}(\mathcal{L}) \begin{bmatrix} V_\mathrm{i}(0) \\ I_\mathrm{i}(0) \end{bmatrix} + \begin{bmatrix} V_\mathrm{icr} + V_\mathrm{ifr} \\ I_\mathrm{icr} + I_\mathrm{ifr} \end{bmatrix}. \tag{4.74}$$

The conductive forcing functions V_icr and I_icr at $z = \mathcal{L}$ have the same form as in (4.34), with the external current being $I_\mathrm{ocf}(z)$, as previously explained.

$$\begin{bmatrix} V_\mathrm{icr} \\ I_\mathrm{icr} \end{bmatrix} = \int_0^{\mathcal{L}} \begin{bmatrix} \Phi_\mathrm{i11}(\mathcal{L}-z) Z'_\mathrm{t} I_\mathrm{ocf}(z) \\ \Phi_\mathrm{i21}(\mathcal{L}-z) Z'_\mathrm{t} I_\mathrm{ocf}(z) \end{bmatrix} \mathrm{d}z \tag{4.75}$$

The field forcing functions V_ifr and I_ifr in (4.74) are defined analogously to (4.34) with the external current being $I_\mathrm{ofM}(z)$.

$$\begin{bmatrix} V_\mathrm{ifr} \\ I_\mathrm{ifr} \end{bmatrix} = \int_0^{\mathcal{L}} \begin{bmatrix} \Phi_\mathrm{i11}(\mathcal{L}-z) Z'_\mathrm{t} I_\mathrm{ofM}(z) \\ \Phi_\mathrm{i21}(\mathcal{L}-z) Z'_\mathrm{t} I_\mathrm{ofM}(z) \end{bmatrix} \mathrm{d}z \tag{4.76}$$

The solution at $z = 0$ can be solved analogously to (4.35) with

$$\begin{bmatrix} V_\mathrm{i}(0) \\ I_\mathrm{i}(0) \end{bmatrix} = \mathbf{\Phi_i}(-\mathcal{L}) \begin{bmatrix} V_\mathrm{i}(\mathcal{L}) \\ I_\mathrm{i}(\mathcal{L}) \end{bmatrix} + \begin{bmatrix} V_\mathrm{icl} + V_\mathrm{ifl} \\ I_\mathrm{icl} + I_\mathrm{ifl} \end{bmatrix}. \tag{4.77}$$

The field forcing functions V_ifl and I_ifl have been added in (4.77) when comparing to (4.35). The conductive forcing functions V_icl and I_icl at $z = 0$ are the same as (4.36), by using

$I_{\mathrm{ocf}}(z)$ instead of $I_{\mathrm{oc}}(z)$.

$$\begin{bmatrix} V_{\mathrm{icl}} \\ I_{\mathrm{icl}} \end{bmatrix} = -\int_0^{\mathcal{L}} \begin{bmatrix} \Phi_{\mathrm{i}11}(-z) Z'_{\mathrm{t}} I_{\mathrm{ocf}}(z) \\ \Phi_{\mathrm{i}21}(-z) Z'_{\mathrm{t}} I_{\mathrm{ocf}}(z) \end{bmatrix} \mathrm{d}z \tag{4.78}$$

The field forcing functions V_{ifl} and I_{ifl} at $z = 0$ are calculated analogously to (4.36), using $I_{\mathrm{ofM}}(z)$ instead of $I_{\mathrm{oc}}(z)$, since $I_{\mathrm{ofM}}(z)$ is the cause of the coupling in this case.

$$\begin{bmatrix} V_{\mathrm{ifl}} \\ I_{\mathrm{ifl}} \end{bmatrix} = -\int_0^{\mathcal{L}} \begin{bmatrix} \Phi_{\mathrm{i}11}(-z) Z'_{\mathrm{t}} I_{\mathrm{ofM}}(z) \\ \Phi_{\mathrm{i}21}(-z) Z'_{\mathrm{t}} I_{\mathrm{ofM}}(z) \end{bmatrix} \mathrm{d}z \tag{4.79}$$

Equations (4.74) and (4.77) represent the complete solution of the inner system including field and conductive coupling. Analogous to section 4.2.2, they can be further interpreted as a TL with the properties of the chain-parameters $\mathbf{\Phi_i}(\mathcal{L})$. In comparison to Fig. 4.9, the circuit model of the inner system was therefore kept unchanged in the macromodel in Fig. 4.15. Only the field forcing functions have been added to the controlled sources, as will be shown later.

So far, the solutions of the inner and outer system of a shielded cable could be represented. Next, the macromodel is developed and explained.

4.3.2 Macromodel with Field Coupling Extension

In Fig. 4.9, the macromodel for a shielded cable was developed for conductive analysis. In this section, this model is extended to include the field coupling of an incident plane wave. The solution for the outer system was presented in (4.70) and (4.71) using the chain-parameter representation which is equivalent to a TL with the forcing functions added. The solution is therefore interpreted as a transmission line in Fig. 4.15, with the forcing functions added to the controlled sources at the ends. The current $I_{\mathrm{ocf}}(z)$ is represented by an additional circuit called "Circuit for I_{ocf}" at the bottom in Fig. 4.15. The current $I_{\mathrm{ocf}}(z)$ comprises the conductive current $I_{\mathrm{oc}}(z)$ in the outer system together with the reflection response of the field-coupled current, as described before. The voltage responses of the field coupling V_{oflM} and V_{ofrM} from (4.67) and (4.68) are therefore not included in this circuit, since they represent the case of a matched line. The boundary conditions are included in the macromodel in Fig. 4.15 so that it can be connected to arbitrary, including non-linear loads.
The inner system of the macromodel in Fig. 4.15 was developed in a form of a TL based on (4.74) and (4.77).

The circuit shown in Fig. 4.15 is the complete macromodel for a shielded cable over a ground plane, which also takes the field coupling into account. A comparison with the model shown in Fig. 4.9 shows that both models have the same structure, with the difference

that the I_{ocf} circuit has been added. The voltages and currents of the macromodel in Fig.4.15 were declared in section 4.2.2. A comparison with Fig. 4.1 shows that the voltage $V_{\mathrm{i}}(0)$ in Fig.4.15 is that between the inner conductor and the shield, $V_{\mathrm{o}}(0)$ is that between the shield and ground, and so on.

The controlled sources in (4.39) are extended by the field coupling as follows:

$$V_{\mathrm{bil}} = V_{\mathrm{il}} + V_{\mathrm{o}}(0) + V_{\mathrm{iclT}} + V_{\mathrm{iflT}} \tag{4.80a}$$

$$I_{\mathrm{bil}} = I_{\mathrm{i}}(0) + (V_{\mathrm{iclT}} + V_{\mathrm{iflT}})/Z_{\mathrm{Ci}} \tag{4.80b}$$

$$V_{\mathrm{bir}} = V_{\mathrm{ir}} + V_{\mathrm{o}}(\mathcal{L}) + V_{\mathrm{icrT}} + V_{\mathrm{ifrT}} \tag{4.80c}$$

$$I_{\mathrm{bir}} = I_{\mathrm{i}}(\mathcal{L}) + (V_{\mathrm{icrT}} + V_{\mathrm{ifrT}})/Z_{\mathrm{Ci}}. \tag{4.80d}$$

The conductive forcing functions V_{iclT} and V_{icrT} were defined in (4.40). The field forcing functions V_{ifr} and I_{ifr} together with V_{ifl} and I_{ifl} were combined into voltage sources using

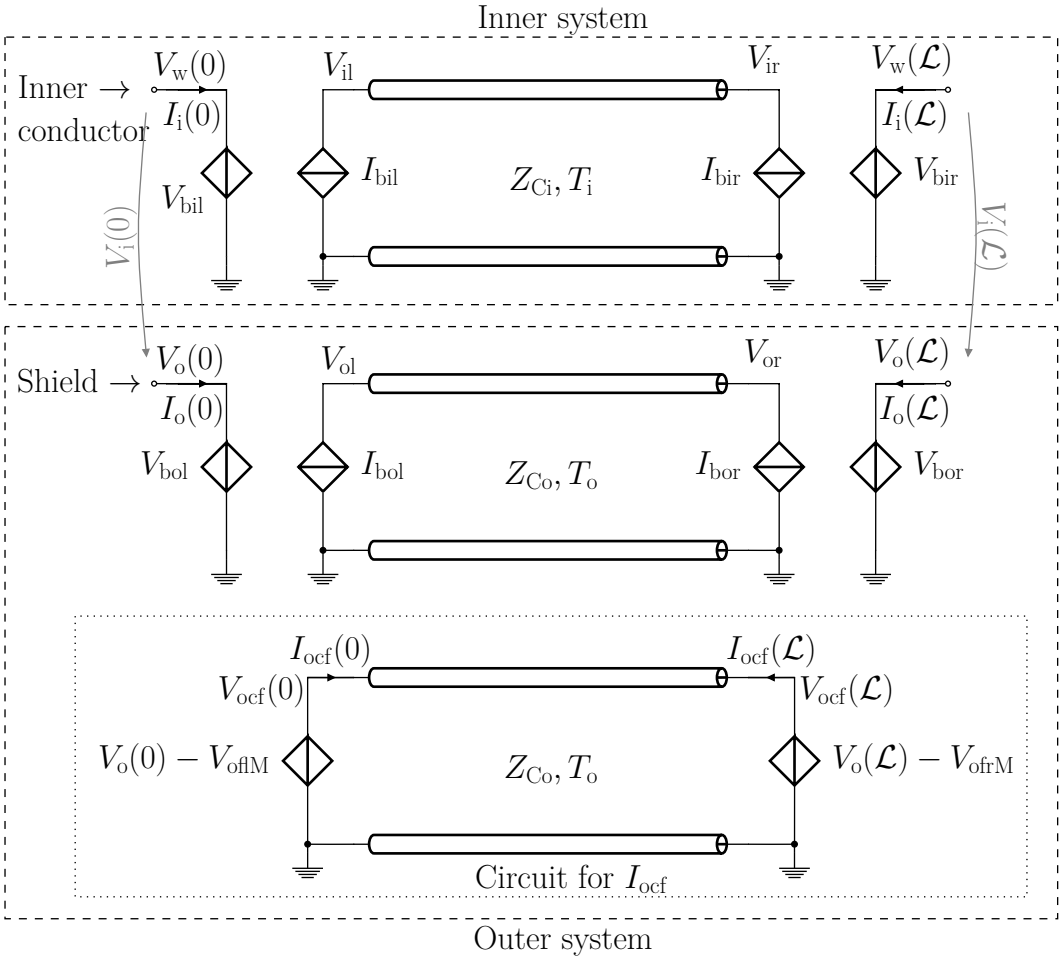

Figure 4.15: Macromodel based on a closed-form solution of a field-coupled shielded cable over a perfectly conductive ground plane.

the Thevenin and Norton sources as explained in (3.78) and (3.79). They are given by

$$V_{\mathrm{ifrT}} = \frac{1}{2} \cdot \left(V_{\mathrm{ifr}} + Z_{\mathrm{Ci}} I_{\mathrm{ifr}} \right) \tag{4.81}$$

$$V_{\mathrm{iflT}} = \frac{1}{2} \cdot \left(V_{\mathrm{ifl}} + Z_{\mathrm{Ci}} I_{\mathrm{ifl}} \right). \tag{4.82}$$

The controlled sources of the outer system in (4.41) are extended by the field coupling sources as follows:

$$V_{\mathrm{bol}} = V_{\mathrm{ol}} + V_{\mathrm{oclT}} + V_{\mathrm{oflM}} \tag{4.83a}$$

$$I_{\mathrm{bol}} = I_{\mathrm{o}}(0) + I_{\mathrm{i}}(0) + (V_{\mathrm{oclT}} + V_{\mathrm{oflM}})/Z_{\mathrm{Co}} \tag{4.83b}$$

$$V_{\mathrm{bor}} = V_{\mathrm{or}} + V_{\mathrm{ocrT}} + V_{\mathrm{ofrM}} \tag{4.83c}$$

$$I_{\mathrm{bor}} = I_{\mathrm{o}}(\mathcal{L}) + I_{\mathrm{i}}(\mathcal{L}) + (V_{\mathrm{ocrT}} + V_{\mathrm{ofrM}})/Z_{\mathrm{Co}}. \tag{4.83d}$$

The forcing functions V_{oclT}, V_{ocrT}, V_{oflM} and V_{ofrM} were defined in (4.42), (4.67) and (4.68), respectively.

To run the model in Fig. 4.15, the following parameters must be entered: Z_{Ci}, Z_{Co}, $\varepsilon_{\mathrm{ri}}$, $\varepsilon_{\mathrm{ro}}$, R'_{t}, L'_{t}, $\mathcal{L}$ and h together with the properties of the incident plane wave. The characteristic impedances Z_{Co} and Z_{Ci} can be calculated with (4.26) and (4.38). As mentioned above, the primary line constants of the cable can be calculated with (2.29) to (2.32) or by simulation with a static 2D solver.
The transfer impedance parameters R'_{t} and L'_{t} must also be added. To execute the model with field coupling, a voltage source must be defined separately, which represents the electric field of the incident plane wave with the designation E_0. The voltage of the source E_0 is contained in (4.67), (4.68) and (4.83), and its coupling behavior can be measured at the terminals of the model in Fig. 4.15. Application examples for conductive and field coupling are presented in section 4.3.4.

It was possible to develop the macromodel of a field-coupled coaxial cable in this section. The model was shown in Fig. 4.15. This model can be used to calculate the voltage response on the loads due to the excitation of a plane wave. The model can also be used for conductive coupling. The conductive forcing functions of the inner system V_{iclT} and V_{icrT} together with those of the outer system V_{oclT}, V_{ocrT} were defined in (4.40) and (4.42), respectively. Circuit models of these functions were developed in section 4.2.3. The field forcing functions V_{ifr}, V_{ifl} in (4.76), (4.79) and V_{oflM}, V_{ofrM} in (4.67), (4.68) are integrated in the controlled sources of the macromodel in (4.80) to (4.83). But these functions still exist in a complex mathematical form that cannot simply be integrated into the SPICE circuit solver. They must first be solved and interpreted as electrical circuits so that they can be integrated. Therefore the field forcing functions are calculated next.

4.3.3 Calculation of the Field Forcing Functions

In (4.80) to (4.83), it was shown that the field forcing functions V_{ifr}, I_{ifr}, V_{oflM}, and V_{ofrM} are part of the macromodel shown in Fig. 4.15. These functions were defined in (4.67), (4.68), (4.76) and (4.79) in an analytical form that cannot be easily integrated into the SPCIE solver. In this section, these functions are solved and circuit models are interpreted from their solutions.

Outer System

The solution of the field coupling to the outer system was solved in (4.67) and (4.68). The solution presented there consists of time delayed electric field components $E_0(t)$. In the SPICE solver, the time delay can be represented by a voltage source $E_0(t)$ feeding a matched transmission. The solutions in (4.67) and (4.68) were therefore represented in SPICE by the circuit shown in Fig. 4.16. The voltage $\mathcal{V}_{\mathrm{i}}$ was modeled by a TL with the time delay T_{o}, as shown in the upper part of Fig. 4.16. The voltages $\mathcal{V}_{\mathrm{ii}}$ and $\mathcal{V}_{\mathrm{iii}}$ with time delays T_{oz} and $T_{\mathrm{o}} + T_{\mathrm{oz}}$ were represented by the second and third TLs. For clarification, the voltages $\mathcal{V}_{\mathrm{i}}$, $\mathcal{V}_{\mathrm{ii}}$ and $\mathcal{V}_{\mathrm{iii}}$ are shown in (4.67), (4.68) and in Fig. 4.16 anyway.

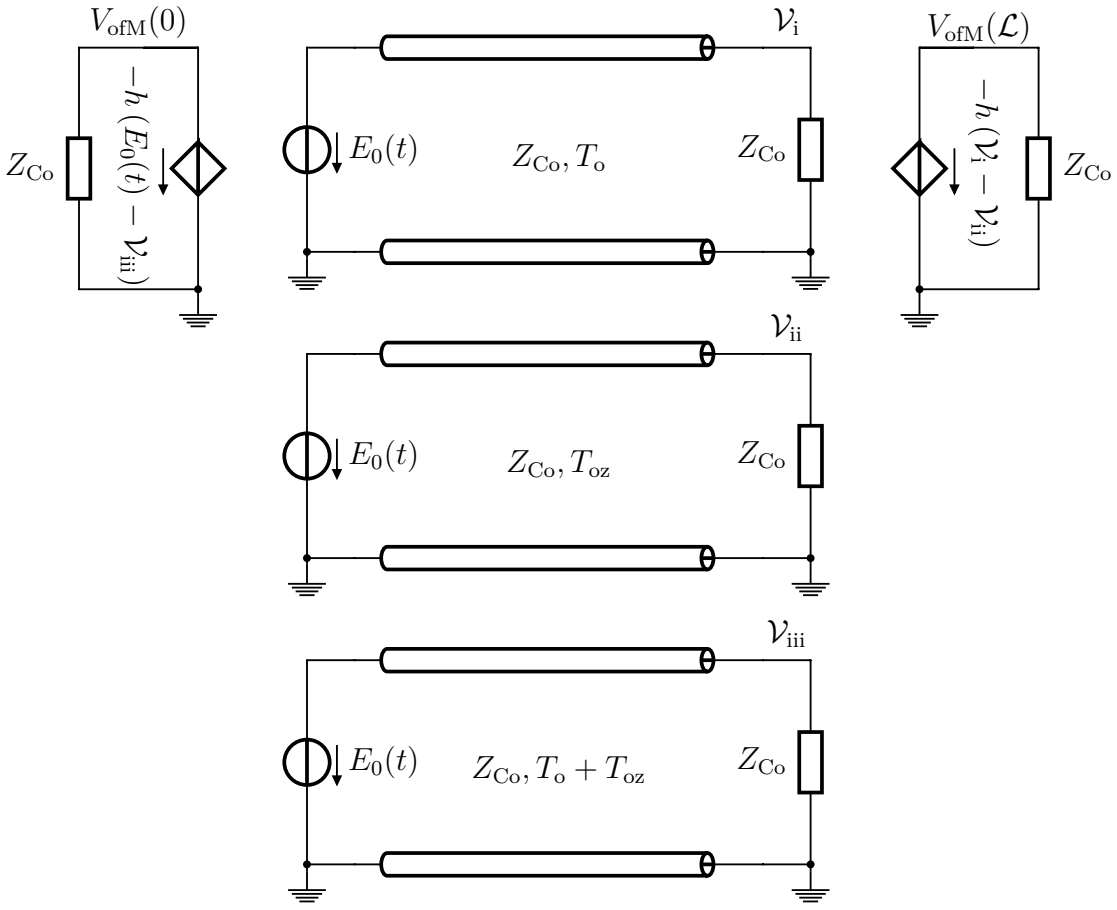

Figure 4.16: Circuit model based on a closed-form solution for calculating the field response at the loads of a shielded cable over a perfectly conducting ground plane.

The controlled sources in Fig. 4.16 are used to sum the elements and apply the mathematical multiplications in (4.67) and (4.68). The circuit presented here was constructed analogously to that of a field-coupled line, as shown in Fig. 3.5.

Inner System

The field forcing functions of the inner system were defined in (4.76) and (4.79). After replacing the sinh and cosh functions in (4.43) with their exponential form and inserting them into (4.76), the voltage V_{ifr} becomes

$$\begin{aligned} V_{\mathrm{ifr}} &= Z'_{\mathrm{t}} \cdot \int_0^{\mathcal{L}} \frac{\mathrm{e}^{\gamma_{\mathrm{i}}(\mathcal{L}-z)} + \mathrm{e}^{-\gamma_{\mathrm{i}}(\mathcal{L}-z)}}{2} \cdot I_{\mathrm{ofM}}(z)\,\mathrm{d}z \\ &= \frac{Z'_{\mathrm{t}}}{2} \cdot \mathrm{e}^{\gamma_{\mathrm{i}}\mathcal{L}} \cdot \int_0^{\mathcal{L}} \mathrm{e}^{-\gamma_{\mathrm{i}}z} \cdot I_{\mathrm{ofM}}(z)\,\mathrm{d}z + \frac{Z'_{\mathrm{t}}}{2} \cdot \mathrm{e}^{-\gamma_{\mathrm{i}}\mathcal{L}} \cdot \int_0^{\mathcal{L}} \mathrm{e}^{\gamma_{\mathrm{i}}z} \cdot I_{\mathrm{ofM}}(z)\,\mathrm{d}z. \end{aligned} \tag{4.84}$$

In the second line of (4.84), $\mathrm{e}^{\gamma_{\mathrm{i}}\mathcal{L}}$ and $\mathrm{e}^{-\gamma_{\mathrm{i}}\mathcal{L}}$ were excluded . Substituting (4.63) for $I_{\mathrm{ofM}}(z)$ and replacing γ_{i} and γ_{o} with the functions in (4.53) and (4.54) that depend on $\sqrt{\varepsilon_{\mathrm{ri}}}$ and $\sqrt{\varepsilon_{\mathrm{ro}}}$, the equation becomes

$$\begin{aligned} V_{\mathrm{ifr}} = {} & \frac{Z'_{\mathrm{t}}}{2}\,\mathrm{e}^{\mathrm{j}\frac{\omega}{v_0}\sqrt{\varepsilon_{\mathrm{ri}}}\mathcal{L}} \cdot \int_0^{\mathcal{L}} \mathrm{e}^{-\mathrm{j}\frac{\omega}{v_0}\sqrt{\varepsilon_{\mathrm{ri}}}z} \left(I_0\,\mathrm{e}^{-\mathrm{j}\frac{\omega}{v_0}\cos(\theta)z} + I_{1\mathrm{M}}\,\mathrm{e}^{-\mathrm{j}\frac{\omega}{v_0}z} + I_{2\mathrm{M}}\,\mathrm{e}^{\mathrm{j}\frac{\omega}{v_0}z} \right) \mathrm{d}z \\ & + \frac{Z'_{\mathrm{t}}}{2}\,\mathrm{e}^{-\mathrm{j}\frac{\omega}{v_0}\sqrt{\varepsilon_{\mathrm{ri}}}\mathcal{L}} \cdot \int_0^{\mathcal{L}} \mathrm{e}^{\mathrm{j}\frac{\omega}{v_0}\sqrt{\varepsilon_{\mathrm{ri}}}z} \left(I_0\,\mathrm{e}^{-\mathrm{j}\frac{\omega}{v_0}\cos(\theta)z} + I_{1\mathrm{M}}\,\mathrm{e}^{-\mathrm{j}\frac{\omega}{v_0}z} + I_{2\mathrm{M}}\,\mathrm{e}^{\mathrm{j}\frac{\omega}{v_0}z} \right) \mathrm{d}z. \end{aligned} \tag{4.85}$$

After calculating the integral, the following equation is obtained

$$\begin{aligned} V_{\mathrm{ifr}} = {} & \frac{Z'_{\mathrm{t}}}{2} \cdot \mathrm{e}^{\mathrm{j}\frac{\omega}{v_0}\sqrt{\varepsilon_{\mathrm{ri}}}\mathcal{L}} \cdot \left[- I_0 \cdot \frac{\mathrm{e}^{-\mathrm{j}\frac{\omega}{v_0}(\sqrt{\varepsilon_{\mathrm{ri}}}+\cos(\theta))\mathcal{L}} - 1}{\mathrm{j}\frac{\omega}{v_0}\left(\sqrt{\varepsilon_{\mathrm{ri}}} + \cos(\theta)\right)} - I_{1\mathrm{M}} \cdot \frac{\mathrm{e}^{-\mathrm{j}\frac{\omega}{v_0}(\sqrt{\varepsilon_{\mathrm{ri}}}+1)\mathcal{L}} - 1}{\mathrm{j}\frac{\omega}{v_0}\left(\sqrt{\varepsilon_{\mathrm{ri}}} + 1\right)} \right. \\ & \left. - I_{2\mathrm{M}} \cdot \frac{\mathrm{e}^{-\mathrm{j}\frac{\omega}{v_0}(\sqrt{\varepsilon_{\mathrm{ri}}}-1)\mathcal{L}} - 1}{\mathrm{j}\frac{\omega}{v_0}\left(\sqrt{\varepsilon_{\mathrm{ri}}} - 1\right)} \right] \\ & + \frac{Z'_{\mathrm{t}}}{2} \cdot \mathrm{e}^{-\mathrm{j}\frac{\omega}{v_0}\sqrt{\varepsilon_{\mathrm{ri}}}\mathcal{L}} \cdot \left[I_0 \cdot \frac{\mathrm{e}^{\mathrm{j}\frac{\omega}{v_0}(\sqrt{\varepsilon_{\mathrm{ri}}}-\cos(\theta))\mathcal{L}} - 1}{\mathrm{j}\frac{\omega}{v_0}\left(\sqrt{\varepsilon_{\mathrm{ri}}} - \cos(\theta)\right)} + I_{1\mathrm{M}} \cdot \frac{\mathrm{e}^{\mathrm{j}\frac{\omega}{v_0}(\sqrt{\varepsilon_{\mathrm{ri}}}-1)\mathcal{L}} - 1}{\mathrm{j}\frac{\omega}{v_0}\left(\sqrt{\varepsilon_{\mathrm{ri}}} - 1\right)} \right. \\ & \left. + I_{2\mathrm{M}} \cdot \frac{\mathrm{e}^{\mathrm{j}\frac{\omega}{v_0}(\sqrt{\varepsilon_{\mathrm{ri}}}+1)\mathcal{L}} - 1}{\mathrm{j}\frac{\omega}{v_0}\left(\sqrt{\varepsilon_{\mathrm{ri}}} + 1\right)} \right]. \end{aligned} \tag{4.86}$$

Performing the same steps for I_{ifr} in (4.76), the equation yields

$$\begin{aligned} I_{\mathrm{ifr}} = \; & \frac{Z'_{\mathrm{t}}}{2Z_{\mathrm{Ci}}} \cdot \mathrm{e}^{\mathrm{j}\frac{\omega}{v_0}\sqrt{\varepsilon_{\mathrm{ri}}}\mathcal{L}} \cdot \Bigg[I_0 \cdot \frac{\mathrm{e}^{-\mathrm{j}\frac{\omega}{v_0}(\sqrt{\varepsilon_{\mathrm{ri}}}+\cos(\theta))\mathcal{L}} - 1}{\mathrm{j}\frac{\omega}{v_0}\left(\sqrt{\varepsilon_{\mathrm{ri}}} + \cos(\theta)\right)} + I_{1\mathrm{M}} \cdot \frac{\mathrm{e}^{-\mathrm{j}\frac{\omega}{v_0}(\sqrt{\varepsilon_{\mathrm{ri}}}+1)\mathcal{L}} - 1}{\mathrm{j}\frac{\omega}{v_0}\left(\sqrt{\varepsilon_{\mathrm{ri}}} + 1\right)} \\ & + I_{2\mathrm{M}} \cdot \frac{\mathrm{e}^{-\mathrm{j}\frac{\omega}{v_0}(\sqrt{\varepsilon_{\mathrm{ri}}}-1)\mathcal{L}} - 1}{\mathrm{j}\frac{\omega}{v_0}\left(\sqrt{\varepsilon_{\mathrm{ri}}} - 1\right)} \Bigg] \\ & + \frac{Z'_{\mathrm{t}}}{2Z_{\mathrm{Ci}}} \cdot \mathrm{e}^{-\mathrm{j}\frac{\omega}{v_0}\sqrt{\varepsilon_{\mathrm{ri}}}\mathcal{L}} \cdot \Bigg[I_0 \cdot \frac{\mathrm{e}^{\mathrm{j}\frac{\omega}{v_0}(\sqrt{\varepsilon_{\mathrm{ri}}}-\cos(\theta))\mathcal{L}} - 1}{\mathrm{j}\frac{\omega}{v_0}\left(\sqrt{\varepsilon_{\mathrm{ri}}} - \cos(\theta)\right)} + I_{1\mathrm{M}} \cdot \frac{\mathrm{e}^{\mathrm{j}\frac{\omega}{v_0}(\sqrt{\varepsilon_{\mathrm{ri}}}-1)\mathcal{L}} - 1}{\mathrm{j}\frac{\omega}{v_0}\left(\sqrt{\varepsilon_{\mathrm{ri}}} - 1\right)} \\ & + I_{2\mathrm{M}} \cdot \frac{\mathrm{e}^{\mathrm{j}\frac{\omega}{v_0}(\sqrt{\varepsilon_{\mathrm{ri}}}+1)\mathcal{L}} - 1}{\mathrm{j}\frac{\omega}{v_0}\left(\sqrt{\varepsilon_{\mathrm{ri}}} + 1\right)} \Bigg]. \end{aligned} \tag{4.87}$$

The two functions V_{ifr} and I_{ifr} should be added on the right-hand side of the inner system in order to take the field coupling into account. A similar step was taken when modeling the field coupling on a single line in Fig. 3.6. It was shown that the current and voltage sources $I_{\mathrm{FT}}(\mathcal{L},\omega)$ and $V_{\mathrm{FT}}(\mathcal{L},\omega)$ can be combined as a single voltage source in Fig. 3.7 . This simplification is now used, where (3.78) is applied to (4.86) and (4.87), resulting in

$$\begin{aligned} V_{\mathrm{ifrT}}(\mathrm{j}\omega) &= \frac{1}{2} \cdot \left(V_{\mathrm{ifr}} + Z_{\mathrm{Ci}} I_{\mathrm{ifr}}\right) \\ &= \frac{Z'_{\mathrm{t}}}{2}\Bigg[- I_0 \frac{\mathrm{e}^{-\mathrm{j}\omega\mathcal{L}\frac{\sqrt{\varepsilon_{\mathrm{ri}}}}{v_0}} - \mathrm{e}^{-\mathrm{j}\omega\mathcal{L}\frac{\cos(\theta)}{v_0}}}{\mathrm{j}\omega\left(\frac{\sqrt{\varepsilon_{\mathrm{ri}}}-\cos(\theta)}{v_0}\right)} - I_{1\mathrm{M}} \frac{\mathrm{e}^{-\mathrm{j}\omega\mathcal{L}\frac{\sqrt{\varepsilon_{\mathrm{ri}}}}{v_0}} - \mathrm{e}^{-\mathrm{j}\omega\frac{\mathcal{L}}{v_0}}}{\mathrm{j}\omega\left(\frac{\sqrt{\varepsilon_{\mathrm{ri}}}-1}{v_0}\right)} \\ &\quad + (I_0 + I_1) \frac{\mathrm{e}^{-\mathrm{j}\omega\mathcal{L}\left(\frac{\sqrt{\varepsilon_{\mathrm{ri}}}+\cos(\theta)+1}{v_0}\right)} - \mathrm{e}^{-\mathrm{j}\omega\mathcal{L}\frac{\cos(\theta)}{v_0}}}{\mathrm{j}\omega\left(\frac{\sqrt{\varepsilon_{\mathrm{ri}}}+1}{v_0}\right)} \Bigg]. \end{aligned} \tag{4.88}$$

Equation (4.88) represents the solution of V_{ifrT} in the frequency domain, but this equation cannot yet be interpreted as an electrical circuit. It is therefore transformed into the time domain using the time delay approach in (3.60)

$$\begin{aligned} & V_{\mathrm{ifrT}}(t) = \\ & \Delta_1 \cdot \Bigg\{ L'_{\mathrm{t}} \Big(\underbrace{E_0(t - T_{\mathrm{i1}})}_{v_{\mathrm{i}}} - \underbrace{E_0(t - T_{\mathrm{i2}})}_{v_{\mathrm{ii}}} \Big) + R'_{\mathrm{t}} \underbrace{\int_0^t \Big(E_0(\tau - T_{\mathrm{i1}}) - E_0(\tau - T_{\mathrm{i2}}) \Big)\, \mathrm{d}\tau}_{v_{\mathrm{iii}}} \Bigg\} \\ & + \Delta_2 \cdot \Bigg\{ L'_{\mathrm{t}} \Big(\underbrace{E_0(t - T_{\mathrm{i3}})}_{v_{\mathrm{iv}}=v_{\mathrm{i}}} - \underbrace{E_0(t - T_{\mathrm{i4}})}_{v_{\mathrm{v}}} \Big) + R'_{\mathrm{t}} \underbrace{\int_0^t \Big(E_0(\tau - T_{\mathrm{i3}}) - E_0(\tau - T_{\mathrm{i4}}) \Big)\, \mathrm{d}\tau}_{v_{\mathrm{vi}}} \Bigg\} \\ & + \Delta_3 \cdot \Bigg\{ L'_{\mathrm{t}} \Big(\underbrace{E_0(t - T_{\mathrm{i5}})}_{v_{\mathrm{vii}}} - \underbrace{E_0(t - T_{\mathrm{i6}})}_{v_{\mathrm{viii}}=v_{\mathrm{ii}}} \Big) + R'_{\mathrm{t}} \underbrace{\int_0^t \Big(E_0(\tau - T_{\mathrm{i5}}) - E_0(\tau - T_{\mathrm{i6}}) \Big)\, \mathrm{d}\tau}_{v_{\mathrm{ix}}} \Bigg\}, \end{aligned} \tag{4.89}$$

where

$$\begin{aligned}
\Delta_1 &= -\frac{h \cdot v_0}{Z_{\mathrm{Co}}\left(\sqrt{\varepsilon_{\mathrm{ri}}} - \cos(\theta)\right)} \\
\Delta_2 &= -\frac{h \cdot v_0 \cdot \left(\mathcal{Q}_{1\mathrm{M}} + \cos(\theta)/2\right)}{Z_{\mathrm{Co}}\left(\sqrt{\varepsilon_{\mathrm{ri}}} - 1\right)} \\
\Delta_3 &= \frac{h \cdot v_0 \cdot \left(\mathcal{Q}_{1\mathrm{M}} + 1 + \cos(\theta)/2\right)}{Z_{\mathrm{Co}}\left(\sqrt{\varepsilon_{\mathrm{ri}}} + 1\right)} \\
T_{\mathrm{i}1} = T_{\mathrm{i}3} &= \mathcal{L}\frac{\sqrt{\varepsilon_{\mathrm{ri}}}}{v_0},\ T_{\mathrm{i}2} = T_{\mathrm{i}6} = \mathcal{L}\frac{\cos(\theta)}{v_0} \\
T_{\mathrm{i}4} &= \frac{\mathcal{L}}{v_0} \text{ and } T_{\mathrm{i}5} = \frac{\mathcal{L}}{v_0}\left(\sqrt{\varepsilon_{\mathrm{ri}}} + \cos(\theta) + 1\right).
\end{aligned} \tag{4.90}$$

The parameter $\mathcal{Q}_{1\mathrm{M}}$ is given in (3.50). The solution of V_{ifrT} in (4.89) exists in a form that can be used to extract a circuit model in the SPICE environment. The time-delayed electric field components are implemented in Fig. 4.17 with an adapted transmission line. The integrals are calculated by feeding a current into a 1 F capacitor using a controlled-voltage current source. Similar steps of the developed model were shown in earlier work in [61].

The field-coupling response on the left-hand side of the inner system in Fig. 4.1, at $z = 0$, can be derived from (4.79) using similar steps as in (4.84) to (4.89). It is given in the time

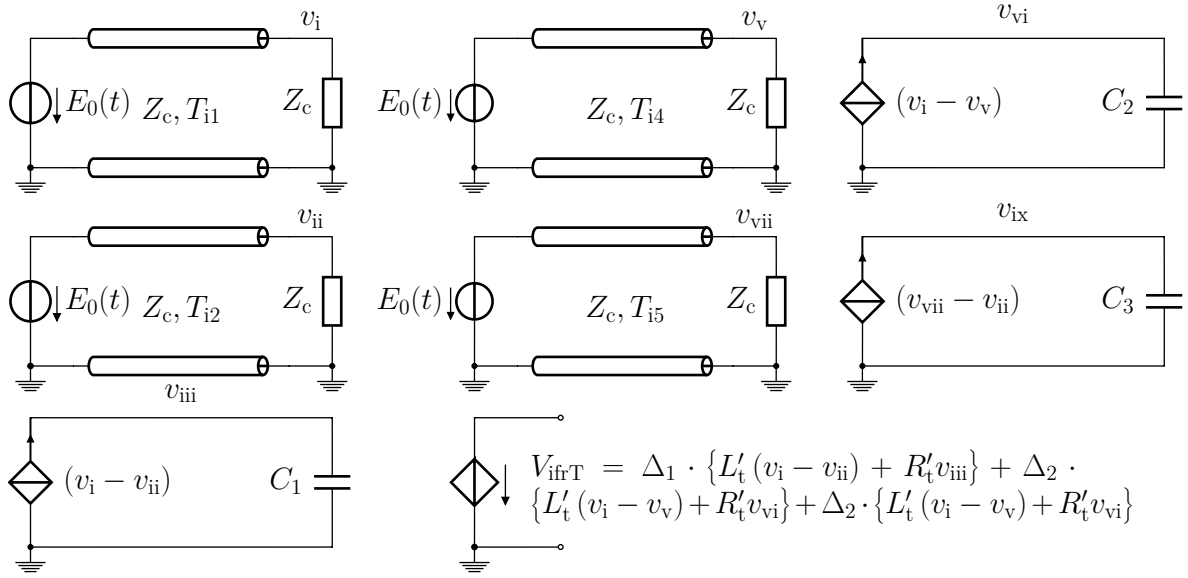

Figure 4.17: Equivalent circuit for the solution of V_{ifrT}.

domain by

$$
\begin{aligned}
V_{\mathrm{ifl T}}(t) &= \frac{1}{2}\cdot\Big(V_{\mathrm{ifl}} + Z_{\mathrm{Ci}} I_{\mathrm{ifl}}\Big) \\
&= \Delta_4 \cdot \left\{ L'_{\mathrm{t}}\Big(E_0(t-T_{\mathrm{i7}}) - E_0(t)\Big) + R'_{\mathrm{t}}\int_0^t \Big(E_0(\tau - T_{\mathrm{i7}}) - E_0(z)\Big)\,\mathrm{d}\tau \right\} \\
&+ \Delta_5 \cdot \left\{ L'_{\mathrm{t}}\Big(E_0(t-T_{\mathrm{i8}}) - E_0(t)\Big) + R'_{\mathrm{t}}\int_0^t \Big(E_0(\tau - T_{\mathrm{i8}}) - E_0(z)\Big)\,\mathrm{d}\tau \right\} \\
&+ \Delta_6 \cdot \left\{ L'_{\mathrm{t}}\Big(E_0(t-T_{\mathrm{i9}}) - E_0(t-T_{\mathrm{i10}})\Big) + R'_{\mathrm{t}}\int_0^t \Big(E_0(\tau - T_{\mathrm{i9}}) - E_0(\tau - T_{\mathrm{i10}})\Big)\,\mathrm{d}\tau \right\},
\end{aligned}
\tag{4.91}
$$

where

$$
\begin{aligned}
&\Delta_4 = \frac{h v_0}{Z_{\mathrm{Co}}\left(\sqrt{\varepsilon_{\mathrm{ri}}} + \cos(\theta)\right)},\ \Delta_5 = \frac{h v_0\Big(\mathcal{Q}_{\mathrm{1M}} + \cos(\theta)/2\Big)}{Z_{\mathrm{Co}}\left(\sqrt{\varepsilon_{\mathrm{ri}}} + 1\right)} \\
&\Delta_6 = -\frac{h v_0}{2 Z_{\mathrm{Co}}\left(\sqrt{\varepsilon_{\mathrm{ri}}} - 1\right)} \\
&T_{\mathrm{i7}} = T_{\mathrm{i9}} = \mathcal{L}\cdot\frac{\sqrt{\varepsilon_{\mathrm{ri}}} + \cos(\theta)}{v_0},\ T_{\mathrm{i8}} = \mathcal{L}\cdot\frac{\sqrt{\varepsilon_{\mathrm{ri}}} + 1}{v_0},\ T_{\mathrm{i10}} = \mathcal{L}\cdot\frac{\cos(\theta)+1}{v_0}.
\end{aligned}
\tag{4.92}
$$

The function of $V_{\mathrm{ifl T}}(t)$ in (4.91) consists of time-delayed elements together with some integrals. Its circuit model is not shown here, since it can be developed with similar steps as in Fig. 4.17.

In this section, the field forcing functions for the inner and outer systems of a shielded cable were calculated and developed in circuit form. Those for the conductive coupling were developed in section 4.2.3. The construction of all these circuits together with the macromodel in Fig. 4.15 allows the model to be run for field and conductive coupling in a SPICE solver. In the next section, the model developed in Fig. 4.15 is validated.

4.3.4 Model Validation of the Field Coupling

Field simulations are performed for model validation. The field simulations are carried out with CST Studio Suite 19 [3] using a co-simulation, where the solver in CST Microwave Studio is combined with the CST Cable Studio harness solver, as described in Figs. 3.9 and 3.10. The macromodel from Fig. 4.15 and the lumped-circuit model from Fig. 4.2 were simulated using LTspice [35]. The simulation results of the lumped-circuit model are presented in this section in order to compare them with the macromodel in terms of time and efficiency. The PC defined in section 4.1.3 was also used here for the simulations. As mentioned above, no measurements were made for field coupling, since such measurements were difficult to realize with quantitatively precise evaluation.

Time Domain

To simulate the field coupling, a 5 m long RG58 cable with a height of 1 cm above the ground plane is considered in Fig. 4.5. The termination loads and the transfer impedance parameters of the cable were defined in section 4.1.3. An immunity test is undertaken in which a uniform plane wave with $\theta = 45°$ was excited. The electric field has a magnitude of 50 $\frac{\mathrm{V}}{\mathrm{m}}$. It has a trapezoidal shape with rise, fall and hold times of 2 ns, 3 ns and 10 ns, respectively. The voltage source V_1 in Fig. 4.5 was short-circuited during this test. The voltages across D_1 and R_{i2}, L_{i1} are shown in Figs. 4.18 and 4.19, respectively. The simulation results are presented for the SPICE macromodel (Macromodel), the SPICE lumped-circuit model (SPICE $N_s = 300$) and those of CST. Since the CST results were compared with the measurement in Fig. 4.12, CST can be used as a reference in this case. For a sufficient accuracy of the lumped-circuit model, the cable was divided into 300 sections. It can be seen that the results agree excellently with each other. A more precise

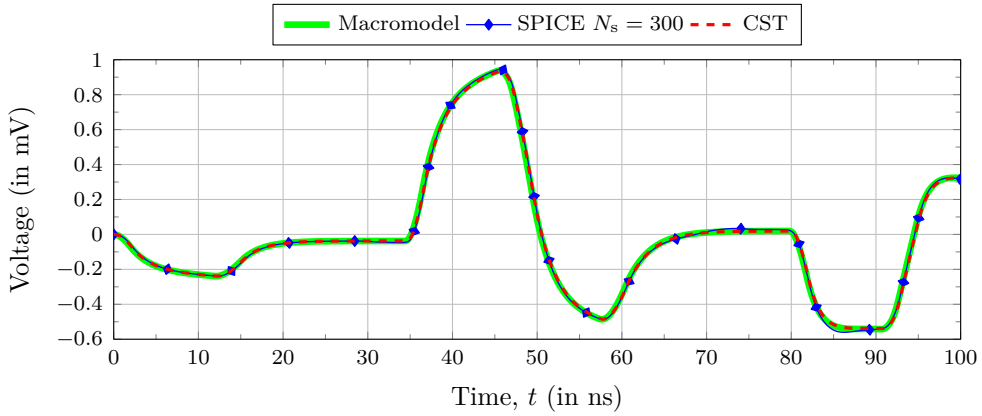

Figure 4.18: Voltage response across D_1 for a single conductor shielded cable in transient analysis.

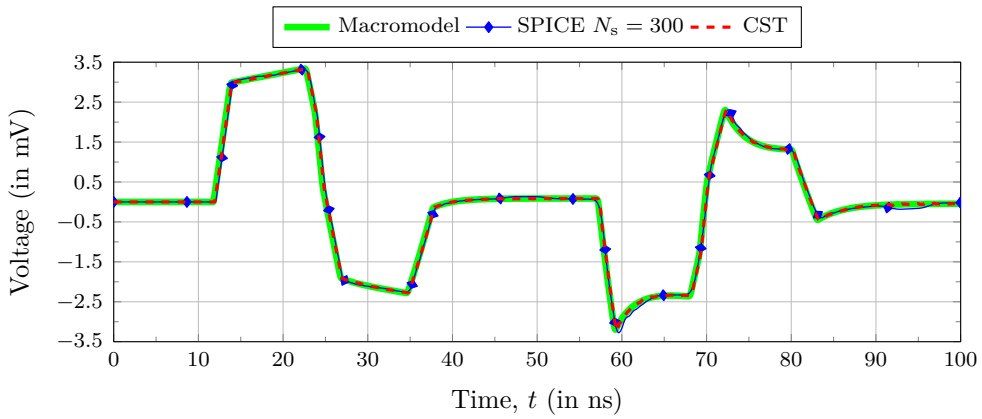

Figure 4.19: Voltage response across R_{i2} and L_{i1} for a single conductor shielded cable in transient analysis.

observation at 85 ns in Fig. 4.18 and at 60 ns, 92 ns in Fig. 4.19 shows a slight deviation of the results for the lumped-circuit model. As discussed in section 4.1, the accuracy of the lumped-circuit model depends on the number of subdivided segments.

The simulation time showed a significant difference when comparing the methods. The simulation time was 9.3 min for CST and 70 s for the lumped-circuit model. In comparison, the macromdel took 1.5 s, which shows a great advantage over the other methods. Unlike the lumped-circuit model, the macromodel should not divide the cable into sections demonstrating the utility and necessity of a SPICE model based on this method.

Frequency Domain

An immunity test is performed in the frequency domain taking into account the field coupling. The cable structure in Fig. 4.5 is considered for this investigation. During the test, the diode D_1 was removed and the voltage source V_1 short-circuited. An incident wave of 50 $\frac{\mathrm{V}}{\mathrm{m}}$ with $\theta = 45°$ was excited. The induced voltage across $R_{\mathrm{i}1}$ is shown in Fig. 4.20 in terms of magnitude and phase. A frequency sweep with 4000 points between 10 kHz and 500 MHz was performed for all simulation models. The resonances at 11.5 MHz and 60 MHz correspond to those of the inner and outer systems, respectively. The results of macromodel and those of CST are in excellent agreement. This also applies to the lumped-circuit model, although slight deviations can be observed at higher frequencies. The duration of the simulations is given as follows: 3.9 s for the macromodel, 38.2 s for

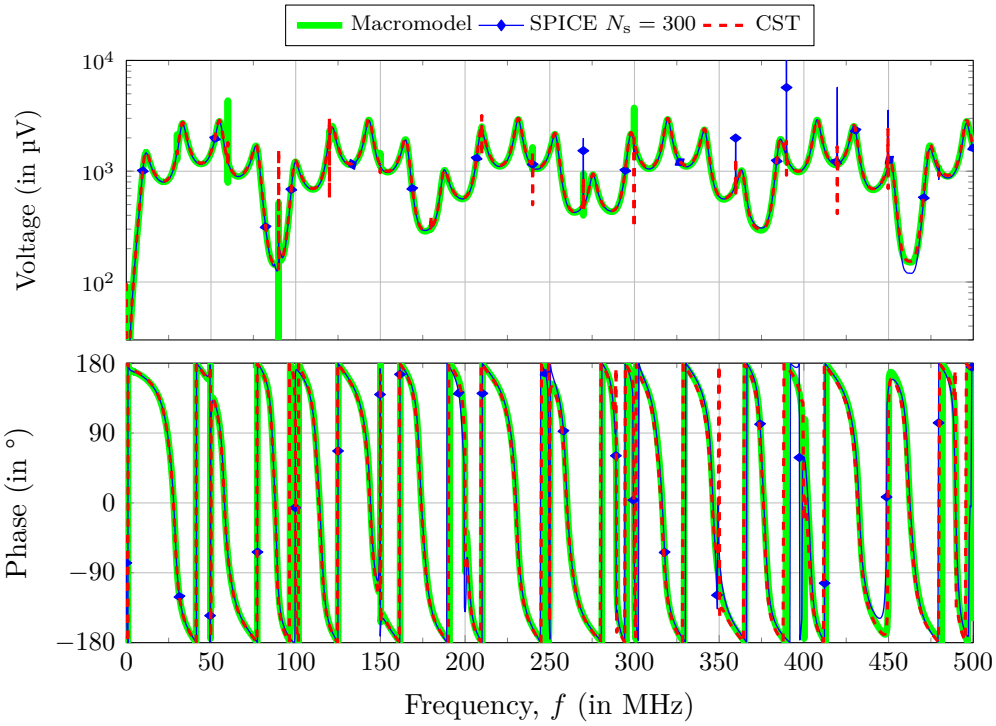

Figure 4.20: Voltage response across $R_{\mathrm{i}1}$ for a single conductor shielded cable in frequency domain.

the lumped-circuit model and 3.3 min for CST.

It should be mentioned here that the model developed in Fig. 4.15 can be used for field or conductive coupling individually or for field and conductive coupling in combination. In this section, only field coupling was considered, since in section 4.2.4 conductive couplings were examined. Further validations of the model with other test settings can be found in the presented work in [61, 69].

In this chapter, circuit models for a single conductor shielded cable were developed in distributed form (lumped-circuit model) and in closed-form (macromodel). Both models were created to analyze conductive coupling by connecting a lumped source to the model terminals or to calculate field coupling on the cable. The developed models are applicable in the time and frequency domains, whereby the validation in sections 4.1.3, 4.2.4 and 4.3.4 was carried out with field simulations and measurements. The lumped-circuit model shown in Fig. 4.2 was interpreted directly from the transmission line equations of a shielded cable in (4.4) as distributed elements connected in series. Field coupling was included in the model by using the scattered voltage formulation as described in section 4.1.2. After a closed-form solution of the shielded line was presented in section 4.2.1, a macromodel was developed in Fig. 4.9. The model presented there considers conductive coupling without field coupling. The field coupling of an incident wave was later extended in section 4.3 and finally a complete macromodel was developed in Fig. 4.15. This model includes the conductive and the field coupling and was validated in section 4.3.4.

In the next chapter, these models will be extended to include shielded multiconductor cables.

5 Circuit Models of Multiconductor Shielded Cables

In this chapter, the circuit models developed for a single conductor shielded cable above a ground plane are expanded to include the case of a shielded cable with n inner conductors. The field and conductive couplings are included in the proposed models. Two types of models have been developed. First, in section 5.1, a lumped-circuit model is presented in which the cable is divided into segments. Equivalent circuit diagrams were developed for each segment and connected in series to represent the entire cable. The second model was developed from a closed-form solution, it is called macromodel. In this case, no segmentation of the cable was necessary. The cable was constructed in the form of transmission lines coupled together. Since many applications relate only to conductive coupling, it was decided to develop the macromodel in section 5.2 only for conductive coupling without field coupling. The model was extended to include field coupling in section 5.3. The model validation of both proposed methods was undertaken by field simulation and experimental measurements in sections 5.1.3, 5.2.3 and 5.3.3.

A shielded cable with n inner conductors is shown in Fig. 5.1. It has a length $\mathcal{L}$ and is positioned at a height h above the ground plane. The following indices were used: i for the inner system, o for the outer system and w for wire. The electrical currents $I_{\mathrm{i}1}$ to $I_{\mathrm{i}n}$ are the currents that flow between the inner conductors and the cable shield. The elements

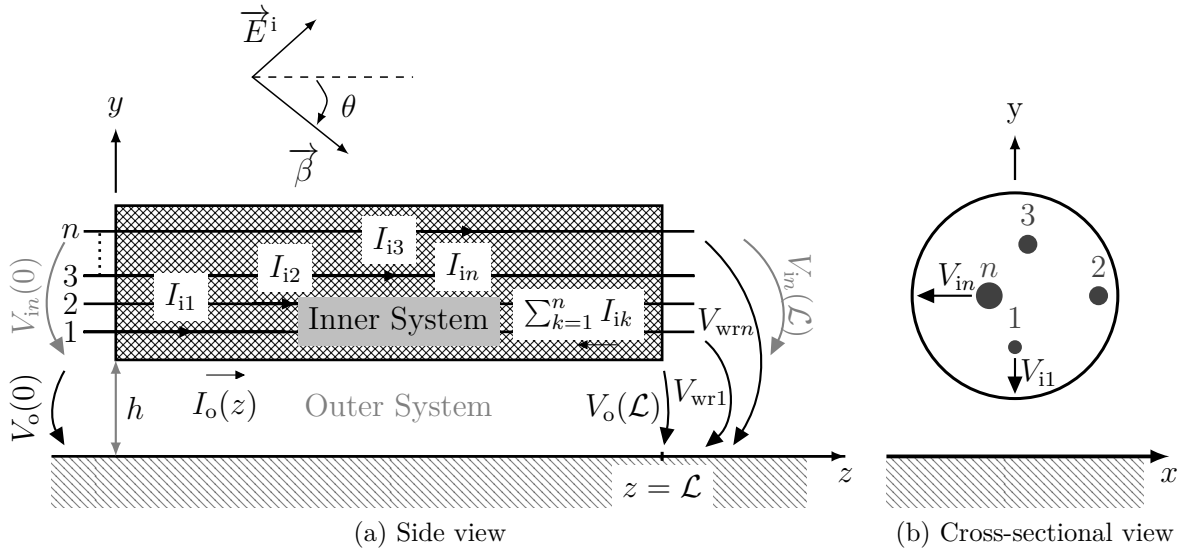

(a) Side view (b) Cross-sectional view

Figure 5.1: Field-coupled shielded multiconductor cable over a perfectly conducting ground plane.

$V_{in}(0)$ and $V_{in}(\mathcal{L})$ in Fig. 5.1 represent the voltages between the nth inner conductor and the cable shield at $z = 0$ and $z = \mathcal{L}$, respectively. In contrast, the parameters V_{wr1} to $V_{\mathrm{wr}n}$ are the voltages between the inner conductors and the ground plane. The elements $V_{\mathrm{o}}(0)$ and $V_{\mathrm{o}}(\mathcal{L})$ are the voltages at $z = 0$ and $z = \mathcal{L}$ for the outer system. The current of the outer system is represented by $I_{\mathrm{o}}(z)$.

Similar to a single conductor cable, a braided shield with a braid angle $\mathcal{G} = 45°$ was considered, resulting in the p.u.l. transfer impedance vector

$$\boldsymbol{Z}'_{\mathrm{t}} = \begin{bmatrix} Z'_{\mathrm{t}1} \\ Z'_{\mathrm{t}2} \\ \vdots \\ Z'_{\mathrm{t}n} \end{bmatrix}, \tag{5.1}$$

where its kth element $[\boldsymbol{Z}'_{\mathrm{t}}]_k = Z'_{\mathrm{t}k} = R'_{\mathrm{t}} + \mathrm{j}\omega L'_{\mathrm{t}k}$ being the transfer impedance relative to the kth wire. For a shielded single conductor cable, the transfer inductance L'_{t} was defined in (4.1) based on the inductive coupling through the openings in the shield. In the case of a shielded multiconductor cable with unbalanced wire configurations where the spacing between the wires and the shield is not constant, as shown in Fig. 5.1b, the wires have unequal mutual inductances, represented by $L'_{\mathrm{t}k}$ for the kth wire [41, 42]. To determine the transfer impedance for shielded multiconductor cables, the IEC 62153-4-3 [51] and IEC 62153-4-6 [53] standards define measurement procedures for balanced cable configurations with all inner conductors connected at both ends, as shown in Fig. 2.15.

Next, a lumped-circuit model for shielded multiconductor cables is developed.

5.1 Lumped-Circuit Model for Shielded Multiconductor Cables

This section introduces a lumped-circuit model for multiconductor shielded cables over a ground plane. The field coupling of a plane wave is included in the model, which enables a field immunity test. In addition, emission tests can be carried out with the model, as the bidirectional coupling between the inner and the outer system is taken into account. As done in section 4.1 for a single conductor shielded cable, the multiconductor cable in Fig. 5.1 was divided into N_{s} segments of length $l_{\mathrm{step}} < \lambda/10$, where λ is the wavelength of the maximum frequency of interest. Equivalent circuit diagrams are created for each segment and connected to represent the entire cable. Each segment is divided into an inner system and an outer system.

The following steps were taken to develop the model. In sections 5.1.1 and 5.1.2 the differential equations of the inner and outer system are derived. From these, the equivalent circuit diagrams were developed. The model validation took place in sections 5.1.3.

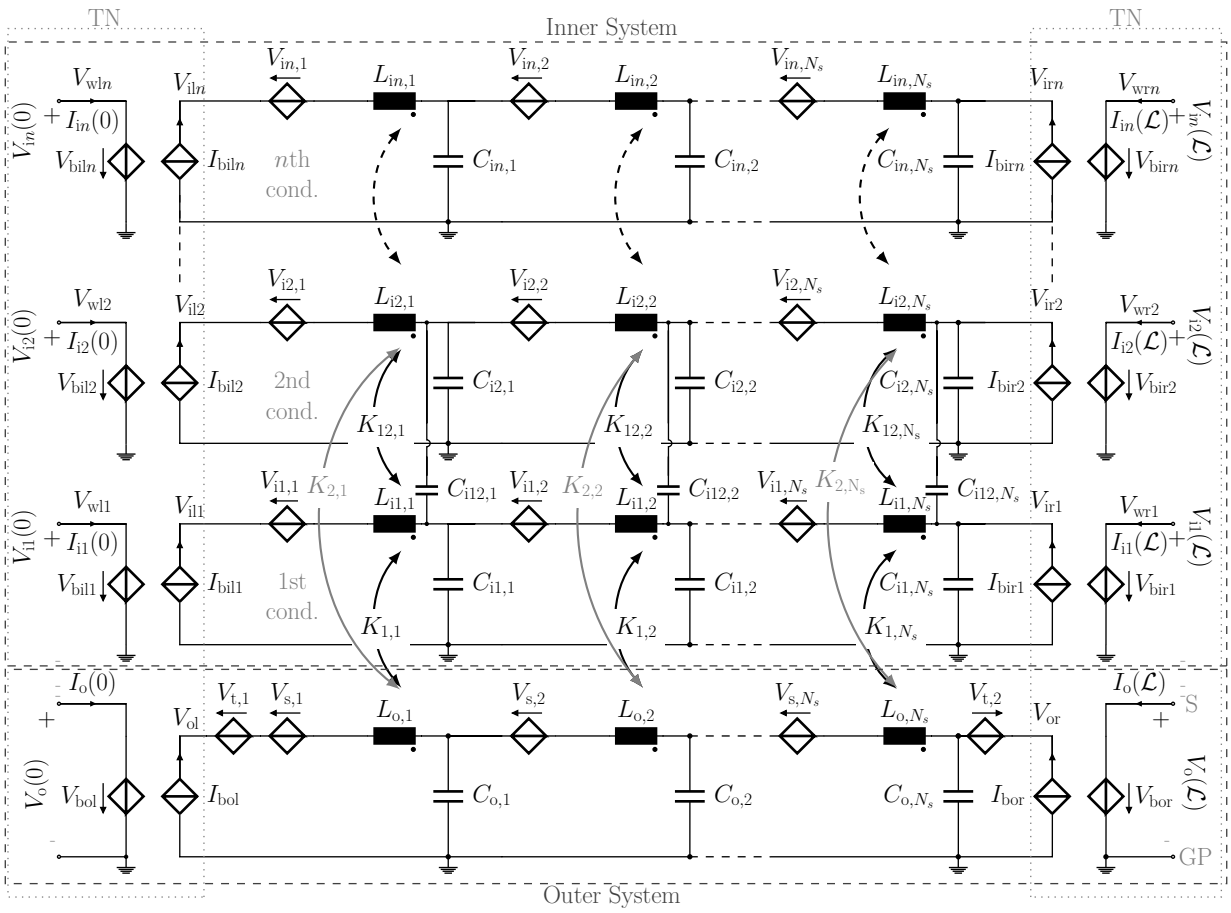

Figure 5.2: Lumped-circuit model of a field-coupled shielded multiconductor cable over a perfectly conductive ground plane. S shield. GP ground plane. TN transformation network.

The lumped-circuit model of the multiconductor cable in Fig. 5.1 is developed in Fig. 5.2. It consists of distributed elements representing the primary line constants of the cable along with the mutual couplings.

At the n-th conductor in Fig. 5.2, the elements $L_{\mathrm{i}n,1\ldots\mathrm{N_s}}$ are the p.u.l. inductances for the 1st to N_sth segments. The capacitances between wires and shield are represented by $C_{\mathrm{i}n,1\ldots\mathrm{N_s}}$. The current-controlled voltage sources in series $V_{\mathrm{i}n,1\ldots\mathrm{N_s}}$ represent the induced voltage by diffusion of the nth inner conductor. The capacitive coupling between the inner wires is represented by $C_{\mathrm{i}jn}$, here for example $C_{\mathrm{i}12,1}$ is that between the first and the second conductor on the 1st segment. The factor K represents the inductive coupling, as will be shown later. The outer system in Fig. 5.2 includes the primary line constants $L_{\mathrm{o},1\ldots\mathrm{N_s}}$ and $C_{\mathrm{o},1\ldots\mathrm{N_s}}$. The current-controlled voltage sources in the outer system $V_{\mathrm{s},1\ldots\mathrm{N_s}}$ and $V_{\mathrm{t},1}, V_{\mathrm{t},2}$ represent the coupling via diffusion together with the field coupling. Further details on the development of these elements will be shown later.

At the left and right ends in Fig. 5.2, transformation networks (TNs) are modeled as for a

single conductor shielded cable in Fig. 4.2. These are used to represent the real connections of the cable. The TNs can represent the voltage for an inner conductor with respect to ground. For a better understanding, the nth wire in Fig. 5.2 can be compared with the real structure in Fig. 5.1. The voltage $V_{\mathrm{i}n}(0)$ in Fig. 5.1 is that between the nth inner conductor and the shield, while $V_{\mathrm{wr}n}$ is the voltage between the nth inner conductor and the ground plane. The same voltages can be observed in the developed model in Fig. 5.2. The remaining parameters $V_{\mathrm{i}n}(\mathcal{L})$, V_{wr1}, $I_{\mathrm{i}n}$, I_{o}, $V_{\mathrm{o}(\mathcal{L})}$ and so on can also be compared in both figures.

The controlled sources used for the nth inner system in Fig. 5.2 are defined analogously to those of the shielded single conductor in (4.2) and (4.3), taking into account the multilines as follows:

$$V_{\mathrm{bil}n} = V_{\mathrm{il}n} + V_{\mathrm{ol}} \tag{5.2a}$$

$$I_{\mathrm{bil}n} = I_{\mathrm{i}n}(0) \tag{5.2b}$$

$$I_{\mathrm{bir}n} = I_{\mathrm{i}n}(\mathcal{L}) \tag{5.2c}$$

$$V_{\mathrm{bir}n} = V_{\mathrm{ir}n} + V_{\mathrm{or}}. \tag{5.2d}$$

Those for the outer system are given by

$$V_{\mathrm{bol}} = V_{\mathrm{ol}} \tag{5.3a}$$

$$I_{\mathrm{bol}} = I_{\mathrm{o}}(0) + I_{\mathrm{i1}}(0) + I_{\mathrm{i2}}(0) + \cdots + I_{\mathrm{i}n}(0) \tag{5.3b}$$

$$I_{\mathrm{bor}} = I_{\mathrm{o}}(\mathcal{L}) + I_{\mathrm{i1}}(\mathcal{L}) + I_{\mathrm{i2}}(\mathcal{L}) + \cdots + I_{\mathrm{i}n}(\mathcal{L}) \tag{5.3c}$$

$$V_{\mathrm{bor}} = V_{\mathrm{or}}. \tag{5.3d}$$

The electrical quantities $V_{\mathrm{il}n}$, V_{ol}, $V_{\mathrm{ir}n}$, V_{or}, V_{ol}, $I_{\mathrm{o}}(0)$, $I_{\mathrm{i1}}(0) \ldots I_{\mathrm{i}n}(0)$ $I_{\mathrm{o}}(\mathcal{L})$, $I_{\mathrm{i1}}(\mathcal{L}) \ldots I_{\mathrm{i}n}(\mathcal{L})$ and V_{or} in (5.2) and (5.3) can be compared in Fig. 5.2. Equations (5.2) and (5.3) can be better understood by considering the transformation matrices in (2.98) and (2.99).

The next two sections provide more details on the development of the distributed elements for the model in Fig. 5.2.

5.1.1 Solution of the Inner System

The differential equation of the inner system for the cable harness in Fig. 5.1 is defined analogously to (4.4). It is given by

$$\frac{\mathrm{d}}{\mathrm{d}z}\begin{bmatrix}\boldsymbol{V}_{\mathrm{i}}(z)\\ \boldsymbol{I}_{\mathrm{i}}(z)\end{bmatrix} = \begin{bmatrix}0 & -\mathrm{j}\omega\boldsymbol{L}'_{\mathrm{i}}\\ -\mathrm{j}\omega\boldsymbol{C}'_{\mathrm{i}} & 0\end{bmatrix}\begin{bmatrix}\boldsymbol{V}_{\mathrm{i}}(z)\\ \boldsymbol{I}_{\mathrm{i}}(z)\end{bmatrix} + \begin{bmatrix}\boldsymbol{V}'_{\mathrm{di}}(z)\\ 0\end{bmatrix}. \tag{5.4}$$

The n-element vectors $\boldsymbol{V}_\mathrm{i}(z)$ and $\boldsymbol{I}_\mathrm{i}(z)$ are the voltage and current of the inner system, where $V_{\mathrm{i}k}(z)$ and $I_{\mathrm{i}k}(z)$ represent the voltage and current of the kth wire with respect to the shield, as shown in Fig. 5.1. The p.u.l. inductance and capacitance for the inner system are given by the $n \times n$ matrices $\boldsymbol{L}'_\mathrm{i}$ and $\boldsymbol{C}'_\mathrm{i}$, respectively. They are full matrices that contain the coupling between the inner conductors in their non-diagonal elements. The matrices $\boldsymbol{L}'_\mathrm{i}$ and $\boldsymbol{C}'_\mathrm{i}$ can be calculated analytically using (2.72) and (2.79) or using a static 2D field solver. The p.u.l. disturbance voltage vector is given by

$$\boldsymbol{V}'_\mathrm{di}(z) = \boldsymbol{Z}'_\mathrm{t} \cdot I_\mathrm{o}(z). \tag{5.5}$$

The current $I_\mathrm{o}(z)$ is that of the outer system as shown in Fig. 5.1 and $\boldsymbol{Z}'_\mathrm{t}$ is the transfer impedance vector defined in (5.1). A comparison of (5.4) with (4.4) shows that both equations have a similar form, with the quantities in (5.4) accounting for the multilines by vector and matrix representations. Equation (4.4) was written in terms of Δz in (4.6) and the equivalent circuit was interpreted from Fig. 2.13. The same work can be done here, each inner conductor of the shielded mutliconductor cable can be interpreted from Fig. 2.13, and the mutual coupling between the inner wires needs to be added. As shown in Fig. 5.2, each wire is represented by a series of N_s segments containing the primary line constants connected in series. The current-controlled voltage sources in series $V_{\mathrm{i}n,1\ldots\mathrm{N_s}}$ represent the induced voltage by diffusion of the nth inner conductor. The controlled voltage source of the kth segment is defined as

$$V_{\mathrm{i}n,k} = R'_{\mathrm{t},k} \cdot I_{\mathrm{o},k}(z) \cdot l_\mathrm{step}. \tag{5.6}$$

The inductive coupling between the nth wire and the outer system in the SPICE environment is realized for the kth segment by the coupling coefficient $K_{n,k}$ as follows:

$$K_{n,k} = -\frac{L'_{\mathrm{t}n}}{\sqrt{L'_{\mathrm{o},k} L'_{\mathrm{i}n,k}}}. \tag{5.7}$$

The inductive coupling between the jth and the nth innner conductor in the kth segment is given by

$$K_{jn,k} = \frac{L'_{\mathrm{i}jn,k}}{\sqrt{L'_{\mathrm{i}n,k} L'_{\mathrm{i}j,k}}}, \tag{5.8}$$

where $L'_{jn,k}$ is the mutual inductance between the jth and the nth conductor. The capacitive coupling is realized by the capacitance $C_{\mathrm{i}jn,k}$ built in Fig. 5.2. It is given by

$$C_{\mathrm{i}jn,k} = C'_{\mathrm{i}jn} \cdot l_\mathrm{step}, \tag{5.9}$$

where the length dependence is eliminated by multiplying the unit length l_{step} from (4.8). The remainder of the components for the jth conductor $L_{\text{i}j,k}$ and $C_{\text{i}j,k}$ are similarly multiplied by the unit length. The same applies to the outer system $L_{\text{o},k}$ and $C_{\text{o},k}$.

Next, the development of the outer system will be described.

5.1.2 Solution of the Outer System

The outer system in Fig. 5.1 is coupled by the inner one via diffusion and inductive coupling. The inductive coupling was introduced in (5.7). The differential equation considering only the coupling from the inner system is defined analogously to (4.22). It is given by

$$\frac{\mathrm{d}}{\mathrm{d}z}\begin{bmatrix} V_{\text{oc}}(z) \\ I_{\text{oc}}(z) \end{bmatrix} = \begin{bmatrix} 0 & -\mathrm{j}\omega L'_{\text{o}} \\ -\mathrm{j}\omega C'_{\text{o}} & 0 \end{bmatrix} \cdot \begin{bmatrix} V_{\text{oc}}(z) \\ I_{\text{oc}}(z) \end{bmatrix} + \begin{bmatrix} V'_{\text{do}}(z) \\ 0 \end{bmatrix}, \tag{5.10}$$

where the p.u.l. disturbance voltage $V'_{\text{do}}(z)$ is given by

$$V'_{\text{do}}(z) = \boldsymbol{Z}'^{\mathrm{T}}_{\text{t}} \cdot \boldsymbol{I}_{\text{i}}(z). \tag{5.11}$$

The elements $V_{\text{oc}}(z)$ and $I_{\text{oc}}(z)$ are the conductive voltage and current of the outer system, as shown in Fig. 5.1 without the c notation. The primary line constants of the outer system are given by L'_{o} and C'_{o}. The index c was used in (5.10) for conductive coupling to distinguish between coupling from the inner system and coupling from the environment by the incident field.
Comparing (5.10) with the one shown in (4.22), it has the same form with the only difference in $V'_{\text{do}}(z)$. That is why the distributed elements in Fig. 5.2 are built in the same way as in Fig. 4.2 for a single conductor shielded cable. The controlled voltage source of the kth segment $V_{\text{s},k}$ includes the coupling via diffusion from the inner system $V_{\text{o},k}$ together with the field coupling from the environment $V_{\text{tan},k}$, as defined in (4.11).

$$V_{\text{s},k} = V_{\text{o},k} + V_{\text{tan},k} \tag{5.12}$$

The diffusion part of the kth segment by considering the multiconductors in the inner system is given by

$$V_{\text{o},k} = R'_{\text{t},k} \cdot l_{\text{step}} \cdot \sum_{u=1}^{n} I_{\text{i}u,k}, \tag{5.13}$$

where $I_{\text{i}u,k}$ is the current in the uth inner conductor on the kth segment. The sum of currents was integrated into the equation in order to take into account the influence of all inner conductors.

The field coupling is included in Fig. 5.2 by $V_{\text{tan},k}$ via $V_{\text{s},k}$ in (5.12) and V_{t1}, V_{t2}. The

tangential voltage $V_{\tan,k}$ remains the same as in (4.18), since the shielded cable was considered as a single conductor above the ground plane for the field coupling. In this case, it does not make any difference whether the cable has one or more inner conductors. An equivalent circuit for $V_{\tan,k}$ has been developed in Fig. 4.3. The same applies to the transverse voltages $V_{\mathrm{t},1}$ and $V_{\mathrm{t},2}$ defined in (4.19) and (4.20). An equivalent circuit for $V_{\mathrm{t},2}$ was shown in Fig. 4.4.

The lumped-circuit model developed in Fig. 5.2 is now ready to be simulated, where the validation will be performed in the next section.

5.1.3 Model Validation

For model validation, Fig. 5.3 shows a balanced quad-core cable with a length of $\mathcal{L} = 3\,\mathrm{m}$, which is positioned at a height of $h = 1\,\mathrm{cm}$ above a ground plane. The cable has 4 inner conductors that are equally spaced with a distance of 1.5 mm between them. The conductors have the same radius with $r_{1-4} = 0.39\,\mathrm{mm}$. They are insulated by a PVC material with a dielectric constant $\varepsilon_{\mathrm{ri}} = 3$.

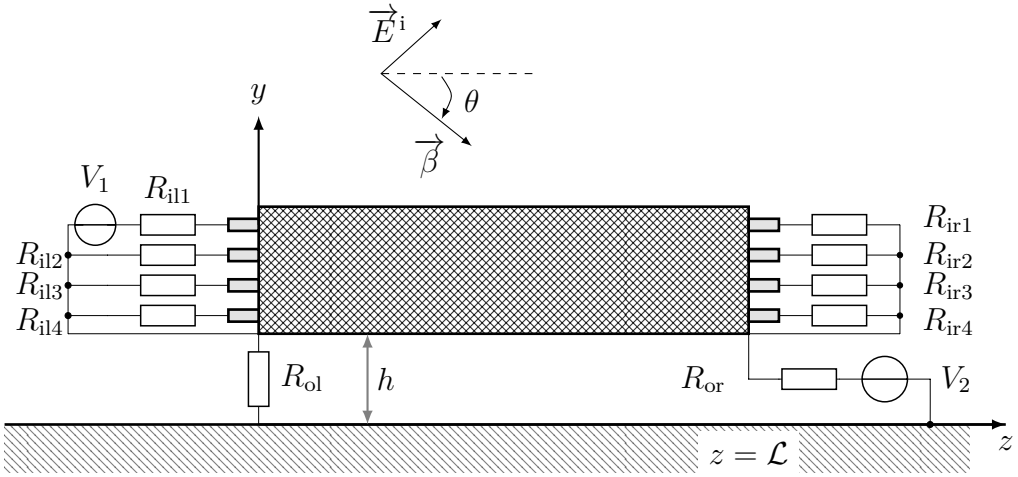

Figure 5.3: Setup circuit for validation of a field-coupled shielded multiconductor cable.

The shield has a diameter of 6.1 mm with an optical coverage of 85 %. It consists of 22 carriers with 6 strands each. The strands diameter is equal to 0.11 mm. The transfer impedance parameters were determined with $R'_{\mathrm{t}1-4} = 23\,\frac{\mathrm{m\Omega}}{\mathrm{m}}$ and $L'_{\mathrm{t}1-4} = 1.7\,\frac{\mathrm{nH}}{\mathrm{m}}$. These are equal for all inner conductors due to the balanced configuration. The primary line constants $\boldsymbol{L}'_{\mathrm{i}}$ and $\boldsymbol{C}'_{\mathrm{i}}$ were calculated using a static solver.

$$\boldsymbol{L}'_{\mathrm{i}} = \begin{bmatrix} 0.35 & 0.13 & 0.13 & 0.09 \\ 0.13 & 0.35 & 0.09 & 0.13 \\ 0.13 & 0.09 & 0.35 & 0.13 \\ 0.09 & 0.13 & 0.13 & 0.35 \end{bmatrix} \mu\mathrm{H/m}$$

$$\boldsymbol{C}'_{\mathrm{i}} = \begin{bmatrix} 119.94 & -33.56 & -33.56 & -5.76 \\ -33.56 & 119.94 & -5.76 & -33.56 \\ -33.56 & -5.76 & 119.94 & -33.56 \\ -5.76 & -33.56 & -33.56 & 119.94 \end{bmatrix} \mathrm{pF/m}$$

The parameters of the outer system were determined with $L'_{\mathrm{o}} = 335.36\,\frac{\mathrm{nH}}{\mathrm{m}}$ and $C'_{\mathrm{o}} = 30.71\,\frac{\mathrm{pF}}{\mathrm{m}}$. The terminations of the inner and outer system in Fig. 5.3 are defined as follows: $R_{\mathrm{il}1-4} = R_{\mathrm{ir}1-4} = 10\,\Omega$ and $R_{\mathrm{ol}} = R_{\mathrm{or}} = 10\,\mathrm{m}\Omega$. The lumped-circuit model of the shielded multiconductor cable over a ground plane developed in Fig. 5.2 has been simulated in the electronic circuit simulator LTspice [35]. The transformation networks from Fig. 5.2 were created directly in LTspice. For the cascaded model of the cable, a netlist was created using MATLAB [68]. A netlist by dividing the cable into 3 sections can be found in Appendix A.2. Similar to the single conductor shielded cable, the simulation results were compared with those of CST Microwave Studio 2019 [3] in the time and frequency domains. The simulation setup of CST Microwave Studio was defined in Figs. 3.9 and 3.10, in which a co-simulation is performed to couple the 3D full wave solver with the circuit solver. The simulation results of CST were validated with measurements in section 5.2.3, therefore this simulation tool will be used as a comparative reference for the considered cases. The same PC defined in section 4.1.3 was used for the simulation. The simulation time of the lumped-circuit model increased by a higher number of sections N_{s}, but the examined examples did not show any convergence problem anyway.

Time Domain

In the transient analysis, the voltage sources V_1 and V_2 in Fig. 5.3 were short-circuited. An immunity test was carried out in which a uniform plane wave with $\theta = 45°$ was excited. The electric field of the incident wave has a trapezoidal shape of $10\,\frac{\mathrm{V}}{\mathrm{m}}$. The rise, hold, and fall times are 2 ns, 10 ns and 3 ns, respectively. The rise time of 2 ns corresponds to $\lambda/10 = 3.45\,\mathrm{cm}$ in the inner system. Therefore, the cable in Fig. 5.3 should be divided into at least 87 sections for adequate results.

The voltage response of the plane wave across $R_{\mathrm{il}1}$ is shown in Fig. 5.4 for a different number of sections. The deviation is relatively large for $N_{\mathrm{s}} = 4$ and $N_{\mathrm{s}} = 16$, where the section length $l_{\mathrm{step}} \gg \lambda/10$. The deviation becomes smaller for $N_{\mathrm{s}} = 87$ with $l_{\mathrm{step}} = \lambda/10$. The result fits well with $N_{\mathrm{s}} = 200$, which further increases the simulation time.

The same behavior can be observed in Fig. 5.5, where the voltage response across $R_{\mathrm{ir}1}$ is shown for a different number of sections. The simulation time of the SPICE model was 21 s for $N_{\mathrm{s}} = 87$ and 130 s for $N_{\mathrm{s}} = 200$. The simulation time with CST was 25 min.

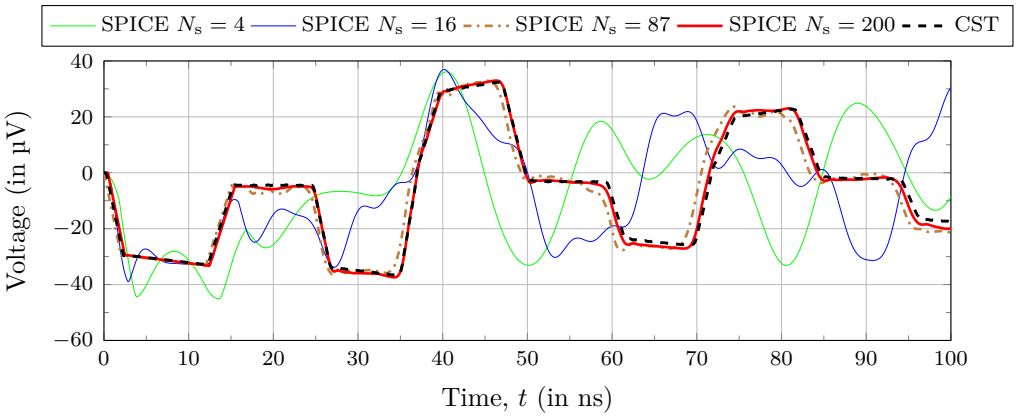

Figure 5.4: Voltage response across R_{il1} for the lumped-circuit model of a quad-core shielded cable in transient analysis.

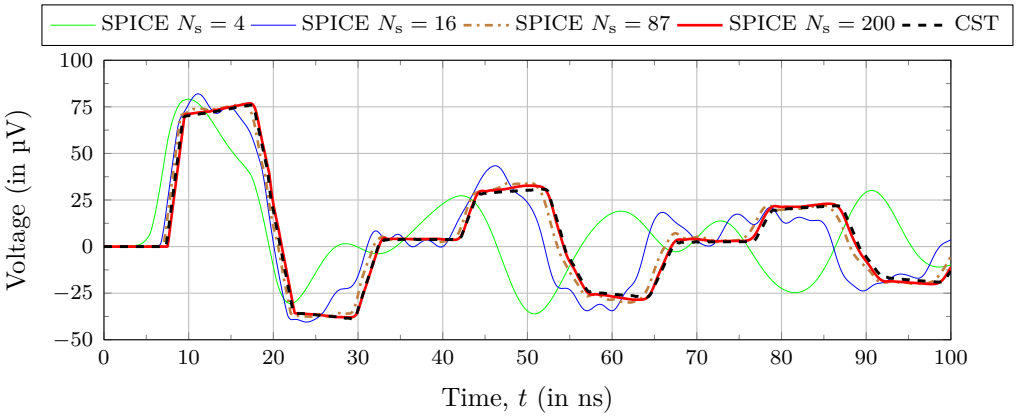

Figure 5.5: Voltage response across R_{ir1} for the lumped-circuit model of a quad-core shielded cable in transient analysis.

Frequency Domain

The coupling from the inner to the outer system was examined in the frequency domain. The voltage source V_1 in Fig. 5.3 is set to 1 V and no field coupling was taken into account. The voltage source V_2 was short-circuited during this test. The voltage across R_{or} is shown in Fig. 5.6 as magnitude and phase for a different number of sections. For $N_s = 16$, the result matches at lower frequencies and shows relatively higher deviations at higher frequencies. For $N_s = 200$, the result fits well. The resonance behavior at 50 MHz corresponds to that of the outer system due to mismatch. At 29 MHz, a weakened resonance effect of the inner system can be observed. The simulation time of the SPICE model was 22 s for $N_s = 200$, in contrast, CST took 52 s.

In this section, a lumped-circuit model for a multiconductor shielded cable over a ground plane was developed in the SPICE environment. The model consists of cascaded cells containing concentrated elements and controlled sources. It has been shown that a larger

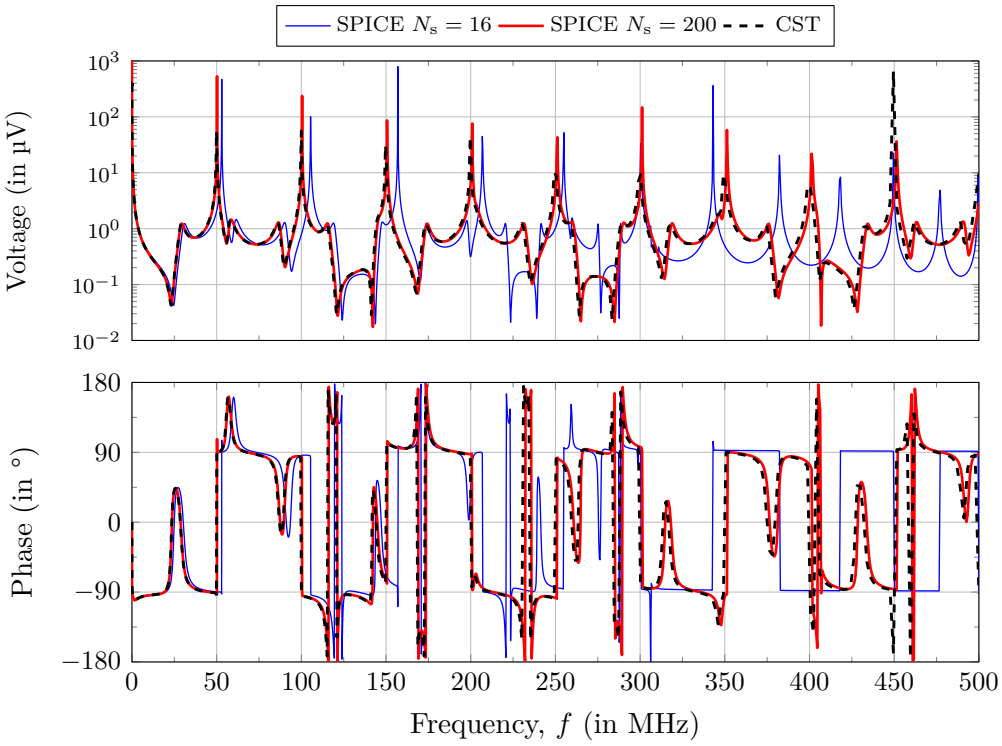

Figure 5.6: Voltage response across R_{or} for the lumped-circuit model of a quad-core shielded cable in frequency domain.

number of cells are required at higher frequencies, resulting in higher computational costs.

Next, a macromodel is derived from the closed-form solution, where the cable is not divided into sections.

5.2 Macromodel for the Analysis of Conductive Coupling

As presented before, accurate results of the lumped-circuit model are associated with a higher computational cost. This shows the limitations of the model for longer cables and higher number of cascaded cells. In this section, these problems were solved by developing a macromodel based on a closed-form solution. As described in section 4.2, a closed-form solution means that the cable is not divided into sections and therefore no cascading processes and no additional elements are required for higher accuracy. The differential equations of a shielded multiconductor cable over a ground plane are solved analytically.

For a constructive structure of this work, it was decided to first develop a macromodel in this section that only takes the conductive coupling into account and later to expand the model to include the field coupling. Therefore, in sections 5.2.1, the transmission line equations for conductive coupling were solved. A macromodel for conductive coupling followed in section 5.2.2. Model validation of conductive coupling was performed in section 5.2.3. The developed macromodel can calculate immunity and emission tests, as the bidirectional

coupling between the inner and the outer system is taken into account.

5.2.1 Conductive Coupling Solution

Two types of coupling are considered in Fig. 5.3: the conductive coupling due to a lumped source and the field coupling due to the incident plane wave. Only conductive coupling is considered in this section, which means that the cause of the disturbance is due to a lumped source rather than an incident wave. An example of conductive coupling is when the voltage source V_2 in Fig. 5.3 is active, the current on the outer side of the shield induces a voltage in the inner system.

Inner System

The differential equation, which only takes into account the conductive coupling of the inner system for a shielded cable with n inner conductors, was derived from Fig. 5.1 in (5.4). It is rewritten here as follows:

$$\frac{\mathrm{d}}{\mathrm{d}z}\begin{bmatrix}\boldsymbol{V}_{\mathrm{ic}}(z)\\ \boldsymbol{I}_{\mathrm{ic}}(z)\end{bmatrix} = \begin{bmatrix}0 & -\mathrm{j}\omega\boldsymbol{L}'_{\mathrm{i}}\\ -\mathrm{j}\omega\boldsymbol{C}'_{\mathrm{i}} & 0\end{bmatrix}\begin{bmatrix}\boldsymbol{V}_{\mathrm{ic}}(z)\\ \boldsymbol{I}_{\mathrm{ic}}(z)\end{bmatrix} + \begin{bmatrix}\boldsymbol{V}'_{\mathrm{dic}}(z)\\ 0\end{bmatrix}. \tag{5.14}$$

The voltage vector $\boldsymbol{V}_{\mathrm{ic}}(z)$ and the current vector $\boldsymbol{I}_{\mathrm{ic}}(z)$ are those of the inner system, as defined in Fig. 5.1 without the c notation. The p.u.l. interference voltage vector $\boldsymbol{V}'_{\mathrm{dic}}(z)$ is given by

$$\boldsymbol{V}'_{\mathrm{dic}}(z) = \boldsymbol{Z}'_{\mathrm{t}} \cdot I_{\mathrm{oc}}(z). \tag{5.15}$$

The element $I_{\mathrm{oc}}(z)$ is the current in the outer system, as shown in Fig. 5.1 without the c notation. The solution of (5.14) becomes more difficult to solve due to the presence of the $n \times n$ full matrices $\boldsymbol{L}'_{\mathrm{i}}$ and $\boldsymbol{C}'_{\mathrm{i}}$, where the voltage and current of each wire affect all others through these matrices. In section 2.2.3, a method for decoupling the voltages and currents using the similarity transformation was presented. Similar to (2.85) and (2.86), $\boldsymbol{L}'_{\mathrm{i}}$ and $\boldsymbol{C}'_{\mathrm{i}}$ are diagonalized as follows:

$$\boldsymbol{L}'_{\mathrm{im}} = \boldsymbol{T}_{\mathrm{V}}^{-1} \cdot \boldsymbol{L}'_{\mathrm{i}} \cdot \boldsymbol{T}_{\mathrm{I}} \tag{5.16a}$$

$$\boldsymbol{C}'_{\mathrm{im}} = \boldsymbol{T}_{\mathrm{I}}^{-1} \cdot \boldsymbol{C}'_{\mathrm{i}} \cdot \boldsymbol{T}_{\mathrm{V}}. \tag{5.16b}$$

The $n \times n$ matrices $\boldsymbol{L}'_{\mathrm{im}}$ and $\boldsymbol{C}'_{\mathrm{im}}$ are diagonal, where the entries in the main diagonal represent the *eigenvalues*. The index m indicates the *modal* character of these matrices. The matrices $\boldsymbol{T}_{\mathrm{V}}$ and $\boldsymbol{T}_{\mathrm{I}}$ are auxiliary matrices that represent in their columns the *eigenvectors* of $\boldsymbol{L}'_{\mathrm{i}}\boldsymbol{C}'_{\mathrm{i}}$ and $\boldsymbol{C}'_{\mathrm{i}}\boldsymbol{L}'_{\mathrm{i}}$, respectively. As stated in (2.82) and (2.83), a change of variables is applied, where the voltage and current vectors are converted into *mode quantities* as

follows:

$$\boldsymbol{V}_{\mathrm{ic}}(z) = \boldsymbol{T}_{\mathrm{V}} \cdot \boldsymbol{V}_{\mathrm{icm}}(z) \tag{5.17a}$$

$$\boldsymbol{I}_{\mathrm{ic}}(z) = \boldsymbol{T}_{\mathrm{I}} \cdot \boldsymbol{I}_{\mathrm{icm}}(z). \tag{5.17b}$$

The vectors $\boldsymbol{V}_{\mathrm{icm}}(z)$ and $\boldsymbol{I}_{\mathrm{icm}}(z)$ represent *modal quantities* with decoupled elements. Substituting (5.17) into (5.14) leads to a *modal* differential equation system. Its solution is derived by applying the chain-parameter representation for a field coupled line as shown in (3.66) to (3.70). The solution at $z = \mathcal{L}$ is therefore given by

$$\begin{bmatrix} \boldsymbol{V}_{\mathrm{icm}}(\mathcal{L}) \\ \boldsymbol{I}_{\mathrm{icm}}(\mathcal{L}) \end{bmatrix} = \boldsymbol{\Phi}_{\mathrm{im}}(\mathcal{L}) \begin{bmatrix} \boldsymbol{V}_{\mathrm{icm}}(0) \\ \boldsymbol{I}_{\mathrm{icm}}(0) \end{bmatrix} + \begin{bmatrix} \boldsymbol{V}_{\mathrm{icrm}} \\ \boldsymbol{I}_{\mathrm{icrm}} \end{bmatrix}, \tag{5.18}$$

where the forcing function vectors $\boldsymbol{V}_{\mathrm{icrm}}$ and $\boldsymbol{I}_{\mathrm{icrm}}$ represent the disturbances at the cable end generated by coupling from the outer system. The *modal* chain-parameter matrix $\boldsymbol{\Phi}_{\mathrm{im}}(\mathcal{L})$ contains the following submatrices [17]:

$$\boldsymbol{\Phi}_{\mathrm{im11}}(\tau) = \frac{1}{2} \cdot \left(\mathrm{e}^{\mathrm{j}\omega\boldsymbol{\Lambda}\tau} + \mathrm{e}^{-\mathrm{j}\omega\boldsymbol{\Lambda}\tau} \right) \tag{5.19a}$$

$$\boldsymbol{\Phi}_{\mathrm{im12}}(\tau) = -\frac{1}{2} \cdot \boldsymbol{Z}_{\mathrm{Cim}} \left(\mathrm{e}^{\mathrm{j}\omega\boldsymbol{\Lambda}\tau} - \mathrm{e}^{-\mathrm{j}\omega\boldsymbol{\Lambda}\tau} \right) \tag{5.19b}$$

$$\boldsymbol{\Phi}_{\mathrm{im21}}(\tau) = -\frac{1}{2} \cdot \left(\mathrm{e}^{\mathrm{j}\omega\boldsymbol{\Lambda}\tau} - \mathrm{e}^{-\mathrm{j}\omega\boldsymbol{\Lambda}\tau} \right) \boldsymbol{Z}_{\mathrm{Cim}}^{-1} \tag{5.19c}$$

$$\boldsymbol{\Phi}_{\mathrm{im22}}(\tau) = \frac{1}{2} \cdot \left(\mathrm{e}^{\mathrm{j}\omega\boldsymbol{\Lambda}\tau} + \mathrm{e}^{-\mathrm{j}\omega\boldsymbol{\Lambda}\tau} \right). \tag{5.19d}$$

The term $\boldsymbol{Z}_{\mathrm{Cim}}$ is the *mode* characteristic impedance matrix. It is given for the kth inner conductor by

$$Z_{\mathrm{Cim}k} = \sqrt{\frac{L_{\mathrm{im}k}}{C_{\mathrm{im}k}}}. \tag{5.20}$$

The propagation constant matrix $\boldsymbol{\Lambda}$ in (5.19) is defined as [17]

$$\boldsymbol{\Lambda}^2 = \boldsymbol{T}_{\mathrm{I}}^{-1} \boldsymbol{C}_{\mathrm{i}} \boldsymbol{L}_{\mathrm{i}} \boldsymbol{T}_{\mathrm{I}}. \tag{5.21}$$

The vectors $\boldsymbol{V}_{\mathrm{icrm}}$ and $\boldsymbol{I}_{\mathrm{icrm}}$ in (5.18) are calculated in a similar way to the shielded single conductors and field-coupled line in (4.34) and (3.68), which are given by

$$\begin{bmatrix} \boldsymbol{V}_{\mathrm{icrm}} \\ \boldsymbol{I}_{\mathrm{icrm}} \end{bmatrix} = \int_0^{\mathcal{L}} \begin{bmatrix} \boldsymbol{\Phi}_{\mathrm{im11}}(\mathcal{L} - z) \boldsymbol{T}_{\mathrm{V}}^{-1} \boldsymbol{Z}_{\mathrm{t}}' I_{\mathrm{oc}}(z) \\ \boldsymbol{\Phi}_{\mathrm{im21}}(\mathcal{L} - z) \boldsymbol{T}_{\mathrm{I}}^{-1} \boldsymbol{Z}_{\mathrm{t}}' I_{\mathrm{oc}}(z) \end{bmatrix} \mathrm{d}z. \tag{5.22}$$

The matrices $\boldsymbol{T}_{\mathrm{V}}^{-1}$ and $\boldsymbol{T}_{\mathrm{I}}^{-1}$ are contained in (5.22) because the forcing functions were calculated in *modal* form, where $\boldsymbol{V}_{\mathrm{icrm}}(z) = \boldsymbol{T}_{\mathrm{V}}^{-1} \boldsymbol{V}_{\mathrm{icr}}(z)$ and $\boldsymbol{I}_{\mathrm{icrm}}(z) = \boldsymbol{T}_{\mathrm{I}}^{-1} \boldsymbol{I}_{\mathrm{icr}}(z)$ (see (5.17)).

Similar to (3.69) and (4.77), the solution at $z = 0$ can be derived by multiplying (5.18) by $\boldsymbol{\Phi}_{\mathrm{im}}(-\mathcal{L})$ and rearranging the equation as follows:

$$\begin{bmatrix} \boldsymbol{V}_{\mathrm{icm}}(0) \\ \boldsymbol{I}_{\mathrm{icm}}(0) \end{bmatrix} = \boldsymbol{\Phi}_{\mathrm{im}}(-\mathcal{L}) \begin{bmatrix} \boldsymbol{V}_{\mathrm{icm}}(\mathcal{L}) \\ \boldsymbol{I}_{\mathrm{icm}}(\mathcal{L}) \end{bmatrix} + \begin{bmatrix} \boldsymbol{V}_{\mathrm{iclm}} \\ \boldsymbol{I}_{\mathrm{iclm}} \end{bmatrix}. \tag{5.23}$$

Equation (5.23) shows the solution of n decoupled transmission lines plus the forcing functions $\boldsymbol{V}_{\mathrm{iclm}}$ and $\boldsymbol{I}_{\mathrm{iclm}}$ added. Similar to (4.29), the conductive forcing functions at $z = 0$ are given by

$$\begin{bmatrix} \boldsymbol{V}_{\mathrm{iclm}} \\ \boldsymbol{I}_{\mathrm{iclm}} \end{bmatrix} = -\int_0^{\mathcal{L}} \begin{bmatrix} \boldsymbol{\Phi}_{\mathrm{im11}}(-z)\boldsymbol{T}_{\mathrm{V}}^{-1}\boldsymbol{Z}_{\mathrm{t}}' I_{\mathrm{oc}}(z) \\ \boldsymbol{\Phi}_{\mathrm{im21}}(-z)\boldsymbol{T}_{\mathrm{I}}^{-1}\boldsymbol{Z}_{\mathrm{t}}' I_{\mathrm{oc}}(z) \end{bmatrix} \mathrm{d}z. \tag{5.24}$$

The current $I_{\mathrm{oc}}(z)$ in (5.22) and (5.24) can be represented analogously to (4.46) as follows:

$$I_{\mathrm{oc}}(z) = \Phi_{\mathrm{o21}}(z-\mathcal{L})V_{\mathrm{oc}}(\mathcal{L}) + \Phi_{\mathrm{o22}}(z-\mathcal{L})I_{\mathrm{oc}}(\mathcal{L}), \tag{5.25}$$

where the chain-parameter representation for two conductor lines was used. The chain-parameters $\Phi_{\mathrm{o21}}(z)$ and $\Phi_{\mathrm{o22}}(z)$ were defined in (4.25). Substituting (5.25) together with the chain parameters $\boldsymbol{\Phi}_{\mathrm{im21}}(z)$ and $\boldsymbol{\Phi}_{\mathrm{im22}}(z)$ from (5.19) into (5.24), the voltage response at $z = 0$ of the conductive coupling in *modal* form becomes

$$\begin{aligned} \boldsymbol{V}_{\mathrm{iclm}} = \quad & \frac{(\boldsymbol{T}_{\mathrm{V}}^{-1}\boldsymbol{Z}_{\mathrm{t}}')^{\boldsymbol{T}} \cdot V_{\mathrm{oc}}(0)}{Z_{\mathrm{Co}}} \int_0^{\mathcal{L}} \frac{\mathrm{e}^{\mathrm{j}\omega\boldsymbol{\Lambda}z} + \mathrm{e}^{-\mathrm{j}\omega\boldsymbol{\Lambda}z}}{2} \cdot \frac{\mathrm{e}^{\mathrm{j}\omega\gamma_{\mathrm{o}}z} - \mathrm{e}^{-\mathrm{j}\omega\gamma_{\mathrm{o}}z}}{2} \mathrm{d}z \\ & - (\boldsymbol{T}_{\mathrm{V}}^{-1}\boldsymbol{Z}_{\mathrm{t}}')^{\boldsymbol{T}} \cdot I_{\mathrm{oc}}(0) \int_0^{\mathcal{L}} \frac{\mathrm{e}^{\mathrm{j}\omega\boldsymbol{\Lambda}z} + \mathrm{e}^{-\mathrm{j}\omega\boldsymbol{\Lambda}z}}{2} \cdot \frac{\mathrm{e}^{\mathrm{j}\omega\gamma_{\mathrm{o}}z} + \mathrm{e}^{-\mathrm{j}\omega\gamma_{\mathrm{o}}z}}{2} \mathrm{d}z. \end{aligned} \tag{5.26}$$

The product $\boldsymbol{T}_{\mathbf{V}}^{-\mathbf{1}}\boldsymbol{Z}_{\mathbf{t}}'$ was transposed and taken outside the integral, since it is independent of the cable length. To return to the original values, a multiplication by $\boldsymbol{T}_{\mathrm{V}}$ is simply applied, where $\boldsymbol{V}_{\mathrm{icl}} = \boldsymbol{T}_{\mathrm{V}}\boldsymbol{V}_{\mathrm{iclm}}$, as defined in (5.17a). The voltage response of the kth conductor becomes

$$\begin{aligned} V_{\mathrm{icl}k} = \quad & \frac{Z_{tk}' \cdot V_{\mathrm{oc}}(0)}{Z_{\mathrm{Co}}} \int_0^{\mathcal{L}} \frac{\mathrm{e}^{\mathrm{j}\omega\Lambda_k z} + \mathrm{e}^{-\mathrm{j}\omega\Lambda_k z}}{2} \cdot \frac{\mathrm{e}^{\mathrm{j}\omega\gamma_{\mathrm{o}}z} - \mathrm{e}^{-\mathrm{j}\omega\gamma_{\mathrm{o}}z}}{2} \mathrm{d}z \\ & - Z_{tk}' \cdot I_{\mathrm{oc}}(0) \int_0^{\mathcal{L}} \frac{\mathrm{e}^{\mathrm{j}\omega\Lambda_k z} + \mathrm{e}^{-\mathrm{j}\omega\Lambda_k z}}{2} \cdot \frac{\mathrm{e}^{\mathrm{j}\omega\gamma_{\mathrm{o}}z} + \mathrm{e}^{-\mathrm{j}\omega\gamma_{\mathrm{o}}z}}{2} \mathrm{d}z. \end{aligned} \tag{5.27}$$

Comparing this solution with the single conductor one shown in (4.51) and (4.59), it can be seen that they are identical with change of variables. Therefore, the equivalent circuit of $V_{\mathrm{icl}k}$ can be interpreted directly from Fig. 4.10.

The remaining conductive forcing functions I_{icrm}, V_{iclm} and I_{iclm} in (5.22) and (5.24) gave the same form too as for the single conductor cable in (4.59)-(4.62). Therefore their

calculations is omit here.

It has been proved so far that the solution of $V_{\mathrm{icl}k}$ of the kth conductor in (5.27) is the same for a single shielded line in (4.58) and thus the equivalent circuit in Fig. 4.10 is the same. It means the coupling behaviour on each conductor of the multiconductor shielded cable is identical to that of a single conductor shielded cable with change of parameters.

The closed-form solution of the inner system, considering only the conductive coupling, has been developed in (5.18) and (5.23) with the forcing functions in (5.22) and (5.24). Next, the closed-form solution of the outer system is developed.

Outer System

The transmission line equation for the outer system in Fig. 5.1, considering only conductive coupling, was presented in (5.10). It is a state-space equation that has the same form of a field-coupled line in (3.14). The equation was solved in (3.66) to (3.70). Its solution can easily be derived using the chain-parameter representation as outlined in (3.66) to (3.70), (4.24) and (4.28). The solution of the outer system at $z = 0$ is therefore given by

$$\begin{bmatrix} V_{\mathrm{oc}}(0) \\ I_{\mathrm{oc}}(0) \end{bmatrix} = \boldsymbol{\Phi}_{\mathbf{o}}(-\mathcal{L}) \begin{bmatrix} V_{\mathrm{oc}}(\mathcal{L}) \\ I_{\mathrm{oc}}(\mathcal{L}) \end{bmatrix} + \begin{bmatrix} V_{\mathrm{ocl}} \\ I_{\mathrm{ocl}} \end{bmatrix}. \tag{5.28}$$

The matrix $\boldsymbol{\Phi}_{\mathbf{o}}(\mathcal{L})$ represents the chain parameters of the outer system as given in (4.25). The same applies to the solution at $z = \mathcal{L}$. It is given by

$$\begin{bmatrix} V_{\mathrm{oc}}(\mathcal{L}) \\ I_{\mathrm{oc}}(\mathcal{L}) \end{bmatrix} = \boldsymbol{\Phi}_{\mathbf{o}}(\mathcal{L}) \begin{bmatrix} V_{\mathrm{oc}}(0) \\ I_{\mathrm{oc}}(0) \end{bmatrix} + \begin{bmatrix} V_{\mathrm{ocr}} \\ I_{\mathrm{ocr}} \end{bmatrix}. \tag{5.29}$$

The conductive forcing functions in (5.28) and (5.29), considering the influence of all inner conductors, are defined analogously to (4.27) and (4.29) as follows:

$$V_{\mathrm{ocr}} = \sum_{k=1}^{n} \left\{ \int_0^{\mathcal{L}} \Phi_{\mathrm{o}11}(\mathcal{L} - z)[\boldsymbol{Z}'_{\mathrm{t}}]_k[\boldsymbol{I}_{\mathrm{ic}}(z)]_k \,\mathrm{d}z \right\} \tag{5.30a}$$

$$I_{\mathrm{ocr}} = \sum_{k=1}^{n} \left\{ \int_0^{\mathcal{L}} \Phi_{\mathrm{o}21}(\mathcal{L} - z)[\boldsymbol{Z}'_{\mathrm{t}}]_k[\boldsymbol{I}_{\mathrm{ic}}(z)]_k \,\mathrm{d}z \right\} \tag{5.30b}$$

$$V_{\mathrm{ocl}} = -\sum_{k=1}^{n} \left\{ \int_0^{\mathcal{L}} \Phi_{\mathrm{o}11}(-z)[\boldsymbol{Z}'_{\mathrm{t}}]_k[\boldsymbol{I}_{\mathrm{ic}}(z)]_k \,\mathrm{d}z \right\} \tag{5.30c}$$

$$I_{\mathrm{ocl}} = -\sum_{k=1}^{n} \left\{ \int_0^{\mathcal{L}} \Phi_{\mathrm{o}21}(-z)[\boldsymbol{Z}'_{\mathrm{t}}]_k[\boldsymbol{I}_{\mathrm{ic}}(z)]_k \,\mathrm{d}z \right\}. \tag{5.30d}$$

Comparing (5.28) to (5.30) with those of the single conductor shielded cable in (4.24) and (4.27) to (4.29), they have the same form, with the sum in (5.30) taking into account multiple inner conductors. Therefore, the solution of the forcing function $V_{\mathrm{ocl}k}$ in (5.30c)

considering the kth inner conductor can be obtained from (4.58) as follows:

$$
\begin{aligned}
V_{\mathrm{ocl}k}(t) = \frac{L'_{\mathrm{t}k}}{4Z_{\mathrm{Cim}k}\left(\xi_{\mathrm{i}}^2 - \xi_{\mathrm{o}}^2\right)} \Bigg[& \\
& \Big(\xi_{\mathrm{i}} - \xi_{\mathrm{o}}\Big) \cdot \Big(v_{\mathrm{i}} - 2V_{\mathrm{icm}k}\big(0,t\big)\Big) + \Big(\xi_{\mathrm{i}} + \xi_{\mathrm{o}}\Big) \cdot \Big(v_{\mathrm{iii}} - 2V_{\mathrm{icm}k}\big(0,t\big)\Big) \Bigg] \\
+ \frac{R'_{\mathrm{t}}}{4Z_{\mathrm{Cim}k}\left(\xi_{\mathrm{i}}^2 - \xi_{\mathrm{o}}^2\right)} & \Big[\Big(\xi_{\mathrm{i}} - \xi_{\mathrm{o}}\Big) \cdot \Big(v_{\mathrm{ii}} - 2v_{\mathrm{v}}\Big) + \Big(\xi_{\mathrm{i}} + \xi_{\mathrm{o}}\Big) \cdot \Big(v_{\mathrm{iv}} - 2v_{\mathrm{v}}\Big)\Big] \\
+ \frac{L'_{\mathrm{t}k}}{4\left(\xi_{\mathrm{i}}^2 - \xi_{\mathrm{o}}^2\right)} & \Big[\Big(\xi_{\mathrm{i}} - \xi_{\mathrm{o}}\Big) \cdot i_{\mathrm{i}} + \Big(\xi_{\mathrm{i}} + \xi_{\mathrm{o}}\Big) \cdot i_{\mathrm{iii}}\Big] \\
+ \frac{R'_{\mathrm{t}}}{4\left(\xi_{\mathrm{i}}^2 - \xi_{\mathrm{o}}^2\right)} & \Big[\Big(\xi_{\mathrm{i}} - \xi_{\mathrm{o}}\Big) \cdot i_{\mathrm{ii}} + \Big(\xi_{\mathrm{i}} + \xi_{\mathrm{o}}\Big) \cdot i_{\mathrm{iv}}\Big].
\end{aligned}
\tag{5.31}
$$

The calculation steps of $V_{\mathrm{ocl}k}$ were shown in (4.51) to (4.55), where a transformation into the time domain was applied in (4.58). The time domain solution was adopted in (5.31). The parameters v_{i} to v_{v} and i_{i} to i_{iv} represent the time-delayed *mode* voltages and currents of the kth conductor $V_{\mathrm{icm}k}(0)$ and $I_{\mathrm{icm}k}(0)$ with respect to the shield. The elements ξ_{i} and ξ_{o} were defined in (4.53) and (4.54), $Z_{\mathrm{Cim}k}$ is the *mode* characteristic impedance of the kth conductor, as defined in (5.20). The equivalent circuit diagram of $V_{\mathrm{ocl}k}(t)$ is the same as that shown in Fig. 4.10. The forcing functions V_{ocr}, I_{ocr}, and I_{ocl} in (5.30) can be evolved in a similar way, but their representation is omitted here for reasons of space and redundancy.

So far, the closed-form solution of the outer system, which considers only the conductive coupling, has been developed in (5.28) and (5.29) with the forcing functions in (5.30). The closed-form solution was also derived for the inner system in an earlier section. A macromodel can now be developed from these solutions, which is presented in the next section.

5.2.2 Macromodel for Conductive Analyses

From the closed-form solutions of the inner and outer systems presented in (5.18), (5.23), (5.28) and (5.29) a macromodel of the shielded multiconductor cable in Fig. 5.1 is derived in this section, in which only the conductive coupling is taken into account.

Comparing the solution of the outer system in (5.28) and (5.29) with that in (2.42), one finds that both equations represent the solution for the voltage and current at the terminals of a transmission line with length $\mathcal{L}$, to which the forcing functions are added. Similar to the work done in Fig. 4.9, these solutions were represented in the macromodel in Fig. 5.7 as a transmission line with controlled sources at the ends. The voltages $V_{\mathrm{oc}}(0)$, $V_{\mathrm{oc}}(\mathcal{L})$ and

currents $I_{\mathrm{oc}}(0)$, $I_{\mathrm{oc}}(\mathcal{L})$ in Fig. 5.7 are those between the shield and the ground plane at $z = 0$ and $z = \mathcal{L}$. They can be compared in Fig. 5.1. The element T_{o} in Fig. 5.7 is the one-way time delay of the outer system as defined in (4.30). The characteristic impedance Z_{Co} has been defined in (4.26). The forcing functions V_{ocr}, V_{ocl}, I_{ocr} and I_{ocl} from (5.30)

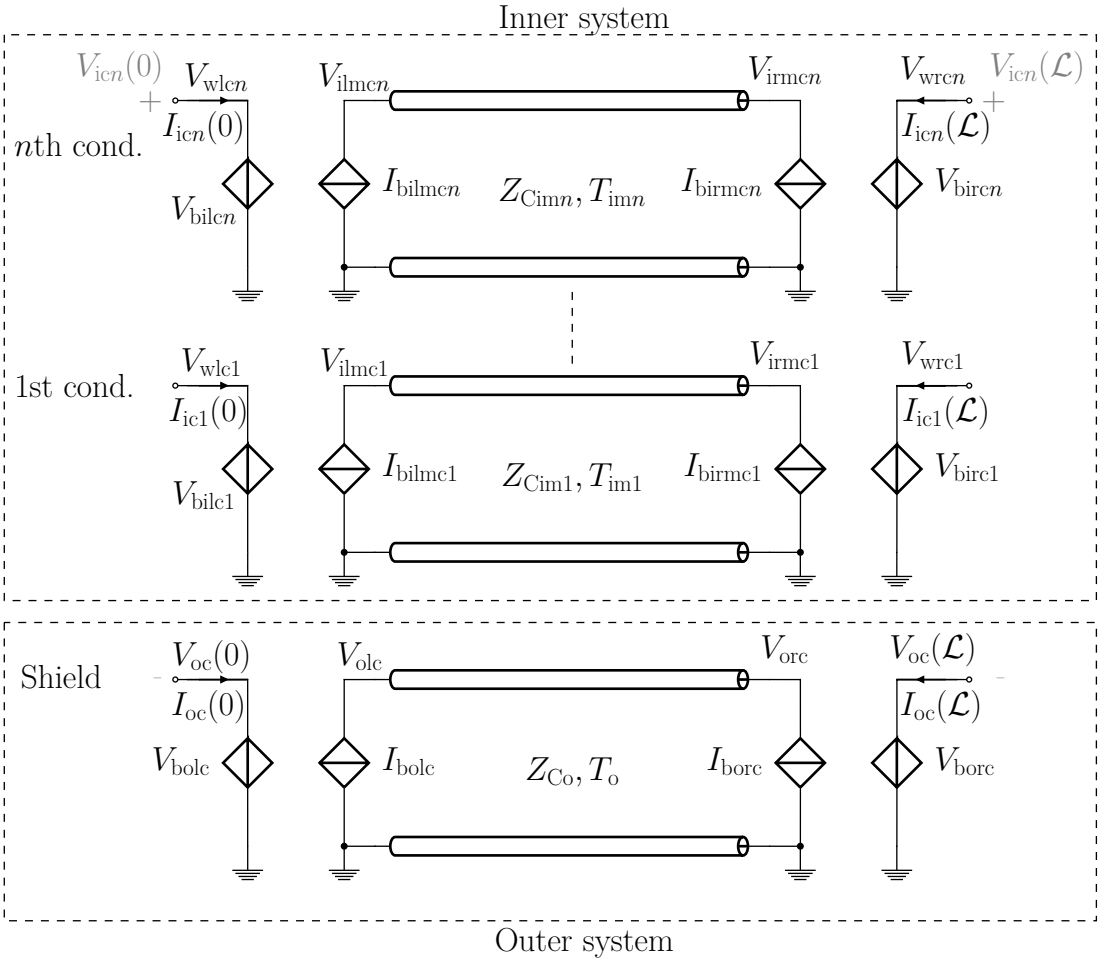

Figure 5.7: Macromodel based on a closed-form solution for conductive analysis of a shielded multiconductor cable over a perfectly conducting ground plane.

are combined using the Thevenin and Norton sources as explained in (3.78) and (3.79), where

$$V_{\mathrm{ocrT}} = \frac{1}{2} \cdot \left(V_{\mathrm{ocr}} + Z_{\mathrm{Co}} I_{\mathrm{ocr}} \right) \tag{5.32a}$$

$$V_{\mathrm{oclT}} = \frac{1}{2} \cdot \left(V_{\mathrm{ocl}} + Z_{\mathrm{Co}} I_{\mathrm{ocl}} \right). \tag{5.32b}$$

The advantage in (5.32) is that the currents I_{ocr}, I_{ocl} and voltages V_{ocr}, V_{ocl} are expressed only in the form of voltages V_{ocrT} and V_{oclT}. These forcing functions are part of the solution in (5.28) and (5.29) and are therefore added to the controlled sources in Fig. 5.7 analogous

to (4.41) as follows:

$$V_{\mathrm{bolc}} = V_{\mathrm{olc}} + V_{\mathrm{oclT}} \tag{5.33a}$$

$$I_{\mathrm{bolc}} = I_{\mathrm{oc}}(0) + \sum_{k=1}^{n} I_{\mathrm{ic}k}(0) + V_{\mathrm{oclT}}/Z_{\mathrm{Co}} \tag{5.33b}$$

$$V_{\mathrm{borc}} = V_{\mathrm{orc}} + V_{\mathrm{ocrT}} \tag{5.33c}$$

$$I_{\mathrm{borc}} = I_{\mathrm{oc}}(\mathcal{L}) + \sum_{k=1}^{n} I_{\mathrm{ic}k}(\mathcal{L}) + V_{\mathrm{ocrT}}/Z_{\mathrm{Co}}. \tag{5.33d}$$

The indices b, o, l and c have been defined before. For example, V_{bolc} represents the behavior voltage source of the outer system on the left side for conductive coupling. A comparison of Fig. 5.7 with Fig. 5.1 facilitates the interpretation of (5.33).

The solution of the inner system was presented in *modal* form in (5.18) and (5.23). These solutions have the same form as for field-coupled multiconductor lines, which were formed in SPICE by building n independent *modal* TLs coupled at their ends via controlled sources [18]. The same approach can be applied here by constructing n TLs in Fig. 5.7 that contain the *modal* characteristic from (5.19). The coupling between the lines is achieved via the controlled sources at the ends in $V_{\mathrm{bilc1\ldots}n}$, $V_{\mathrm{birc1\ldots}n}$, $I_{\mathrm{birmc1\ldots}n}$ and $I_{\mathrm{bilmc1\ldots}n}$.
The controlled sources of the kth conductor are defined analogous to (4.39) as follows:

$$V_{\mathrm{bilc}k} = \sum_{u=1}^{n} \left\{ [\boldsymbol{T}_{\mathrm{V}}]_{ku} [\boldsymbol{V}_{\mathrm{ilmc}}]_u \right\} + V_{\mathrm{iclT}k} + V_{\mathrm{oc}}(0) \tag{5.34a}$$

$$V_{\mathrm{birc}k} = \sum_{u=1}^{n} \left\{ [\boldsymbol{T}_{\mathrm{V}}]_{ku} [\boldsymbol{V}_{\mathrm{irmc}}]_u \right\} + V_{\mathrm{icrT}k} + V_{\mathrm{oc}}(\mathcal{L}) \tag{5.34b}$$

$$I_{\mathrm{bilmc}k} = \sum_{u=1}^{n} \left\{ [\boldsymbol{T}_{\mathrm{I}}^{-1}]_{ku} [\boldsymbol{I}_{\mathrm{ic}}]_u(0) + \frac{[\boldsymbol{T}_{\mathrm{I}}^{-1}]_{ku} [\boldsymbol{V}_{\mathrm{iclT}}]_u}{[\boldsymbol{Z}_{\mathrm{Cim}}]_u} \right\} \tag{5.34c}$$

$$I_{\mathrm{birmc}k} = \sum_{u=1}^{n} \left\{ [\boldsymbol{T}_{\mathrm{I}}^{-1}]_{ku} [\boldsymbol{I}_{\mathrm{ic}}]_u(\mathcal{L}) + \frac{[\boldsymbol{T}_{\mathrm{I}}^{-1}]_{ku} [\boldsymbol{V}_{\mathrm{icrT}}]_u}{[\boldsymbol{Z}_{\mathrm{Cim}}]_u} \right\}. \tag{5.34d}$$

The transformation of the *mode* voltages and currents to the actual quantities is done in $V_{\mathrm{bilc}k}$ and $V_{\mathrm{birc}k}$ in Fig. 5.7 according to (5.17). For example, the transformation into actual voltages is achieved in (5.34a) with $\sum_{u=1}^{n} \left\{ [\boldsymbol{T}_{\mathrm{V}}]_{ku} [\boldsymbol{V}_{\mathrm{ilmc}}]_u \right\}$ according to (5.17). The forcing functions of the kth conductor $V_{\mathrm{iclT}k}$ and $V_{\mathrm{icrT}k}$ in (5.34) have the same form as that defined in (5.32), (3.78) and (3.79), taking into account the parameter changes due to the *modal* representation. They are given by

$$V_{\mathrm{iclT}k} = \frac{1}{2} \cdot \left(V_{\mathrm{icl}k} + Z_{\mathrm{Cim}k} \cdot I_{\mathrm{icl}k} \right) \tag{5.35a}$$

$$V_{\mathrm{icrT}k} = \frac{1}{2} \cdot \left(V_{\mathrm{icr}k} + Z_{\mathrm{Cim}k} \cdot I_{\mathrm{icr}k} \right), \tag{5.35b}$$

where $V_{\mathrm{icl}k}$ and $V_{\mathrm{icr}k}$ were defined in (5.22) and (5.24). The *modal* characteristic impedances Z_{Cim1} to $Z_{\mathrm{Cim}n}$ can be solved with (5.20). A comparison of the parameters can be carried out between Fig. 5.1 and 5.7. Here, for example, $V_{\mathrm{ic}n}(0)$ and $V_{\mathrm{ic}n}(\mathcal{L})$ are the voltages between the nth conductor to the shield at $z = 0$ and $z = \mathcal{L}$. The voltage V_{wrc1} is that between the 1st conductor and the ground plane, etc.
The transit time of the kth *modal* line in Fig. 5.7 is defined as

$$T_{\mathrm{im}k} = \frac{1}{v_{\mathrm{im}k}}, \tag{5.36}$$

where the propagation velocity $v_{\mathrm{im}k}$ is given by

$$v_{\mathrm{im}k} = \frac{1}{\sqrt{L'_{\mathrm{im}k} C'_{\mathrm{im}k}}}. \tag{5.37}$$

The inner system of a multiconductor shielded cable was developed in the SPICE environment on the basis of (5.18) and (5.23) as n TLs, which are coupled at the ends via controlled sources. The controlled sources were defined in (5.34). The inner system was thus fully developed.

In this section, a macromodel was developed to analyze the conductive coupling of multiconductor shielded cables. To execute the model, the primary line constants of the cable should be determined and included in (5.16a) and (5.16b) for diagonalization. In a later step, the *modal* characteristic impedance should first be calculated for each inner conductor using (5.20) and then inserted into Fig. 5.7. The time delays T_{im1} to $T_{\mathrm{im}n}$ of the inner system should also be solved from (5.36). For the outer system, the time delay and the characteristic impedance can be taken from (4.30) and (4.26). Application examples in time and frequency domain for this model are shown in the next section.

5.2.3 Model Validation of the Conductive Coupling

Field simulations and measurements are carried out to investigate the conductive coupling on the shielded cable. The macromodel developed in Fig. 5.7 is built in LTspice [35] for simulations. The CST Studio Suite 19 software [3] is used for field simulations. The setup in Figs. 3.9 and 3.10 is applied in CST, using a co-simulation to combine CST Microwave Studio and CST Cable Studio.

A commercially available balanced quad-core cable was used for the validation. The cable was positioned 1 cm above a ground plane (see Fig. 5.3). The parameters of the cable are given in section 5.1.3. To operate the macromodel defined in Fig. 5.7, the transformation matrices $\boldsymbol{T}_{\mathrm{V}}$ and $\boldsymbol{T}_{\mathrm{I}}$ were first calculated, as they appear in (5.16) and (5.34). They are

given by

$$\boldsymbol{T}_\mathrm{V} = \boldsymbol{T}_\mathrm{I} = \frac{1}{2}\begin{bmatrix} -1 & 1 & -1 & -1 \\ -1 & -1 & 1 & -1 \\ -1 & -1 & -1 & 1 \\ -1 & 1 & 1 & 1 \end{bmatrix}.$$

The *modal* characteristic impedances in Fig. 5.7 were calculated using (5.20), where $Z_{\mathrm{Cim1}} = 122.8\,\Omega$, $Z_{\mathrm{Cim2}} = 31.9\,\Omega$, $Z_{\mathrm{Cim3}} = 45.9\,\Omega$ and $Z_{\mathrm{Cim4}} = 45.9\,\Omega$. The transit time of the *modal* transmission lines was calculated using (5.36), where $T_{\mathrm{im1-4}} = 17.33\,\mathrm{ns}$ for all inner conductors. The characteristic impedance of the outer system Z_{Co} in Fig. 5.7 is equal to $104.5\,\Omega$.

Time Domain

A measurement was carried out with the setups shown in Fig. 5.8. The commercially available quad-core cable with a length of 3 m according to section 5.1.3 was measured.

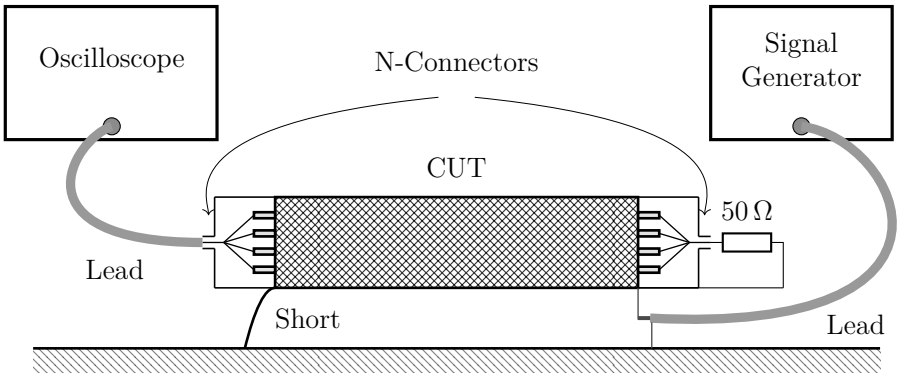

Figure 5.8: Measurement setup in the time domain of a shielded multiconductor cable.

It has been found that the measurements provide useful results when performed in a closed system with the inner conductors always remaining under the shield. This was achieved by joining the inner conductors together and connecting them to the pin of an N-connector, where the cable shield was directly attached to the outer conductor of the connector, as shown in Fig. 5.8. The cable under test (CUT) was placed over a ground plane using insulating material. On the right-hand side, a $50\,\Omega$ coaxial load was connected between the inner conductors and the shield, as shown in Fig. 5.8. At the left-hand side, the shield was grounded with a copper tape, this is realized in the simulation with a resistance of $10\,\mathrm{m}\Omega$. A $0\,/10\,\mathrm{V}$ square wave with a rise and fall time of 8 ns was fed using a signal generator. The holding time is 50 ns. The voltage response was measured at the left end between the wires and the shield with an oscilloscope.

The results are compared with those of the macromodel and CST in Fig. 5.9. The measured

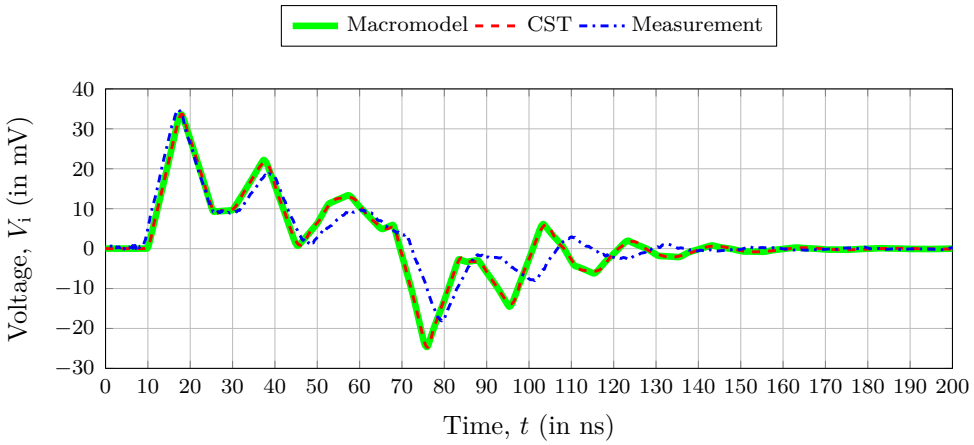

Figure 5.9: Voltage response between the connected inner conductors and shield for the quad-core cable.

curves are attenuated faster over time. This effect occurs because the CUT contains losses that are not taken into account in the simulations. These losses are caused by ohmic losses, including skin effect, eddy currents and dielectric losses. One can also observe a slight shift of the maxima and minima over the time axis. These deviations can occur due to the inaccurate known electrical properties of the inner insulating material and the jacket material of the CUT. The specified materials from the data sheet have been used for simulations.

Frequency Domain

The defined quad-core cable in section 5.1.3 with a length of 3 m was also used for frequency domain measurements. The measurement setup is shown in Fig. 5.10. A vector network analyzer was used for the measurement. Port 1 was connected at the left end between wires and shield. Port 2 was connected to the right end between shield and ground. The measuring cables named *Leads* were calibrated out during the measurement. To obtain a

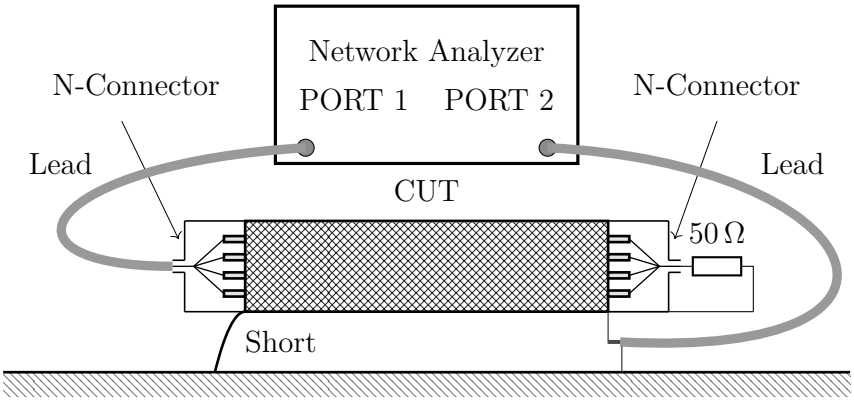

Figure 5.10: Measurement setup in the frequency domain of a shielded multiconductor cable.

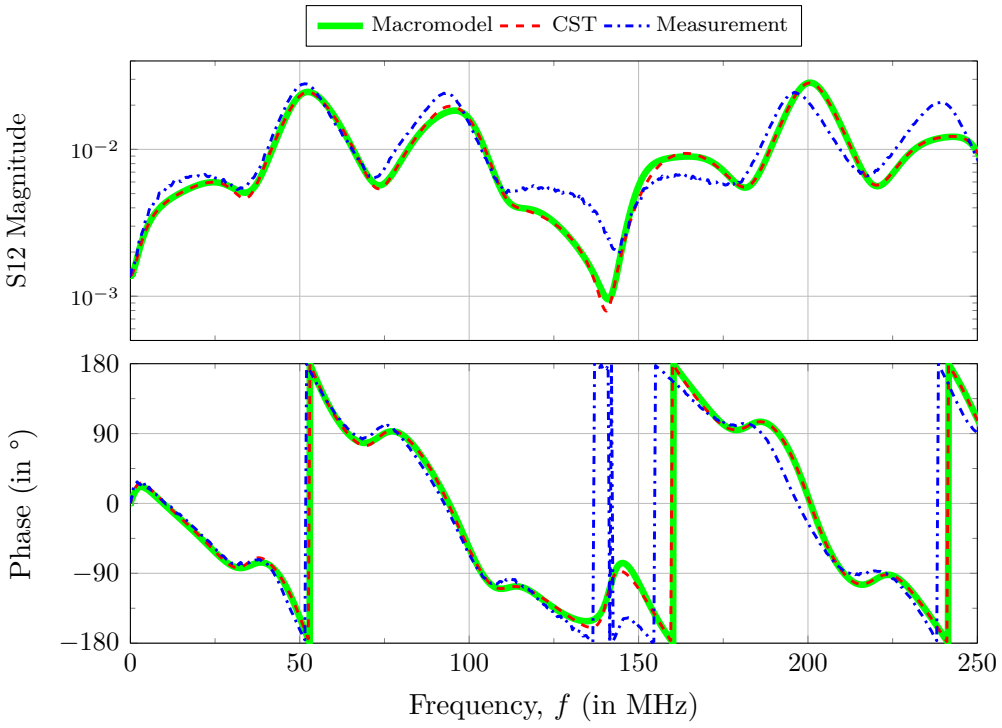

Figure 5.11: Measurement of the transmission coefficient S_{12} for the quad-core cable.

closed system, all inner conductors were joined together at the cable ends and connected to the pins of the N-connectors, as shown in Fig. 5.10.

A frequency sweep was performed between 10 kHz and 250 MHz with 1050 points. The transmission parameter S_{12} were measured as shown in Fig. 5.11. The results agree well, as can be seen. The measured magnitude is attenuated via the frequency, whereas the simulation models do not take cable losses into account. The phase shows a slight shift at some frequencies. As interpreted in the time domain measurement, these deviations can occur due to the inaccurate known electrical properties of the inner insulating material and the jacket material of the measured cable. A phase change from $-180°$ to $180°$ can be observed at about 140 MHz. The reason is that in this area the imaginary part of S_{12} is close to zero, due to small deviations it is polarized with positive and negative values.

So far, the macromodel of a multiconductor shielded cable has been developed and validated for conductive coupling. The field coupling will be considered next.

5.3 Macromodel for the Analysis of Field Coupling

In this section, the field coupling is considered and the model from Fig. 5.7 is extended accordingly. The developed macromodel in this section can calculate the voltage response at the loads of a shielded cable due to the coupling of an incident plane wave. In addition, emission tests can be carried out, as the bidirectional coupling between the inner and

the outer system is taken into account. The model can therefore calculate the field and conductive coupling, as will be shown later. The extension of the transmission line equations with field coupling is done in section 5.3.1. The macromodel including field coupling is presented in section 5.3.2. Model validation of field coupling is performed in section 5.3.3.

5.3.1 Field Coupling Solution

In this section, the previously calculated closed-form solutions are extended to include the field coupling of an incident plane wave. The solutions are presented separately for the outer and inner systems of a multiconductor shielded cable.

Outer System

In the field coupling calculations, the coaxial cable above the ground plane in section 4.3.1 was assumed to be a single conductor. The same assumptions can be made for the multiconductor cable. The field coupling to the outer system is therefore independent of whether the cable has one or more conductors within the shield. This means that the differential equations of the coaxial cable in (4.12) and the solutions calculated in (4.67), (4.68) also apply to the shielded multiconductor cable. The voltage response of a field-coupled cable was determined for matched terminations in (4.67), (4.68). It is rewritten here as follows:

$$V_{\mathrm{oflM}}(t) = -h\Big[E_0(t) - E_0(t - T_{\mathrm{o}} - T_{\mathrm{oz}})\Big] \tag{5.38a}$$

$$V_{\mathrm{ofrM}}(t) = -h\Big[E_0(t - T_{\mathrm{o}}) - E_0(t - T_{\mathrm{oz}})\Big], \tag{5.38b}$$

where $V_{\mathrm{oflM}}(t)$ is the voltage response at the left-hand side of the outer system and $V_{\mathrm{ofrM}}(t)$ is that at the right-hand side. The parameters T_{o} and T_{oz} represent the one-way time delay of the outer system and that along the z-axis as defined in (4.30) and (4.69). The parameter $E_0(t)$ represents the electric field of the incident wave and h is the height of the cable above the ground plane, as shown in Fig. 5.1. The circuit model of V_{oflM} and V_{ofrM}, can be seen directly from Fig. 4.16. The coupling response of an incident plane wave to a shielded multiconductor cable can therefore be calculated at the ends of the outer system with (5.38) and Fig. 4.16.

To extend the presented solution in (5.28) and (5.29) with field coupling, V_{oflM} and V_{ofrM}

from (5.38) must be added as follows:

$$\begin{bmatrix} V_\mathrm{o}(\mathcal{L}) \\ I_\mathrm{o}(\mathcal{L}) \end{bmatrix} = \mathbf{\Phi_o}(\mathcal{L}) \begin{bmatrix} V_\mathrm{o}(0) \\ I_\mathrm{o}(0) \end{bmatrix} + \begin{bmatrix} V_\mathrm{ocr} + V_\mathrm{ofrM} \\ I_\mathrm{ocr} \end{bmatrix} \tag{5.39}$$

$$\begin{bmatrix} V_\mathrm{o}(0) \\ I_\mathrm{o}(0) \end{bmatrix} = \mathbf{\Phi_o}(-\mathcal{L}) \begin{bmatrix} V_\mathrm{o}(\mathcal{L}) \\ I_\mathrm{o}(\mathcal{L}) \end{bmatrix} + \begin{bmatrix} V_\mathrm{ocl} + V_\mathrm{oflM} \\ I_\mathrm{ocl} \end{bmatrix}. \tag{5.40}$$

The elements $V_\mathrm{o}(0)$, $I_\mathrm{o}(0)$, $V_\mathrm{o}(\mathcal{L})$ and $I_\mathrm{o}(\mathcal{L})$ represent the voltage and current of the outer system at $z = 0$ and $z = \mathcal{L}$, as shown in Fig. 5.1. The parameters V_ocr, I_ocr, V_ocl and I_ocl are the forcing functions due to the conductive coupling as shown in (5.30).
It can be clearly seen that the solution in (5.39) and (5.40) has the same form as for the shielded single line in (5.28) and (5.29). Therefore, the macromodel of the outer system for a shielded multiconductor cable in Fig. 5.12 can simply be taken from that of a single conductor cable in Fig. 5.7. The circuit labeled "Circuit for I_ocf" in Fig. 5.12 represents the electrical current $I_\mathrm{ocf}(z)$. It is the current $I_\mathrm{oc}(z)$ given by a concentrated source in the outer system, along with the reflection response of the field coupled current, as described in section 4.2.2. It was proved so far that the solution in (5.39) and (5.40) is that for the outer system with field coupling extension.

In this section, the field coupling solution was extended for the outer system of a shielded multiconductor cable. Its circuit model in Fig. 5.12 is taken directly from that of a single conductor cable, since both have the same solution. Next, the field coupling is integrated into the inner system.

Inner System

The differential equation of the inner system for a shielded cable with n inner conductors in Fig. 5.1 was shown in (5.4). It is rewritten here, including the field and conductive coupling, as follows:

$$\frac{\mathrm{d}}{\mathrm{d}z} \begin{bmatrix} \boldsymbol{V}_\mathrm{i}(z) \\ \boldsymbol{I}_\mathrm{i}(z) \end{bmatrix} = \begin{bmatrix} 0 & -\mathrm{j}\omega \boldsymbol{L}'_\mathrm{i} \\ -\mathrm{j}\omega \boldsymbol{C}'_\mathrm{i} & 0 \end{bmatrix} \begin{bmatrix} \boldsymbol{V}_\mathrm{i}(z) \\ \boldsymbol{I}_\mathrm{i}(z) \end{bmatrix} + \begin{bmatrix} \boldsymbol{V}'_\mathrm{di}(z) \\ 0 \end{bmatrix}, \tag{5.41}$$

where the p.u.l. interference voltage vector $\boldsymbol{V}'_\mathrm{di}(z)$ is given by

$$\boldsymbol{V}'_\mathrm{di}(z) = \boldsymbol{Z}'_\mathrm{t} \cdot I_\mathrm{o}(z) = \boldsymbol{Z}'_\mathrm{t} \cdot \Big(I_\mathrm{ofM}(z) + I_\mathrm{ocf}(z) \Big). \tag{5.42}$$

The current of the outer system $I_\mathrm{o}(z)$ in Fig. 5.1 has been divided into two parts, $I_\mathrm{ofM}(z)$ and $I_\mathrm{ocf}(z)$, as described in section 4.3.1. The current $I_\mathrm{ofM}(z)$ is generated by field coupling on the outer system with matched termination loads, as shown in (4.63). The electric current $I_\mathrm{ocf}(z)$ comprises the conductive current $I_\mathrm{oc}(z)$ in the outer system together with

the reflection response of the field-coupled current.

The solution of (5.41) becomes more difficult to solve due to the presence of the $n \times n$ full matrices $\boldsymbol{L}'_{\mathrm{i}}$ and $\boldsymbol{C}'_{\mathrm{i}}$, where the voltage and current of each wire affect all others through these matrices. In section 5.3.1, a method was presented to decouple the voltages and currents using the similarity transformation.

Since the differential equation system (5.41) has the same mathematical form as (5.14), the solution of the first can be simply taken from (5.18) and (5.23) with extension of the field coupling. Hence the solution of (5.41) can be written as follows:

$$\begin{bmatrix} \boldsymbol{V}_{\mathrm{im}}(\mathcal{L}) \\ \boldsymbol{I}_{\mathrm{im}}(\mathcal{L}) \end{bmatrix} = \boldsymbol{\Phi}_{\mathrm{im}}(\mathcal{L}) \begin{bmatrix} \boldsymbol{V}_{\mathrm{im}}(0) \\ \boldsymbol{I}_{\mathrm{im}}(0) \end{bmatrix} + \begin{bmatrix} \boldsymbol{V}_{\mathrm{icrm}} + \boldsymbol{V}_{\mathrm{ifrm}} \\ \boldsymbol{I}_{\mathrm{icrm}} + \boldsymbol{I}_{\mathrm{ifrm}} \end{bmatrix} \tag{5.43}$$

$$\begin{bmatrix} \boldsymbol{V}_{\mathrm{im}}(0) \\ \boldsymbol{I}_{\mathrm{im}}(0) \end{bmatrix} = \boldsymbol{\Phi}_{\mathrm{im}}(-\mathcal{L}) \begin{bmatrix} \boldsymbol{V}_{\mathrm{im}}(\mathcal{L}) \\ \boldsymbol{I}_{\mathrm{im}}(\mathcal{L}) \end{bmatrix} + \begin{bmatrix} \boldsymbol{V}_{\mathrm{iclm}} + \boldsymbol{V}_{\mathrm{iflm}} \\ \boldsymbol{I}_{\mathrm{iclm}} + \boldsymbol{I}_{\mathrm{iflm}} \end{bmatrix}. \tag{5.44}$$

The vectors $\boldsymbol{V}_{\mathrm{im}}(z)$ and $\boldsymbol{I}_{\mathrm{im}}(z)$ represent *modal quantities* with decoupled elements, as described in section 5.3.1. The *modal* chain-parameter matrix $\boldsymbol{\Phi}_{\mathrm{im}}(z)$ was defined in (5.19). The forcing function vectors $\boldsymbol{V}_{\mathrm{icrm}}$, $\boldsymbol{V}_{\mathrm{ifrm}}$, $\boldsymbol{I}_{\mathrm{icrm}}$, $\boldsymbol{I}_{\mathrm{ifrm}}$, $\boldsymbol{V}_{\mathrm{iclm}}$, $\boldsymbol{V}_{\mathrm{iflm}}$, $\boldsymbol{I}_{\mathrm{iclm}}$ and $\boldsymbol{I}_{\mathrm{iflm}}$ in (5.43) and (5.44) represent the resulting disturbances at the cable end, including the field and the conductive coupling. The conductive forcing functions were calculated in (5.22) and (5.24). They are rewritten here depending on $I_{\mathrm{ocf}}(z)$:

$$\begin{bmatrix} \boldsymbol{V}_{\mathrm{icrm}} \\ \boldsymbol{I}_{\mathrm{icrm}} \end{bmatrix} = \int_0^{\mathcal{L}} \begin{bmatrix} \boldsymbol{\Phi}_{\mathrm{im11}}(\mathcal{L}-z)\boldsymbol{T}_{\mathrm{V}}^{-1}\boldsymbol{Z}'_{\mathrm{t}} I_{\mathrm{ocf}}(z) \\ \boldsymbol{\Phi}_{\mathrm{im21}}(\mathcal{L}-z)\boldsymbol{T}_{\mathrm{I}}^{-1}\boldsymbol{Z}'_{\mathrm{t}} I_{\mathrm{ocf}}(z) \end{bmatrix} \mathrm{d}z \tag{5.45}$$

$$\begin{bmatrix} \boldsymbol{V}_{\mathrm{iclm}} \\ \boldsymbol{I}_{\mathrm{iclm}} \end{bmatrix} = -\int_0^{\mathcal{L}} \begin{bmatrix} \boldsymbol{\Phi}_{\mathrm{im11}}(-z)\boldsymbol{T}_{\mathrm{V}}^{-1}\boldsymbol{Z}'_{\mathrm{t}} I_{\mathrm{ocf}}(z) \\ \boldsymbol{\Phi}_{\mathrm{im21}}(-z)\boldsymbol{T}_{\mathrm{I}}^{-1}\boldsymbol{Z}'_{\mathrm{t}} I_{\mathrm{ocf}}(z) \end{bmatrix} \mathrm{d}z. \tag{5.46}$$

In (5.27), it has been proven that the forcing function of conductive coupling for the kth inner conductor $V_{\mathrm{icl}k}$ has an identical solution to that shown in (4.51) and (4.59) for a single conductor cable. The equivalent circuit of $V_{\mathrm{icl}k}$ was therefore interpreted directly from Fig. 4.10. It was also interpreted that the conductive forcing functions $\boldsymbol{I}_{\mathrm{icrm}}$, $\boldsymbol{V}_{\mathrm{iclm}}$ and $\boldsymbol{I}_{\mathrm{iclm}}$ in (5.22) and (5.24) have the same form as for the shielded cable in (4.59)-(4.62). Therefore their calculation is not necessary here.

The field forcing functions on the right-hand side of the cable are solved analogous to (4.76) with

$$\begin{bmatrix} \boldsymbol{V}_{\mathrm{ifrm}} \\ \boldsymbol{I}_{\mathrm{ifrm}} \end{bmatrix} = \int_0^{\mathcal{L}} \begin{bmatrix} \boldsymbol{\Phi}_{\mathrm{im11}}(\mathcal{L}-z)\boldsymbol{T}_{\mathrm{V}}^{-1}\boldsymbol{Z}'_{\mathrm{t}} I_{\mathrm{ofM}}(z) \\ \boldsymbol{\Phi}_{\mathrm{im21}}(\mathcal{L}-z)\boldsymbol{T}_{\mathrm{I}}^{-1}\boldsymbol{Z}'_{\mathrm{t}} I_{\mathrm{ofM}}(z) \end{bmatrix} \mathrm{d}z. \tag{5.47}$$

The field forcing functions on the left-hand side of the cable are defined analogously to (4.79) as follows:

$$\begin{bmatrix} \boldsymbol{V}_{\mathrm{iflm}} \\ \boldsymbol{I}_{\mathrm{ifrm}} \end{bmatrix} = -\int_0^{\mathcal{L}} \begin{bmatrix} \boldsymbol{\Phi}_{\mathrm{im11}}(-z)\boldsymbol{T}_{\mathrm{V}}^{-1}\boldsymbol{Z}'_{\mathrm{t}} I_{\mathrm{ofM}}(z) \\ \boldsymbol{\Phi}_{\mathrm{im21}}(-z)\boldsymbol{T}_{\mathrm{I}}^{-1}\boldsymbol{Z}'_{\mathrm{t}} I_{\mathrm{ofM}}(z) \end{bmatrix} \mathrm{d}z. \tag{5.48}$$

The forcing functions in (5.47) and (5.48) exist in *modal* form with $\boldsymbol{V}_{\mathrm{ifr,lm}}(z) = \boldsymbol{T}_{\mathrm{V}}^{-1}\boldsymbol{V}_{\mathrm{ifr,l}}(z)$, $\boldsymbol{I}_{\mathrm{ifr,lm}}(z) = \boldsymbol{T}_{\mathrm{I}}^{-1}\boldsymbol{I}_{\mathrm{ifr,l}}(z)$, as described in (5.17). The vectors $\boldsymbol{V}_{\mathrm{ifr,l}}(z)$ and $\boldsymbol{I}_{\mathrm{ifr,l}}(z)$ represent the actual and not the *modal* field coupling response at the ends of the cable in Fig. 5.1.

Applying similar steps to the field forcing functions in (5.47) and (5.48), their kth conductor response becomes

$$\begin{bmatrix} V_{\mathrm{ifr}k} \\ I_{\mathrm{ifr}k} \end{bmatrix} = \int_0^{\mathcal{L}} \begin{bmatrix} [\boldsymbol{\Phi}_{\mathrm{im11}}(\mathcal{L}-z)]_k \cdot Z'_{\mathrm{t}k} \cdot I_{\mathrm{ofM}}(z) \\ [\boldsymbol{\Phi}_{\mathrm{im21}}(\mathcal{L}-z)]_k \cdot Z'_{\mathrm{t}k} \cdot I_{\mathrm{ofM}}(z) \end{bmatrix} \mathrm{d}z \tag{5.49}$$

$$\begin{bmatrix} V_{\mathrm{ifl}k} \\ I_{\mathrm{ifl}k} \end{bmatrix} = -\int_0^{\mathcal{L}} \begin{bmatrix} [\boldsymbol{\Phi}_{\mathrm{im11}}(-z)]_k \cdot Z'_{\mathrm{t}k} \cdot I_{\mathrm{ofM}}(z) \\ [\boldsymbol{\Phi}_{\mathrm{im21}}(-z)]_k \cdot Z'_{\mathrm{t}k} \cdot I_{\mathrm{ofM}}(z) \end{bmatrix} \mathrm{d}z. \tag{5.50}$$

The same can be concluded here, where (5.49) and (5.50) have the same mathematical form as that of the single conductor cable in (4.76) and (4.79). For this reason, the analytical solutions in (4.89) and (4.91) as well as the equivalent circuit diagram in Fig. 4.17 can be used for the kth conductor of the shielded multiconductor cable. This demonstrates that the coupling behaviour on each conductor is identical to that of a single conductor shielded cable with change of variables.

So far the closed-form solution for the inner system has been shown in (5.43) and (5.44). Both equations show the solution of n decoupled transmission lines plus the forcing functions added at the ends. The interpretation of these solutions as circuit models has been applied in Fig. 5.12. The macromodel shown there is described in the next section.

5.3.2 Macromodel with Field Coupling Extension

A macromodel of a multiconductor shielded cable was developed in Fig. 5.7 for conductive analysis. In this section, this model is extended to include the field coupling of an incident plane wave. The solution for the outer system was presented in (5.39) and (5.40) using the chain-parameter representation which is equivalent to a TL with the forcing functions added. It is therefore interpreted as a transmission line in Fig. 5.12, with the forcing functions added to the controlled sources at the ends. The voltages $V_{\mathrm{o}}(0)$, $V_{\mathrm{o}}(\mathcal{L})$ and currents $I_{\mathrm{o}}(0)$, $I_{\mathrm{o}}(\mathcal{L})$ in Fig. 5.12 are those between the shield and the ground plane which can be compared in Fig. 5.1. The current $I_{\mathrm{ocf}}(z)$ from (5.42) is represented by an additional circuit called "Circuit for I_{ocf}" at the bottom in Fig. 5.12. The current $I_{\mathrm{ocf}}(z)$ comprises the conductive current $I_{\mathrm{oc}}(z)$ in the outer system together with the reflection

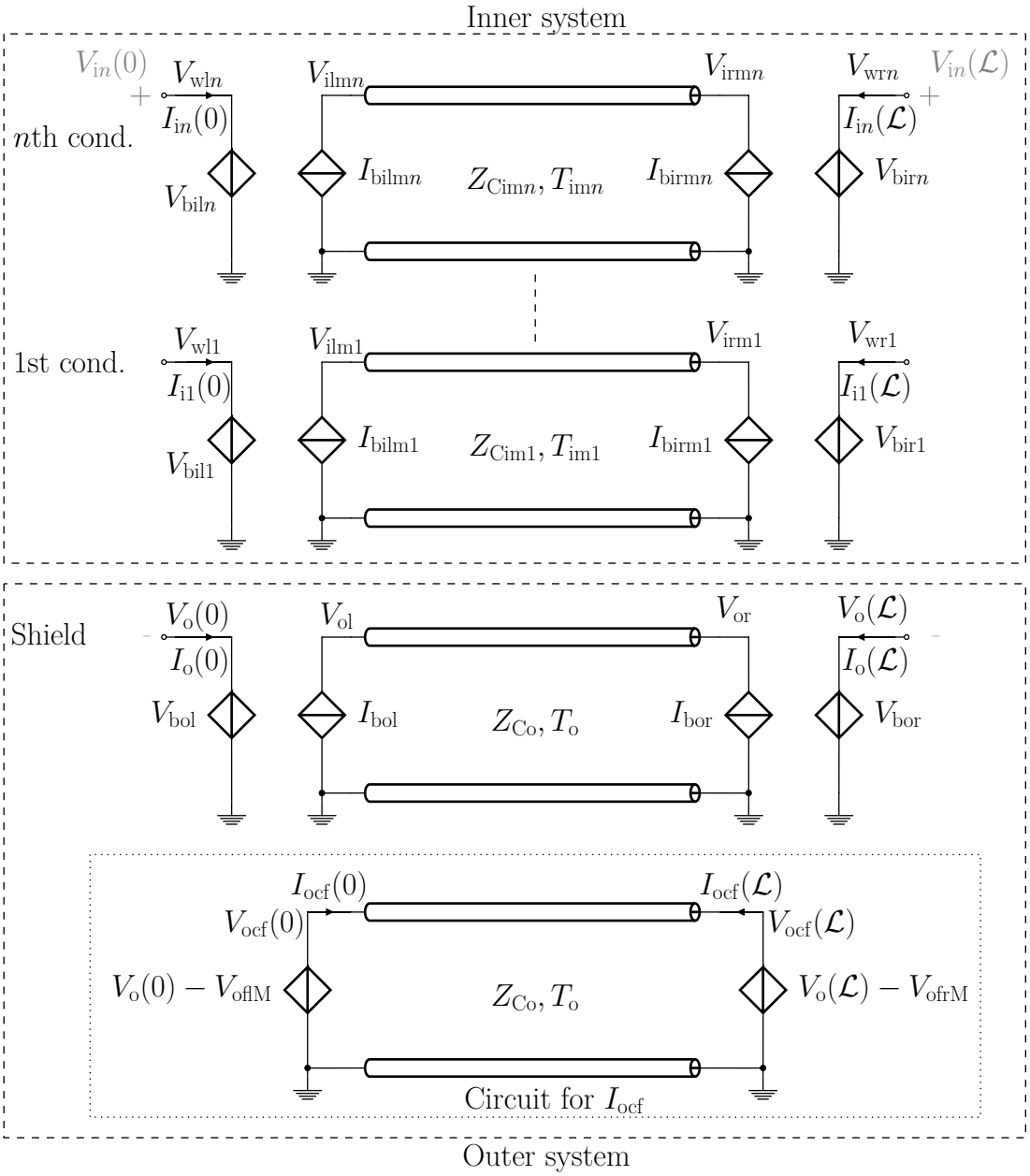

Figure 5.12: Macromodel based on a closed-form solution of a field-coupled shielded multiconductor cable over a perfectly conducting ground plane.

response of the field-coupled current, as described before. The voltage responses of the field coupling V_{ofIM} and V_{ofrM} from (5.38) are therefore not included in this circuit, since they represent the case of a matched line. The boundary conditions are included anyway in the macromodel in Fig. 5.12 so that it can be connected to arbitrary, including non-linear loads. The element T_{o} in Fig. 5.12 is the one-way time delay of the outer system as defined in (4.30). The characteristic impedance Z_{Co} has been defined in (4.26).
The controlled sources of the conductive coupling in (5.33) are extended to include the

field coupling functions as follows:

$$V_{\mathrm{bol}} = V_{\mathrm{ol}} + V_{\mathrm{oclT}} + V_{\mathrm{oflM}} \tag{5.51a}$$

$$I_{\mathrm{bol}} = I_{\mathrm{o}}(0) + \sum_{k=1}^{n} I_{\mathrm{i}k}(0) + (V_{\mathrm{oclT}} + V_{\mathrm{oflM}})/Z_{\mathrm{Co}} \tag{5.51b}$$

$$V_{\mathrm{bor}} = V_{\mathrm{or}} + V_{\mathrm{ocrT}} + V_{\mathrm{ofrM}} \tag{5.51c}$$

$$I_{\mathrm{bor}} = I_{\mathrm{o}}(\mathcal{L}) + \sum_{k=1}^{n} I_{\mathrm{i}k}(\mathcal{L}) + (V_{\mathrm{ocrT}} + V_{\mathrm{ofrM}})/Z_{\mathrm{Co}}. \tag{5.51d}$$

These functions are implemented in the controlled sources in Fig. 5.12. The terms V_{oclT} and V_{ocrT} in (5.51) combine the voltage and current forcing functions into voltage sources, as defined in (5.32). The field response at the ends, represented by V_{oflM} and V_{ofrM}, can be taken directly from the circuit model shown in Fig. 4.16, where $V_{\mathrm{oflM}} = V_{\mathrm{ofM}}(0)$ and $V_{\mathrm{ofrM}} = V_{\mathrm{ofM}}(\mathcal{L})$.

A circuit model was developed for the inner system of a shielded multiconductor cable in Fig. 5.7 that considers only conductive coupling. The model was interpreted from (5.18) and (5.23) as n transmission lines coupled to the line ends via the controlled sources. Since (5.43) and (5.44) have the same mathematical form as (5.18) and (5.23) with field coupling extension, the equivalent circuit diagram of (5.18) and (5.23) in Fig. 5.7 can be used for (5.43) and (5.44). Therefore, in Fig. 5.12, a circuit model with n TLs was developed with the forcing functions added to their controlled sources. The voltages $V_{in}(0)$ and $V_{in}(\mathcal{L})$ in Fig. 5.12 are those between the nth wire and the shield at $z = 0$ and $z = \mathcal{L}$. They can be compared in Fig. 5.1. The remaining elements $V_{\mathrm{wl}n}$, $V_{\mathrm{wr}n}$, V_{wr1} etc. can also be compared in the same figures.

The controlled sources of the kth conductor are defined analogously to (5.34) with extension of the field coupling functions. They are given by

$$V_{\mathrm{bil}k} = \sum_{u=1}^{n} \left\{ [\boldsymbol{T}_{\mathrm{V}}]_{ku} [\boldsymbol{V}_{\mathrm{ilm}}]_u \right\} + V_{\mathrm{Fl}k} + V_{\mathrm{o}}(0) \tag{5.52a}$$

$$V_{\mathrm{bir}k} = \sum_{u=1}^{n} \left\{ [\boldsymbol{T}_{\mathrm{V}}]_{ku} [\boldsymbol{V}_{\mathrm{irm}}]_u \right\} + V_{\mathrm{Fr}k} + V_{\mathrm{o}}(\mathcal{L}) \tag{5.52b}$$

$$I_{\mathrm{bilm}k} = \sum_{u=1}^{n} \left\{ [\boldsymbol{T}_{\mathrm{I}}^{-1}]_{ku} [\boldsymbol{I}_{\mathrm{i}}]_u(0) + \frac{[\boldsymbol{T}_{\mathrm{I}}^{-1}]_{ku} [\boldsymbol{V}_{\mathrm{Fl}}]_u}{[\boldsymbol{Z}_{\mathrm{Cim}}]_u} \right\} \tag{5.52c}$$

$$I_{\mathrm{birm}k} = \sum_{u=1}^{n} \left\{ [\boldsymbol{T}_{\mathrm{I}}^{-1}]_{ku} [\boldsymbol{I}_{\mathrm{i}}]_u(\mathcal{L}) + \frac{[\boldsymbol{T}_{\mathrm{I}}^{-1}]_{ku} [\boldsymbol{V}_{\mathrm{Fr}}]_u}{[\boldsymbol{Z}_{\mathrm{Cim}}]_u} \right\}, \tag{5.52d}$$

where

$$V_{\mathrm{Fl}k} = V_{\mathrm{iflT}k} + V_{\mathrm{iclT}k} \tag{5.53a}$$

$$V_{\mathrm{Fr}k} = V_{\mathrm{ifrT}k} + V_{\mathrm{icrT}k}. \tag{5.53b}$$

If one compares (5.52) with (5.34), it can be seen that the field functions $V_{\mathrm{iflT}k}$ and $V_{\mathrm{ifrT}k}$ have been included in $V_{\mathrm{Fl}k}$ and $V_{\mathrm{Fr}k}$. These functions are defined as follows:

$$V_{\mathrm{iflT}k} = \frac{1}{2} \cdot \left(V_{\mathrm{ifl}k} + Z_{\mathrm{Cim}k} \cdot I_{\mathrm{ifl}k} \right) \tag{5.54a}$$

$$V_{\mathrm{ifrT}k} = \frac{1}{2} \cdot \left(V_{\mathrm{ifr}k} + Z_{\mathrm{Cim}k} \cdot I_{\mathrm{ifr}k} \right), \tag{5.54b}$$

where the Thevenin and Norton sources have been applied as explained in (3.78) and (3.79). The *modal* characteristic impedances Z_{Cim1} to $Z_{\mathrm{Cim}n}$ can be solved with (5.20). The time delays T_{im1} to $T_{\mathrm{im}n}$ are defined in (5.36). Since the controlled sources were defined in (5.51) and (5.52), the macromodel is thus completely described.

In this section, the macromodel of a field-coupled shielded multiconductor cable was developed in Fig. 5.12. The model was designed on a SPICE basis. The outer system was interpreted from the solutions in (5.28) and (5.29) as a TL with controlled sources at its ends. The controlled sources are defined in (5.51) and include the forcing functions of conductive and field coupling. The inner system was developed from the *modal* solution in (5.43) and (5.44) as n decoupled transmission lines plus the controlled sources added at the ends. The inclusion of the field and conductive forcing functions was applied in the controlled sources in (5.52). The transformation from *mode* to actual voltages and currents at the terminals in Fig. 5.12 was achieved with the same sources in (5.52).

In order to execute the model, the primary line constants of a shielded multiconductor cable should be determined and included in (5.16a) and (5.16b) for diagonalization. In a later step, the *modal* characteristic impedance should first be calculated for each inner conductor using (5.20) and then inserted into Fig. 5.12. The time delays T_{im1} to T_{imn} should also be solved from (5.36). For the outer system, the time delay and the characteristic impedance can be taken from (4.30) and (4.26). To simulate the field coupling in the model, a voltage source with the designation E_0 must be defined separately, which represents the electric field of the incident plane wave. The voltage of the source E_0 is coupled to the outer system in Fig. 5.12 via (5.38) and (5.51). The coupling of E_0 to the inner system in Fig. 5.12 is achieved via (4.63), (5.47), (5.48) and (5.52).

A model validation of the developed macromodel is demonstrated in the next section.

5.3.3 Model Validation of the Field Coupling

Field simulations are performed to validate the macromodel developed in Fig. 5.12. The macromodel was built in LTspice [35] for simulations. The CST Studio Suite 19 software [3] was used to examine the field coupling. The setup in Figs. 3.9 and 3.10 is applied in CST, using a co-simulation to combine CST Microwave Studio and CST Cable Studio. This section also presents the simulation results of the lumped-circuit model in order to compare

them with the macromodel in terms of time and efficiency. The PC defined in section 4.1.3 is also used here for the simulations. As mentioned above, no measurements were made for field coupling, since such measurements were difficult to realize with quantitatively precise evaluation. The cable presented in Fig. 5.3 is used for validation. The parameters of the cable together with the values for the termination loads are given in section 5.1.3. The transformation matrices $\boldsymbol{T}_\mathrm{V}$ and $\boldsymbol{T}_\mathrm{I}$, the *modal* characteristic impedances $Z_{\mathrm{Cim1\cdots4}}$, the transit time of the *modal* transmission lines $T_{\mathrm{im1\cdots4}}$ and the characteristic impedance of the outer system Z_Co were defined in section 5.2.3.

Time Domain

To investigate the field coupling, the voltage sources V_1 and V_2 in Fig. 5.3 were short-circuited. A uniform plane wave with $\theta = 45°$ is excited. The electric field of the incident wave has a trapezoidal shape of $10\,\frac{\mathrm{V}}{\mathrm{m}}$, with rise, hold, and fall times of 2 ns, 10 ns, and 3 ns, respectively. The voltage response across R_il1 and R_ir1 in Fig. 5.3 is shown in Figs. 5.13 and 5.14. The results of the macromodel are designated "Macromodel", those

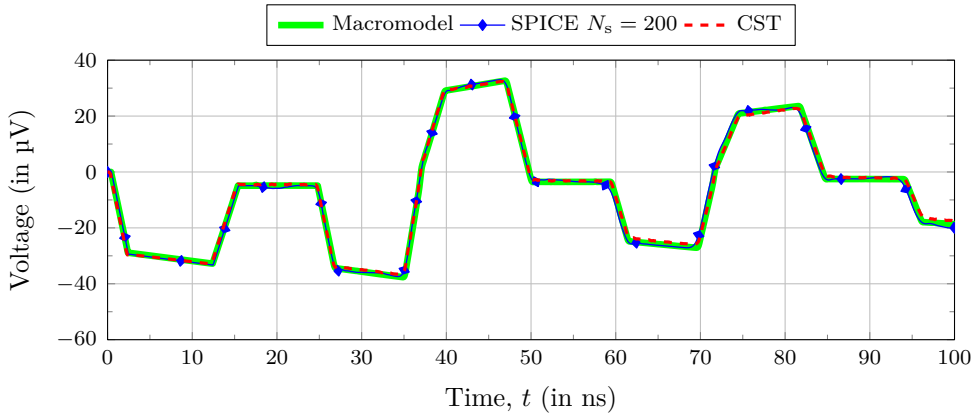

Figure 5.13: Voltage response across R_il1 of a quad-core shielded cable in transient analysis.

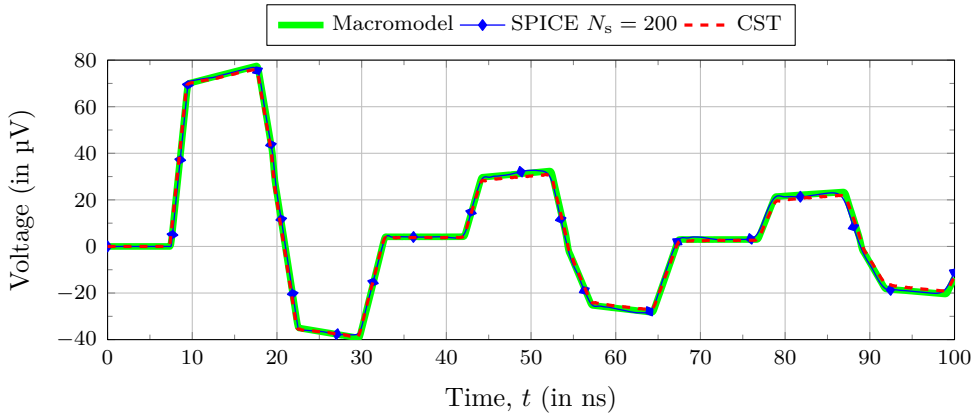

Figure 5.14: Voltage response across R_ir1 of a quad-core shielded cable in transient analysis.

of the lumped-circuit model with 200 sections "SPICE $N_s = 200$" and the result of CST Studio Suite "CST". The results of all three simulation models fit together well. A closer observation shows that the curves of macromodel and CST match better than those of SPICE $N_s = 200$. Another advantage of the macromodel is shown in the simulation time, which took 1.3 s. In comparison, CST and SPICE $N_s = 200$ took 25 min and 130 s, respectively.

Frequency Domain

The cable structure in Fig. 5.3 was also used to validate the field coupling in the frequency domain. An immunity test was carried out while taking field and conductive coupling into account. The voltage source V_2 in Fig. 5.3 was set to 10 mV and an incident wave of $\theta = 45°$ was excited, the electric field of which is $50\,\frac{\mathrm{V}}{\mathrm{m}}$. In this case, the field and the conductive coupling are considered simultaneously. The voltage source V_1 in Fig. 5.3 was short-circuited during this test. The induced voltage at R_{il3} with respect to magnitude and phase is shown in Fig. 5.15. The resonances at 29 and 50 MHz correspond to those of the inner and outer systems, respectively. The results of the SPICE model based on the closed-form solution "Macromodel" are in excellent agreement with those of CST. This also applies to the lumped-circuit model "SPICE $N_s = 200$", although slight deviations can be observed at higher frequencies.

The simulation lasted 4 s for the macromodel, 22 s for SPICE $N_s = 200$ and 2.8 min for

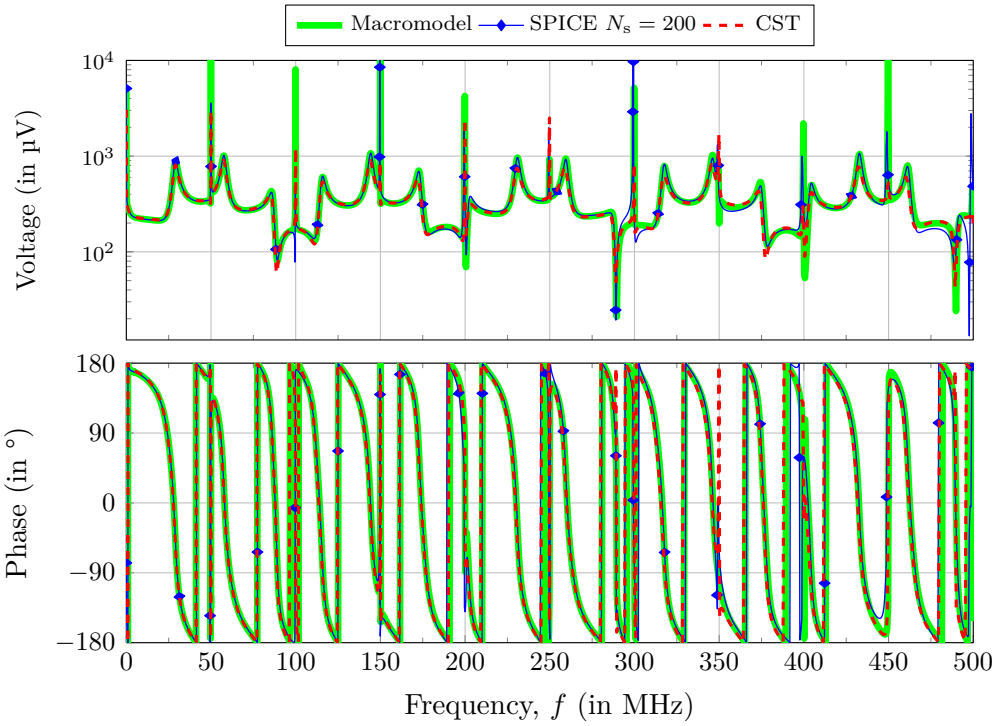

Figure 5.15: Voltage response across R_{il3} of a quad-core cable in frequency domain.

CST. The simulation times in [61, 65, 69, 70] may be different in some cases because either a different cable length or a different number of simulation points were used for the same cable length. In this work, the boundary conditions in CST were uniformly redefined for all simulation examples. The same number of simulation points was defined in each of the CST and SPICE programs to allow comparison.

In this chapter, circuit models for multiconductor shielded cables were developed in distributed form (lumped-circuit model) and in closed-form (macromodel). Both models are suitable for SPICE solvers to analyze the conductive coupling by connecting a lumped source to the model terminals or to calculate the field coupling. The developed models are directly applicable in the frequency domain and in the time domain, where no IFT is required. Validation of the models was performed with field simulations and measurements in sections 5.1.3, 5.2.3 and 5.3.3.

The lumped-circuit model was presented in Fig. 5.2. It was interpreted directly from the transmission line equations of a shielded cable in (5.1.1) and (5.10) as distributed elements connected in series. Field coupling was included in the model by using the scattered voltage formulation as described in section 4.1.2.

A macromodel of a shielded multiconductor cable was developed in Fig. 5.7. The model presented there considers conductive coupling without field coupling. The field coupling of an incident wave was later extended in section 5.3 and finally a complete macromodel was developed in Fig. 5.12. This model includes the conductive and the field coupling.

Since the aim of this work has been achieved with the circuit models developed for the shielded single and multiconductor cables, this leads to the summary.

6 Conclusions and Future Work

This chapter briefly summarizes the main results and conclusions of this work. The development phases of the SPICE models for shielded cables are shortly explained with references to the thesis. An outlook on future work and possible extensions of the developed models is given.

6.1 Research Summary

Based on the problem that there are no suitable models in circuit simulators such as SPICE for shielded cables that are placed over a ground plane, solutions were presented in this work. Existing solutions are either not suitable for time-domain simulations, do not account for the bidirectional coupling between the inner and outer systems of the cable, or do not account for the field coupling of an incident wave. All these shortcomings are resolved in this work, in which circuit models for single and multiconductor cables with braided shield have been developed in SPICE. The presented models can calculate the voltage response across the cable loads from an incident plane wave or due to a lumped source connected to the cable terminals. The bidirectional coupling between the inner and outer system of the cable is taken into account so that immunity and emission tests can be performed. The models are derived from classical transmission line theory and can be used in the frequency domain and in the time domain together with non-linear loads, where no IFT is required.

To calculate the field coupling on a shielded line above a ground plane, the cable was considered as a single conductor. Therefore, in Chapter 3, the field coupling on a single conductor over a ground plane was investigated. Scattered voltage and total voltage formulations were used for the calculation. As part of this work, the scattered voltage solution was further developed in a suitable form that a circuit model was created (see Fig. 3.5). It has been shown that the circuit models of the field-coupled line are equivalent when using the scattered voltage and total voltage formulations. This is considered an important and new finding compared to the state of the art. The model presented can calculate the field coupling at the loads of a single conductor over a ground plane; it was used in later sections for modeling the shielded cables. The model validation provided excellent results in the time and frequency domains compared to full-wave field simulations.

Circuit models were developed in Chapter 4 based on two methods for a single conductor shielded cable that is placed over a ground plane, taking conductive and field coupling into

account. The first method presents a lumped-circuit model with cascaded elements, where the cable was divided into segments (see Fig. 4.2). The model consists of the primary line constants in distributed form along with controlled sources and coupling coefficients to enable bidirectional coupling between the inner and outer systems. The field coupling is integrated into this model via controlled sources. Since the lumped-circuit model requires more computational effort for higher accuracy, a closed-form solution was developed in the second method without discretizing the cable into segments. From this solution, a circuit macromodel was developed in Fig. 4.9. It consists of two transmission lines that represent the inner and outer systems and are coupled at the ends via controlled sources. The developed model is suitable only for conductive coupling, where the voltage response at the cable loads can be calculated by connecting a concentrated source to any terminal. The field coupling was extended into the macromodel in Fig. 4.15, where the scattered voltage formulation was used for the calculation. A major advantage of the proposed macromodels is that equivalent circuits were developed for the coupling functions between the inner and outer systems and to the field, where no Laplace sources were used in SPICE. It was found that the lumped-circuit model is easy to create. On the other hand, the macromodel with a closed-form solution can simulate any cable length without reaching a limit. The lumped-circuit model and the macromodel were validated by measurements and field simulations.

In Chapter 5, the developed circuit models are extended to consider multiconductor shielded cables. Lumped-circuit models and macromodels were developed to account for the field and bidirectional coupling between the inner and outer systems of the cable. The model validation of the multiconductor shielded cable using full-wave field simulations and measurements also gave very good results.

6.2 Future Work

The SPICE models of the shielded cables proposed in this work do not take into account the cable losses, which is noticeable in the results when compared with measurements. Since EMC engineers want to use these models to capture the complete behavior of a system, it would be an important step to include frequency-dependent losses in the models in the future.

In addition, multiple shielded cables and cables with multiple shields are often used in practice. For broadband applications of the developed models, it would be necessary to consider the crosstalk between multiple cables and to extend these models for cables with multiple screens.

Bibliography

[1] C. R. Paul. *Introduction to electromagnetic compatibility*. Wiley series in microwave and optical engineering. Wiley, Hoboken, NJ, 2. ed. edition, 2006.

[2] F. M. Tesche, M. Ianoz, and T. Karlsson. *EMC analysis methods and computational models*. Wiley, New York and Chichester, 1997.

[3] CST STUDIO SUITE. [Online]. Available: `https://www.3ds.com/de/produkte-und-services/simulia/produkte/cst-studio-suite/`, Accessed: 2021-01-22.

[4] A. A. Smith. *Coupling of external electromagnetic fields to transmission lines*. University Microfilms International, Ann Arbor, Mich., 1987.

[5] A. Agrawal, H. Price, and S. Gurbaxani. Transient response of multiconductor transmission lines excited by a nonuniform electromagnetic field. In *1980 Antennas and Propagation Society*, pages 432–435, June 1980.

[6] C. Taylor, R. Satterwhite, and C. Harrison. The response of a terminated two-wire transmission line excited by a nonuniform electromagnetic field. *IEEE Transactions on Antennas and Propagation*, 13(6):987–989, 1965.

[7] R. Perez. *Handbook of electromagnetic compatibility*. Academic Press, San Diego and London, 1995.

[8] C. E. Baum, T. K. Liu, and F. M. Tesche. On the analysis of general multiconductor transmission-line networks. *Interaction Note*, 350(6):467–547, 1978.

[9] F. Rachidi. Formulation of the field-to-transmission line coupling equations in terms of magnetic excitation field. *IEEE Transactions on Electromagnetic Compatibility*, 35(3):404–407, Aug 1993.

[10] S. V. Tkachenko, R. Rambousky, and J. B. Nitsch. Electromagnetic field coupling to a thin wire located symmetrically inside a rectangular enclosure. *IEEE Transactions on Electromagnetic Compatibility*, 55(2):334–341, 2013.

[11] F. Gronwald. *Antenna theory in resonating systems derived from fundamental electromagnetism: Univ., Habil.-Schr., 2006*, volume Band 16 of *Res electricae Magdeburgenses*. Otto-von-Guericke-Universität, Magdeburg, 2006.

[12] M. Magdowski, S. V. Tkachenko, and R. Vick. Coupling of stochastic electromagnetic fields to a transmission line in a reverberation chamber. *IEEE Transactions on Electromagnetic Compatibility*, 53(2):308–317, May 2011.

[13] S. Tkachenko, R. Rambousky, and J. B. Nitsch. Analysis of induced currents on a thin wire located symmetrically inside a cylinder. *IEEE Transactions on Electromagnetic Compatibility*, 56(6):1649–1656, 2014.

[14] I. Wuyts and D. de Zutter. Circuit model for plane-wave incidence an multiconductor transmission lines. *IEEE Transactions on Electromagnetic Compatibility*, 36(3):206–212, 1994.

[15] Y. Kami and R. Sato. Circuit-concept approach to externally excited transmission lines. *IEEE Transactions on Electromagnetic Compatibility*, EMC-27(4):177–183, Nov 1985.

[16] M. Raya and R. Vick. SPICE models for one-conductor and three-conductor lines excited by a uniform plane wave. In *2019 IEEE International Symposium on Electromagnetic Compatibility, Signal Power Integrity (EMC+SIPI)*, pages 360–365, July 2019.

[17] C. R. Paul. *Analysis of multiconductor transmission lines*. Wiley, Hoboken, N.J. and Chichester, 2nd ed. edition, 2008.

[18] C. R. Paul. A SPICE model for multiconductor transmission lines excited by an incident electromagnetic field. *IEEE Transactions on Electromagnetic Compatibility*, 36(4):342–354, 1994.

[19] I. Maio, F. G. Canavero, and B. Dilecce. Analysis of crosstalk and field coupling to lossy MTLs in a SPICE environment. *IEEE Transactions on Electromagnetic Compatibility*, 38(3):221–229, 1996.

[20] I. Erdin, A. Dounavis, R. Achar, and M. S. Nakhla. A SPICE model for incident field coupling to lossy multiconductor transmission lines. *IEEE Transactions on Electromagnetic Compatibility*, 43(4):485–494, Nov 2001.

[21] M. Omid, Y. Kami, and M. Hayakawa. Field coupling to nonuniform and uniform transmission lines. *IEEE Transactions on Electromagnetic Compatibility*, 39(3):201–211, Aug 1997.

[22] Feko. [Online]. Available: `https://altairhyperworks.com/product/FEKO/`, Accessed: 2020-03-19.

[23] M. Tyni. The transfer impedance of coaxial cables with braided outer conductor. In *Proc. 3rd Int. Symp. EMC, Wroclaw, Poland*, page 410–418, September 1976.

[24] S. Sali. An improved model for the transfer impedance calculations of braided coaxial cables. *IEEE Transactions on Electromagnetic Compatibility*, 33(2):139–143, May 1991.

[25] S. A. Schelkunoff. The electromagnetic theory of coaxial transmission lines and cylindrical shields. *The Bell System Technical Journal*, 13(4):532–579, Oct 1934.

[26] E. F. Vance. *Coupling to shielded cables*. Wiley, S.l., 1978.

[27] K. S. H. Lee and C. E. Baum. Application of modal analysis to braided-shield cables. *IEEE Transactions on Electromagnetic Compatibility*, EMC-17(3):159–169, Aug 1975.

[28] S. Caniggia and F. Maradei. Equivalent circuit models for the analysis of coaxial cables immunity. In *2003 IEEE Symposium on Electromagnetic Compatibility. Symposium Record (Cat. No.03CH37446)*, volume 2, pages 881–886 vol.2, Aug 2003.

[29] S. Caniggia and F. Maradei. SPICE-like models for the analysis of the conducted and radiated immunity of shielded cables. *IEEE Transactions on Electromagnetic Compatibility*, 46(4):606–616, 2004.

[30] A. F. H. Hassan. *Modeling of single and double-shielded cables for EMC applications*, volume Band 69 of *Res electricae Magdeburgenses Band 69*. Otto-von-Guericke-Universität, Magdeburg, 1. auflage edition, 2016.

[31] H. Xie, J. Wang, R. Fan and Y. Liu. SPICE models for radiated and conducted susceptibility analyses of multiconductor shielded cables. *Progress In Electromagnetics Research*, 103:241–257, 2010.

[32] H. Xie, J. Wang, R. Fan, and Y. Liu. SPICE models to analyze radiated and conducted susceptibilities of shielded coaxial cables. *IEEE Transactions on Electromagnetic Compatibility*, 52(1):215–222, 2010.

[33] SACAMOS. [Online]. Available: `http://www.sacamos.org/`, Accessed: 2021-01-22.

[34] NGSPICE. [Online]. Available: `http://ngspice.sourceforge.net/`, Accessed: 2021-01-20.

[35] LTspice. [Online]. Available: `https://www.analog.com/en/design-center/design-tools-and-calculators/ltspice-simulator.html`, Accessed: 2021-01-20.

[36] PSPICE. [Online]. Available: `https://www.orcad.com/`, Accessed: 2021-01-20.

[37] A. Orlandi. Frequency- and time-domain modeling of the transfer impedance and distributed longitudinal induced voltage by means of a SPICE equivalent circuit. *IEEE Transactions on Electromagnetic Compatibility*, 45(1):125–129, Feb 2003.

[38] A. Orlandi. Circuit model for bulk current injection test on shielded coaxial cables. *IEEE Transactions on Electromagnetic Compatibility*, 45(4):602–615, 2003.

[39] A. Orlandi. Full SPICE model for transfer impedance and transfer admittance inclusion in shielded coaxial cables analysis. *IEE Proceedings - Science, Measurement and Technology*, 150(6):297–306, Nov 2003.

[40] G. Antonini, A. C. Scogna, A. Orlandi, and R. M. Rizzi. Experimental validation of circuit models for bulk current injection (BCI) test on shielded coaxial cables. In *2004 International Symposium on Electromagnetic Compatibility (IEEE Cat. No.04CH37559)*, volume 1, pages 63–68 vol.1, Aug 2004.

[41] G. Antonini and A. Orlandi. Spice equivalent circuit of a two-parallel-wires shielded cable for evaluation of the RF induced voltages at the terminations. *IEEE Transactions on Electromagnetic Compatibility*, 46(2):189–198, 2004.

[42] G. Antonini, A. C. Scogna, and A. Orlandi. Grounding, unbalancing and length effects on termination voltages of a twinax cable during bulk current injection. *IEEE Transactions on Electromagnetic Compatibility*, 46(2):302–308, May 2004.

[43] W.C. Johnson. *Transmission Lines and Networks*. Electronics Series. McGraw-Hill, 1950.

[44] F. H. Branin. Transient analysis of lossless transmission lines. *Proceedings of the IEEE*, 55(11):2012–2013, 1967.

[45] IEEE guide on shielding practice for low voltage cables. *IEEE Std 1143-2012 (Revision of IEEE Std 1143-1994)*, pages 1–91, 2013.

[46] C. R. Paul. Transmission-line modeling of shielded wires for crosstalk prediction. *IEEE Transactions on Electromagnetic Compatibility*, EMC-23(4):345–351, 1981.

[47] K. H. Gonschorek and R. Vick. *Electromagnetic Compatibility for Device Design and System Integration*. 01 2009.

[48] B. Demoulin and L. Kone. Shielded cables transfer impedance measurements. *IEEE Electromagnetic Compatibility Society Newsletter*, _:38–45, 2010.

[49] S. Sali. Cable shielding measurements at microwave frequencies. *IEEE Transactions on Electromagnetic Compatibility*, 46(2):178–188, 2004.

[50] L. Jung and J. Luiken ter Haseborg. Evaluation of measured complex transfer impedances and transfer admittances for the characterization of shield inhomogeneities of multiconductor cables. *IEEE Transactions on Electromagnetic Compatibility*, 41(4):460–468, 1999.

[51] *Metallic communication cable test methods*, volume IEC 62153-4-3 of *International standard*. International Electrotechnical Commission, Geneva, Part 4-3: Electromagnetic compatibility(EMC) - Surface transfer impedance – Triaxial method edition.

[52] *Metallic communication cable test methods*, volume IEC 62153-4-8 of *Norme internationale International standard*. International Electrotechnical Commission, Geneva, 1st ed. edition, 2006.

[53] *Metallic cables and other passive components test methods*, volume IEC 62153-4-6 of *International standard*. International Electrotechnical Commission, Geneva, Switzerland, edition 2.0 edition, 2017.

[54] M. Bluhm, E. Peroglio, G. Pierucci, V. Squizzato, and R. E. Zich. Measurements of transfer impedance with the line injection method on cables and connectors. In *IEEE International Symposium on Electromagnetic Compatibility. Symposium Record (Cat. No.00CH37016)*, volume 2, pages 599–604 vol.2, 2000.

[55] H.-Y. Lee, H.-S. Oh, and D.-C. Park. Measurement of transfer impedance on shielded multiconductor telecommunication cables using IEC 96-1 line injection method. In *2003 IEEE International Symposium on Electromagnetic Compatibility, 2003. EMC '03.*, volume 2, pages 1012–1015 Vol.2, 2003.

[56] P. Degauque and J. Hamelin. *Compatibilité électromagnétique: bruits et perturbations radioélectriques*. Collection technique et scientifique des télécommunications. Dunod, 1990.

[57] D. A. Weston. *Electromagnetic compatibility : principles and applications*, volume 73 of *Electrical engineering and electronics 73*. Dekker, New York [u.a.], 1991. VIII, 686 S, Ill., graph. Darst.

[58] H. Kaden. *Wirbelströme und Schirmung in der Nachrichtentechnik*. Klassiker der Technik Ser. Springer, Berlin, Heidelberg, 2nd ed. edition, 2007.

[59] B. Demoulin. *Etude de la pénétration des ondes électromagnétiques à travers des blindages homogènes ou des tresses à structure coaxiale*. Ph.D. thesis, Universite des Sciences et Techniques de Lille, France, 17 June, 1981.

[60] T. Kley. Optimized single-braided cable shields. *IEEE Transactions on Electromagnetic Compatibility*, 35(1):1–9, Feb 1993.

[61] M. Raya and R. Vick. SPICE models of shielded single and multiconductor cables for EMC analyses. *IEEE Transactions on Electromagnetic Compatibility*, 62(4):1563–1571, 2020.

[62] F. Rachidi and S. V. Tkachenko. Electromagnetic field interaction with transmission lines: From classical theory to HF radiation effects. 2008.

[63] C.R. Paul. *Analysis of Linear Circuits*. Circuits and systems series. McGraw-Hill, 1989.

[64] T. Weiland. A discretization method for the solution of Maxwell's equations for six-component fields. *Archiv Elektronik und Uebertragungstechnik*, 31:116–120, April 1977.

[65] M. Raya, M. Magdowski, and R. Vick. SPICE-based lumped circuit model of shielded cables for EMC analyses. In *2020 International Symposium on Electromagnetic Compatibility - EMC EUROPE*, pages 1–5, 2020.

[66] C. Marlier, A. Videt, and N. Idir. NIF-Based frequency-domain modeling method of three-wire shielded energy cables for EMC simulation. *IEEE Transactions on Electromagnetic Compatibility*, 57(1):145–155, Feb 2015.

[67] Y. Huangfu, L. Di Rienzo, and S. Wang. Frequency-dependent multi-conductor transmission line model for shielded power cables considering geometrical dissymmetry. *IEEE Transactions on Magnetics*, 54(3):1–4, March 2018.

[68] The MathWorks Inc., MATLAB (Version R2015b). [Online]. Available: `https://www.mathworks.com/`, Accessed: 2020-03-19.

[69] M. Raya and R. Vick. Network model of shielded cables for the analysis of conducted immunity and emissions. *IEEE Transactions on Electromagnetic Compatibility*, 61(4):1167–1174, Aug 2019.

[70] M. Raya and R. Vick. Network model of shielded cables for radiated and conducted EMC analysis. In *2019 IEEE International Symposium on Electromagnetic Compatibility, Signal Power Integrity (EMC+SIPI)*, pages 304–309, July 2019.

A Appendix

A.1 Netlist of the Lumped-Circuit Model for an RG58 Cable

Shown here is a netlist for the RG58 cable used for validation in Section 4.1.3. Compared to Fig. 4.2, the netlist for the cable itself is shown without the TNs at the ends. The cable has been divided into 8 sections. The presented netlist can be directly imported and simulated in any SPICE simulation program. A voltage source representing the electric field of the incident wave should be connected to the node `Source`. The nodes `In1`, `In17`, `O0` and `O18` are the connections of the inner conductor and the shield respectively.

```
.SUBCKT Netlist_Single_Shielded_Ns=8 Source O0 0 In1  O18 0 In17
* +++++++++++++++++++ Section 1 ++++++++++++++++++++++++++
*** Field Coupling Section 1 ***
** Transverse Voltage Vt,1, see (4.19) **
Rsource Source 0 50
BfoT1 O1 O0 V=  0.01414214*V(Source)
* V(Source)=E0 --> electric field
** Tangential Voltage, see Fig. 4.3 **
Bf1 Of1 0 V=  0.03344482e-9*V(Source)
Tf1 Of1 0 Of2 0 Td=  0.52553458n Z0=50
Rf1 Of2 0 50
Bfd1 Ofd1 0 V=V(Of2)
Cfd1 Ofd1 0 1
.ic V(Ofd1)=0
*** Outer System Section 1, see Fig. 4.2 ***
Bfo1 O2 O1 V=  0.22222222*I(Cfd1) + I(Li1)*3111.111u
Lo1 O2 O3 115.625n Rser=0
Cos1 O3 0   4.752p
*** Inner System Section 1, see Fig. 4.2 ***
B1 In2 In1 V=I(Lo1)*3111.111u
Li1 In2 In3  50.368n Rser=0
Cis2 In3 0  20.181p
K_1 Li1 Lo1  -0.00291196
* +++++++++++++++++++ Section 2 ++++++++++++++++++++++++++
*** Field Coupling Section 2 ***
```

```
Bf2 Of3 0 V=  0.03344482e-9*V(Source)
Tf2 Of3 0 Of4 0 Td=  1.05106917n Z0=50
Rf2 Of4 0 50
Bfd2 Ofd2 0 V=V(Of4)
Cfd2 Ofd2 0 1
.ic V(Ofd2)=0
*** Outer System Section 2 ***
Bfo2 O4 O3 V=  0.22222222*I(Cfd2) + I(Li2)*3111.111u
Lo2 O4 O5 115.625n Rser=0
Cos2 O5 0   4.752p
*** Inner System Section 2 ***
B2 In4 In3 V=I(Lo2)*3111.111u
Li2 In4 In5  50.368n Rser=0
Cis3 In5 0  20.181p
K_2 Li2 Lo2  -0.00291196
* +++++++++++++++++++ Section 3 ++++++++++++++++++++++++++
*** Field Coupling Section 3 ***
Bf3 Of5 0 V=  0.03344482e-9*V(Source)
Tf3 Of5 0 Of6 0 Td=  1.57660375n Z0=50
Rf3 Of6 0 50
Bfd3 Ofd3 0 V=V(Of6)
Cfd3 Ofd3 0 1
.ic V(Ofd3)=0
*** Outer System Section 3 ***
Bfo3 O6 O5 V=  0.22222222*I(Cfd3) + I(Li3)*3111.111u
Lo3 O6 O7 115.625n Rser=0
Cos3 O7 0   4.752p
*** Inner System Section 3 ***
B3 In6 In5 V=I(Lo3)*3111.111u
Li3 In6 In7  50.368n Rser=0
Cis4 In7 0  20.181p
K_3 Li3 Lo3  -0.00291196
* +++++++++++++++++++ Section 4 ++++++++++++++++++++++++++
*** Field Coupling Section 4 ***
Bf4 Of7 0 V=  0.03344482e-9*V(Source)
Tf4 Of7 0 Of8 0 Td=  2.10213833n Z0=50
Rf4 Of8 0 50
Bfd4 Ofd4 0 V=V(Of8)
Cfd4 Ofd4 0 1
```

```
.ic V(Ofd4)=0
*** Outer System Section 4 ***
Bfo4 O8 O7 V=  0.22222222*I(Cfd4) + I(Li4)*3111.111u
Lo4 O8 O9 115.625n Rser=0
Cos4 O9 0   4.752p
*** Inner System Section 4 ***
B4 In8 In7 V=I(Lo4)*3111.111u
Li4 In8 In9  50.368n Rser=0
Cis5 In9 0  20.181p
K_4 Li4 Lo4  -0.00291196
* +++++++++++++++++++ Section 5 ++++++++++++++++++++++++++
*** Field Coupling Section 5 ***
Bf5 Of9 0 V=  0.03344482e-9*V(Source)
Tf5 Of9 0 Of10 0 Td=  2.62767291n Z0=50
Rf5 Of10 0 50
Bfd5 Ofd5 0 V=V(Of10)
Cfd5 Ofd5 0 1
.ic V(Ofd5)=0
*** Outer System Section 5 ***
Bfo5 O10 O9 V=  0.22222222*I(Cfd5) + I(Li5)*3111.111u
Lo5 O10 O11 115.625n Rser=0
Cos5 O11 0   4.752p
*** Inner System Section 5 ***
B5 In10 In9 V=I(Lo5)*3111.111u
Li5 In10 In11  50.368n Rser=0
Cis6 In11 0  20.181p
K_5 Li5 Lo5  -0.00291196
* +++++++++++++++++++ Section 6 ++++++++++++++++++++++++++
*** Field Coupling Section 6 ***
Bf6 Of11 0 V=  0.03344482e-9*V(Source)
Tf6 Of11 0 Of12 0 Td=  3.15320750n Z0=50
Rf6 Of12 0 50
Bfd6 Ofd6 0 V=V(Of12)
Cfd6 Ofd6 0 1
.ic V(Ofd6)=0
*** Outer System Section 6 ***
Bfo6 O12 O11 V=  0.22222222*I(Cfd6) + I(Li6)*3111.111u
Lo6 O12 O13 115.625n Rser=0
Cos6 O13 0   4.752p
```

```
*** Inner System Section 6 ***
B6 In12 In11 V=I(Lo6)*3111.111u
Li6 In12 In13  50.368n Rser=0
Cis7 In13 0  20.181p
K_6 Li6 Lo6  -0.00291196
* +++++++++++++++++++ Section 7 ++++++++++++++++++++++++++
*** Field Coupling Section 7 ***
Bf7 Of13 0 V=  0.03344482e-9*V(Source)
Tf7 Of13 0 Of14 0 Td=  3.67874208n Z0=50
Rf7 Of14 0 50
Bfd7 Ofd7 0 V=V(Of14)
Cfd7 Ofd7 0 1
.ic V(Ofd7)=0
*** Outer System Section 7 ***
Bfo7 O14 O13 V=  0.22222222*I(Cfd7) + I(Li7)*3111.111u
Lo7 O14 O15 115.625n Rser=0
Cos7 O15 0   4.752p
*** Inner System Section 7 ***
B7 In14 In13 V=I(Lo7)*3111.111u
Li7 In14 In15  50.368n Rser=0
Cis8 In15 0  20.181p
K_7 Li7 Lo7  -0.00291196
* +++++++++++++++++++ Section 8 ++++++++++++++++++++++++++
*** Field Coupling Section 8 ***
Bf8 Of15 0 V=  0.03344482e-9*V(Source)
Tf8 Of15 0 Of16 0 Td=  4.20427666n Z0=50
Rf8 Of16 0 50
Bfd8 Ofd8 0 V=V(Of16)
Cfd8 Ofd8 0 1
.ic V(Ofd8)=0
*** Outer System Section 8 ***
Bfo8 O16 O15 V=  0.22222222*I(Cfd8) + I(Li8)*3111.111u
Lo8 O16 O17 115.625n Rser=0
Cos8 O17 0   4.752p
*** Inner System Section 8 ***
B8 In16 In15 V=I(Lo8)*3111.111u
Li8 In16 In17  50.368n Rser=0
Cis9 In17 0  20.181p
K_8 Li8 Lo8  -0.00291196
```

```
*** Vt2, see Fig. 4.4 ***
BfT1 OfTt1 0 V=  0.01414214*V(Source)
Tftt2 OfTt1 0 OfTt2 0 Td=  4.72981125n Z0=50
ROfT1 OfTt2 0 50
BfoT9 O17 O18 V=V(OfTt2)
.ends
```

A.2 Netlist of the Lumped-Circuit Model for a Multiconductor Shielded Cable

This section provides a netlist for the quad-core shielded cable used for validation in Section 5.1.3. The netlist represents the equivalent circuit diagram of the cable shown in Fig. 5.2 without the TNs at the ends. To avoid space and redundancy, the netlist is shown when the cable has been divided into only 3 sections. The netlist shown can be directly imported and simulated in any SPICE simulation program. The node `Source` should be connected to a voltage source representing the electric field of the incident wave. The nodes `Ina1`, `Inb1`, `Inc1` and `Ind1` are the connections of the inner conductors on the left-hand side of the cable. On the right-hand side are the nodes `Ina10`, `Inb10`, `Inc10` and `Ind10`. The nodes `O0` and `O11` are the connections of the shield on the left and right sides, respectively. The resistors `Rto`k, `Rt_a`k, `Rt_b`k, `Rt_c`k and `Rt_d`k of the kth section were used to prevent convergence. These have very low values and therefore have no influence on the simulation results.

```
.SUBCKT Netlist_MTL Source O0 0 Ina1 Inb1 Inc1 Ind1 0 O11 0 Ina10
Inb10 Inc10 Ind10 0
* +++++++++++++++++++ Section 1 ++++++++++++++++++++++++++
*** Field Coupling Section 1 ***
** Transverse Voltage Vt,1, see (4.19) **
Rsource Source 0 1
BfoT1 O1 O0 V=  0.01414214*V(Source)
** Tangential Voltage, see Fig. 4.3 **
Bf1 Of1 0 V=  0.03344482e-9*V(Source)
Tf1 Of1 0 Of2 0 Td=  1.77367922n Z0=50
Rf1 Of2 0 50
Bfd1 Ofd1 0 V=V(Of2)
Cfd1 Ofd1 0 1
*** Outer System Section 1, see Fig. 5.2 ***
Bfo1 O2 O1 V=  0.75000000*I(Cfd1) + I(li_a1)*17250u +
I(li_b1)*17250u + I(li_c1)*17250u + I(li_d1)*17250u
```

```
Rto1 O2 O3   0.75000000u
Lo1 O3 O4 271.77000000n Rser=0
Cos1 O4 0  23.02927500p
K_a1 li_a1 Lo1  -0.00473237
K_b1 li_b1 Lo1  -0.00473237
K_c1 li_c1 Lo1  -0.00473237
K_d1 li_d1 Lo1  -0.00473237
K_ab1 li_a1 li_b1   0.36873198
K_ac1 li_a1 li_c1   0.36873198
K_ad1 li_a1 li_d1   0.25441814
K_bc1 li_b1 li_c1   0.25441814
K_bd1 li_b1 li_d1   0.36873198
K_cd1 li_c1 li_d1   0.36873198
*** Inner System Section 1, see Fig. 5.2 ***
*  conductor a
Ba1 Ina2 Ina1 V=I(Lo1)*17250u
Rt_a1 Ina2 Ina3   0.75000000u
li_a1 Ina3 Ina4 267.09235006n Rser=0
ci_a1 Ina4 0  35.29213194p
ci_ab1 Ina4 Inb4  25.17309761p
ci_ac1 Ina4 Inc4  25.17309765p
ci_ad1 Ina4 Ind4   4.32372544p
*  conductor b
Bb1 Inb2 Inb1 V=I(Lo1)*17250u
Rt_b1 Inb2 Inb3   0.75000000u
li_b1 Inb3 Inb4 267.09235006n Rser=0
ci_b1 Inb4 0  35.29213194p
ci_bc1 Inb4 Inc4   4.32372544p
ci_bd1 Inb4 Ind4  25.17309765p
*  conductor c
Bc1 Inc2 Inc1 V=I(Lo1)*17250u
Rt_c1 Inc2 Inc3   0.75000000u
li_c1 Inc3 Inc4 267.09235015n Rser=0
ci_c1 Inc4 0  35.29213190p
*  conductor d
Bd1 Ind2 Ind1 V=I(Lo1)*17250u
Rt_d1 Ind2 Ind3   0.75000000u
li_d1 Ind3 Ind4 267.09235015n Rser=0
ci_d1 Ind4 0  35.29213190p
```

```
* +++++++++++++++++++ Section 2 +++++++++++++++++++++++++
*** Field Coupling Section 2 ***
Bf2 Of3 0 V=  0.03344482e-9*V(Source)
Tf2 Of3 0 Of4 0 Td=  3.54735843n Z0=50
Rf2 Of4 0 50
Bfd2 Ofd2 0 V=V(Of4)
Cfd2 Ofd2 0 1
*** Outer System Section 2 ***
Bfo2 O5 O4 V=  0.75000000*I(Cfd2) +  I(li_a2)*17250u +
I(li_b2)*17250u +  I(li_c2)*17250u +  I(li_d2)*17250u
Rto2 O5 O6   0.75000000u
Lo2 O6 O7 271.77000000n Rser=0
Cos2 O7 0  23.02927500p
K_a2 li_a2 Lo2  -0.00473237
K_b2 li_b2 Lo2  -0.00473237
K_c2 li_c2 Lo2  -0.00473237
K_d2 li_d2 Lo2  -0.00473237
K_ab2 li_a2 li_b2   0.36873198
K_ac2 li_a2 li_c2   0.36873198
K_ad2 li_a2 li_d2   0.25441814
K_bc2 li_b2 li_c2   0.25441814
K_bd2 li_b2 li_d2   0.36873198
K_cd2 li_c2 li_d2   0.36873198
*** Inner System Section 2 ***
*  conductor a
Ba2 Ina5 Ina4 V=I(Lo2)*17250u
Rt_a2 Ina5 Ina6   0.75000000u
li_a2 Ina6 Ina7 267.09235006n Rser=0
ci_a2 Ina7 0  35.29213194p
ci_ab2 Ina7 Inb7  25.17309761p
ci_ac2 Ina7 Inc7  25.17309765p
ci_ad2 Ina7 Ind7   4.32372544p
*  conductor b
Bb2 Inb5 Inb4 V=I(Lo2)*17250u
Rt_b2 Inb5 Inb6   0.75000000u
li_b2 Inb6 Inb7 267.09235006n Rser=0
ci_b2 Inb7 0  35.29213194p
ci_bc2 Inb7 Inc7   4.32372544p
ci_bd2 Inb7 Ind7  25.17309765p
```

```
*  conductor c
Bc2 Inc5 Inc4 V=I(Lo2)*17250u
Rt_c2 Inc5 Inc6   0.75000000u
li_c2 Inc6 Inc7 267.09235015n Rser=0
ci_c2 Inc7 0  35.29213190p
*  conductor d
Bd2 Ind5 Ind4 V=I(Lo2)*17250u
Rt_d2 Ind5 Ind6   0.75000000u
li_d2 Ind6 Ind7 267.09235015n Rser=0
ci_d2 Ind7 0  35.29213190p
* ++++++++++++++++++++ Section 3 ++++++++++++++++++++++++++
*** Field Coupling Section 3 ***
Bf3 Of5 0 V=  0.03344482e-9*V(Source)
Tf3 Of5 0 Of6 0 Td=  5.32103765n Z0=50
Rf3 Of6 0 50
Bfd3 Ofd3 0 V=V(Of6)
Cfd3 Ofd3 0 1
*** Outer System Section 3 ***
Bfo3 O8 O7 V=  0.75000000*I(Cfd3) +  I(li_a3)*17250u +
I(li_b3)*17250u +  I(li_c3)*17250u +  I(li_d3)*17250u
Rto3 O8 O9   0.75000000u
Lo3 O9 O10 271.77000000n Rser=0
Cos3 O10 0  23.02927500p
K_a3 li_a3 Lo3  -0.00473237
K_b3 li_b3 Lo3  -0.00473237
K_c3 li_c3 Lo3  -0.00473237
K_d3 li_d3 Lo3  -0.00473237
K_ab3 li_a3 li_b3   0.36873198
K_ac3 li_a3 li_c3   0.36873198
K_ad3 li_a3 li_d3   0.25441814
K_bc3 li_b3 li_c3   0.25441814
K_bd3 li_b3 li_d3   0.36873198
K_cd3 li_c3 li_d3   0.36873198
*** Inner System Section 3 ***
*  conductor a
Ba3 Ina8 Ina7 V=I(Lo3)*17250u
Rt_a3 Ina8 Ina9   0.75000000u
li_a3 Ina9 Ina10 267.09235006n Rser=0
ci_a3 Ina10 0  35.29213194p
```

```
ci_ab3 Ina10 Inb10  25.17309761p
ci_ac3 Ina10 Inc10  25.17309765p
ci_ad3 Ina10 Ind10   4.32372544p
*  conductor b
Bb3 Inb8 Inb7 V=I(Lo3)*17250u
Rt_b3 Inb8 Inb9   0.75000000u
li_b3 Inb9 Inb10 267.09235006n Rser=0
ci_b3 Inb10 0  35.29213194p
ci_bc3 Inb10 Inc10   4.32372544p
ci_bd3 Inb10 Ind10  25.17309765p
*  conductor c
Bc3 Inc8 Inc7 V=I(Lo3)*17250u
Rt_c3 Inc8 Inc9   0.75000000u
li_c3 Inc9 Inc10 267.09235015n Rser=0
ci_c3 Inc10 0  35.29213190p
*  conductor d
Bd3 Ind8 Ind7 V=I(Lo3)*17250u
Rt_d3 Ind8 Ind9   0.75000000u
li_d3 Ind9 Ind10 267.09235015n Rser=0
ci_d3 Ind10 0  35.29213190p
*** Vt2, see Fig. 4.4 ***
BfT1 OfTt1 0 V=  0.01414214*V(Source)
Tftt2 OfTt1 0 OfTt2 0 Td=  7.09471687n Z0=50
ROfT1 OfTt2 0 50
BfoT4 O10 O11 V=V(OfTt2)
.ends
```

Res Electricae Magdeburgenses

MAgdeburger FOrum zur Elektrotechnik

MAFO-01 Orths, A.: *Multikriterielle, optimale Planung von Verteilungsnetzen im liberalisierten Energiemarkt unter Verwendung von spieltheoretischen Verfahren*, 2003. ISBN 3-929757-57-5.

MAFO-02 Purmann, M.: *Optimierung des Betriebsverhaltens von PEM-Brennstoffzellen unter Berücksichtigung von elektrischem und Gesamtwirkungsgrad bei unterschiedlichen Lastanforderungen und Betriebsparametern*, 2004. ISBN 3-929757-63-X.

MAFO-03 Al-Hamid, M.: *Extraktion von höheren Moden in TEM-Wellenleitern*, 2004. ISBN 3-929757-64-8.

MAFO-04 Haase, H., J. Nitsch, and T. Steinmetz: *Transmission-Line Super Theory – A new Approach to an Effective Calculation of Electromagnetic Interference*, 2004. ISBN 3-929757-67-2.

MAFO-05 Bachry, A.: *Power Quality Studies in Distribution Systems Involving Spectral Decomposition*, 2004. ISBN 3-929757-68-0.

MAFO-06 Styczynski, Z. A.: *Power Network and Renewables – A Scientific Report*, 2004. ISBN 3-929757-69-9.

MAFO-07 Blume, E.: *Numerische Analyse der Kopplung linearer Antennen innerhalb eines Resonators*, 2004. ISBN 3-929757-71-0.

MAFO-08 Handschin, E. and Z. A. Styczynski: *Power System Application of the Modern Battery Storage*, 2004. ISBN 3-929757-75-3.

MAFO-09 Haase, H.: *Full-Wave Field Interactions of Nonuniform Transmission Lines*, 2005. ISBN 3-929757-78-8.

MAFO-10 Nitsch, D.: *Die Wirkung eingekoppelter ultrabreitbandiger elektromagnetischer Impulse auf komplexe elektronische Systeme*, 2005. ISBN 3-929757-79-6.

MAFO-11 Hadzi-Kostova, B.: *Protection Concepts in Distribution Networks with Decentralized Energy Resources*, 2005. ISBN 3-929757-84-2.

MAFO-12 Steinmetz, T.: *Ungleichförmige und zufällig geführte Mehrfachleitungen in komplexen technischen Systemen*, 2006. Nummerierung geändert, ISBN 3-929757-98-2.

MAFO-13 Styczynski, Z. and J. Haubrock: *Influence of Distributed and Renewable Generation on Power System Security – Proceedings of the CRIS Workshop 2006*, 2006. ISBN 3-929757-99-0.

MAFO-14 Heideck, G.: *Ein autonomes Brennstoffzellensystem: Optimierungsansätze*, 2006. ISBN 3-929757-94-X.

MAFO-15 Styczynski, Z. und H.-D. Musikowski: *Dresdener Kreis Elektroenergieversorgung 7*, 2006. ISBN 3-929757-85-0.

MAFO-16 Gronwald, F.: *Antenna Theory in Resonating Systems derived from Fundamental Electromagnetism*, 2007. ISBN 3-929757-93-1.

MAFO-17 Krauthäuser, H.G.: *Grundlagen und Anwendungen von Modenverwirbelungskammern*, 2007. ISBN 978-3-929757-43-9.

MAFO-18 Dzienis, C.: *Ersatzmodelle nichtlinearer Lasten in elektrischen Verteilungsnetzen*, 2007. ISBN 978-3-929757-07-1.

MAFO-19 Styczynski, Z. and J. Haubrock: *Renewable and Dispersed Power Generation in Power Systems*, 2007. ISBN 978-3-929757-44-6.

MAFO-20 Haubrock, J.: *Parametrierung elektrischer Äquivalentschaltbilder von PEM-Brennstoffzellen*, 2008. ISBN 978-3-940961-02-0.

MAFO-21 Angelov, A. N.: *Rechnergestütztes Lernen im Bereich der Regenerativen Energien (Ausgewählte Aspekte)*, 2008. ISBN 978-3-940961-03-7.

MAFO-22 Komarnicki, P.: *Anwendung hochgenauer, synchroner Messungen zur Verbesserung des Betriebs von Verteilungsnetzen*, 2008. ISBN 978-3-940961-04-4.

MAFO-23 Roggatz, C.: *Trainingssimulator für die Führung von elektrischen Systemen mit dezentralen Energieeinspeisungen – Trainingsszenarien und Umsetzung*, 2008. ISBN 978-3-940961-05-1.

MAFO-24 Rudion, K.: *Aggregated Modelling of Wind Farms*, 2008. ISBN 978-3-940961-14-3.

MAFO-25 Ganjavi, M. R.: *Protection System Coordination Using Expert System*, 2008. ISBN 978-3-940961-15-0.

MAFO-26 Bofinger, S.: *Energieversorgungsnetze mit einem hohen Anteil an photovoltaischer Solarenergie: Standortbestimmung, Solarstromprognose, Netzintegration*, 2008. ISBN 978-3-940961-25-9.

MAFO-27 Styczynski, Z. and P. Komarnicki: *Distributed and Renewable Power Generation*, 2008. ISBN 978-3-940961-26-6.

MAFO-28 Kochetov, S. V.: *Time- and Frequency-Domain Modeling of Passive Interconnection Structures in Field and Circuit Analysis*, 2008. ISBN 978-3-940961-27-3.

MAFO-29 Magdowski, M.: *Entwicklung und Validierung eines Werkzeugs zur Berechnung der elektromagnetischen Einkopplung von stochastischen Feldern in Leitungsstrukturen*, 2008. ISBN 978-3-940961-28-0.

MAFO-30 Sonnemann, F.: *Elektromagnetische Effekte an elektrischen Zündmitteln (EED) mit angeschlossener Zündkreiselektronik (ZKE) bei impulsförmiger, breitbandiger Bestrahlung*, 2009. ISBN 978-3-940961-32-7.

MAFO-31 Smieja, T.: *Multikriterielle Planung interregionaler Elektrizitätsnetze im liberalisierten Energiemarkt*, 2009. ISBN 978-3-940961-35-8.

MAFO-32 Heyde, C. O.: *Dynamic Voltage Security Assessment for On-Line Control Room Application*, 2010. ISBN 978-3-940961-40-2.

MAFO-33 Styczynski, Z. A. and N. I. Voropai (Editors): *Renewable Energy Systems Fundamentals, Technologies, Techniques and Economics*, 2010. ISBN 978-3-940961-42-6.

MAFO-34 Styczynski, Z. A. и N. I. Voropai (Editors): Renewable Energy Systems Fundamentals, Technologies, Techniques and Economics (Russian Version), 2010. ISBN 978-3-940961-44-0.

MAFO-35 Styczynski, Z. A. and A. Lindemann (Editors): *Integration of Renewable Energies into the Grid / Proceedings of the Power & Energy Student Summit 2010*, 2010. ISBN 978-3-940961-47-1.

MAFO-36 Styczynski, Z. A. und H.-D. Musikowski (Editors): *Dresdener Kreis Elektroenergieversorgung 11*, 2010. ISBN 978-3-940961-51-8.

MAFO-37 Gurbiel, M. A.: *Definition and Testing of a Digital Interface of a Power Substation*, 2011. ISBN 978-3-940961-54-9.

MAFO-38 Lombardi, P.: *Multi Criteria Optimization of an Autonomous Virtual Power Plant*, 2011. ISBN 978-3-940961-55-6.

MAFO-39 Powalko, M.: *Beobachtbarkeit eines elektrischen Verteilungsnetzes – Ein Beitrag zum Smart Grid*, 2011. ISBN 978-3-940961-62-4.

MAFO-40 Styczynski, Z. A., K. Rudion, and C. Nguyen-Mau (Editorial Board): *Power System Dynamic Security Assessment*, 2011. ISBN 978-3-940961-61-7.

MAFO-41 Käbisch, M: *Optimale Dimensionierung und Betriebsführung einer brennstoffzellenbasierten Auxiliary Power Unit im Fahrzeug*, 2011. ISBN 978-3-940961-67-9.

MAFO-42 Styczynski, Z. A. und N. I. Voropai (Editors): *Special Issue Grant 220 Russian Federation SSmart Grid for Efficient Energy Power System for the Future", Proceedings Volume I*, 2012. ISBN 978-3-940961-74-7.

MAFO-43 Styczynski, Z. A., P. Komarnicki und A. Naumann (Editors): *Abschlussbericht Harz.ErneuerbareEnergien-mobility*, 2012. ISBN 978-3-940961-71-6.

MAFO-44 Heuer, M.: *Diagnosetool für stationär betriebene PEM-Brennstoffzellensysteme*, 2012. ISBN 978-3-940961-77-8.

MAFO-45 Stötzer, M.: *Demand Side Integration in elektrischen Verteilnetzen – Potenzialanalyse und Bewertung*, 2012. ISBN 978-3-940961-78-5.

MAFO-46 Magdowski, M.: *Vergleich der Einkopplung deterministischer und statistischer elektromagnetischer Felder in Leitungen*, 2012. ISBN 978-3-940961-75-4.

MAFO-47 Naumann, A.: *Leitwarte im Smart Grid*, 2012. ISBN 978-3-940961-81-5.

MAFO-48 Rudion, K.: *Offshore Power System Planning – Selected Aspects*, 2012. ISBN 978-3-940961-82-2.

MAFO-49 Nguyen-Mau, C.: *Electric Power System Stability Enhancement by Voltage Source Converter based High Voltage Direct Current Technology*, 2012. ISBN 978-3-940961-84-6.

MAFO-50 Guo, H.: *Measurement-Based Load Modeling for Smart Grid Planning*, 2012. ISBN 978-3-940961-86-0.

MAFO-51 Styczynski, Z. A.: *Proceedings No. 2 in the Scope of Mega Grant Baikal*, 2013. ISBN 978-3-940961-95-2.

MAFO-52 Styczynski, Z. A.: *Proceedings No. 3 in the Scope of Mega Grant Baikal*, 2013. ISBN 978-3-940961-98-3.

MAFO-53 Wenge, C.: *Optimaler Betrieb von mobilen Speichern im Smart Grid. -Mobilitätsleitwarte-*, 2013. ISBN 978-3-944722-01-6.

MAFO-54 Röhrig, C.: *Smart Distribution Planung unter Berücksichtigung von residualen Lasten*, 2014. ISBN 978-3-944722-06-1.

MAFO-55 Middelstädt, F.: *Research of SEM Poles of Complex Wire Structures*, 2014. ISBN 978-3-944722-07-8.

MAFO-56 Styczynski, Z. A. (Editor): *Power Network and Renewables – A Scientific Report – 15 Years Research*, 2014. ISBN 978-3-944722-08-5.

MAFO-57 Solonina, N. N., V. S. Stepanov, and K. V. Suslov: *Information technology in intelligent power networks*, 2014. ISBN 978-3-944722-13-9.

MAFO-58 Krebs, R.: *Fundamentals of Power System Protection*, 2014. ISBN 978-3-944722-15-3.

MAFO-59 Moskalenko, N.: *Optimal Dynamic Energy Management System in Smart Homes*, 2014. ISBN 978-3-944722-16-0.

MAFO-60 Hauer, I.: *Optimale Last- und Erzeugungsanpassung bei kritischen Netzzuständen – Algorithmen und deren Bewertung*, 2014. ISBN 978-3-944722-18-4.

MAFO-61 Richter, M.: *Dresdner Kreis Elektroenergieversorgung 15, Begleitband zum Workshop 2014*, 2014. ISBN 978-3-944722-21-4.

MAFO-62 Styczynski, Z. A., A. Richter und P. Kühne: *Second ELECON Workshop – Begleitband zum Workshop 2014*, 2014. ISBN 978-3-944722-23-8.

MAFO-63 Bernstein, P.: *Modellgestützte optimale Betriebsführung von PEM-Brennstoffzellen für autonome Anlagen*, 2015. ISBN 978-3-944722-24-5.

MAFO-64 Rabe, S.: *Betrieb einer Zweipunkt-Offshore-HGÜ-Verbindung – Modelluntersuchungen*, 2015. ISBN 978-3-944722-31-3.

MAFO-65 Arendarski, B.: *Reliability Assessment of Smart Grids*, 2015. ISBN 978-3-944722-32-0.

MAFO-66 Pan, X.: *Numerisches EMV-Simulationsverfahren zur Berechnung der Störaussendung elektrischer Antriebssysteme in Hybridfahrzeugen*, 2016. ISBN 978-3-944722-34-4.

MAFO-67 Richter, M.: *PMU-basierte Zustandsabschätzung in Smart Distribution*, 2016. ISBN 978-3-944722-43-6.

MAFO-68 Bielchev, I.: *Adaptiver Distanzschutz im Standard IEC 61850*, 2016. ISBN 978-3-944722-45-0.

MAFO-69 Hassan, A.: *Modeling of Single and Double-Shielded Cables for EMC Applications*, 2016. ISBN 978-3-944722-41-2.

MAFO-70 Liu, X.: *Control of Voltage Source Converter Based High Voltage Direct Current Transmission Systems for Grid Code Compliance*, 2016. ISBN 978-3-944722-46-7.

MAFO-71 Kaiser, M.: *Fusion of Interventional Ultrasound & X-ray*, 2016. ISBN 978-3-944722-51-1.

MAFO-72 Grieger, F.: *Ein Beitrag zur Bestimmung der Zuverlässigkeit von Leistungshalbleiterbauelementen unter Berücksichtigung der Anwendung*, 2016. ISBN 978-3-944722-52-8.

MAFO-73 Li, M.: *Towards a Robust Electromagnetic Tracking System for Use in Medical Applications*, 2018. ISBN 978-3-944722-66-5.

MAFO-74 Klabunde, C., J. Dancker, N. Gast, T. Schröter, F. Schulz, J. Rossberg und A. Richter: *Statusbericht der Otto-von-Guericke-Universität Magdeburg zum Verbundprojekt: Intelligentes Multi-Energie-System (SmartMES)*, 2018. ISBN 978-3-944722-69-6.

MAFO-75 Schröter, T.: *19. Dresdner Kreis Elektroenergieversorgung, Begleitband zum Workshop 2018 in Magdeburg*, 2018. ISBN 978-3-944722-79-5.

MAFO-76 Klabunde, C., J. Dancker, N. Gast, T. Schröter, F. Schulz und J. Rossberg: *Intelligentes Multi-Energie-System (SmartMES) – Statusbericht der Otto-von-Guericke-Universität Magdeburg zum Verbundprojekt, 2. Statusseminar 04. April 2019 in Magdeburg*, 2019. ISBN 987-3-944722-80-1.

MAFO-77 Helm, S., J. Dancker, M. Fritsch und T. Schröter: *Power and Energy Student Summit 2019, 09.–11. Juli*, 2019. ISBN 978-3-944722-84-9.

MAFO-78 Chychykina, I.: *Comparison of Different Redispatch Optimization Strategies*, 2019. ISBN 978-3-944722-89-4.

MAFO-79 Balischewski, S.: *Multifunktionaler Einsatz von Batteriespeichern in elektrischen Verteilnetzen*, 2020. ISBN 978-3-944722-92-4.

MAFO-80 Petzold, J.: *Analytische Beschreibung der Kopplung elektromagnetischer Felder durch Aperturen in Resonatoren*, 2020. ISBN 978-3-944722-91-7.

MAFO-81 Middelstädt, L.: *Transiente Effekte in leistungselektronischen Schaltungen mit schnellschaltenden Leistungshalbleitern unter besonderer Berücksichtigung der elektromagnetischen Verträglichkeit*, 2020. ISBN 978-3-944722-95-5.

MAFO-82 Liu, Y.: *Contribution to Improve the EMI Performance of Electrical Drive Systems in Vehicles With Special Consideration of Power Semiconductor Modules*, 2021. ISBN 978-3-948749-01-9.

MAFO-83 Gerlach, A.: *Regelung von direktangetriebenen elektrischen Maschinen für Verbrennungsmotoren*, 2021. ISBN 978-3-948749-03-3.

MAFO-84 Zhang, Y.: *Analysis and Control of Resonances in HVDC Connected DFIG-Based Offshore Wind Farms*, 2021. ISBN 978-3-948749-05-7.

MAFO-85 Pannicke, E.: *Empfangsspulen für bildgeführte Eingriffe mittels Magnetresonanztomographie*, 2021. ISBN 978-3-948749-12-5.

MAFO-86 Kasper, J.: *Analysis of the Stochastic Electromagnetic Field Coupling to Single and Multiconductor Transmission Line Structures*, 2021. ISBN 978-3-948749-13-2.

MAFO-87 Hauer, I.: *Abschlussbericht zum Projekt InKola: Infrastrukturkopplung – Platzierung und Betrieb von Ladestationen aus Verkehrs- und Energienetzsicht*, 2022. ISBN 978-3-948749-15-6.